INFORMATION TO USERS

This manuscript has been reproduced from the microfilm master. UMI films the text directly from the original or copy submitted. Thus, some thesis and dissertation copies are in typewriter face, while others may be from any type of computer printer.

The quality of this reproduction is dependent upon the quality of the copy submitted. Broken or indistinct print, colored or poor quality illustrations and photographs, print bleedthrough, substandard margins, and improper alignment can adversely affect reproduction.

In the unlikely event that the author did not send UMI a complete manuscript and there are missing pages, these will be noted. Also, if unauthorized copyright material had to be removed, a note will indicate the deletion.

Oversize materials (e.g., maps, drawings, charts) are reproduced by sectioning the original, beginning at the upper left-hand corner and continuing from left to right in equal sections with small overlaps. Each original is also photographed in one exposure and is included in reduced form at the back of the book.

Photographs included in the original manuscript have been reproduced xerographically in this copy. Higher quality 6" x 9" black and white photographic prints are available for any photographs or illustrations appearing in this copy for an additional charge. Contact UMI directly to order.

UMI

A Bell & Howell Information Company
300 North Zeeb Road, Ann Arbor MI 48106-1346 USA
313/761-4700 800/521-0600

Electronic Structures of Iron Monocarbide (FeC) and Rhenium Mononitride (ReN)

by

Jianying Cao

B. Eng., Harbin Institute of Technology, China, 1982
M. Sc., Harbin Institute of Technology, China, 1984

A Dissertation Submitted in Partial Fulfillment of the
Requirements for the Degree of

DOCTOR OF PHILOSOPHY

in the Department of Physics and Astronomy

We accept this dissertation as conforming to the required standard

Dr. J. B. Tatum, Co-Supervisor (Department of Physics and Astronomy)

Dr. C. X. W. Qian, Co-Supervisor (Department of Chemistry)

Dr. R. E. Horita, Departmental Member (Department of Physics and Astronomy)

Dr. L. P. Robertson, Departmental Member (Department of Physics and Astronomy)

Dr. W. J. Balfour, Outside Member (Department of Chemistry)

Dr. A. J. Merer, External Examiner (Department of Chemistry, University of British Columbia)

ABSTRACT

This dissertation presents detailed studies of the electronic structures of two molecular systems, iron monocarbide (FeC) and rhenium mononitride (ReN). There had been no research on either molecule prior to the present investigation.

FeC is the first 3d transition metal carbide to have been characterized spectroscopically. The ground electronic state of FeC has been established in our studies to be an inverted $^3\Delta$ ($\delta^3\sigma^1$) state, based on the experimental observations and molecular orbital considerations. Laser-induced-fluorescence signals originating from the two lowest spin components of the ground $X^3\Delta_i$ state were observed. Investigation of the excitation spectrum of the molecule revealed two $^3\Delta_3$ states and two $^3\Delta_2$ states. A strongly perturbed band at 448nm was also rotationally analyzed and deperturbed. It involves three vibronic states with Ω=3.

The $^1\Delta_2$ state with the same electron configuration as the ground state was determined to be 3480±50cm^{-1} above the $X^3\Delta_2$ state in the dispersed fluorescence spectrum. A four-state model has been developed to investigate the interactions between the $^1\Delta$ state and the $X^3\Delta_i$ state. It was found that the singlet state has a strong influence on the effective rotational constants, as well as the relative energies, of the three spin components of the ground state. The model yielded a value of a_δ=372±0.5cm^{-1} for the spin-orbit constant of the non-bonding δ orbital, which is significantly different from the atomic value ζ_{3d}(Fe)=417 cm^{-1} but close to that observed for FeO (379.79cm^{-1}).

Rotational analyses of the LIF excitation spectrum of ReN revealed that the [18.5]1 electronic state was strongly perturbed. Detailed studies of the [18.5]1-X0$^+$ band system showed that heterogeneous interactions ($\mathbf{J}_a$-uncoupling) were responsible for the perturbations. A "filtered" LIF technique was used in the experiment to separate excitation spectra contributed from different electronic states which were perturbing each other.

Dispersed fluorescence spectra of ReN yielded many low-lying electronic states. The symmetry of these low-lying states, in Hund's case (a) notation, have been established to be $^3\Sigma_1^-$, $^3\Delta_3$, $^3\Delta_2$, $^3\Delta_1$, and $^1\Sigma_{0^-}^+$, respectively, based on their energies and their connections with other excited states. The spin-orbit constant of the non-bonding δ orbital of ReN has been determined to be 2455±50cm^{-1}.

Dr. J. B. Tatum, Co-Supervisor (Department of Physics and Astronomy)

Dr. C. X. W. Qian, Co-Supervisor (Department of Chemistry)

Dr. R. E. Horita, Departmental Member (Department of Physics and Astronomy)

Dr. L. P. Robertson, Departmental Member (Department of Physics and Astronomy)

Dr. W. J. Balfour, Outside Member (Department of Chemistry)

Dr. A. J. Merer, External Examiner (Department of Chemistry, University of British Columbia)

Table of Contents

Abstract ii
Table of Contents iv
List of Tables vii
List of Figures viii
Acknowledgments xi
Dedication xii
1. Introduction 1
2. Basic Theories of the Diatomic Molecule 7
2.1 Introduction 7
2.2 Basic Concepts of Quantum Mechanics 8
2.2.1 systems 8
2.2.2 wavefunctions 9
2.2.3 operators 10
2.2.4 angular momentum 14
2.2.5 coupling of two angular momenta 17
2.2.6 the Schrödinger equation 18
2.3 States of the Diatomic Molecule 20
2.3.1 the electronic states of the diatomic molecule 20
2.3.1.1 states of a one-electron system 20
2.3.1.2 states of a many-electron system 25
2.3.2 vibration and rotation of a diatomic molecule 30
2.3.3 the total wavefunctions of a diatomic molecule 34
2.4 Derivation of the Electronic Wavefunctions 37
2.4.1 electron configuration 37
2.4.2 eigenfunctions of S^2 and S_z 38
2.4.3 eigenfunctions for a given electron configuration 41
2.5 Selection Rules for Electric Dipole Transitions 47
2.6 Perturbation Theory 49

2.7 The Matrix Elements 56
3. Experimental Details 61
3.1 Introduction 61
3.2 Laser Vaporization Molecular Beam Source 64
3.2.1 the sample gas and the vacuum chamber 64
3.2.2 the molecular beam valve 65
3.2.3 the metal rod and the vaporization laser 68
3.3 The Laser-induced-fluorescence Techniques 69
3.3.1 the laser-induced-fluorescence 69
3.3.2 the excitation laser 72
3.3.3 the fluorescence collection system 72
3.4 The Data Processing System 74
3.4.1 the oscilloscope 74
3.4.2 computer interface and software 75
3.4.3 experimental procedure 76
4. The Electronic Structure and Perturbations of Iron Monocarbide (FeC) 78
4.1 Introduction 78
4.2 Excitation Spectra of FeC 81
4.3 Rotational Analyses 89
4.4 The Vibrational Analyses 93
4.5 Excited State Lifetimes 99
4.6 Dispersed fluorescence Spectra of FeC 103
4.7 The Electron Configuration of the Ground State 111
4.8 The Spin-orbit Constant 115
4.9 The Electron Configurations of the Excited State 123
4.10 Perturbations in FeC 128
4.11 Concluding Remarks 138
5. Electronic Structure and Perturbations of Rhenium Mononitride (ReN) 140
5.1 Introduction 140
5.2 The Ground Electronic State 142

5.3 Deperturbation Analyses of the [18.5]1 State 151
5.4 The low-lying Electronic States 178
5.5 Conclusions 184
6. Other Published Work 185
7. References 195

List of Tables

Table 2.1: Eigenfunctions of $\hat{S}^2$ and $\hat{S}_z$ for $\Sigma = S$ components 42

Table 2.2: Modified wavefunctions of $\hat{S}^2$ and $\hat{S}_z$ for $\Sigma = S$ components 46

Table 4.1: Rotational assignments and vacuum wavenumbers (in cm^{-1}) for the 0-0 band of the $(I)^3\Delta_3 - X^3\Delta_3$ system at 493.0nm 83

Table 4.2: Bandheads, band origins, rotational constants, and vibronic assignments of the observed FeC bands 91

Table 4.3: Observed isotope band head shifts due to the naturally occurring minor species $^{54}Fe^{12}C$ and $^{54}Fe^{13}C$ 98

Table 4.4: Excited state lifetimes of FeC 101

Table 4.5: Observed low lying vibronic state energies of FeC from dispersed fluorescence spectra 108

Table 4.6: Summary of all currently known electronic states of FeC 124

Table 4.7: Rotational energy levels of the three interacting excited vibronic states associated with the 488nm band 131

Table 4.8: Spectroscopic parameters (in cm^{-1}) of the deperturbed three excited vibronic states associated with the 488nm band 133

Table 5.1: Rotational constants (in cm^{-1}) obtained for the X0$^+$ state of $^{185}Re^{14}N$ and $^{187}Re^{14}N$ 144

Table 5.2: Rotational constants (in cm^{-1}) obtained for the [23.8]1 state of $^{185}Re^{14}N$ and $^{187}Re^{14}N$ 145

Table 5.3: Bandheads, band origins, rotational constants, and vibronic assignment of the observed $^{187}Re^{14}N$ bands 152

Table 5.4: Rotational assignments of the 540nm band 158

Table 5.5: Spectroscopic parameters (in cm^{-1}) of the deperturbed $Re^{14}N$ [18.5]1 (v'=0,1) and [18.5]2 (v'=0,1) vibronic states 161

Table 5.6: Summary of all observed low-lying vibronic states of $^{187}Re^{14}N$ from dispersed fluorescence spectra 176

List of Figures

Figure 2.1: Spherical polar coordinates 21

Figure 2.2: Cylindrical coordinates 23

Figure 2.3: Electronic, vibrational, and rotational energy levels of a diatomic molecule (schematic) 32

Figure 3.1: Experimental setup 63

Figure 3.2: Molecular beam laser vaporization source 66

Figure 3.3: Absorption and fluorescence process in LIF technique 70

Figure 4.1: The LIF excitation spectra of the 493.0nm transition 82

Figure 4.2: A summary of $Fe^{12}C$ bands observed in this study 85

Figure 4.3: The $Fe^{12}C$ LIF spectrum of the $(I)^3\Delta_2 \leftarrow X^3\Delta_2$ 2-0 band at 465 4nm 87

Figure 4.4: Isotope shifts of all observed bands 95

Figure 4.5: Electron configurations and related states of CrN 96

Figure 5.6: The LIF decay curve observed at 493.0nm 100

Figure 4.7: Dispersed fluorescence (DF) spectra of $Fe^{12}C$ observed with the $(I)^3\Delta_3$ state 104

Figure 4.8: Dispersed fluorescence (DF) spectra of $Fe^{12}C$ observed with the $(I)^3\Delta_2$ state 105

Figure 4.9: Dispersed fluorescence (DF) spectra of $Fe^{12}C$ observed with the $(II)^3\Delta_3$ state 106

Figure 4.10: Dispersed fluorescence (DF) spectra of $Fe^{12}C$ observed with the $(III)^3\Delta_2$ state 107

Figure 4.11: Dispersed fluorescence (DF) spectra of $Fe^{12}C$ observed with the $(I)^3\Delta_2$ and the $(III)^3\Delta_2$ states 109

Figure 4.12: The qualitative FeC molecular orbital diagram and the electron configuration of the $^3\Delta_i$ ground state 112

Figure 4.13: Function $y = 1 + x(x - \sqrt{x^2 + 1})$ 120

Figure 4.14: Determination of the molecular spin-orbit constant from the energy spacing between the triplet and the singlet states 122
Figure 4.15: The strongly perturbed 488nm band of FeC 129
Figure 4.16: The deperturbation analysis of the 488nm band assuming homogeneous interactions 134
Figure 4.17: The deperturbation analysis of the 488nm band assuming heterogeneous interactions 135
Figure 4.18: Rotational constant B_v of the $(I)^3\Delta_3$ state 137
Figure 5.1: The laser excitation spectrum of the 0-0 band of the [23.8]1-X0$^+$ system of the $^{187}Re^{14}N$ molecule at 420.9nm 143
Figure 5.2: The qualitative ReN molecular orbital diagram and the electron configuration of the $^3\Sigma^-$ ground state 146
Figure 5.3: Observed vibronic transitions in the LIF spectrum of $^{187}Re^{14}N$ 153
Figure 5.4: The perturbed 0-0 band of the [18.5]1-X0$^+$ system at 540nm 154
Figure 5.5: The effective rotational constant B defined from the difference combinations 156
Figure 5.6: $Re^{14}N$ and $Re^{15}N$ [18.5]1-X0$^+$ bands near 540nm 157
Figure 5.7: The experimental $Re^{14}N$ 540nm band and a simulation based on our deperturbation analysis 162
Figure 5.8: Rotational constants of the vibrational levels of the [18.5]1 state 163
Figure 5.9: LIF spectra associated with the [18.5]1-X0$^+$ and [18.5]2-X0$^+$ systems 165
Figure 5.10: LIF spectra associated with the [18.5]1-X0$^+$ and [18.5]2-X0$^+$ systems 167
Figure 5.11: Lifetimes of the [18.5]1 state as a function of vibrational and rotational quantum numbers 168
Figure 5.12: Dispersed fluorescence spectra of ReN, following the excitation to the [18.5]1 state 170
Figure 5.13: Dispersed fluorescence spectra of ReN, following the excitation to the [22.2]1 state 171

Figure 5.14: Dispersed fluorescence spectra of ReN, following the excitation to the [23.8]1 state 172

Figure 5.15: Dispersed fluorescence spectra of ReN, following the excitation to the [24.7]0^+ state 173

Figure 5.16: Dispersed fluorescence spectra of ReN, following the excitation to the [26.0]0^+ state 174

Figure 5.17: Dispersed fluorescence spectra of ReN, following the excitation to the [18.5]2 state 175

Figure 5.18: Observed emissions and electronic states of ReN 179

Acknowledgments

Many people were of great assistance to me in the completion of this dissertation. I would like to thank all of them. I am especially grateful to

Dr. Charles X. W. Qian, my supervisor, for his continuous scientific advice and financial support during my time at UVic. Many comments from him and many insightful discussions with him have benefited me greatly.

Dr. Walter J. Balfour for what I have learned from him about spectroscopy. His critical proofreading and suggestions also helped to make this dissertation acceptable.

Dr. Jeremy B. Tatum for his longtime encouragement and some helpful discussions.

Dr. C. V. V. Prasad for his contributions in the rotational analyses of all regular FeC LIF excitation spectral bands.

Mr. Scott J. Rixon for his contributions in analyses of all regular ReN LIF excitation spectral bands.

Dr. Chi Zhou for providing Figure 4.5 and other unpublished data on CrN.

Mr. Scott Fougere for his help in recording the DF spectra of FeC.

Dr. Hans-Peter Loock for his contributions in building up the experimental setups and developing software during the early stage of the projects.

Other labmates, Ms Romey Heuff, Dr. Yifei Wang, and Mr. Roy Jensen, for their instructive discussions and their friendship.

Dedication

to

Michelle and Vicky

Chapter 1

Introduction

Transition elements can be defined as those that have unpaired d electron(s), *i.e.*, the elements of the periodic table from group 3 to group 10 (IUPAC proposal 1985, [1]) (or group IIIB to group VIIIB in Chemical Abstracts Service group notation [1]). These elements are characterized by the participation of d orbitals in chemical bond formation (therefore the group 11 elements, sometimes even the group 12 elements, are often included among the transition elements in view of their active d electrons). Transition elements are also known as transition metals because of their typical metallic properties. In the following the elements from scandium (Sc) to nickel (Ni) will be referred to as 3d transition metals, while those from yttrium (Y) to palladium (Pd) will be referred to as 4d transition metals. Those elements which have unpaired f electron(s) as well as unpaired d electrons (so called inner-transition elements) will not be considered here because of their distinctive features from other transition metals. So the 5d transition metals include lanthanum (La) and elements from hafnium (Hf) to platinum (Pt).

Transition metal containing diatomic molecules are very important in astrophysics [2]. For instance, the band systems of TiO and VO completely dominate the spectra of cooler (M-type) stars if the stars contain metal-rich recycled supernova material [3], and are used to classify these stars on the MK system [3-6]. At high resolution the rotational line strengths can even be used as a thermometer for the circumstellar envelope [7].

The ^{56}Fe nucleus is the most stable nucleus in terms of binding energy per nucleon, so that it is the final product in the thermal fusion processes that fuel stars. The abundance of this nucleus has important implications for nucleosynthesis, and detecting iron

containing molecules is of particular interest for astrophysicists. The molecule FeH has been identified in the spectra of sunspots and cool stars [8-9]. FeO was searched for in interstellar sources [10] but never detected. One of the iron containing molecules searched for most recently is FeCO [11] in interstellar objects under different physical conditions in various evolutionary stages, including IRC+10216 as a carbon rich standard object, NML-Tau and IRC+10529 as oxygen rich standard objects, CRL618, CRL2688, and OH231.8+4.2 as protoplanetary nebulae, Sgr-B2, NGC7538, and L1157 as star forming regions, and L134N as a dark cloud. All these searches were carried out in conjunction with precise laboratory spectroscopy measurements.

The recent discovery of metal containing molecules, such as molecules bearing magnesium (MgCN and MgNC [12-13]), aluminum (AlCl and AlF [1.14]), sodium (NaCl and NaCN [14-15]), and even potassium (KCl [14]), in the circumstellar envelope of the late-type carbon star IRC+10216 has inspired spectroscopic interests in FeF [16]. It also raised the hope that iron-containing molecules, in addition to FeH, would eventually be observed in circumstellar or even interstellar material because of the relatively high (0.003%) cosmic abundance of iron compared with that of magnesium, aluminum, sodium, and potassium. Particularly, the detection of SiC [17] in IRC+10216 gives evidence that refractory elements combined with carbon exist, at least in the carbon rich envelope of IRC+10216.

Interstellar studies of transition metal monocarbides have not been carried out so far because spectroscopic studies for these elusive molecules are sparse, and most of these species still remain to be discovered experimentally. For instance, before our publication of the spectroscopic data of FeC in 1995 [18] there were only five transition metal

monocarbides, *viz.*, YC [19], RuC [20-21], RhC [22-24], IrC [25-27], and PtC [28-32], where detailed gas phase spectra had been reported. Of these five species the molecule YC was discovered in 1994 [19], while the ground electronic state of the molecule RuC was not characterized until 1996 [33]. Additional transition monocarbides were discovered in the 1990s, including CoC [34-35], NiC [33, 36], CrC [33], and MoC [33].

The steady growth of work on transition metal containing diatomic systems in the 1990s has benefited from the recent developments of experimental techniques. The most important development is in the creation of transition metal containing molecules at very low internal temperature. Conventionally the solid metals had to be vaporized in a high temperature oven. The metal vapor was then mixed with necessary reactive gases to form desirable metal diatomic molecules [23]. Because of the high temperature necessary to melt metals, the corresponding spectra are always congested and valuable information about low J rotational levels is masked. Besides, the yields of the metal containing molecules are quite low. Successful modifications have been made in various groups by, for example, introducing flowing gas discharges [37], electron bombarding of the metal covered anode in a hollow cathode lamp [38], and combining of laser-ablation with a molecular beam [19]. Laser ablation of metals followed by a supersonic expansion of a molecular beam has been adopted by many research groups [18-19, 34-35] for its high efficiency in the formation of metal containing molecules.

Understanding of the bonding between transition metal atoms and other compounds (including atoms, molecules, and radicals) is essential in catalytic cycles and organometallic chemistry, and presents considerable challenges both experimentally and theoretically. Even the simplest diatomic systems, *i.e.*, MX (M=transition metal atoms, X

= hydrogen (H), fluorine (F), oxygen (O), nitrogen (N), or carbon (C)), have attracted a significant amount of interest among experimentalists [2] and theoreticians [39]. The unique features that make the transition metal containing molecules different from others are the small energy gaps and the similar spatial extent of the metal *n*d, (*n*+1)s, and (*n*+1)p orbitals ($n = 3, 4$, and 5 for 3d, 4d, and 5d transition metal atoms, respectively). Many unpaired *n*d, (*n*+1)s, and (*n*+1)p electrons give rise to a great number of low-lying atomic electronic states [40], which, in turn, results in very complicated electronic structure for transition metal containing molecules. Another consequence of many low-lying atomic electronic states with different occupations of the *n*d, (*n*+1)s, and (*n*+1)p orbitals is the variety of bonding mechanisms that occur [39]. For instance, the low-lying electronic states of both FeH and FeF can be understood in terms of Fe^+ energy levels in the negatively charged ligand (H^- or F^-) field and are expected to have similar energy level patterns to that of Fe^+ [6]. However, because of the sensitive dependence of the molecular energy levels on many effects, different bonding schemes dominate in these two molecules and result in a $^4\Delta$ [1.41-1.43] and a $^6\Delta$ [1.44-1.47] ground electronic state for FeH and FeF, respectively.

Spectroscopy is an important tool to probe molecular structure and identify new molecules, especially for diatomic molecules. So far spectroscopic studies for the 3d transition metal monoxides [2], monofluorides [16], and monohydrides [48-49] have been completed, at least for the ground electronic states of the entire series. Studies on the 3d transition metal mononitrides are rather limited: for only four of them, *i.e.*, ScN [50], TiN [50-52], VN [53-55] and CrN [56-57], are spectroscopic data available. Work on the

carbides is even sparser. There was no experimental information on gas phase 3d transition metal carbides published until iron carbide (FeC) was discovered in our laboratory [18]. Data on cobalt carbide (CoC) became available at almost the same time [34-35].

What keeps studies on transition metal containing diatomic molecules challenging is not only the difficulties to create those species but also the exceeding complexities of the spectra. Frequently even the identification of the ground electronic state is a hard task. This is partially because of the many possible low lying electronic states and partially because of the deceptively simple appearance of the ground states when spin-orbit splitting becomes very large. For instance, it took more than seventy years to establish the $^3\Delta_i$ symmetry of the ground electronic state of iron monoxide (FeO) [58] following the first observation of the molecule in 1910 [59].

The excited states of transition metal containing molecules are often characterized by their irregular energy level patterns. Even though irregularity (or perturbation) exists essentially in all molecules [60], it is especially complicated for transition metal containing molecules. For example, the perturbations in FeO are so severe that the "orange" band system of FeO was claimed to represent a new kind of diatomic spectrum where the regular structure of an electronic state is destroyed by a multitude of perturbations by lower lying electronic states [61].

Ab initio calculations on transition metal containing molecules are also challenging. The difficulty lies in properly treating the electron correlation effects in the molecules [2]. A quite small change in the model can lead to very different predictions for the energy level order and properties of the low-lying electronic states. There are many theoretical studies on FeH [43, 48, 62-65]; most of them have concentrated on determining the

identity of the ground electronic state. Early studies failed to produce a $^4\Delta$ ground state [48, 62-63] because of the large dynamic correlation energy difference in the $^4\Delta$ state and the $^6\Delta$ state. More recent studies [43, 64] yielded the correct $^4\Delta$ ground state, but these calculations required a large Gaussian basis set, an extensive treatment of correlation, and the inclusion of inner-shell correlation effects. The calculations on FeO, one of the most extensively researched metal oxides [66], are also sensitive to the complexity of the trial functions [67]. Nevertheless, *ab initio* electronic structure calculations have made it possible to treat transition metal containing molecules more quantitatively, emphasizing the need for high quality experimental data [2].

This dissertation is aimed at contributing to an understanding of transition metal containing diatomic molecules with detailed electronic structure analyses of two newly discovered molecules, *i.e.*, iron monocarbide (FeC) and rhenium mononitride (ReN). It is organized as follows: first, the necessary theoretical background is presented in Chapter 2, which includes the basic concepts of diatomic molecular structure, the derivation of spin wavefunctions and the total molecular wavefunctions, and the perturbation theory. A detailed description of the experimental apparatus, including the formation of the molecular beam, the detection of the species of interest, the processing of experimental data, and the overall control of the experiment, is given in Chapter 3. Finally, in Chapter 4 and Chapter 5, the electronic structures of FeC and ReN are discussed in depth.

Chapter 2

Basic Theories of the Diatomic Molecule

2.1 Introduction

The electronic structure and spectra of the diatomic molecule, as well as their perturbations, have been the subjects of many publications [60, 68-69]. In general the related theories have been well established, even though the application of these theories to individual molecular systems is quite complicated [61].

This chapter will only briefly cover the theories which are necessary for the discussions in this dissertation. A simple non-relativistic treatment of the diatomic molecule, consistent with the Born-Oppenheimer approximation and the Hund's case (a) angular momentum coupling scheme [68], is described as the zeroth order approximation. In this treatment the motions of the electrons, the vibrations of the nuclei, and the rotations of the molecular frame are considered separately The total molecular wavefunctions, the corresponding energies, and the electric dipole transition selection rules are presented. The couplings of the total electronic orbital angular momentum, the total electron spin, and the rotational angular momentum of the molecular frame, as well as the spin-orbit interactions, are introduced as perturbations. Because of the nature of the molecular systems under investigation and the limited resolution of our experiment, the perturbations arising from the spins of the nuclei, the electron spin-spin interactions, and the electron spin-rotation interactions need not be considered.

2.2 Basic Concepts of Quantum Mechanics

2.2.1 systems

A free diatomic molecule can be viewed as a closed system of two positively charged nuclei and several, say k, negatively charged electrons, with no interaction with the external environment. The force which holds the system together is mainly the Coulombic force between each pair of charged particles,

$$\mathbf{F}_{ij} = \frac{Q_i Q_j}{r_{ij}^2} \frac{\mathbf{r}_{ij}}{r_{ij}} \qquad (2.1)$$

where $\mathbf{F}_{ij}$ is the force on the ith particle applied by the jth particle; Q_i and Q_j are, respectively, the charges of the two particles; $\mathbf{r}_{ij}$ is the distance vector pointing from the jth particle to the ith particle.

For a neutral diatomic molecule in its stable states, the average magnitudes of the resultant force on each individual particle (nucleus or electron) are comparable, yet the mass of a nucleus and that of an electron differ by several orders of magnitude. As a result, in the center-of-mass frame of reference, the lighter electrons move much faster than the heavier nuclei: the mean speed of each particle is inversely proportional to its mass. In the case of the lightest nucleus, *i.e.*, the hydrogen nucleus H^+ which consists of only one proton, the ratio between the mass of the nucleus and that of an electron is

$$\frac{m_{proton}}{m_{electron}} = 1836 \qquad (2.2)$$

In a semiclassical point of view, the electrons move at least 1800 times faster than the nuclei in a diatomic molecule. We can therefore treat the nuclei as if they are at rest, and view the electrons as a sub-system moving in the electrostatic field of the nuclei. The

nuclei then move slowly, keeping the electron sub-system always at one of its stable states. This approximation which allows one to separate the motions of the electrons and the nuclei was justified in detail by Born and Oppenheimer [70].

The electrons in the electrostatic field of the "rest" nuclei move so fast that their effects on the nuclei, as well as on each other, are equivalent to those of the continuously distributed "electron cloud". The electron cloud effectively serves as a glue to hold the two nuclei together forming a diatomic molecule.

2.2.2 wavefunctions

In quantum mechanics the state of a k-electron system is described by a complex function Φ of the coordinates

$$\Phi = \Phi(q) \tag{2.3}$$

where q is the collection of all electron coordinates

$$q = \{\mathbf{r}_1, \mathbf{r}_2, \cdots, \mathbf{r}_k\} \tag{2.4}$$

The square of the modulus of this function determines the spatial probability density distribution of the k electrons, *i.e.*,

$$P = |\Phi|^2 \, dq \tag{2.5}$$

is the probability that the first electron is in the volume $d\tau_1 = dx_1 dy_1 dz_1$, the second electron is in the volume $d\tau_2 = dx_2 dy_2 dz_2$, ..., and the kth electron is in the volume $d\tau_k = dx_k dy_k dz_k$, $(dq = d\tau_1 d\tau_2 \cdots d\tau_k)$. Clearly the wavefunction (2.3) should be normalized so that:

$$\int |\Phi|^2 \, dq = 1 \qquad (2.6)$$

The probability density distribution function Φ is called the *wavefunction* of the k-electron system.

Because of the unique correlation between the states of a physical system and the wavefunctions which describe the states mathematically, the two terms (*i.e.*, the *state* and the *wavefunction*) are used interchangeably.

2.2.3 operators

One of the distinguishing features of quantum mechanics is that some physical quantities, under certain restrictions, can only take a set of discrete values. For instance, as Bohr first noticed, an atom cannot exist in states having any arbitrary energy, but only in states with certain distinct energy values [40]. States, where the physical quantity f has a definite value, are called the *eigenstates* of the given physical quantity f, and the corresponding wavefunctions Φ_n are called the *eigenfunctions* (where n is a quantum number or a set of quantum numbers, which fully distinguishes the eigenstates of the physical quantity f from each other). It is convenient to use Dirac notation for both the eigenfunction and the eigenstate. The notation $|n>$ is understood to represent both the wavefunction Φ_n:

$$|n> = \Phi_n \qquad (2.7)$$

and the state which is described by the wavefunction. The values which a given physical quantity f can take are called its *eigenvalues*, and are denoted by f_n. The eigenvalues f_n and the eigenfunctions Φ_n for a given physical quantity f can be determined from the non-

trivial solutions of the eigenequation

$$\hat{f}|n>= f_n|n> \tag{2.8}$$

where $\hat{f}$ is a mathematical operator representing the physical quantity f in quantum mechanics, *e.g.*, the coordinate operator $\hat{\mathbf{r}}$ and the linear momentum operator $\hat{\mathbf{p}}$ are defined as:

$$\hat{\mathbf{r}} = \mathbf{r} \tag{2.9}$$

$$\hat{\mathbf{p}} = -i\hbar\nabla \tag{2.10}$$

where $\hbar$ is the Planck constant divided by 2π; ∇ the differentiation operator. Other important operators are the orbital angular momentum operators (to be discussed in section 2.2.4) and the Hamiltonian operator (to be discussed in section 2.2.6).

The condition for the existence of states which are simultaneously the eigenstates of two physical quantities f and g is that the two operators commute with each other:

$$[\hat{f},\hat{g}] = 0 \tag{2.11}$$

where

$$[\hat{f},\hat{g}] = \hat{f}\hat{g} - \hat{g}\hat{f} \tag{2.12}$$

is the commutator of the two operators.

There are some special operators. One group of such operators is the parity operators, including the inversion operator $\hat{i}$ which changes the sign of all the Cartesian coordinates of the wavefunction:

$$\hat{i}\Phi(q) = \Phi(-q) \tag{2.13}$$

and the plane-reflection operator $\hat{\sigma}$ which changes the sign of only the y coordinates, supposing the reflection plane is the xz plane:

$$\hat{\sigma}\Phi(x_1, y_1, z_1, x_2, y_2, z_2, \ldots) = \Phi(x_1, -y_1, z_1, x_2, -y_2, z_2, \ldots) \qquad (2.14)$$

It is easy to find the eigenvalues for the operator $\hat{i}$ (*e.g.*, applying the operator twice on its eigenfunctions):

$$P_i = \pm 1 \qquad (2.15)$$

When $P_i = +1$ the wavefunction is said to be even, and when $P_i = -1$ the wavefunction is said to be odd.

Like the inversion operator $\hat{i}$, the eigenvalues of the reflection operator $\hat{\sigma}$ are

$$P_s = \pm 1 \qquad (2.16)$$

Another group of operators is the permutation operators $\hat{P}_{ij}$ which exchange the ith and the jth particles in the system:

$$\hat{P}_{ij}\Phi(\cdots, q_i, \cdots, q_j, \cdots) = \Phi(\cdots, q_j, \cdots, q_i, \cdots) \qquad (2.17)$$

where q_i (q_j) is a collection of all variables (including coordinates and spins) associated with the ith (jth) particle.

In quantum mechanics, identical particles (*e.g.*, electrons) are indistinguishable, so that the states of a system obtained from each other by merely interchanging any two of the identical particles must be physically equivalent. Mathematically the wavefunctions can differ at most by a sign upon the permutation operation. In other words, if the ith particle and the jth particle of the system are identical, then

$$\hat{P}_{ij}\Phi = P_{ij}\Phi \qquad (2.18)$$

where the eigenvalues

$$P_{ij} = \pm 1 \qquad (2.19)$$

When $P_{ij} = +1$ the wavefunction is said to be symmetric with respect to an exchange of the identical particles, and when $P_{ij} = -1$ it is said to be antisymmetric. Based on the laws of relativistic quantum mechanics [71] it can be shown that wavefunctions must be antisymmetric with respect to an exchange of any two electrons in the system.

If a two-electron wavefunction $\Phi(q_1, q_2)$ is not antisymmetric, a new antisymmetric function $\Phi'(q_1, q_2)$ can always be constructed as

$$\Phi'(q_1, q_2) = \sqrt{\tfrac{1}{2}}\left[\Phi(q_1, q_2) - \Phi(q_2, q_1)\right] \tag{2.20}$$

which possesses all the physical characteristics of the original wavefunction $\Phi(q_1, q_2)$. In general, an arbitrary k-electron wavefunction $\Phi(q_1, q_2, \cdots, q_k)$ can always be made antisymmetric by transforming it into

$$\Phi'(q_1, q_2, \cdots, q_k) = N \cdot \sum (-1)^{k_{\alpha\beta\cdots\gamma}} \Phi(q_\alpha, q_\beta, \cdots, q_\gamma) \tag{2.21}$$

where N is a proper normalization factor; $k_{\alpha\beta\cdots\gamma}$ is the number of permutations needed to bring the arrangement $\{q_\alpha, q_\beta, \cdots, q_\gamma\}$ into $\{q_1, q_2, \cdots, q_k\}$; the summation is over all k! possible arrangements of $\{q_\alpha, q_\beta, \cdots, q_\gamma\}$.

A special case occurs when the function $\Phi(q_1, q_2, \cdots, q_k)$ is a linear combination of functions which are the products of single variable functions, for example:

$$\begin{aligned}&\Phi(q_1, q_2, \cdots, q_k)\\ &\quad = C^{I}\phi_1^{I}(q_1)\phi_2^{I}(q_2)\cdots\phi_k^{I}(q_k) + C^{II}\phi_1^{II}(q_1)\phi_2^{II}(q_2)\cdots\phi_k^{II}(q_k) + \cdots\end{aligned} \tag{2.22}$$

where C^{I}, C^{II}, ..., are constants; Φ is not antisymmetric regarding a permutation of any pair of electrons. In this case the antisymmetrized function Φ' of (2.22) can be expressed as a sum of Slater determinants:

$$\Phi'(q_1,q_2,\cdots,q_k) = C^I|\phi_1^I(q_1)\phi_2^I(q_2)\cdots\phi_k^I(q_k)| + C^{II}|\phi_1^{II}(q_1)\phi_2^{II}(q_2)\cdots\phi_k^{II}(q_k)|+\cdots \tag{2.23}$$

where the Slater determinant is defined as:

$$|\phi_1(q_1)\phi_2(q_2)\cdots\phi_k(q_k)| = \sqrt{\frac{1}{k!}}\begin{vmatrix} \phi_1(q_1) & \phi_1(q_2) & \cdots & \phi_1(q_k) \\ \phi_2(q_1) & \phi_2(q_2) & \cdots & \phi_2(q_k) \\ \vdots & \vdots & \ddots & \vdots \\ \phi_k(q_1) & \phi_k(q_2) & \cdots & \phi_k(q_k) \end{vmatrix} \tag{2.24}$$

The third group of operators which cannot be expressed by ordinary mathematical operators is the spin and spin related angular momenta, which will be discussed in following sections.

2.2.4 angular momentum

In quantum mechanics the orbital angular momentum operator $\hat{\mathbf{l}}$ of a particle can be defined from its analog in classical mechanics:

$$\hat{\mathbf{l}} = \hat{\mathbf{r}} \times \hat{\mathbf{p}} \tag{2.25}$$

The commutation relations of the Cartesian components of $\hat{\mathbf{l}}$ are

$$[\hat{l}_x, \hat{l}_y] = i\hbar\hat{l}_z \tag{2.26}$$

$$[\hat{l}_y, \hat{l}_z] = i\hbar\hat{l}_x \tag{2.27}$$

$$[\hat{l}_z, \hat{l}_x] = i\hbar\hat{l}_y \tag{2.28}$$

Since the Cartesian components of the orbital angular momentum do not commute with each other, there is no state which is simultaneously an eigenstate of any two of these angular momentum components. On the other hand, the square of the angular momentum, defined as

$$\hat{\mathbf{l}}^2 = \hat{l}_x^2 + \hat{l}_y^2 + \hat{l}_z^2 \tag{2.29}$$

has the commutation properties

$$[\hat{\mathbf{l}}^2, \hat{l}_x] = 0 \tag{2.30}$$

$$[\hat{\mathbf{l}}^2, \hat{l}_y] = 0 \tag{2.31}$$

$$[\hat{\mathbf{l}}^2, \hat{l}_z] = 0 \tag{2.32}$$

Hence we can construct wavefunctions $|\gamma_{l^2}, \gamma_{l_z}>$ that are simultaneously eigenfunctions of $\hat{\mathbf{l}}^2$ and one of the Cartesian components of $\hat{\mathbf{l}}$ ($\hat{l}_z$):

$$\hat{\mathbf{l}}^2 |\gamma_{l^2}, \gamma_{l_z}> = \gamma_{l^2} |\gamma_{l^2}, \gamma_{l_z}> \tag{2.33}$$

$$\hat{l}_z |\gamma_{l^2}, \gamma_{l_z}> = \gamma_{l_z} |\gamma_{l^2}, \gamma_{l_z}> \tag{2.34}$$

It turns out that the eigenvalues γ_{l^2} and γ_{l_z} are

$$\gamma_{l^2} = l(l+1)\hbar^2 \tag{2.35}$$

$$\gamma_{l_z} = m_l \hbar \tag{2.36}$$

where

$$l = 0, 1, 2, \cdots \tag{2.37}$$

$$m_l = 0, \pm 1, \pm 2, \cdots \pm l \tag{2.38}$$

Experimental results show that elementary particles like electrons should be assigned a certain "intrinsic" angular momentum, which is unconnected with motions in space but related purely to relativistic effects. There is no classical analog for this kind of angular momentum; therefore it cannot be defined like (2.25). Nevertheless, a general angular momentum **j** can be defined such that the Cartesian components of its operator $\hat{\mathbf{j}}$

obey the commutation rules (2.26)-(2.28). The angular momentum defined in this way still has the commutation properties (2.30)-(2.32), and possesses simultaneous eigenfunctions of $\hat{j}^2$ and $\hat{j}_z$ with eigenvalues

$$\gamma_{j^2} = j(j+1)\hbar^2 \tag{2.39}$$

which is the squared magnitude of the angular momentum, and

$$\gamma_{j_z} = m_j\hbar \tag{2.40}$$

which is the projection of the angular momentum on the z axis, where

$$j = 0, \tfrac{1}{2}, 1, \tfrac{3}{2}, 2, \cdots \tag{2.41}$$

$$m_j = \begin{cases} 0, \pm 1, \pm 2, \cdots, \pm j & \text{when } j \text{ is integral} \\ \pm\tfrac{1}{2}, \pm\tfrac{3}{2}, \pm\tfrac{5}{2}, \cdots, \pm j & \text{when } j \text{ is half-integral} \end{cases} \tag{2.42}$$

The simultaneous eigenfunctions of $\hat{j}^2$ and $\hat{j}_z$ with quantum numbers j and m_j are written, in Dirac notation, as $|j,m_j>$.

In the case of electron spin s, the quantum number s can take only one value:

$$s = \tfrac{1}{2} \tag{2.43}$$

while the quantum number m_s for the projection of s on the z axis is

$$m_s = \pm\tfrac{1}{2} \tag{2.44}$$

Two important angular momentum related operators are the raising operator $\hat{j}^+$ defined as

$$\hat{j}^+ = \hat{j}_x + i\hat{j}_y \quad \text{where } i = \sqrt{-1} \tag{2.45}$$

and the lowering operator $\hat{j}^-$ defined as

$$\hat{\mathbf{j}}^{-} = \hat{\mathbf{j}}_x - i\hat{\mathbf{j}}_y \tag{2.46}$$

The effects of these two operators on the eigenfunction $|j,m_j>$ are

$$\hat{\mathbf{j}}^{\pm}|j,m_j> = \sqrt{j(j+1) - m_j(m_j \pm 1)}\hbar|j,m_j \pm 1> \tag{2.47}$$

2.2.5 coupling of two angular momenta

Any two angular momenta, $\mathbf{j}_1$ and $\mathbf{j}_2$, can be coupled to form a new angular momentum $\mathbf{j}$, just as in classical mechanics:

$$\mathbf{j} = \mathbf{j}_1 + \mathbf{j}_2 \tag{2.48}$$

The corresponding operators of the resultant angular momentum still satisfy the commutation rules (2.26)-(2.28) and (2.30)-(2.32).

There are two ways to describe the compound system. One is to use the uncoupled representation where the basis functions

$$|j_1,m_1;j_2,m_2> = |j_1,m_1>|j_2,m_2> \tag{2.49}$$

are simultaneous eigenfunctions of the operators $\hat{\mathbf{j}}_1^2$, $\hat{j}_{1z}$, $\hat{\mathbf{j}}_2^2$, and $\hat{j}_{2z}$:

$$\hat{\mathbf{j}}_1^2|j_1,m_1;j_2,m_2> = j_1(j_1+1)\hbar^2|j_1,m_1;j_2,m_2> \tag{2.50}$$

$$\hat{j}_{1z}|j_1,m_1;j_2,m_2> = m_1\hbar|j_1,m_1;j_2,m_2> \tag{2.51}$$

$$\hat{\mathbf{j}}_2^2|j_1,m_1;j_2,m_2> = j_2(j_2+1)\hbar^2|j_1,m_1;j_2,m_2> \tag{2.52}$$

$$\hat{j}_{2z}|j_1,m_1;j_2,m_2> = m_2\hbar|j_1,m_1;j_2,m_2> \tag{2.53}$$

Another way is to use the coupled representation where the basis functions are simultaneously the eigenfunctions of $\hat{\mathbf{j}}^2$, $\hat{j}_z$, $\hat{\mathbf{j}}_1^2$, and $\hat{\mathbf{j}}_2^2$:

$$\hat{\mathbf{j}}^2|(j_1,j_2);j,m>=j(j+1)\hbar^2|(j_1,j_2);j,m> \tag{2.54}$$

$$\hat{j}_z|(j_1,j_2);j,m>=m\hbar|(j_1,j_2);j,m> \tag{2.55}$$

$$\hat{\mathbf{j}}_1^2|(j_1,j_2);j,m>=j_1(j_1+1)\hbar^2|(j_1,j_2);j,m> \tag{2.56}$$

$$\hat{\mathbf{j}}_2^2|(j_1,j_2);j,m>=j_2(j_2+1)\hbar^2|(j_1,j_2);j,m> \tag{2.57}$$

These two sets of basis functions are equivalent and are connected by a linear transformation:

$$|(j_1,j_2);j,m>=\sum_{m_1+m_2=m} C(j_1,j_2,j;m_1,m_2,m)|j_1,m_1>|j_2,m_2> \tag{2.58}$$

or

$$|j_1,m_1>|j_2,m_2>=\sum_{m=m_1+m_2} C(j_1,j_2,j;m_1,m_2,m)|(j_1,j_2);j,m> \tag{2.59}$$

where the coefficients $C(j_1,j_2,j;m_1,m_2,m)$ are called Clebsch-Gordan coefficients.

2.2.6 the Schrödinger equation

The energy operator is the most important operator because its eigenstates, *i.e.*, the stationary states, are the naturally occurring states. For a closed system, or a system in a constant conservative external field, the energy of the system is always conserved. Such systems, *e.g.*, a free diatomic molecule or the electrons in the Coulombic field of the two "rest" nuclei, will, once in a stationary state, remain in the state forever.

The energy operator in quantum mechanics is closely related to the Hamilton function in classical mechanics. The operator is, therefore, called the Hamiltonian of a system, and is denoted by $\hat{H}$. The non-relativistic Hamiltonian has the form:

$$\hat{H} = -\sum_i \frac{\hbar^2}{2m_i} \nabla_i^2 + U(q) \tag{2.60}$$

where m_i is the mass of the ith particle in the system; the operator ∇_i^2 acts only on the ith particle's coordinates; U(q) is the potential function including both the interaction potential among the particles and the potential due to external fields; q is the collection of coordinates defined in (2.4).

The eigenequation

$$\hat{H}\Phi_n = E_n \Phi_n \tag{2.61}$$

is named the Schrödinger equation. The eigenfunctions (Φ_n) of the Schrödinger equation correspond to the stationary states of the system. The stationary state with the smallest possible eigenvalue of the energy (E_0) is called *the ground state* of the system.

Operators corresponding to physical quantities which are conserved commute with the Hamiltonian. These physical quantities, if they also commute with each other, can simultaneously have definite values in the stationary states. So the stationary states are not only characterized by energy, but also by other conserved physical quantities.

Among the various stationary states there may be some which correspond to the same value of the energy but differ in the values of some other conserved physical quantities. Such energies, to which several different stationary states correspond, are said to be *degenerate* [72]. The states are also said to be *degenerate*.

2.3 States of the Diatomic Molecule

2.3.1 the electronic states of the diatomic molecule

2.3.1.1 states of a one-electron system

The non-relativistic Hamiltonian for a one-electron system in an external field with the potential function U(**r**) has the form:

$$\hat{H} = -\frac{\hbar^2}{2m}\nabla^2 + U(\mathbf{r}) \tag{2.62}$$

If U(**r**) is spherically symmetric, *e.g.*, the Coulombic field of the nucleus in an atom, it is convenient to use spherical polar coordinates (Figure 2.1):

$$\hat{H} = -\frac{\hbar^2}{2mr^2}\frac{\partial}{\partial r}\left(r^2\frac{\partial}{\partial r}\right) + \frac{\hat{l}^2}{2mr^2} + U(r) \tag{2.63}$$

where

$$\hat{l}^2 = -\frac{\hbar^2}{\sin\theta}\frac{\partial}{\partial\theta}\left(\sin\theta\frac{\partial}{\partial\theta}\right) - \frac{\hbar^2}{\sin^2\theta}\frac{\partial^2}{\partial^2\phi} \tag{2.64}$$

is the operator of the squared orbital angular momentum.

In the spherically symmetric field, $l^2, l_z, s^2,$ and s_z are conserved. Hence we consider the stationary states which are simultaneously the eigenstates of the operators $\hat{l}^2, \hat{l}_z, \hat{s}^2,$ and $\hat{s}_z$. The eigenfunctions have the form:

$$|n,l,m_l,s,m_s\rangle = |n,l\rangle|l,m_l\rangle|s,m_s\rangle \tag{2.65}$$

which is separated into the radial part $|n,l\rangle$, the angular part $|l,m_l\rangle$, and the spin part $|s,m_s\rangle$. In the case of the Coulombic potential the energy of the electron is solely determined by the quantum number n:

$$e = e(n) \tag{2.66}$$

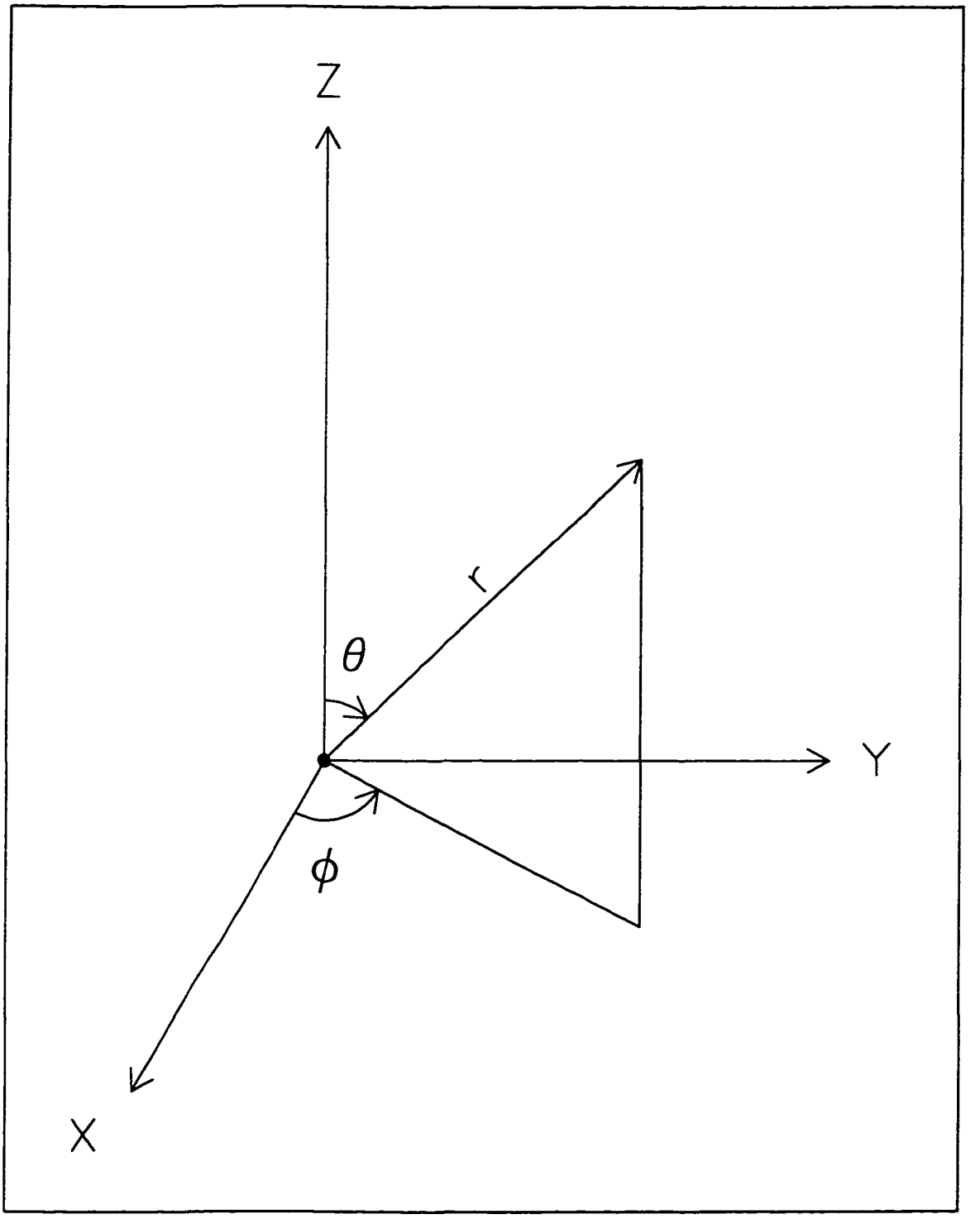

Figure 2.1 Spherical polar coordinates. ($0 \leq \theta \leq \pi$, $0 \leq \phi < 2\pi$, $0 \leq r < +\infty$)

The quantum number l can only take a limited number of values:

$$l = 0, 1, 2, \cdots, n-1 \tag{2.67}$$

In general case, *e.g.*, when the electron is moving in the effective field of the nucleus and other electrons in a many-electron atom, the energy is a function of both the quantum numbers n and l:

$$e = e(n, l) \tag{2.68}$$

Each energy $e(n,l)$ is $2(2l+1)$-fold degenerate: the factor $(2l+1)$ comes from the different values of m_l and it is doubled because of two possible spin directions.

There is a generally accepted notation for the states of an electron in a spherically symmetric field: they are labeled by the principal quantum number n followed by Latin letters according to the quantum number l as follows:

$$\begin{array}{cccccccccc} l & = & 0 & 1 & 2 & 3 & 4 & 5 & 6 & 7 & \cdots \\ & & s & p & d & f & g & h & i & k & \cdots \end{array} \tag{2.69}$$

So we can speak of the 3s states (or 3s electrons) which have the quantum numbers $n = 3$ and $l = 0$.

If the external field is cylindrically symmetric, *e.g.*, the Coulombic field of the two nuclei in a diatomic molecule, the magnitude of the orbital angular momentum is no longer conserved, but the projection of the angular momentum on the symmetry axis (the z-axis) is still conserved. Since the spin is not included in the Hamiltonian explicitly, spin s is still conserved. We should look for the stationary states which are also the eigenstates of the operators $\hat{l}_z$, $\hat{s}^2$, and $\hat{s}_z$.

In cylindrical coordinates (Figure 2.2) the Hamiltonian (2.62) has the form:

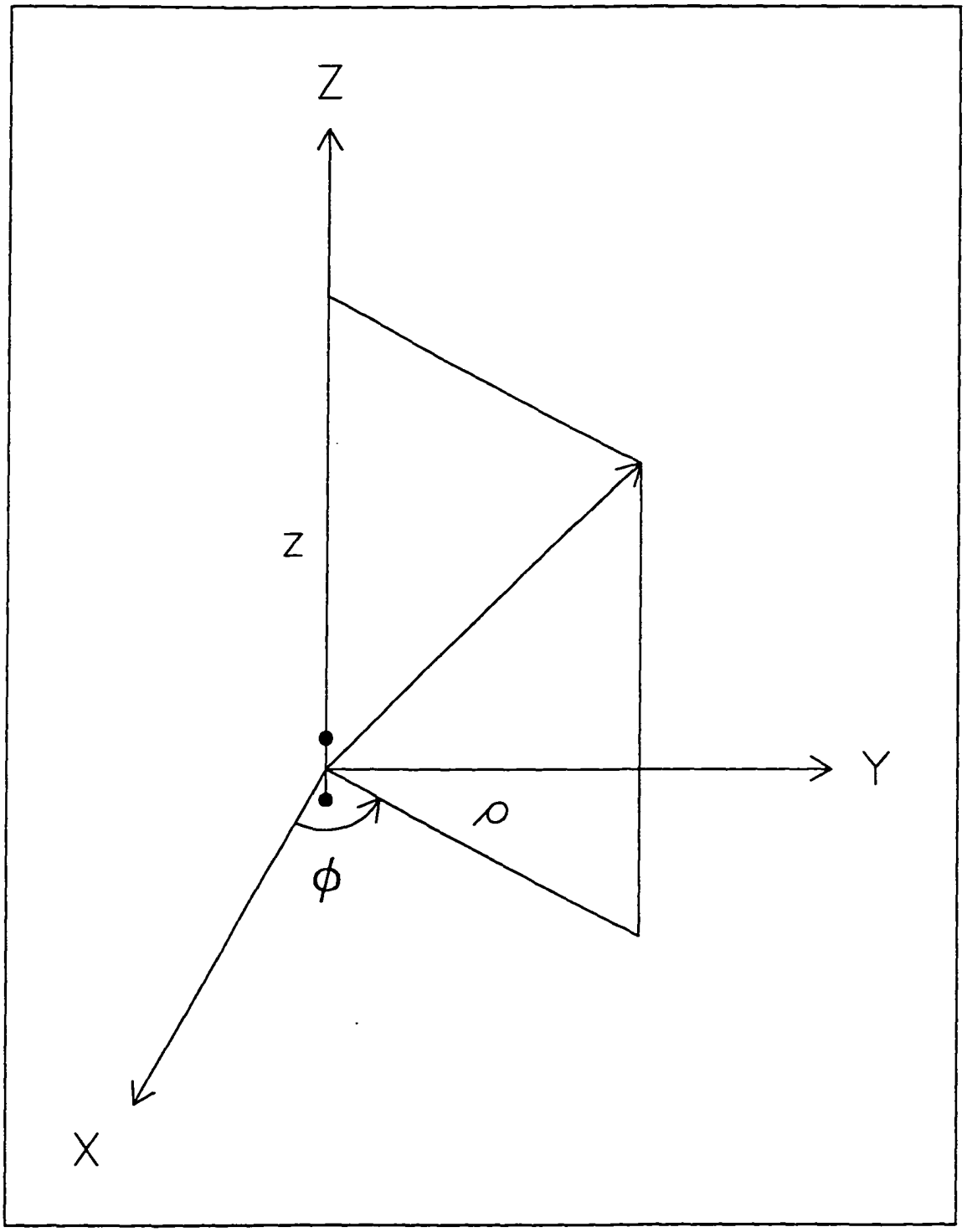

Figure 2.2 Cylindrical coordinates. ($0 \leq \phi < 2\pi$, $-\infty < z < +\infty$, $0 \leq \rho < +\infty$)

$$\hat{H} = -\frac{\hbar^2}{2m}\left[\frac{1}{\rho}\frac{\partial}{\partial\rho}\left(\rho\frac{\partial}{\partial\rho}\right)+\frac{\partial^2}{\partial z^2}\right]+\frac{\hat{l}_z^2}{2m\rho^2}+U(\rho,z) \tag{2.70}$$

where

$$\hat{l}_z = -i\hbar\frac{\partial}{\partial\phi} \tag{2.71}$$

is the operator of the projection of the orbital angular momentum on the symmetry axis. The eigenfunctions of the Hamiltonian (2.70) have the form:

$$|n,m_l,s,m_s\rangle = |n,\lambda\rangle|m_l\rangle|s,m_s\rangle \tag{2.72}$$

where the quantum number

$$\lambda = |m_l| \tag{2.73}$$

characterizes the magnitude of the projection of the orbital angular momentum on the symmetry axis; the quantum number n is used to number the states with the same quantum number λ. Since the square of the operator $\hat{l}_z$ appears in the Hamiltonian (2.70), the states with the quantum number $m_l = \pm\lambda$ are degenerate:

$$e = e(n,\lambda) \tag{2.74}$$

Energies with the same quantum number λ are numbered (in the order of increasing energy) by the principal quantum number n which takes values:

$$n = \lambda+1, \lambda+2, \lambda+3, \cdots \tag{2.75}$$[1]

As in the case of a spherically symmetric field, there is a generally accepted notation for the states of an electron in a cylindrically symmetric field: they are labeled by the quantum number n followed by the Greek letters according to the value of λ as

[1] It is very often to have the quantum number n start from 1, regardless of λ value. We follow this practice in the dissertation.

follows:

$$\begin{array}{cccccccc} \lambda & = & 0 & 1 & 2 & 3 & 4 & \cdots \\ & & \sigma & \pi & \delta & \phi & \gamma & \cdots \end{array} \qquad (2.76)$$

The states of single electrons characterized by the quantum numbers n and λ, or n and l, are called *orbitals*. Traditionally electron spin is not included in the concept on orbital. The spin can take two distinct directions for a given orbital. In order to specify the spin direction, one of the spin functions, defined as

$$\alpha = |s, m_s = \tfrac{1}{2}> \qquad (2.77)$$

or

$$\beta = |s, m_s = -\tfrac{1}{2}> \qquad (2.78)$$

is attached to the label. Also a superscript "±" can be used to specify the sign of m_l. Thus the orbital symbol 2δ means one-electron states characterized by quantum numbers $n = 2$, $\lambda = 2$. The symbol $2\delta^{-}\alpha$ indicates the one-electron state with quantum numbers $n = 2$, $m_l = -2$, and $m_s = \frac{1}{2}$. Spin specified states are called *spin-orbitals*.

2.3.1.2 states of a many-electron system

In the non-relativistic approximation, the stationary states of many electrons in an atom or a diatomic molecule are determined by the Schrödinger equation for the system of electrons which move in the Coulombic field of the nucleus or of the nuclei and interact electrically with each other. Again the spin operators of the electrons do not appear explicitly in the Schrödinger equation.

For a many-electron atomic system, the motion of the center-of-mass, which is

also the center-of-charge, of the system can be treated as that of a "particle" of mass equal to the sum of all electrons' masses, and of charge equal to the sum of all electrons' charges. The orbital angular momentum of this "particle", **L**, is the total angular momentum of the system, or the vectorial sum of all electrons' orbital angular momenta:

$$\mathbf{L} = \sum_i \mathbf{l}_i \tag{2.79}$$

Similarly, the spin of the "particle", **S**, is the total spin of the system, or the vectorial sum of all electrons' spins:

$$\mathbf{S} = \sum_i \mathbf{s}_i \tag{2.80}$$

The potential function of the "particle" is a complicated function of the internal coordinates, *i.e.*, the relative positions of all electrons in the system. But the potential function has the same symmetry, with respect to the coordinates of the "particle", as the external field. In other words, if we make a symmetry transformation of the external field, the potential function remains unchanged. Thus for a spherically symmetric external field (*e.g.*, in an atom) the orbital angular momentum of the "particle", which is also the total orbital angular momentum of the system, is conserved. So is the total spin because the spin operators are not explicitly included in the Schrödinger equation. Hence the stationary states of the many-electron system in an atom are fully characterized by the total angular momentum **L**, which is described by $|L,M_L>$, and the total spin **S**, which is described by $|S,M_S>$, as well as the energy of the system:

$$\Phi = |L,M_L,S,M_S> \tag{2.81}$$

As in the case of a one-electron system, the energy of the many-electron system is independent of the directions of the angular momenta, and states with given L and S are

degenerate, the degree of degeneracy being (2L+1)(2S+1).

The angular momenta **L** and **S** may be coupled to form the total angular momentum of the system:

$$\mathbf{J} = \mathbf{L} + \mathbf{S} \tag{2.82}$$

The total angular momentum **J** is always conserved even when the relativistic effects, which can destroy the separate conservation of the angular momenta **L** and **S**, are large. When the relativistic effects are very small they can be treated as a perturbation. This perturbation splits the (2L+1)(2S+1) degenerate states with given L and S into a number of groups with slightly different energies. Each of these groups is then characterized by the quantum number J, and called the fine-structure component of the term.

We will use the word "*term*" to indicate a group of electronic states, which share a set of quantum numbers and are normally degenerate within a certain approximation. The atomic term symbols are ${}^{2S+1}L$ with the letter L replaced by the capital Latin letters S, P, D, *etc.*, according to:

$$\begin{array}{cccccccccc} L & = & 0 & 1 & 2 & 3 & 4 & 5 & 6 & 7 & \cdots \\ & & S & P & D & F & G & H & I & K & \cdots \end{array} \tag{2.83}$$

The number 2S+1 in the symbol is called the multiplicity of the term, indicating the number of fine-structure components of the term (when $S \leq L$). The quantum number J usually appears as a subscript to the term symbol to specify the fine-structure component. Because of the spherical symmetry of the external field, parity regarding the inversion operator $\hat{i}$ (2.13) is applicable here. A superscript "o" is used to label a term which is odd. Thus the term symbols ${}^3P_0$ and ${}^4S^o_{3/2}$ denote the atomic terms with $L = 1$, $S = 1$,

$J = 0$, even parity, and $L = 0$, $S = \frac{3}{2}$, $J = \frac{1}{2}$, odd parity, respectively.

For a diatomic molecule, the field in which the electrons move is cylindrically symmetric about the axis passing through the nuclei. In this case the magnitude of the total orbital angular momentum is not conserved, but the projection of the angular momentum on the axis is. Also, as we have seen in the previous section for the one-electron system, the states differing only in the sign of the quantum number M_L are degenerate, and only the absolute value of the quantum number

$$\Lambda = |M_L| \tag{2.84}$$

is needed to classify the electronic terms of a diatomic molecule. The degree of degeneracy for a given Λ is 2 (corresponding to $M_L = \pm\Lambda$) if $\Lambda \neq 0$, or 1 if $\Lambda = 0$. The total spin S is still conserved as in the case of an atom, increasing the degree of degeneracy by a factor of (2S+1).

When the relativistic effects are small but not negligible the 2(2S+1) or (2S+1) degenerate states with given Λ and S are regrouped according to the projection of the total electronic angular momentum

$$\mathbf{J}_a = \mathbf{L} + \mathbf{S} \tag{2.85}$$

on the symmetry axis:

$$M_{J_a} = M_L + M_S \tag{2.86}$$

For a given set of quantum numbers Λ and S, states with the same quantum number

$$\Omega = |M_{J_a}| \tag{2.87}$$

are degenerate, if $S \leq \Lambda$. The degree of degeneracy related to Ω is 2 if $\Omega \neq 0$, or 1 if $\Omega = 0$. Before the wavefunctions have been antisymmetrized they are characterized by

three quantum numbers M_L, S, and M_S:

$$\Phi_{el} = |M_L, S, M_S> \tag{2.88}$$

The electronic terms of the diatomic molecule are labeled as $^{2S+1}\Lambda$ with the letter Λ replaced by the capital Greek letters Σ, Π, Δ, *etc.* according to

$$\begin{array}{ccccccccc} \Lambda & = & 0 & 1 & 2 & 3 & 4 & \cdots \\ & & \Sigma & \Pi & \Delta & \Phi & \Gamma & \cdots \end{array} \tag{2.89}$$

The quantum number $\Lambda + \Sigma$ appears in the term symbol as a subscript. The quantum number Σ is defined as the value of M_S which combines with $M_L = +\Lambda$ to form the given value of Ω :

$$\begin{aligned} \Omega &= |M_{J_a}| \\ &= |M_L + M_S| \\ &= |\Lambda + \Sigma| \end{aligned} \tag{2.90}$$

Since the external field is cylindrically symmetric, the symmetry with respect to the reflection operator $\hat{\sigma}$ (2.14) is applicable here. When $\Lambda \neq 0$, the states with $P_\sigma = \pm 1$ are degenerate. When $\Lambda = 0$ (the Σ terms), the $P_\sigma = +1$ state and the $P_\sigma = -1$ state are not degenerate. Superscript "$\pm$" is used to distinguish the Σ terms with different eigenvalues of $\hat{P}_\sigma$. For instance, the symbol $^3\Sigma_0^-$ labels a molecular term which has quantum numbers $S = 1$, $\Lambda = 0$, $\Lambda + \Sigma = 0$, and is antisymmetric about any plane containing the axis.

If the relativistic effects are very strong, both S and Λ are not conserved. $\mathbf{J}_a$ is not conserved either. Only Ω is a good quantum number and is used to label electronic states in a diatomic molecule.

2.3.2 vibration and rotation of a diatomic molecule

As has been discussed at the beginning of this chapter, the great difference in the masses of the nuclei and the electrons makes it possible to separate the motions of the nuclei and the electrons. In this approximation the electrons in the diatomic molecule can be treated as a sub-system only of electrons moving in the cylindrically symmetric electrical field of the two nuclei. The stationary states of such an electron system (the electronic states of the molecule) are, in the absence of relativistic effects, characterized by their energy (E), magnitude of the projection of the total orbital angular momentum on the internuclear axis (Λ), multiplicity ($2S+1$), and projection of the total spin on the axis (Σ)

However, the states of the diatomic molecule as a whole should include the motions of the nuclei. Without electrons in the molecule the bare nuclei would fly apart from each other because of the repulsive Coulombic force between the two positively charged particles. With the electrons present the nuclei are attracted to the negatively charged electron cloud. It is the balance of the repulsion and the attraction which leads to a minimum in potential energy. The nuclei vibrate around the minimum (equilibrium) position.

For any given diatomic molecule, at any given internuclear distance R, there exists a set of stationary states of the electron system. Each state is associated with an eigenenergy E. With a slight change of internuclear distance each individual eigenfunction also changes slightly but all characteristic quantum numbers remain unchanged except the energy E, *i.e.*, the electronic terms are conserved with respect to the change of the internuclear distance but their eigenenergies are a function of the distance. Thus in order

to change the positions of the nuclei, not only has work to be done against the Coulombic force between them, but also work must be supplied to make up the electronic eigenenergy change. In other words, the potential energy V(R) that governs the motion of the nuclei is the sum of the Coulombic potential energy and the electronic energy. Only if the potential energy V(R), which, in general, is different for different electronic terms, has a minimum in its dependence on the internuclear distance R (Figure 2.3) , is the electronic state in question a stable state of the molecule.

The relative motion of the nuclei can be considered to be that of two particles interacting with each other in accordance with the potential V(R). When the motion of the nuclei is very slow it can be regarded as a small vibration about the equilibrium position R_e. Accordingly we can expand V(R) in a series of powers of $\xi=R-R_e$. To the second order we have:

$$V(R) = V_e + \frac{1}{2}\mu\omega_e^2\xi^2 \qquad (2.91)$$

where $V_e=V(R_e)$ is the minimum value of V(R); μ is the reduced mass of the two nuclei; ω_e is the frequency of the vibration. The first term in (2.91) is a constant, while the second term corresponds to a one-dimensional harmonic oscillator. Hence the electronic-vibrational energies can be written as

$$E = V_e + \hbar\omega_e(v+\tfrac{1}{2}) \qquad (2.92)$$

where the first term is the electronic energy (E_{el}); the second term is the vibrational energy (E_{vib}) of the nuclei with vibrational quantum number v ($v = 0, 1, 2, 3, \cdots$). The corresponding vibrational eigenstates are denoted by $|v>$:

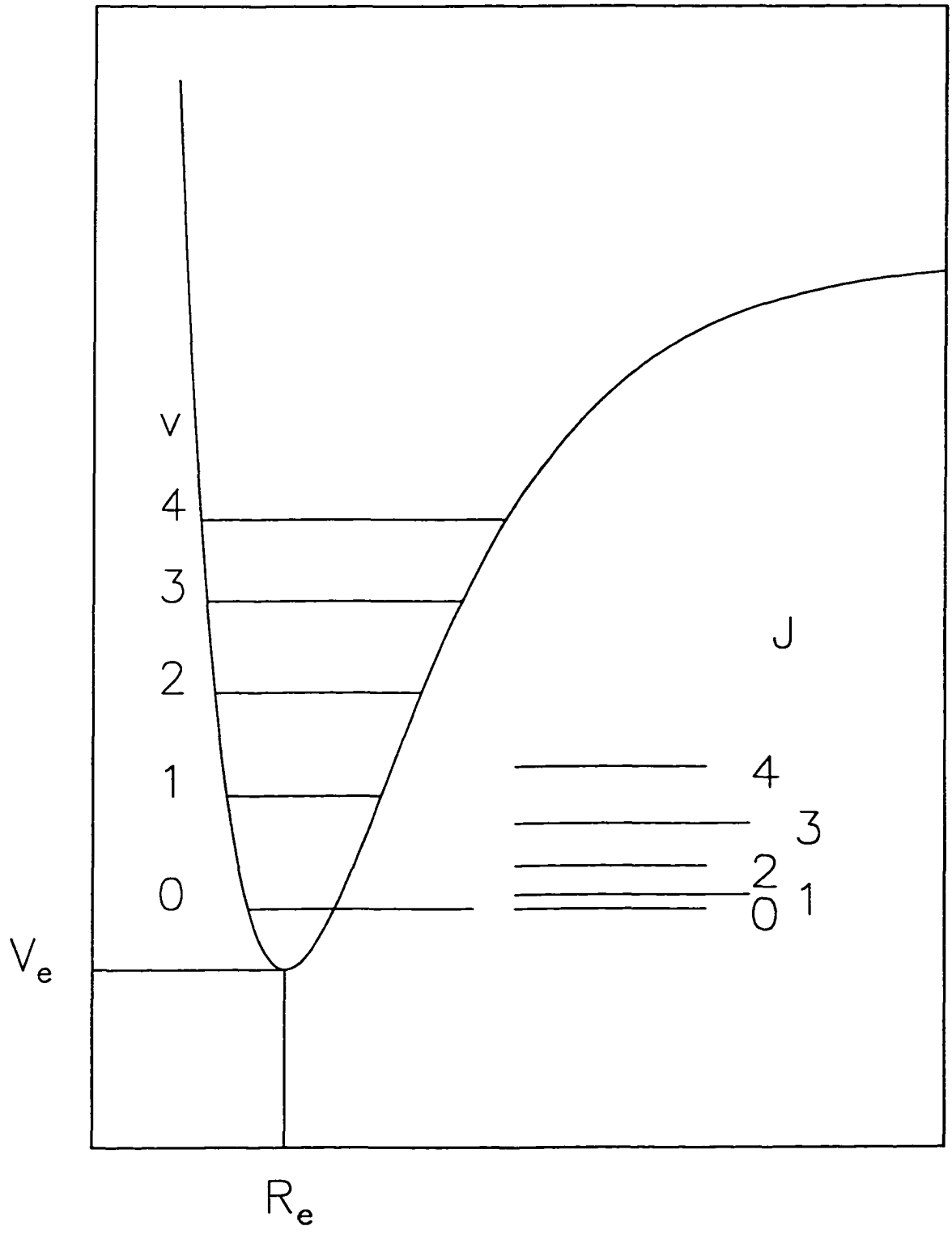

Figure 2.3 Electronic, vibrational, and rotational energy levels of a diatomic molecule (schematic). The energy gaps between rotational levels have been greatly exaggerated.

$$\Phi_{vib} = |v> \tag{2.93}$$

So far we have neglected the rotation of the molecule. If the motion of the nuclei is slow, the rotation of the molecule is like a symmetric top with energies [68]:

$$E_{rot} = B_e[J(J+1) - \Omega^2] \tag{2.94}$$

where J ($J = \Omega, \Omega+1, \Omega+2, \cdots$) is the rotational quantum number; Ω is the absolute value of the projection of the total angular momentum **J** on the internuclear axis (2.87); B_e is the rotational constant defined as

$$B_e = \frac{\hbar^2}{2I} = \frac{\hbar^2}{2\mu R_e^2} \tag{2.95}$$

The eigenstates of the symmetric top are characterized by three quantum numbers:

$$\Phi_{rot} = |J, M_J, M> \tag{2.96}$$

where the quantum number M_J is the projection of **J** on the molecule fixed symmetry axis and is equal to the quantum number M_{J_a} defined in (2.85); M is the projection of **J** on a space fixed direction and can take values from $M = J$ to $M = -J$. Since the energy expression (2.94) is independent of M, there is a (2J+1)-fold degeneracy arising from M for each given rotational quantum number J.

Thus, in a certain approximation, the energies of the diatomic molecule are composed of three independent parts (Figure 2.3):

$$\begin{aligned} E &= E_{el} + E_{vib} + E_{rot} \\ &= V_e + \hbar\omega_e(v+\tfrac{1}{2}) + B_e[J(J+1) - \Omega^2] \end{aligned} \tag{2.97}$$

The corresponding total wavefunctions of the diatomic molecule are the products of three wavefunctions for the three motions:

$$|J,M_J,M,M_L,S,M_S,v>=|M_L,S,M_S>|v>|J,M_J,M> \qquad (2.98)$$

where $|M_L,S,M_S>$ is the electronic eigenfunction (2.88); $|v>$ is the vibrational eigenfunction (2.93); $|J,M_J,M>$ is the rotational eigenfunction for the symmetric top (2.96).

2.3.3 the total wavefunctions of a diatomic molecule

Up to this point we have discussed the electronic motion, the nuclear vibration, and the rotation of the diatomic molecule as a whole. The total wavefunctions of the molecule have the form of (2.98), which is a product of the electronic wavefunction, the vibrational wavefunction, and the rotational wavefunction. However, because of the homogeneity and isotropy of the laboratory space, the total wavefunction of an isolated diatomic molecule should also be an eigenfunction of the inversion operator $\hat{i}$ (2.13). With the Condon and Shortley phase convention for the electronic orbital wavefunctions it is shown [60] that the total wavefunctions of the diatomic molecule, labeled by the quantum number J, Λ, S, Σ, $M_J(=\Lambda+\Sigma)$, v, M, and the parity $P_i=\pm 1$ are:

(i) $^{2S+1}\Sigma_0^{\pm}$

(i.a) S = even integral number (2S+1 = 1, 5, 9 ...)

$$|^{2S+1}\Sigma_{0^-}^{+},JM,v,+> = |\Lambda=0,S,\Sigma=0>|J,M_J=0,M>|v> \quad \text{(for even J)} \qquad (2.99)$$

$$|^{2S+1}\Sigma_{0^-}^{+},JM,v,-> = |\Lambda=0,S,\Sigma=0>|J,M_J=0,M>|v> \quad \text{(for odd J)} \qquad (2.100)$$

$$|^{2S+1}\Sigma^{-}_{0^-}, JM, v, + > = |\Lambda = 0, S, \Sigma = 0 > |J, M_J = 0, M > |v > \quad \text{(for odd J)} \tag{2.101}$$

$$|^{2S+1}\Sigma^{-}_{0^-}, JM, v, - > = |\Lambda = 0, S, \Sigma = 0 > |J, M_J = 0, M > |v > \quad \text{(for even J)} \tag{2.102}$$

(i.b) S = odd integral number (2S+1 = 3, 7, 11 ...)

$$|^{2S+1}\Sigma^{+}_{0^-}, JM, v, + > = |\Lambda = 0, S, \Sigma = 0 > |J, M_J = 0, M > |v > \quad \text{(for odd J)} \tag{2.103}$$

$$|^{2S+1}\Sigma^{+}_{0^-}, JM, v, - > = |\Lambda = 0, S, \Sigma = 0 > |J, M_J = 0, M > |v > \quad \text{(for even J)} \tag{2.104}$$

$$|^{2S+1}\Sigma^{-}_{0^-}, JM, v, + > = |\Lambda = 0, S, \Sigma = 0 > |J, M_J = 0, M > |v > \quad \text{(for even J)} \tag{2.105}$$

$$|^{2S+1}\Sigma^{-}_{0^-}, JM, v, - > = |\Lambda = 0, S, \Sigma = 0 > |J, M_J = 0, M > |v > \quad \text{(for odd J)} \tag{2.106}$$

(ii.) $^{2S+1}\Lambda_{0}, \Lambda \neq 0$

$$|^{2S+1}\Lambda_{0^-}, JM, v, + > = \sqrt{\tfrac{1}{2}}\left[|\Lambda, S, \Sigma, > + (-1)^{J-S}|-\Lambda, S, -\Sigma, >\right]|J, M_J = 0, M > |v > \tag{2.107}$$

$$|^{2S+1}\Lambda_{0^-}, JM, v, - > = \sqrt{\tfrac{1}{2}}\left[|\Lambda, S, \Sigma, > - (-1)^{J-S}|-\Lambda, S, -\Sigma, >\right]|J, M_J = 0, M > |v > \tag{2.108}$$

(iii.) $^{2S+1}\Sigma^{-}_{M_J}, M_J \neq 0$

$$|^{2S+1}\Sigma^{-}_{M_J}, JM, v, \pm > = \sqrt{\tfrac{1}{2}}\left[|\Lambda = 0, S, \Sigma, > |J, M_J, M > \mp (-1)^{J-S}|\Lambda = 0, S, -\Sigma, > |J, -M_J, M >\right]|v > \tag{2.109}$$

(iv) $^{2S+1}\Lambda_{M_J}, \Lambda \neq 0^{-}, M_J \neq 0$

$$
\begin{aligned}
&|^{2S+1}\Lambda_{M_J}\ \ JM,v\pm> \\
&\quad =\sqrt{\tfrac{1}{2}}\Big[|\Lambda\ S\ \Sigma>|J,M_J,M> \\
&\qquad \pm(-1)^{J-S}|-\Lambda\ S\ -\Sigma>|J,-M_J,M>\Big]|v>
\end{aligned}
\tag{2.110}
$$

Another convenient way to label the parity is to use the *e/f* labels introduced by Kopp and Hougen [73] and extended by Brown *et al.*[74]. Those energy levels whose total parity is $(-1)^J$ or $(-1)^{J-\frac{1}{2}}$ are classified as *e* levels, while those whose total parity is $(-1)^{J+1}$ or $(-1)^{J+\frac{1}{2}}$ are classified as *f* levels. With this classification, a Σ_0 electronic state with an even number of electrons can have either *e* levels or *f* levels: when S is an even number (*i.e.*, $2S+1=1,5,9,\cdots$) a Σ_0^+ state has only *e* levels while a Σ_0^- state has only *f* levels, when S is an odd number (*i.e.*, $2S+1=3,7,\cdots$) a Σ_0^- state has only *e* levels while a Σ_0^+ state has only *f* levels. For all other electronic states both *e* and *f* levels exist for any given J, and the *e* and *f* levels for a given J are degenerate under the current approximation.

2.4 Derivation of the Electronic Wavefunctions

2.4.1 electron configuration

In a many-electron system all electrons interact electrically with each other; each electron experiences a complicated and non-symmetric electric field. We can, strictly speaking, consider only states of the system as a whole. Nevertheless, it is found that we can introduce the idea of the states of each individual electron in the system, as being the stationary states of the motion of each electron in some effective field which is the sum of the external field and the fields obtained by averaging over all possible positions of the other electrons. These effective fields are, in general, different for different electrons in the system, and have to be determined simultaneously.

The effective fields should have the same symmetry as the external field. Thus, to a certain approximation, we can still characterize each individual electron and its stationary states by the concept of orbitals introduced in the previous section for the one-electron system. A distribution of electrons in the system among different orbitals is called an electron configuration. The electron configuration can be expressed by putting a right superscript on the orbital symbol to indicate the number of electrons in the orbital. For instance, the electron configuration $8\sigma^2 3\pi^4 1\delta^3 9\sigma^1$ shows that there are two electrons in the orbital 8σ, four electrons in the orbital 3π, three electrons in the orbital 1δ, and one electron in the orbital 9σ.

In the electron configuration there should be no more than one electron in a spin-orbital. This is the so called Pauli exclusion principle. Degenerate orbitals with the same λ value form a shell. When the maximum number of electrons are distributed in a shell, the

shell is said to be full or closed and to form a closed shell. For instance, a σ shell is closed with two electrons because there are only two spin-orbitals ($m_l = 0$, and $m_s = \pm\frac{1}{2}$) for a σ shell; the π, δ, ... shells are closed with four electrons, respectively, because there are four spin-orbitals ($m_l = \pm\lambda$, and $m_s = \pm\frac{1}{2}$) in each shell.

When a shell is closed, the net contribution of spin and orbital angular momentum from the shell is zero. In the derivation of terms from the electron configuration a closed shell can be ignored; only the electrons in open shells need be considered [68].

2.4.2 eigenfunctions of S^2 and S_z

Spin eigenfunctions, $|S, M_S>$, of a many-electron system can be built up by adding electrons one by one. For a one-electron system there are only doublet terms ($S = s = \frac{1}{2}$) and the spin eigenfunctions of the system are simply the one electron spin eigenfunctions

$$|S = \tfrac{1}{2}, M_S = \tfrac{1}{2}> = \alpha \qquad (2.111)$$

and

$$|S = \tfrac{1}{2}, M_S = -\tfrac{1}{2}> = \beta \qquad (2.112)$$

where the one electron spin eigenfunctions α and β are defined in (2.77) and (2.78). With two electrons, the resultant total spin can take values $S = 1$ (triplet term) and $S = 0$ (singlet term), and the corresponding total spin eigenfunctions, using the Clebsch-Gordan coefficients given in [75], are:

$$|S = 1, M_S = 1> = \alpha(1)\alpha(2) \qquad (2.113)$$

$$|S=1,M_S=0>=\sqrt{\tfrac{1}{2}}[\alpha(1)\beta(2)+\beta(1)\alpha(2)] \tag{2.114}$$

$$|S=1,M_S=-1>=\beta(1)\beta(2) \tag{2.115}$$

and

$$|S=0,M_S=0>=\sqrt{\tfrac{1}{2}}[\alpha(1)\beta(2)-\beta(1)\alpha(2)] \tag{2.116}$$

The eigenfunction (2.114) can actually be deduced by applying the lowering operator $\hat{S}^-$ on (2.113) according to (2.47):

$$\hat{S}^-|S=1,M_S=1>=\hbar\sqrt{2}|S=1,M_S=0> \tag{2.117}$$

$$\begin{aligned}\hat{S}^-|S=1,M_S=1>&=(\hat{s}_1^-+\hat{s}_2^-)\alpha(1)\alpha(2)\\&=[\hat{s}_1^-\alpha(1)]\alpha(2)+\alpha(1)[\hat{s}_2^-\alpha(2)]\\&=\hbar[\beta(1)\alpha(2)+\alpha(1)\beta(2)]\end{aligned} \tag{2.118}$$

and then setting (2.117) and (2.118) equal. Similarly, the eigenfunction (2.115) can be obtained from (2.114). So it is necessary only to specify the spin eigenfunction of the component with $M_S = S$ for a given term.

If the spin eigenfunction (2.111) represents a one-electron spin state with the spin direction upwards, then the function (2.113) represents a two electron spin state which is formed by adding the second electron spin, with its direction upwards, to the first electron spin, and the function (1.116) with the second spin directed downwards.

In general, for a given (k-1)-electron system term represented by the spin eigenfunction $|S,M_S=S>$, new k-electron system terms with $S'=S+\frac{1}{2}$ and $S'=S-\frac{1}{2}$ (if S>0) can be formed by adding the kth electron, with its spin up and down, respectively, to the (k-1)-electron system. The corresponding eigenfunctions are:

$$|S' = S+\tfrac{1}{2}, M_S' = S' >= |S, M_S = S > \alpha(k) \tag{2.119}$$

and

$$\begin{aligned} |S' = S-\tfrac{1}{2}, M_S' = S' > \\ = \sqrt{\tfrac{1}{2S(2S+1)}}\left[2S|S, M_S = S > \beta(k) - (\hat{S}^-|S, M_S = S >)\alpha(k)/\hbar\right] \end{aligned} \tag{2.120}$$

where

$$\hat{S}^- = \sum_{i=1}^{k-1} \hat{s}_i^- \tag{2.121}$$

$$\hat{s}_i^- \alpha(i) = \hbar\beta(i) \tag{2.122}$$

$$\hat{s}_i^- \beta(i) = 0 \tag{2.123}$$

From the triplet two-electron term (2.113) we can add the third electron spin with its direction upwards to form a quartet term:

$$\begin{aligned} |S' = \tfrac{3}{2}, M_S' = \tfrac{3}{2} > &= |S = 1, M_S = 1 > \alpha(3) \\ &= \alpha(1)\alpha(2)\alpha(3) \end{aligned} \tag{2.124}$$

or with the electron spin downwards to a doublet term:

$$\begin{aligned} |S' = \tfrac{1}{2}, M_S' = \tfrac{1}{2} > \\ &= \sqrt{\tfrac{1}{6}}\left[2|S = 1, M_S = 1 > \beta(3) - \left(\hat{S}^-|S = 1, M_S = 1 >\right)\alpha(3)/\hbar\right] \\ &= \sqrt{\tfrac{1}{6}}\left[2\alpha(1)\alpha(2)\beta(3) - \left(\alpha(1)\beta(2) + \beta(1)\alpha(2)\right)\alpha(3)\right] \\ &= \sqrt{\tfrac{1}{6}}\left[2\alpha(1)\alpha(2)\beta(3) - \alpha(1)\beta(2)\alpha(3) - \beta(1)\alpha(2)\alpha(3)\right] \end{aligned} \tag{2.125}$$

For the singlet two electron system term (2.116) since $S = 0$, a third electron can only be added to the system, with the spin up, to form a doublet state:

$$
\begin{aligned}
|S' = \tfrac{1}{2}, M_S' = \tfrac{1}{2}> &= |S = 0, M_S = 0> \alpha(3) \\
&= \sqrt{\tfrac{1}{2}}\left[\alpha(1)\beta(2) - \beta(1)\alpha(2)\right]\alpha(3) \\
&= \sqrt{\tfrac{1}{2}}\left[\alpha(1)\beta(2)\alpha(3) - \beta(1)\alpha(2)\alpha(3)\right]
\end{aligned}
\qquad (2.126)
$$

Spin eigenfunctions for up to four electrons are listed in Table 2.1. There is a subtle difference between this table and Table 2.4 of reference [60] in that the ordering of one-electron spin eigenfunctions in each product is reversed for these two tables. This is because of the process used to build up the eigenfunction. In reference [60] the last two electrons are coupled first, then the third one is added, and so on until the first electron is included. Mathematically the different approaches (that of our Table 2.1 and that of Table 2.4 of reference [60]) give two different sets of basis functions.

2.4.3 eigenfunctions for a given electron configuration

In the orbital approximation the motions of the various electrons can be viewed as independent of one another, each electron is fully described by its own wavefunctions in the form of (2.65) or (2.72). The wavefunctions of the system may be expressed in the form of the products of these one-electron wavefunctions, *e.g.*, in the case of a two-electron diatomic molecular system:

$$\Phi(1,2) = \phi_a(1)\phi_b(2) \qquad (2.127)$$

where the subscript is used to distinguish the two occupied spin-orbitals; the number in the parentheses is used to indicate the electron that is occupying the corresponding spin-orbital. Thus the wavefunction (2.127) implies that the first electron is in the spin-orbital "a" while the second electron is in the spin-orbital "b". For the diatomic molecule system the wavefunction (2.127) can be written as

Table 2.1 Eigenfunctions of $\hat{S}^2$ and $\hat{S}_z$ for $\Sigma = S$ components.

one electron 1 doublet	two electrons 1 singlet 1 triplet	three electrons 2 doublets 1 quartet	four electrons 2 singlets 3 triplets 1 quintet
(2) α	(3) $\alpha\alpha$	(4) $\alpha\alpha\alpha$	(5) $\alpha\alpha\alpha\alpha$
			(3) $\sqrt{\frac{1}{12}}(3\alpha\alpha\alpha\beta - \alpha\alpha\beta\alpha - \alpha\beta\alpha\alpha - \beta\alpha\alpha\alpha)$
		(2) $\sqrt{\frac{1}{6}}(2\alpha\alpha\beta - \alpha\beta\alpha - \beta\alpha\alpha)$	(3) $\sqrt{\frac{1}{6}}(2\alpha\alpha\beta\alpha - \alpha\beta\alpha\alpha - \beta\alpha\alpha\alpha)$
			(1) $\sqrt{\frac{1}{12}}(2\alpha\alpha\beta\beta - \alpha\beta\alpha\beta - \beta\alpha\alpha\beta - \alpha\beta\beta\alpha - \beta\alpha\beta\alpha + 2\beta\beta\alpha\alpha)$
	(1) $\sqrt{\frac{1}{2}}(\alpha\beta - \beta\alpha)$	(2) $\sqrt{\frac{1}{2}}(\alpha\beta\alpha - \beta\alpha\alpha)$	(3) $\sqrt{\frac{1}{2}}(\alpha\beta\alpha\alpha - \beta\alpha\alpha\alpha)$
			(1) $\sqrt{\frac{1}{4}}(\alpha\beta\alpha\beta - \beta\alpha\alpha\beta - \alpha\beta\beta\alpha + \beta\alpha\beta\alpha)$

The number in the bracket indicates the spin multiplicity, 2S+1, of the corresponding term. The arrangement of the table follows the building process of the spin eigenfunctions.

$$\begin{aligned}\Phi &= |n_1,\lambda_1>|n_1,m_{l1}>|\sigma_1>|n_2,\lambda_2>|n_2,m_{l2}>|\sigma_2> \\ &= |n_1,\lambda_1>|n_2,\lambda_2>|n_1,m_{l1}>|n_2,m_{l2}>|\sigma_1>|\sigma_2>\end{aligned} \tag{2.128}$$

where

$$|\sigma_i>=\begin{cases}\alpha(i) & \text{when } m_s=\frac{1}{2} \\ \beta(i) & \text{when } m_s=-\frac{1}{2}\end{cases} \tag{2.129}$$

On the other hand, the wavefunctions of the stationary states of the many-electron diatomic molecular system must be simultaneously the eigenfunctions of the projection of the total orbital angular momentum on the internuclear axis (L_z) and the total spin (S^2 and S_z), but not necessarily eigenfunctions of individual spins. Although the wavefunction (2.128) is an eigenfunction of $\hat{L}_z=\hat{l}_{z1}+\hat{l}_{z2}$ with eigenvalue $M_L=m_{l1}+m_{l2}$, it is not, in general, an eigenfunction of spin operators S^2 and S_z. A spin eigenfunction $|S,M_S>$ developed in the previous section has to be used to replace the factor $|\sigma_1>|\sigma_2>$ in (2.128).

The total spin of the system S can be formed by coupling the two individual electron spins s_1 and s_2 as discussed in the previous section. For instance, the eigenfunction of a singlet state with $S=0$ is given by

$$|S=0,M_S=0>=\sqrt{\tfrac{1}{2}}\big(\alpha(1)\beta(2)-\beta(1)\alpha(2)\big) \tag{2.130}$$

By substituting the spin eigenfunction (2.130) into the wavefunction (2.128) we get

$$\begin{aligned}|M_L,S=0,M_S=0>=&\sqrt{\tfrac{1}{2}}|n_1,\lambda_1>|n_2,\lambda_2>|m_{l1}>|m_{l2}>\alpha(1)\beta(2) \\ &-\sqrt{\tfrac{1}{2}}|n_1,\lambda_1>|n_2,\lambda_2>|m_{l1}>|m_{l2}>\beta(1)\alpha(2)\end{aligned} \tag{2.131}$$

So, in order to be the eigenfunction of S^2 and S_z, the wavefunction (2.128), in general,

should be modified, by employing spin eigenfunctions in Table 2.1, to be a linear combination of one-electron wavefunction products:

$$\Phi(1,2) = C_1\phi_a(1)\phi_b(2) + C_2\phi_c(1)\phi_d(2) \qquad (2.132)$$

where the orbitals a and c are the same in their radial and orbital angular momentum parts and differ at most in their spin part, similarly for the orbitals b and d. The wavefunction (2.132) is similar to (2.22) and should further be modified by replacing the products with corresponding Slater determinants (2.24) in order to be an eigenfunction of the permutation operator (2.17):

$$\Phi(1,2) = C_1|\phi_a(1)\phi_b(2)| + C_2|\phi_c(1)\phi_d(2)| \qquad (2.133)$$

In general, when a molecular electron configuration is given, the first step towards constructing the eigenfunctions is to find the appropriate orbital angular momentum eigenfunctions in the form

$$|M_L\rangle = |m_{l1}\rangle|m_{l2}\rangle\cdots|m_{lk}\rangle \qquad (2.134)$$

and spin eigenfunctions which are given in Table 2.1. One then expands the product of the spin eigenfunctions and the orbital angular momentum eigenfunctions to express the wavefunction of the system as a linear combination of products of one-electron spin orbital wavefunctions like (2.132). Finally, we replace each individual product in the summation with its Slater determinant defined in (2.24).

If there are two electrons (say the ith and the jth electrons) which differ only in the spin part of their one-electron wavefunctions (equivalent electrons), the spin eigenfunctions given in Table 2.1 cannot be used directly in constructing electronic eigenfunctions. They have to be modified in the following way: (i) combine all $\alpha(i)\beta(j)$ and $\beta(i)\alpha(j)$ terms according to $\alpha(i)\beta(j) = -\beta(i)\alpha(j)$; (ii) delete all $\alpha(i)\alpha(j)$ and

$\beta(i)\beta(j)$ terms; (iii) renormalize the modified spin wavefunction. Normally the final form of a modified k-electron spin wavefunction is the same as a (k-2)-electron spin wavefunction if the existence of the ith and the jth electrons is ignored. The most frequently encountered situation is that the first two electrons are paired electrons. In this case the modified k-electron spin wavefunction is simply the product of $\alpha(1)\beta(2)$ and a (k-2)-electron spin eigenfunction for the rest of the electrons, as shown by Table 2.2.

Table 2.2 Modified wavefunctions of $\hat{S}^2$ and $\hat{S}_z$ for $\Sigma = S$ components.

one electron 1 doublet	two electrons 1 singlet	three electrons 1 doublet	four electrons 1 singlet 1 triplets
(2) α	~	~	~
			~
		~	~
			~
	(1) $\alpha\beta$	(2) $\alpha\beta\alpha$	(3) $\alpha\beta\alpha\alpha$
			(1) $\sqrt{\frac{1}{2}}\alpha\beta(\alpha\beta-\beta\alpha)$

This table applies when the first two electrons are in the same orbital. The number in the bracket indicates the spin multiplicity, 2S+1, of the corresponding term. The arrangement of the table is the same as in Table 2.1. Those eigenfunctions which are excluded by the Pauli exclusive principle are replaced by ~.

2.5 Selection Rules for Electric Dipole Transitions

When the interactions between the diatomic molecule system and the photon (*i.e.*, the electro-magnetic field) are included in the Schrödinger equation, transitions between the stationary states of the molecular system can occur. The system originally in its ground state $|g>$, *i.e.*, the lowest stationary state, can be excited to a higher state $|e>$ by absorbing a photon if the energy of the photon matches the energy gap between the two states:

$$h\nu = E_e - E_g \tag{2.135}$$

Similarly, the system originally in an excited state $|e>$ can transit to the ground state $|g>$ or another low-lying excited state $|e'>$, and emit a photon to carry the excess energy.

Under the electric dipole approximation, states which can be coupled by a photon have to meet certain requirements. These requirements are called selection rules. In general, because of the symmetry properties of the electric dipole moment, only states with different parities (regarding the operator $\hat{i}$) can be coupled, or symbolically:

$$\begin{aligned} &+ \leftarrow\!\!\rightarrow - \\ &+ \leftarrow\!|\!\rightarrow +, \quad - \leftarrow\!|\!\rightarrow - \end{aligned} \tag{2.136}$$

Secondly, the selection rules for a symmetric top are:

$$\Delta J = 0, \pm 1 \tag{2.137}$$

$$\Delta M_J = 0, \pm 1 \tag{2.138}$$

$$\Delta M = 0, \pm 1 \tag{2.139}$$

with the exceptions:

$$J = 0 \leftarrow\!|\!\rightarrow J = 0 \tag{2.140}$$

$$M_J = 0 \leftarrow|\rightarrow M_J = 0 \quad \text{when } \Delta J = 0 \tag{2.141}$$

$$M = 0 \leftarrow|\rightarrow M = 0 \text{ when } \Delta J = 0 \tag{2.142}$$

When the basis functions (2.99)-(2.110) are used (*i.e.*, with the Hund's case (a) angular momentum coupling scheme), the selection rule (2.138) can be further specialized to:

$$\Delta\Lambda = 0,\pm 1 \tag{2.143}$$

$$\Delta S = 0 \tag{2.144}$$

$$\Delta\Sigma = 0 \tag{2.145}$$

and

$$\Sigma^{+} \longleftrightarrow \Sigma^{+}, \quad \Sigma^{-} \longleftrightarrow \Sigma^{-}, \quad \text{but} \quad \Sigma^{+} \leftarrow|\rightarrow \Sigma^{-} \tag{2-146}$$

In terms of *e/f* levels, the selection rules (2.136) and (2.137) can be combined to give

$$e \longleftrightarrow e \text{ and } f \longleftrightarrow f \quad \text{when } \Delta J = \pm 1 \tag{2.147}$$

$$e \longleftrightarrow f \qquad \text{when } \Delta J = 0 \tag{2.148}$$

2.6 Perturbation Theory

In quantum mechanics any physical system is fully described by its Hamiltonian, the total energy operator $\hat{H}$. However, the Schrödinger equation (2.61) can be solved exactly only in a few very simple cases. Fortunately, many Hamiltonians contain terms of different order of magnitude. Such that when the small terms are neglected, the simplified Schrödinger equation can be solved exactly. In such cases, the first step in solving the Schrödinger equation is to solve exactly the simplified equation, and the second step is to calculate approximately the corrections due to the small terms that have been neglected. The general method for calculating these corrections is usually called perturbation theory [72].

Let the Hamiltonian of a given physical system be of the form

$$\hat{H} = \hat{H}^0 + \hat{H}' \tag{2.149}$$

where the effect of the perturbing operator $\hat{H}'$ is small compared with the original operator $\hat{H}^0$. If $\{ E_i^0 \}$ and $\{ \Phi_i^0 \}$ are, respectively, the eigenenergies and the eigenfunctions of the operator $\hat{H}^0$, we can express the Hamiltonian (2.149) in the form of matrix

$$\hat{H} = \begin{bmatrix} E_1^0 & 0 & \cdots & 0 \\ 0 & E_2^0 & & \\ \vdots & & \ddots & \\ 0 & & & E_n^0 \end{bmatrix} + \begin{bmatrix} H'_{11} & H'_{12} & \cdots & H'_{1n} \\ H'_{21} & H'_{22} & & \\ \vdots & & \ddots & \\ H'_{n1} & & & H'_{nn} \end{bmatrix} \tag{2.150}$$

where the complete set of the eigenfunctions $\{ \Phi_i^0 \}$ has been taken as basis set, and

$$\begin{aligned} H'_{ij} &= \langle \Phi_i^0 | \hat{H}' | \Phi_j^0 \rangle \\ &= \int \Phi_i^{0*} \hat{H}' \Phi_j^0 dq \end{aligned} \tag{2.151}$$

are the matrix elements of $\hat{H}'$.

Applying general perturbation theory [72] to the problem, we get the eigenenergies

$$E_i = E_i^0 + H'_{ii} + \sum_{j \neq i} \frac{|H'_{ij}|^2}{E_i^0 - E_j^0} \qquad (2.152)$$

to second-order, and the eigenfunctions

$$\Phi_i = \Phi_i^0 + \sum_{j \neq i} \frac{H'^{*}_{ij}}{E_i^0 - E_j^0} \Phi_j^0 \qquad (2.153)$$

to first-order.

It is clear that the diagonal matrix elements and the off-diagonal matrix elements of $\hat{H}'$ play different roles in the corrections. The diagonal matrix elements, H'_{ii}, give the first-order corrections to the eigenenergies E_i and contribute nothing to the eigenfunctions Φ_i. Their role is simply to shift the zeroth-order energy levels by H'_{ii}. The off-diagonal matrix elements, H'_{ij}, contribute to the second-order corrections of the eigenenergies E_i and the first-order corrections to the eigenfunctions Φ_i. The corrections from the off-diagonal matrix elements are important only when the absolute values of H'_{ij} are larger than, or comparable to, the energy intervals between the states Φ^0_i and Φ^0_j.

Practically, perturbation theory can be applied to a given physical system in a stepwise way: first one makes a correction for the most significant matrix elements; then for the second most significant ones; and so on until a satisfactory result is achieved.

The most common cases are where there are only two interacting states which have energies very close to each other. In such a case the perturbation problem can be reduced to a two-level problem (supposing the corrections from the diagonal elements have been done in the previous step):

$$\hat{H}^0 = \begin{bmatrix} E_1^0 & 0 \\ 0 & E_2^0 \end{bmatrix} \tag{2.154}$$

$$\hat{H}' = \begin{bmatrix} 0 & H'_{12} \\ H'^{*}_{12} & 0 \end{bmatrix} \tag{2.155}$$

$$\hat{H} = \hat{H} + \hat{H}' = \begin{bmatrix} E_1 & H'_{12} \\ H'^{*}_{12} & E_2 \end{bmatrix} \tag{2-156}$$

If $E_2^0 \geq E_1^0$ and $|H'_{12}|^2 + (E_2^0 - E_1^0)^2 \neq 0$, the Schrödinger equation can be solved exactly:

$$E_1 = \frac{E_2^0 + E_1^0}{2} - \sqrt{\left(\frac{E_2^0 - E_1^0}{2}\right)^2 + |H'_{12}|^2} \tag{2.157}$$

$$E_2 = \frac{E_2^0 + E_1^0}{2} + \sqrt{\left(\frac{E_2^0 - E_1^0}{2}\right)^2 + |H'_{12}|^2} \tag{2.158}$$

$$\Phi_1 = \frac{E_2^0 - E_1}{\sqrt{(E_2^0 - E_1)^2 + |H'_{12}|^2}} \Phi_1^0 - \frac{H'^{*}_{12}}{\sqrt{(E_2^0 - E_1)^2 + |H'_{12}|^2}} \Phi_2^0 \tag{2.159}$$

$$\Phi_2 = \frac{H'_{12}}{\sqrt{(E_2 - E_1^0)^2 + |H'_{12}|^2}} \Phi_1^0 + \frac{E_2 - E_1^0}{\sqrt{(E_2 - E_1^0)^2 + |H'_{12}|^2}} \Phi_2^0 \tag{2.160}$$

Conclusions can be drawn from (2.157) to (2.160):

a). The interacting levels are pushed away from each other. The lower level, E_1^0, is lowered by an amount

$$\Delta = E_1^0 - E_1 = \sqrt{\left(\frac{E_2^0 - E_1^0}{2}\right)^2 + H'^2_{12}} - \frac{E_2^0 - E_1^0}{2} \tag{2.161}$$

which is exactly the same amount as the higher level, E_2^0, is lifted, *i.e.*, $E_2 - E_2^0 = \Delta$ (Figure 2.4).

b). The shifts of the two levels are not larger than $|H'_{12}|$, *i.e.*, $\Delta \leq |H'_{12}|$. The equal sign is true only when the original levels are degenerate: $E_2^0 = E_1^0$ (Figure 2.5).

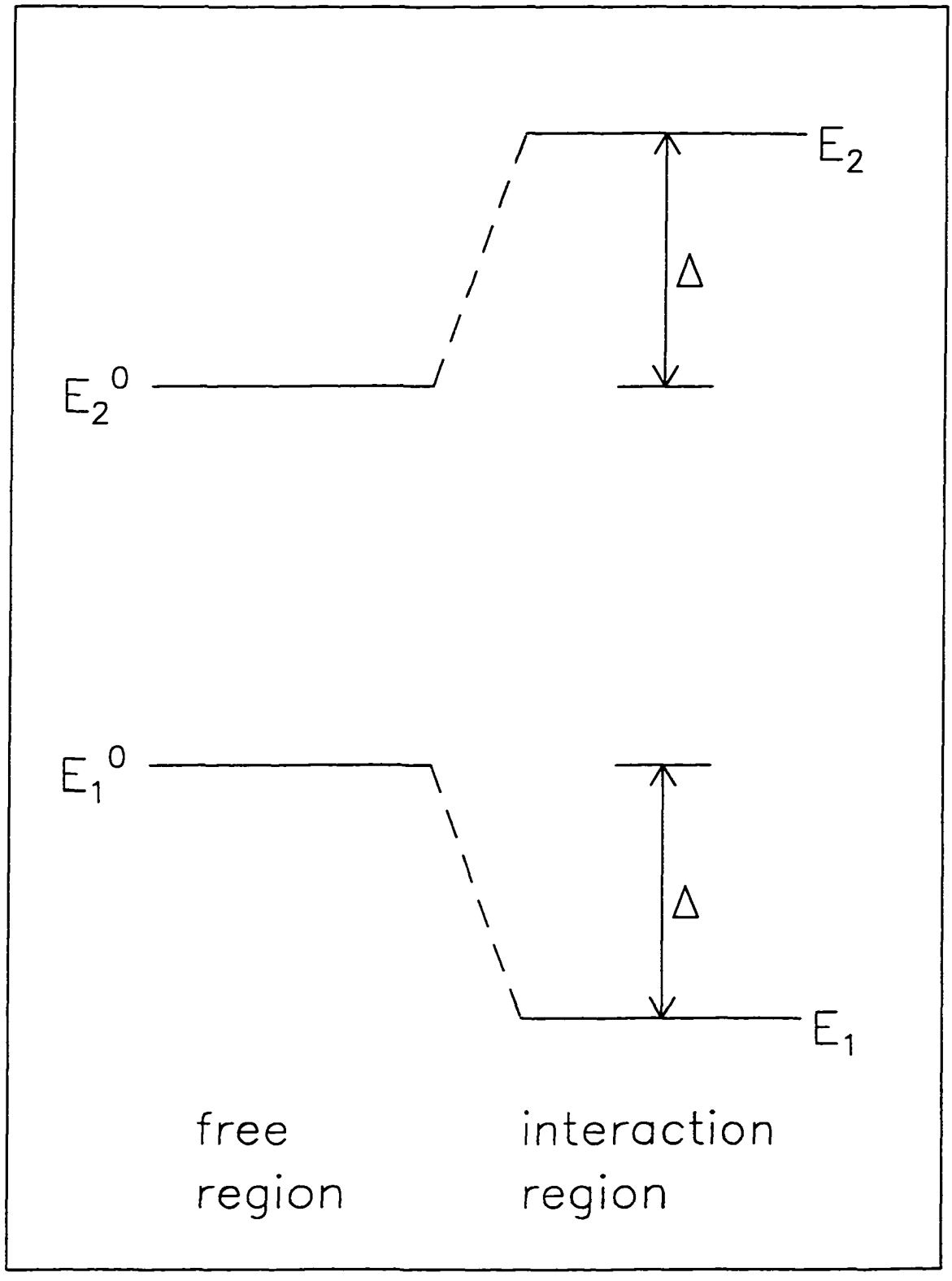

Figure 2.4 Energy level shifts upon an interaction.

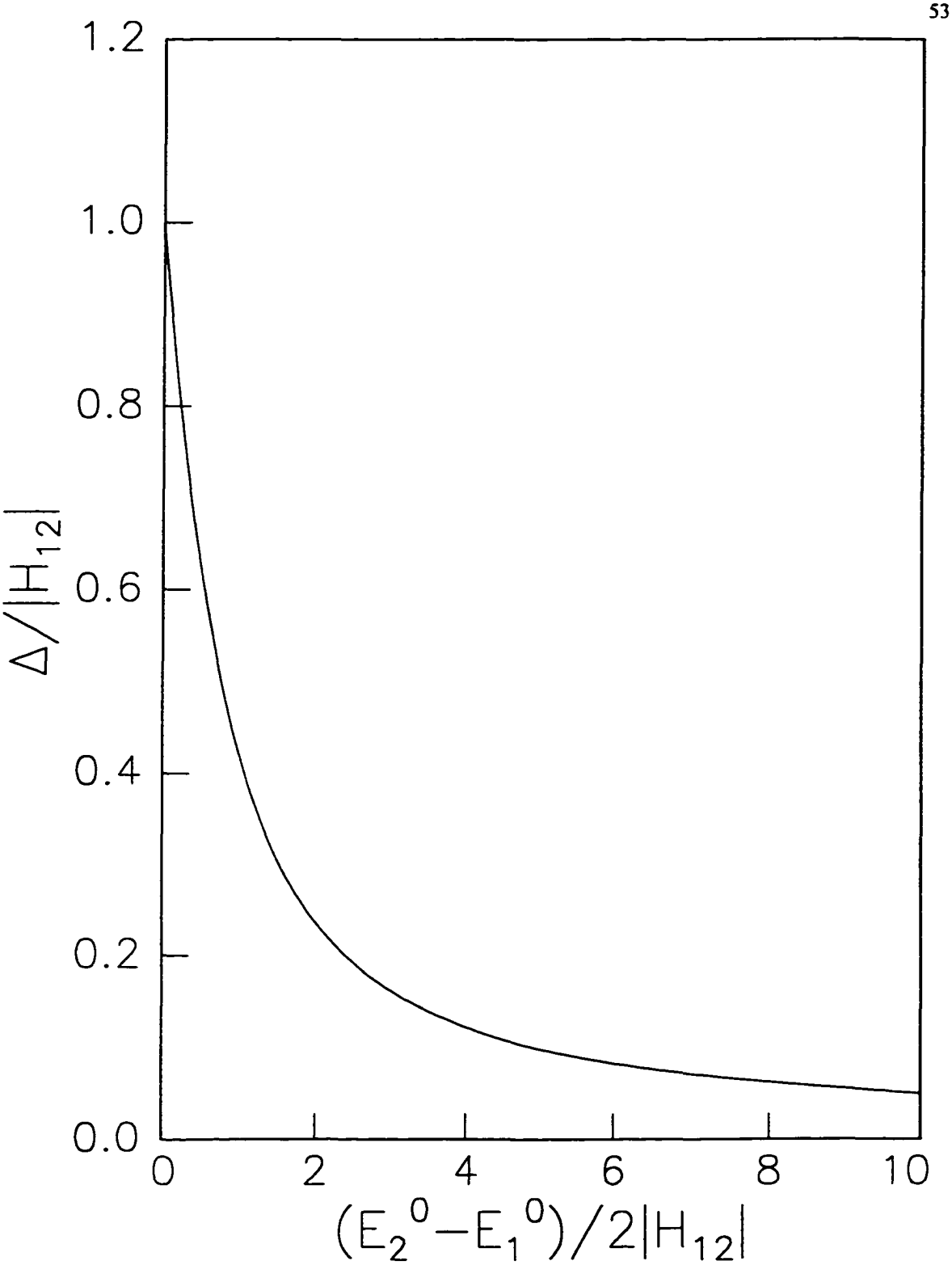

Figure 2.5 Energy shift *versus* original energy gap, in units of the off-diagonal interaction matrix element.

c). The resultant states, Φ_1 and Φ_2, are mixtures of the two original states, Φ_1^0 and Φ_2^0. The contamination of Φ_2^0 in Φ_1, or Φ_1^0 in Φ_2, is a monotonically decreasing function of $\frac{E_2^0 - E_1^0}{2|H'_{12}|}$ (Figure 2.6). When the original levels are degenerate, Φ_2^0 and Φ_1^0 are mixed with equal contributions to both Φ_1 and Φ_2.

d). As a result of the mixing, the state Φ_1, which originates from the state Φ_1^0, has some character of the state Φ_2^0. The same is true for Φ_2 regarding Φ_1^0.

e). The sum of the mean values of any physical quantity in the states Φ_1 and Φ_2 is equal to the sum of those in the states Φ_1^0 and Φ_2^0.

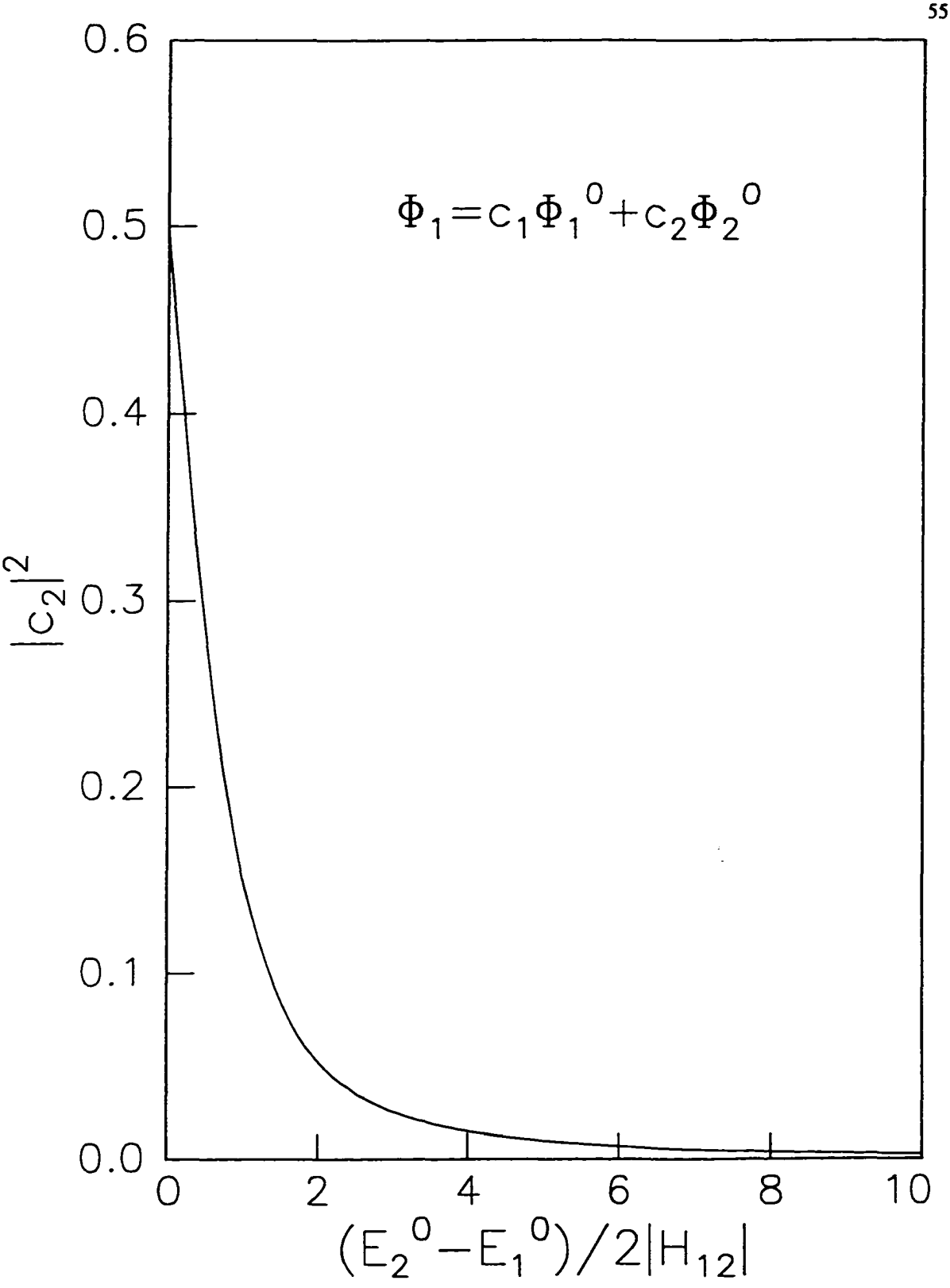

Figure 2.6 The contamination of Φ_2^0 in the state Φ_1.

2.7 The Matrix Elements

For a diatomic molecule system consisting of nuclei, Z_A and Z_B, and k electrons, the Hamiltonian $\hat{H}$ in the molecular frame can be partitioned into three parts, *i.e.*, the electronic Hamiltonian $\hat{H}^{el}$, the rotational Hamiltonian $\hat{H}^{rot}$, and the vibrational Hamiltonian $\hat{H}^{vib}$ [60, 69, 76-80]:

$$\hat{H} = \hat{H}^{el} + \hat{H}^{rot} + \hat{H}^{vib} \tag{2.162}$$

The electronic Hamiltonian, $\hat{H}^{el}$, describes the motion of the electrons in the field of two "clamped" nuclei. It includes the kinetic energies of all electrons, the electrostatic energies between any pair of electron-electron, electron-nucleus, and nucleus-nucleus, and spin-orbit interaction energies:

$$\hat{H}^{el} = \sum_i \left(-\frac{\hbar^2}{2m}\nabla_i^2 - Z_A\frac{e^2}{r_{Ai}} - Z_B\frac{e^2}{r_{Bi}}\right) + \sum_{i\neq j}\frac{e^2}{r_{ij}} + Z_A Z_B\frac{e^2}{R} + \hat{H}^{so} \tag{2.163}$$

where m is the mass of an electron; r_{Ai} and r_{Bi} are the distances from the ith electron to nucleus A and B, respectively; r_{ij} is the distance between the ith electron and the jth electron; R is the distance between the two nuclei. The spin-orbit operator $\hat{H}^{so}$ has the effective form

$$\hat{H}^{so} = \sum \hat{a}_i \hat{l}_i \cdot \hat{s}_i \qquad \text{with} \quad \hat{a}_i \hat{l}_i = \sum_K \frac{\alpha^2}{2}\frac{Z_{eff,K}}{r_{iK}^3}\hat{l}_{iK} \tag{2.164}$$

where l_{iK} is the orbital angular momentum of electron i about nucleus K; $Z_{eff,K}$ is the effective charge of the Kth nucleus; s_i is the spin angular momentum of the ith electron.

Following the procedure outlined in [60], and using the basis functions (2.99)-(2.110) and Table 2.1 or 2.3, calculation of the spin-orbit interaction matrix elements can be reduced to the level of one-electron wavefunctions:

$$H_{ij} = \langle \Phi_i | \hat{H}^{so} | \Phi_j \rangle = H_e \langle v_i | v_j \rangle \tag{2.165}$$

where

$$H_e = \langle \Phi_{el}^{i} | \hat{H}^{so} | \Phi_{el}^{j} \rangle \tag{2.166}$$

is a constant independent of vibrational and rotational quantum numbers; Φ_{el}^{i} and Φ_{el}^{j} are electronic wavefunctions in the form of (2.131); $\langle v_i | v_j \rangle$ is the overlap integral of the two vibrational functions. The selection rules for the spin-orbit interactions are:

$$\Delta J = 0 \tag{2.167}$$

$$\Delta S = 0, \pm 1 \tag{2.168}$$

$$\Delta M_J (= \Delta\Lambda + \Delta\Sigma) = 0 \tag{2.169}$$

$$\Delta\Lambda = 0, \pm 1 \tag{2.170}$$

$$e \longleftrightarrow e \quad f \longleftrightarrow f \quad e \longleftarrow\!\!\!\!\!\!\rightarrow f \tag{2.171}$$

where the selection rules (2.167) and (2.171) are general for all types of perturbations, and will not be repeated again in the rest of this dissertation.

When the spin-orbit interactions are very strong, the good quantum numbers S, Λ, and Σ are destroyed. Only J and $\Omega = |M_J|$ are conserved.

The rotational Hamiltonian $\hat{H}^{rot}$ describes the rotation of the molecular frame. It has the form

$$\hat{H}^{rot} = B(R)(\hat{J} - \hat{L} - \hat{S})^2 \tag{2.172}$$

where all angular momenta are assumed dimensionless since the factors of $\hbar$ are included in the rotational constant

$$B(R) = \frac{\hbar^2}{2\mu R^2} \tag{2.173}$$

It can be further expanded to

$$\hat{H}^{rot} = B(R)(\hat{J}^2 + \hat{L}^2 + \hat{S}^2 - 2\hat{J}\cdot\hat{L} - 2\hat{J}\cdot\hat{S} + 2\hat{L}\cdot\hat{S}) \tag{2.174}$$

The operators in (2.174), which have non-zero off-diagonal matrix elements, are

$$\hat{H}^{se} = B(R)(L^+\cdot S^- + L^-\cdot S^+) \tag{2.175}$$

$$\hat{H}^{S} = -B(R)(J^+\cdot S^- + J^-\cdot S^+) \tag{2.176}$$

$$\hat{H}^{L} = -B(R)(J^+\cdot L^- + J^-\cdot L^+) \tag{2.177}$$

where $A^{\pm} = A_x \pm iA_y$ $(\mathbf{A} = \mathbf{J}, \mathbf{L}, \mathbf{S})$; all angular momenta are defined *in the molecular frame* [81], and have the non-zero matrix elements:

$$<J, M_J \mp 1|\hat{J}^{\pm}|J, M_J> = \sqrt{J(J+1) - M_J(M_J \mp 1)} \tag{2.178}$$

$$<S, \Sigma \pm 1|\hat{S}^{\pm}|S, \Sigma> = \sqrt{S(S+1) - \Sigma(\Sigma \pm 1)} \tag{2.179}$$

$$<\Lambda \pm 1|\hat{L}^{\pm}|\Lambda> \neq 0 \tag{2.180}$$

The difference in behavior of $J^{\pm}$ from $S^{\pm}$ is described by Hougen in [81].

The operator $\hat{H}^{se}$ is called the spin-electronic operator. It has non-zero matrix elements of the form

$$H^{se}_{ij} = B_{v_i v_j} H_e \tag{2.181}$$

where the parameter H_e in this dissertation is used to represent a constant independent of the vibrational and the rotational quantum numbers;

$$B_{v_i v_j} = <v_i|B(R)|v_j> \tag{2.182}$$

The selection rules for the spin-electronic interactions are:

$$\Delta S = 0 \tag{2.183}$$

$$\Delta M_J (= \Delta\Lambda + \Delta\Sigma) = 0 \tag{2.184}$$

$$\Delta\Lambda = \pm 1 \tag{2.185}$$

The operator $\hat{H}^S$ is called the S-uncoupling operator. It has non-zero matrix elements

$$H^S_{ij} = -B_{v_i v_j} \sqrt{S(S+1) - \Sigma_i \Sigma_j} \sqrt{J(J+1) - \Omega_i \Omega_j} \tag{2.186}$$

The selection rules for the S-uncoupling interactions are:

$$\Delta S = 0 \tag{2.187}$$

$$\Delta M_J (= \Delta\Lambda + \Delta\Sigma) = \pm 1 \tag{2.188}$$

$$\Delta\Lambda = 0 \tag{2.189}$$

The operator $\hat{H}^L$ is called the L-uncoupling operator. It has non-zero matrix elements

$$H^L_{ij} = -B_{v_i v_j} H_e \sqrt{J(J+1) - \Omega_i \Omega_j} \tag{2.190}$$

The selection rules for the L-uncoupling interactions are:

$$\Delta S = 0 \tag{2.191}$$

$$\Delta M_J (= \Delta\Lambda + \Delta\Sigma) = \pm 1 \tag{2.192}$$

$$\Delta\Lambda = \pm 1 \tag{2.193}$$

When spin-orbit interactions are very strong, we should use $\mathbf{J}_a$, the total electronic angular momentum, to replace L+S in (2.172). Then (2.174) becomes

$$\mathbf{H}^{rot} = B(R)(\mathbf{J}^2 + \mathbf{J}_a^2 - 2\mathbf{J}\cdot\mathbf{J}_a) \tag{2.194}$$

The operator in (2.195), which has non-zero off-diagonal matrix elements, is

$$\hat{H}^{J_a} = -B(R)(J^+ \cdot J_a^- + J^- \cdot J_a^+) \tag{2.195}$$

This operator may be called the J_a-uncoupling operator. It has non-zero matrix elements

$$\hat{H}_{ij}^{J_a} = -B_{v_i v_j} H_e \sqrt{J(J+1) - \Omega_i \Omega_j} \tag{2.196}$$

with selection rules:

$$\Delta S = 0 \tag{2.197}$$

$$\Delta M_J (= \Delta\Lambda + \Delta\Sigma) = \pm 1 \tag{2.198}$$

Chapter 3

Experimental Details

3.1 Introduction

Laser vaporization of a solid metal target in a molecular beam has been proved to be an effective way to produce metal containing radicals. In 1981, Dietz *et al.* reported their initial success in forming cold beams of aluminum clusters by combining the laser vaporization technique with pulsed supersonic nozzle technology [82]. Their apparatus involves the use of Nd:YAG laser pulses (6ns duration of FWHM of the second harmonic at 532nm) to produce a high temperature metal vapor plasma within the throat of a pulsed supersonic nozzle with a 28.5atm. backing pressure of helium. Under the conditions typically employed in this type of experiment [83] the metal plasma is quickly cooled back to near room temperature due to the high effective carrier gas density over the target at the moment of vaporization and the tightly restricted heating region of the target surface. During the cooling process the ions and the electrons begin to recombine to form neutral atoms and further to form clusters through condensation [83]. At the end of the plasma thermalization/cluster formation channel, the gas becomes supersonic as it is allowed to expand freely into a large vacuum chamber. Collisions within the subsequent supersonic expansion then cool the metal clusters in the beam to an extremely low internal as well as translational temperature.

An appealing aspect of this cluster beam generation technique is its generality [82]. Any metal or mixture of metals may be used, and even the most refractory material is readily vaporized by pulsed Nd:YAG lasers. Supersonic metal clusters have been obtained with a wide variety of high-boiling metals including molybdenum (bp=4612 °C) and

tungsten (bp=5660 °C).

One of the instructive aspects of reference [82] was the observation of Al_n-C_3H_6O and Al_n-C_2H_3O (n=1,2,3,...) in the time-of-flight (TOF) mass spectrum of a supersonic aluminum cluster beam produced by laser vaporization of an aluminum rod inside a pulsed supersonic nozzle. Acetone impurity in the helium carrier gas proved to be responsible for the formation of acetone-Al_n and acetyl-Al_n species. This result clearly shows that the laser ablation technique is not restricted to pure metal clusters, but can equally well be applied to studies of reactions between metals and other compounds. Gas phase reactions of hydrogen with iron clusters were conducted in 1985 [84]. Efficient formation of transition metal monoxide was observed in 1986 by adding a small amount of oxygen to the carrier gas while a Pb rod was vaporized by a laser beam [85]. High resolution spectroscopic studies of ZrO on all five isotopic species (^{90}ZrO, ^{91}ZrO, ^{92}ZrO, ^{94}ZrO, and ^{96}ZrO) were conducted in 1988 on a similar molecular beam apparatus [86].

In this chapter we summarize the experimental setup which combines the techniques of laser vaporization in a molecular beam and laser induced fluorescence (LIF) spectroscopy in our laboratory. The setup is shown schematically in Figure 3.1. It consists of three parts with different functions: the laser vaporization molecular beam source mixes sample gas and metal vapor to produce species of interest in a molecular beam; the LIF detecting system excites the species and collects partially dispersed fluorescence following laser excitation; the data processing system manipulates the time varying electrical signal from the LIF detecting system and processes the signal into a suitable data format.

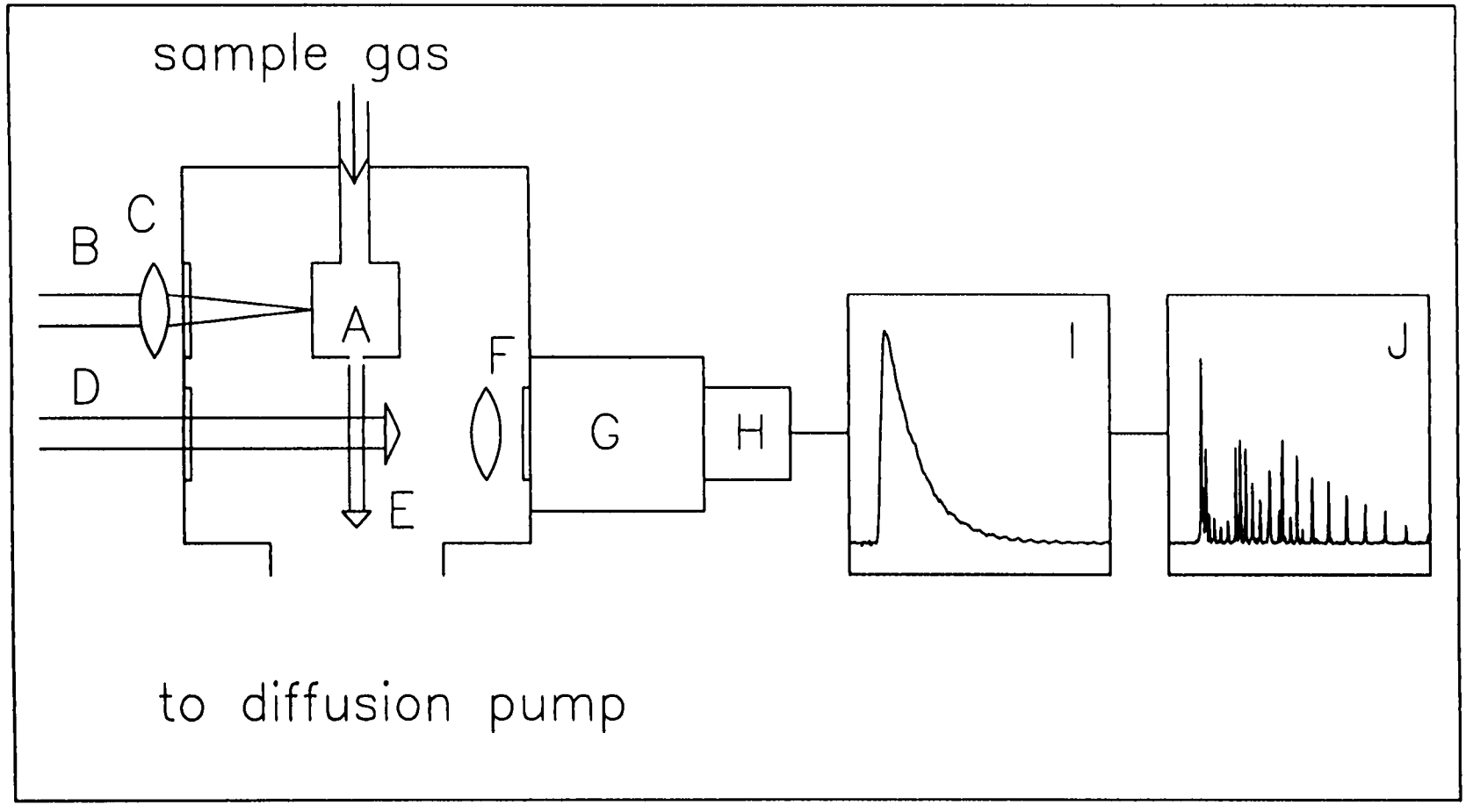

Figure 3.1 Experimental setup. A: molecular beam laser vaporization source (Figure 3.2 for details); B: vaporization laser beam, C: focus lens; D: excitation (probe) laser beam; E: molecular beam; F: collecting lens; G: monochromator; H: PMT; I: digital oscilloscope; J: PC computer.

3.2 Laser Vaporization Molecular Beam Source

3.2.1 the sample gas and the vacuum chamber

The pulsed molecular beam is formed by expanding a high pressure sample gas into a high vacuum chamber through a homemade pulsed valve. The major advantage of using a molecular beam in spectroscopic studies, instead of a gas cell, is that the molecular beam provides a limited volume that contains gaseous molecules with high density, narrow velocity spread, and low temperature. More importantly in the present experiments is the fact that the molecular beam ensures a rapid cooling of the highly ionized plasma, formed during laser heating of a piece of metal, to form neutral species of interest.

The low temperature of the beam ensures that only a few rotational energy levels of the ground vibronic state of the radicals are significantly populated. This greatly reduces the complexities associated with the molecular spectra of transition metal containing radicals. The beam temperature was estimated, by monitoring the rotational state distribution of the diatomic molecules, to be between 20K to 200K, depending on the expansion conditions.

Different gases were seeded in the helium carrier gas in order to make species of interest. For instance, CH_4 was used to form metal carbides; NH_3 was used to form metal nitrides; O_2 for metal oxides; and H_2 for hydrides. The sample gases are normally seeded in small concentration (2%~10%) in pure helium at a total pressure of one atm. The container of sample gas is a 10 liter glass bulb with two outlets, one of which is connected to a gas preparing system and another to the pulsed molecular beam valve.

The vacuum environment in which the molecular beam is formed and propagated is a 30cm×30cm ×30cm black anodized cubic aluminum chamber. The chamber is evacuated

by a diffusion pump (Edwards, Diffstak 160) which is backed by a mechanical pump (Edwards, E2M8). The chamber pressure is monitored using an ion pressure gauge (Granville-Phillips, 274012) combined with a thermocouple pressure gauge (Granville-Phillips, 270006), while the backing pressure is monitored using a thermocouple pressure gauge of the same type. Ion pressure gauge readings of 1×10^{-4} and 1×10^{-5} Torr are typical with the molecular beam switched on and off, respectively.

3.2.2 the molecular beam valve

Within the vacuum chamber there is a molecular beam valve connected to the external gas supply through a Teflon tube (Figure 3.2). The pulsed molecular beam valve was designed following the description of Proch and Trickl [87]. A piezoelectric disk translator (Physik Instrument, P286.20) is driven by a homemade pulsed power supply to move an aluminum piston surrounded by diluted sample gas. The tip of this piston is sealed with a rubber O-ring from a 0.5 mm aperture. The valve can be opened (by lifting the piston) for an adjustable period of time such that the sample gas is allowed to expand into the vacuum chamber, and cool down to a lower temperature. The pulsed power supply allows for adjustment of the opening of the valve (through the driving voltage, up to 500V), the pulse duration (~200μs), and the timing of the molecule beam pulse.

The pulse duration and the driving voltage largely determine the molecular beam conditions. A large voltage leads to a large amplitude motion of the piezocrystal and therefore a large gas throughput. However, high driving voltages also cause excessive strain on the disk translator and possible damage. Long pulse duration increases the load on the diffusion pump and therefore the pressure in the vacuum chamber, without

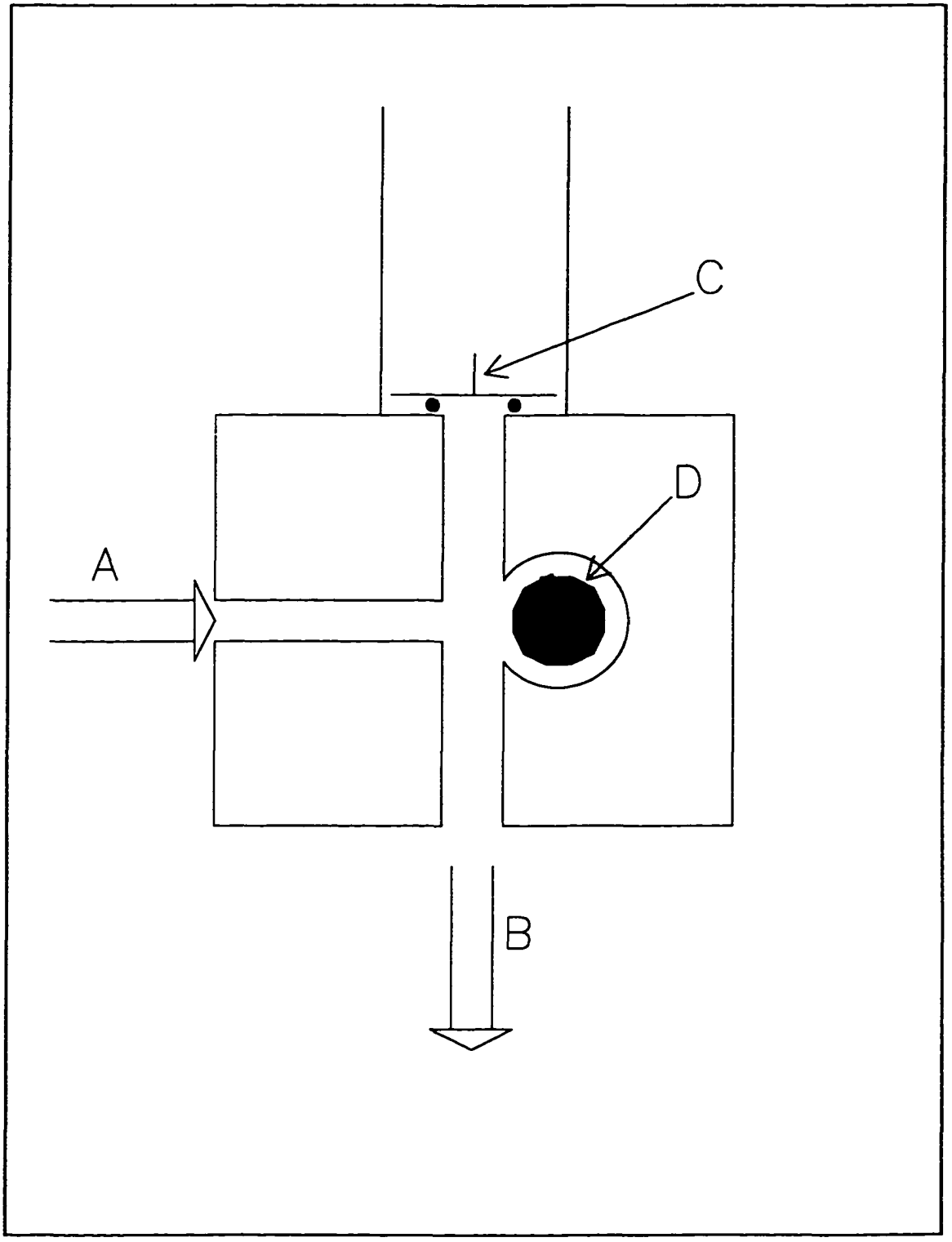

Figure 3.2 Molecular beam laser vaporization source. A: vaporization laser; B: molecular beam; C: piezoelectric valve; D: rotating-translating metal rod.

influencing the sample gas density in the beam but increasing the beam temperature slightly. On the other hand, if the pulse duration is too short, there is not enough time for the aluminum piston to respond fully to form a good molecular beam. Since the temperature is somewhat critical in the experiments, both the driving voltage and the pulse duration were optimized to maximize the LIF signal while keeping the gas load as low as possible.

A reaction chamber, attached below the valve, has three mutually perpendicular channels. The main channel (2mm in diameter, 17mm or 25 mm long, right below the valve) allows the sample gas to flow from the valve to the vacuum chamber. The physical dimension of this channel is critical to the species produced as a result of the reaction between the metal vapor and the sample gas. An example of such an influence was observed in our experiments. Efficient formation of rhenium nitride (ReN) was achieved with the short channel (17mm), whereas the situation was very unstable with the longer channel (25 mm). The second channel, with a larger dimension (d=5.5mm), allows for insertion of a metal rod (5 mm in diameter). This channel lies 13 mm downstream of the valve and is exposed to both the main channel and a third channel. The third channel allows the vaporization laser to strike the metal rod placed in the second channel.

3.2.3 the metal rod and the vaporization laser

Metal vapor is produced in the reaction chamber downstream of the pulsed molecular valve, by laser ablation of a suitable metal rod. The reaction of the sample gas with the metal vapor yields the radicals of interest. For instance, with an iron rod and CH_4 gas, C_2, C_3, CH, FeC, (and possibly $FeCH_3$) were produced and identified.

Figure 3.2 shows the cross section of the reaction chamber where the metal vapor is produced. The metal rod (a cast iron rod for FeC or a 99.99% purity rhenium rod purchased from Johnson-Matthey for ReN), 30 mm long × 5 mm diameter, is placed in the path of the ablation laser. Driven by a stepping motor, the rod rotates and translates continuously during the experiment to expose a fresh area of surface. Under circumstances when the motor stops turning, a few laser shots are enough to drill a hole through the rod. The ablated area of the rod is also exposed to the main channel through which the sample gas was expanded and mixed with the plasma.

The second harmonic (532nm) output of a Nd:YAG laser (Continuum NY61) is used as the vaporization source. There are two reasons to use the second harmonic of the YAG laser: for safety reason, the IR fundamental (1064nm) is not used; the second harmonic (532nm), instead of the third harmonic (355nm), is used since the former provided sufficient energy to vaporize even the most refractory metals such as rhenium (bp=5900K).

The second harmonic output at 532nm is generated using a "SHG Type II" KDP crystal. The power at 532nm can be reduced continuously without a significant change in beam alignment or beam quality by slightly misaligning the SHG crystal. This reduction of the laser power can greatly reduce the background noise in the spectra if the LIF signals are strong. The laser beam, about 8ns duration (FWHM), is focused onto the rod using a convex (converging) lens (f.l. = 50 cm). The arrival time of laser pulse with respect to the opening of the pulsed molecular beam valve is carefully adjusted to allow for maximum product yield.

3.3 The LIF Technique

3.3.1 the laser-induced-fluorescence

Molecular spectroscopy can be roughly classified into two categories, absorption spectroscopy and fluorescence spectroscopy.

Traditionally in absorption spectroscopy experiments, a broad continuum light source (*e.g.*, the emission from high pressure Xe lamp arc) is passed through the sample. The transmitted light is then dispersed and its intensity is recorded as a function of wavelength. The spectral resolution is basically determined by the resolving power of the dispersing instrument, while the detection sensitivity is strongly limited by the minimum absorbed power which can be measured.

The development of laser techniques has changed spectroscopic studies dramatically. First, the dispersing element is incorporated into the laser source thus no high resolution dispersing instrument is needed in absorption experiments. Laser wavelengths can be pre-calibrated and are easily tunable. By scanning the laser wavelength, the absorption as a function of wavelength is obtained which mimics the absorption spectrum. Secondly, highly sensitive detection methods are available for laser absorption spectroscopy [88]. In these methods the absorbed laser energy is converted into other easily detectable forms. For instance, the laser energy can be transferred into fluorescence energy (excitation spectroscopy), thermal energy (photoacoustic spectroscopy), electrical energy (optogalvanic spectroscopy), part of the ionization energy (ionization spectroscopy), *etc*.

For a typical molecule with energy levels as illustrated in Figure 3.3, if only the ground energy level is significantly populated, whenever the laser wavelength is tuned to

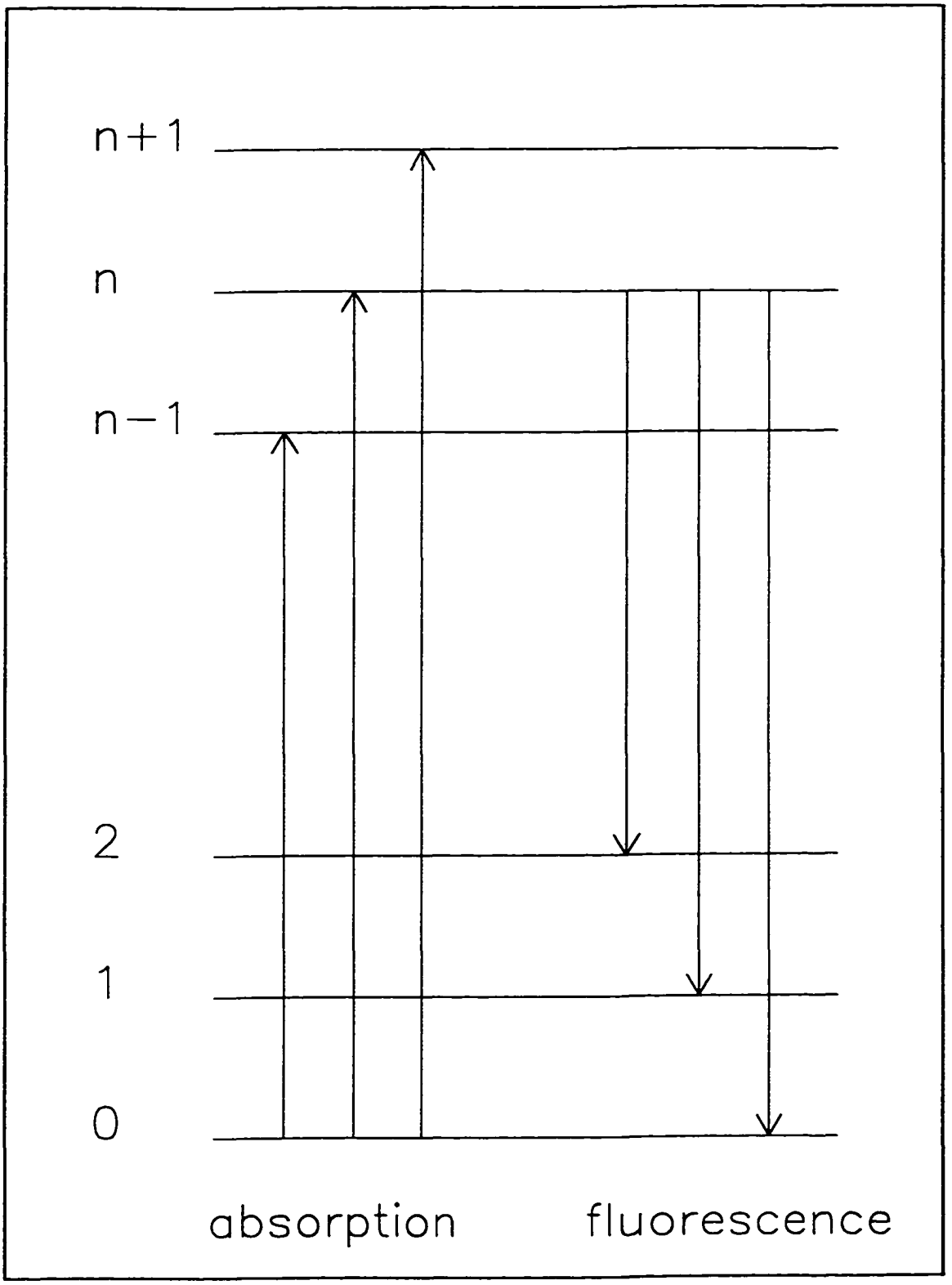

Figure 3.3 Absorption and fluorescence processes in a LIF experiment.

an absorption transition (*e.g.*, the $E_n - E_0$ transition), a fraction of the molecules will be excited from the ground state (E_0) to the higher state (E_n) following the absorption of photons. These excited molecules will eventually return to their ground state *via* spontaneous transitions to lower states $E_k < E_n$ ($k = 0, 1, 2, \ldots, n-1$) and emit photons with appropriate energies. A record of the laser-induced-fluorescence intensity as a function of the excitation laser wavelength is called an excitation spectrum. It is worth pointing out that the intensity of laser-induced-fluorescence is zero if the laser wavelength is not tuned to an absorption transition. This makes the excitation spectroscopy a zero-background technique, which is highly sensitive.

One can also excite molecules and record the dispersed fluorescence as a function of the fluorescence wavelength (DF spectrum). The source used to excite molecules strongly influences the appearance of the DF spectrum since it determines the population distribution of the excited states. Again laser excited DF spectroscopy is the simplest. In these experiments the laser wavelength is tuned to an absorption transition (*e.g.*, E_n - E_0 transition) to populate a particular excited state (E_n). The fluorescence from this state is then dispersed and recorded. The spectral resolution is limited by the dispersing instrument.

The LIF related absorption and fluorescence spectra provide different information on the molecular system. In a cold molecular beam where molecules are essentially in their ground vibronic state, absorption can start only from that state. Thus a visible-UV absorption spectrum maps higher energy levels. In fluorescence spectroscopy, since a particular excited state is predominantly populated, all fluorescence transitions share this common energy level. The fluorescence spectrum therefore provides information about the

low-lying energy levels (Figure 3.3).

3.3.2 the excitation laser

The LIF spectra were recorded using a YAG-dye laser system. A Nd:YAG laser (Lumonics YM600) operating at 355nm is used to pump a dye laser (Lumonics HD-300). The dispersing element in the dye laser is a 2400 groove/mm reflecting grating. The output wavelength of the dye laser has been calibrated and checked in a number of ways: by means of a neon hollow cathode lamp, an I_2 cell, a cold NO $A^2\Sigma \leftarrow X^2\Pi$ γ-band absorption spectrum (frequency doubled), known transitions in the radicals C_2 and C_3, and metal atomic lines in the spectral region of interest. With the present equipment the absolute wavelength accuracy is within 1 cm^{-1} whereas the relative wavelength reading, within a single band, is precise to 0.1cm^{-1}.

3.3.3 the fluorescence collection system

The LIF photon signal of the radicals is collected by a lens, filtered by a monochromator, and converted into an electrical signal by a photomultiplier tube (PMT). The collection lens (f.l.=75mm, 50mm diameter) is placed inside the vacuum chamber. It was designed to image the fluorescent spot - the crossing area of the molecular beam and the excitation laser - onto the entrance slit of the monochromator.

The monochromator (Jobin Yvon, H20) works as a wavelength band pass filter. It was used in three different modes in our experiments: i). As a broad band pass filter (about 30nm) with both the entrance and the exit slits removed. This broad bandwidth filtering allows for a maximum collection of emissions to many lower vibronic states, while

effectively reducing the scattered light of both the vaporization and the probing lasers. It also reduces broad continuous emission from the plasma. ii). With the entrance and the exit slits (1mm width) the monochromator has a bandwidth of about $100cm^{-1}$. This resolution is sufficient for vibrational analysis of dispersed fluorescence spectra. In this working mode the excitation laser wavelength is tuned to a particular transition and the grating of the monochromator is rotated to obtain DF spectra. iii). The monochromator was also used to record emission filtered excitation spectra. In this mode the monochromator with the slits was fixed at a particular wavelength and the emission to a particular vibronic state was monitored. This mode of operation proved to be invaluable in understanding a perturbed spectrum. Since different excited states emit to different lower states, the component related to a particular transition in the perturbed spectrum can be isolated [56].

The light transmitted through the monochromator is finally detected using a photomultiplier tube (Hamamatsu, R106UH). The PMT R106UH has a spectral range 160~650nm peaked at 340nm with high anode sensitivity (typically 150mA/lm), high current amplification (typically 3.0×10^7), and short response time (rise time 2.2ns).

3.4 The Data Processing System

3.4.1 the oscilloscope

The electrical signal from the PMT is detected and digitized on a digital oscilloscope (Tektronix 2440; 500MHz). The oscilloscope has two independent input channels that can be programmed individually for deflection, input impedance, and AC/DC coupling. Calibrated deflection factors are available in a 1-2-5 sequence from 2 mV to 5 V per division. Input impedance can be set to 1 MΩ or 50 Ω, and coupling can be AC (only if impedance is 1 MΩ), DC, or ground. In all our experiments the coupling is set to DC and the input impedance to 50 Ω to match the impedance of the coaxial transmission cable.

Signals were recorded with an acquisition rate of 500M samples/second. The delay time from "trigger zero" to the actual sampling interval was adjusted by means of a B-delay scan to match the flight time of the species of interest from the laser ablation point to the laser excitation spot downstream in the molecular beam. This sampling interval consists of 1024 channel-voltage data pairs. While the time resolution can be 2 ns between adjacent points, the voltage resolution is determined by the 8 bit A/D converter to be 1/250 of the full deflection, *i.e.*, 80 μV at the minimum deflection of 2 mV/division.

The oscilloscope is triggered by a 5 V external signal. The general purpose interface bus (GPIB) (National Instruments, NI 488.2) allows for fast data transfer from the oscilloscope to the data acquisition computer (Powerwave, 386 PC; 25MHz). The oscilloscope is set at the "Fast Transmit" mode in order to transfer the acquired waveform at the highest possible rate. When in "Normal Mode" the oscilloscope is waiting for a

request from the computer before starting to send the waveform, whereas in the "Fast Transmit" mode it works in an "acquire-transmit-rearm" sequence. Since the number of requested waveforms is given in a single command at the beginning of each sequence, and the oscilloscope does not "listen" to the computer before the last waveform is transmitted, there is very little dead time between acquisitions. In this way the acquisition rate for a large number of waveforms can be greatly improved. Only by using the "Fast Transmit" mode can the data acquisition, transmission, and some manipulations be done at the experiments' pace of 10Hz.

3.4.2 computer interface and software

The data acquisition computer is a 386/25 MHz IBM compatible PC, which was equipped with a GPIB board (National Instruments, NI 488.2), a counter/timer card (Advantech, PCL-830), an A/D converter (Laboratory Technologies, PCL-711S) one parallel and two serial (RS232) ports. Many of these interfaces were manipulated via a suite of QuickBasic® (QB) programs with several assembly code drivers.

The GPIB board was accessed via the QuickBasic driver (QBIB.COM), which was made accessible by a QuickBasic declaration file (QBDECL.BAS) at the beginning of each program. Similarly the timer card was accessed via an assembly code software driver (PCL830.BIN). The timer card has a 1 MHz on-board time base and 20 independent counters, which are used to trigger the series of events. A separate QuickBasic program (TIMER.BAS) was written to generate 10 pulse outputs with individually adjustable pulsewidths and delay times. The A/D converter board is accessed via a home-written assembly code driver (ADCONV.ASM). The standard parallel communication port

(COM1) is used as an interface to the probe dye laser.

Accurate triggering (ns resolution) is crucial for the experiments. Generally the master trigger frequency is defined by the clock of the timer/counter card and set to 10 Hz. The timer board triggers a whole series of events. The two Nd:YAG laser lamps are triggered by channel 5 and 7 outputs of the timer board, respectively, and the homemade nozzle driver by channel 9. The Q-switching of the lasers and the triggering of the oscilloscope are controlled via a commercial four-channel delay generator (Princeton Applied Research, EG&G 9650), which in turn is triggered by channel 2 of the timer board. The delay generator offered four independent and two dependent outgoing triggers with variable delays with respect to the incoming trigger in the range of 0 to 100 ms in steps of 10 ps. The jitters were specified by the manufacturer as being $< (50\text{ps} + 10^{-8}\Delta t_{delay})$ for successive pulses.

3.4.3 experimental procedure

Experiments were performed in three different fashions. First, excited state lifetimes were obtained by averaging waveforms transmitted from the oscilloscope. In this working mode, the excitation laser wavelength was fixed while the waveforms were averaged for one thousand laser shots and recorded in the computer. The waveforms reflect the LIF intensity decay, and are therefore measurements of the excited state lifetime. Second, excitation spectra were achieved by integrating the waveforms for each excitation laser wavelength. The excitation wavelength was scanned, in steps of 0.001nm, to get a series of integrated LIF intensity. At each wavelength the waveforms were integrated and averaged for five to ten laser shots. Third, dispersed fluorescence spectra

were also recorded by integrating the waveforms. But in this working mode the excitation laser wavelength was fixed at a pre-selected value while the monochromator was scanning in steps of 0.5nm from a wavelength about 20nm shorter than the excitation laser wavelength to 900nm. Normally 20 laser shots were averaged for DF spectra.

Chapter 4

The Electronic Structure and Perturbations of Iron Monocarbide (FeC)

4.1 Introduction

Iron, Fe, is an element important to our daily life, the planet, and the Universe. It is also very complex in view of its atomic energy level structure. Even high level *ab initio* calculations cannot yield a reliable energy separation between the ground state $^5D(3d^64s^2)$ and the first excited state $^5F(3d^74s^1)$ within 0.2eV [89]. The complexity of the atomic structure makes the understanding of iron-containing molecules a challenge both experimentally and theoretically.

Iron monohydride, FeH, is the only iron-containing molecule observed (to date) in astrophysical sources, being found in the atmospheres of stars and in sunspots [8-9]. However, controversy existed even for the identity of the ground state [90-91]. All early theoretical studies predicted a $^6\Delta$ ground state [48, 62-63]. It was not until 1988 that an extensive *ab initio* calculation yielded a $^4\Delta$ ground state [64]. In this calculation a large Gaussian basis set and an extensive treatment of electron correlation, including the inner-shell electron correlation, were implemented [43].

The energy levels of iron monofluoride, FeF, are expected to show a similar pattern to those of FeH and Fe^+ [16, 44-45]. *Ab initio* calculations on this radical are straightforward since only a single ionic bond is formed [46-47]. In 1978 Pouilly *et al.* observed emission spectra of the FeF in a liquid nitrogen-cooled hollow cathode discharge [44]. Aided by theoretical considerations [45] they assigned the ground state as a $^6\Delta$ state. A Fourier transform emission spectrum involving the low-lying $^4\Delta$ state was later

recorded [92]. For the isovalent FeCl system, debates on whether the ground state might be a $^4\Sigma$ state or a $^6\Sigma$ state lasted many years [68]. It was only in 1980 that the spectrum of FeCl was compared and recognized to be analogous with that of FeF [93].

Iron monoxide, FeO, is one of the most extensively studied transition metal containing diatomic molecules [66]. Its complex spectrum in the orange region has been recognized for almost a century [59]. The lower state of the "orange" system was assigned to be the ground state of the molecule [94] based on the infrared spectrum of matrix isolated FeO. In 1981, the ground state was finally identified as a $^5\Delta$ state [58]. Several *ab initio* calculations were conducted [66-67] on the molecule, but there was a disagreement on the symmetry of the ground state.

There are still no gas phase spectroscopic data available for iron mononitride, FeN, although FeN may be a key in the understanding of nitrogen fixation, an important process both in the biosphere of our planet and in industry. An infrared spectrum of matrix isolated FeN was observed in 1996 [95]. Because of the lack of rotational motion in a solid matrix, it was not possible to identify the symmetry and the spin multiplicity of the ground state from the experimental data. Theoretical calculations [95-98] identified the existence of a group of low-lying electronic states: $^2\Delta$, $^4\Pi$, $^4\Phi$, and $^6\Sigma^+$, with $^2\Delta$ as the most probable candidate for the ground state.

Iron monocarbide, FeC, was first observed in 1995 [18] in our laboratory. Based on the experimental observations and the *ab initio* calculations on RuC [99-101], the ground state of FeC was assigned as a $^3\Delta$ state. The pure rotational spectrum of the molecule was reported by Allen *et al.* last year [102]. Their analysis yielded more accurate spectroscopic parameters for the ground electronic state. Very recently Brugh and Morse

published their ionization work on FeC [103], extending the observed optical spectrum further to the red.

Spectroscopic studies on other transition metal monocarbides were also reported in recent years. Prior to 1980, there were publications on gas phase spectroscopic studies of four transition metal monocarbides, *i.e.*, PtC [28-32], RhC [22-24], IrC [25-27], and RuC [20-21]. In 1994 Simard *et al.* [19] in a new approach obtained a spectrum of YC in molecular beam studies. This pioneering experiment has since been repeated to produce other radicals such as FeC [18], CrC [33], CoC [34-35], NiC [33, 36], MoC [33], and PdC [33].

In this chapter we present our spectroscopic characterization of iron monocarbide, FeC. Gas phase jet-cooled laser induced fluorescence (LIF) spectra of $Fe^{12}C$ and $Fe^{13}C$ in the region of 430 to 500nm have been recorded. Rotational analyses have been carried out for a majority of the observed bands. Excited state lifetimes have been measured. Dispersed fluorescence spectra were also recorded following laser excitation at selected wavelengths. The electronic structure of FeC is established based on experimental observation and MO considerations, as well as on early *ab initio* calculations on RuC.

Several experimental observations (e.g., LIF spectra, excited state lifetime measurements, isotope shifts) suggested the existence of extensive perturbations in the wavelength region investigated. Deperturbation analyses were attempted and their implications on the electronic structure of FeC are discussed.

4.2 LIF Spectra of FeC

The reaction products of laser ablation of iron and methane doped in helium were examined in a supersonic molecular beam, using the laser-induced-fluorescence (LIF) technique. In addition to the well known Swan system [104] of C_2 bands, the spectrum showed 12 red-degraded bands in the 430-500 nm region, which could not be attributed to any previously known molecule. These bands are believed to be from FeC because of the presence of iron and carbon in the molecular beam. A reproduction of the strongest of these bands, with its R-band head at 493.0nm, is given in Figure 4.1(a). The rotational assignments and vacuum wave numbers are listed in Table 4.1. The band has integral rotational quantum number J and only one set of P, Q, and R branches, suggesting the spectrum carrier is a linear molecule with odd spin multiplicity. All three branches have similar intensities at low J. At high J, the Q branch falls off faster than the P and R branches, indicating a $\Delta\Omega = 0$ type transition. Due to the low temperature molecular beam conditions, the first lines of the three branches were easily identified. This allowed a definite assignment of Ω values in both the lower and the upper states. No Λ-type doubling was detected at the current resolution of the experiments. Most of the experimentally observed bands of FeC have an appearance similar to the 493.0nm band. Some of them belong to $\Omega' = 3 \leftarrow \Omega'' = 3$ type transitions, others are associated with $\Omega' = 2 \leftarrow \Omega'' = 2$ type transitions. Several bands appeared severely perturbed.

The observed rotational constants are about 0.5~0.6cm^{-1}, strongly supporting the suggestion that the carrier is a diatomic species, most probably the iron monocarbide, FeC. This conjecture was readily confirmed when experiments were repeated using ^{13}C labeled methane in place of natural methane and the corresponding bands were found shifted in

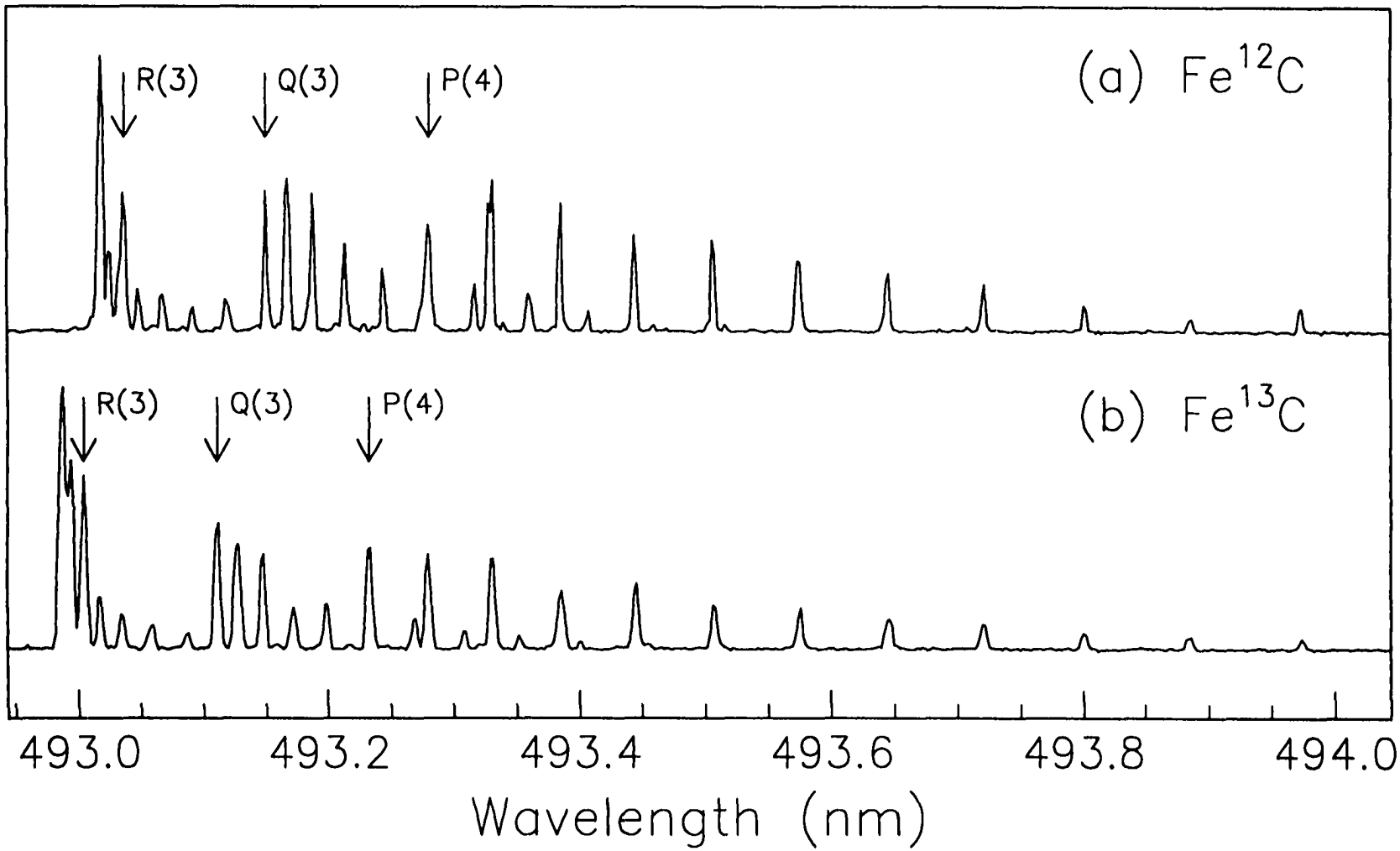

Figure 4.1 The LIF excitation spectra of the 493.0nm transition for the $Fe^{12}C$ (a) and $Fe^{13}C$ (b) molecules. The first lines in the P, Q, and R branches are marked with arrows.

Table 4.1 Rotational assignments and vacuum wavenumbers (in cm^{-1}) for the 0-0 band of the $(1)^3\Delta_3 - X^3\Delta_3$ system at 493.0nm.

	$Fe^{12}C$			$Fe^{13}C$		
J	R(J)	Q(J)	P(J)	R(J)	Q(J)	P(J)
3	20277.28(4)	20272.59(1)		20278.59(5)	20274.15(-4)	
4	20277.77(8)	20271.85(-3)	20267.25(2)	20279.00(4)	20273.50(-3)	20269.14(-3)
5	20278.02(5)	20271.03(4)	20265.12(-6)	20279.25(3)	20272.67(-2)	20267.25(0)
6	20278.02(-5)	20269.96(3)	20262.90(-6)	20279.25(-6)	20271.69(0)	20265.12(-5)
7	20278.02(3)	20268.73(4)	20260.52(-4)	20279.25(2)	20270.54(1)	20262.90(-1)
8	20277.77(3)	20267.25(-3)	20257.97(-1)	20279.00(2)	20269.14(-5)	20260.44(-5)
9	20277.28(-3)	20265.69(0)	20255.18(-4)	20278.59(2)	20267.66(-3)	20257.97(7)
10	20276.78(7)	20263.97(5)	20252.23(-7)	20278.02(2)	20266.10(7)	20255.10(-5)
11	20275.96(3)	20262.00(2)	20249.11(-8)	20277.36(10)	20264.29(9)	20252.23(-1)
12	20274.97(0)	20259.86(0)	20245.92(1)	20276.29(-6)	20262.32(12)	20249.20(4)
13	20273.91(7)	20257.56(0)	20242.39(-6)	20275.14(-14)	20260.11(6)	20245.92(1)
14	20272.59(6)		20238.79(-3)			20242.39(-10)
15	20271.03(-2)		20234.94(-7)			20238.79(-13)
16	20269.30(-9)		20231.01(-2)			
17			20226.92(5)			20231.26(-1)

Note: The numbers in parentheses indicate the differences, in $10^{-2}cm^{-1}$ units, between the observed wavenumbers and the ones calculated with parameters given in Table 4.2

wavelengths (Figure 4.1) and modified in rotational spacing. Experiments carried out under similar conditions with a rhodium rod yield a rich spectrum of rhodium monocarbide, consisting of all the bands reported by Lagerqvist and Scullman [23] and other RhC bands carrying important information on low J levels. With the iron rod, the experimentally determined ratios of rotational constants in the 493.0nm ^{12}C and ^{13}C spectra agree closely with the theoretically expected value for FeC. Blue-shifted bandheads due to the naturally occurring minor species ^{54}FeC can also be identified in the spectra but their structure is generally too weak and overlapped with the strong ^{56}FeC bands to permit detailed rotational analysis.

Figure 4.2 summarizes all observed band systems for $Fe^{12}C$. The principal band system (system I) of the $Fe^{12}C$ spectrum includes bands having their R-branch bandheads near 493.0nm, 476.2nm, 461.1nm, and 448.0nm. These bands form a vibrational progression. The corresponding bands in the $Fe^{13}C$ spectrum have their R-branch bandheads moved to 493.0nm, 476.6nm, 461.8nm, and 449.0nm, respectively. The very small shift observed in the 493.0nm band position upon isotopic substitution (Figure 4.1) indicates that this band is a $\Delta v=0$ band. Under the low temperature conditions in our experiments, the most populated vibronic state, from which the strongest LIF signal originates, must be the ground vibronic state with $v''=0$. Hence the 493.0nm band is a 0-0 band. Likewise the 476.2nm, 461.1nm, and 448.0nm bands, which share a common lower state with the 493.0nm band, were assigned as the related 1-0, 2-0, and 3-0 bands in what we shall refer to as system I. The first lines in their spectra are unambiguously R(3), Q(3), and P(4). It may also be remarked that the Q-branch intensities fall off rapidly with increasing J and there is no noticeable Λ-type doubling in either electronic state. These

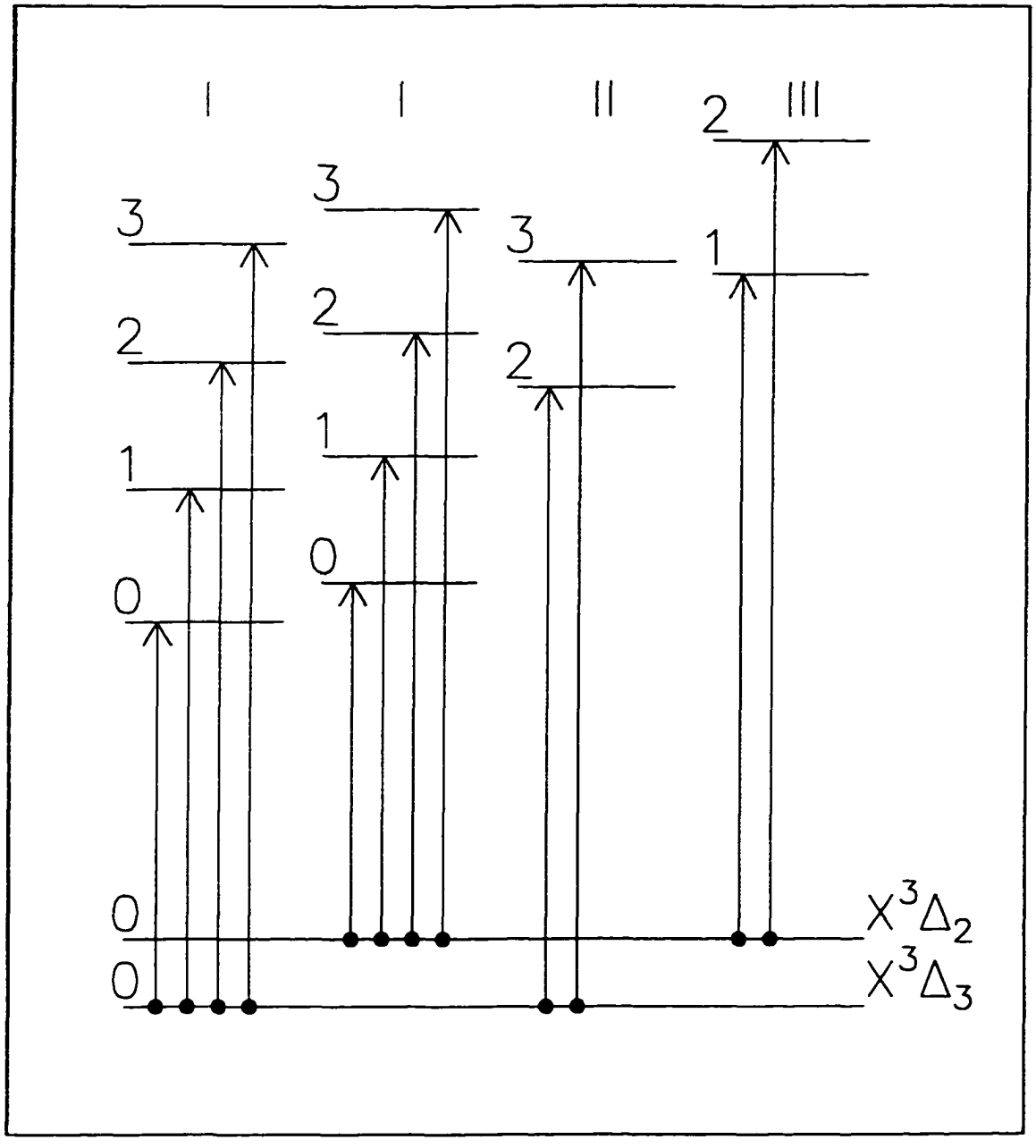

Figure 4.2 A summary of $Fe^{12}C$ bands observed in this study. The vibrational assignments are shown on each vibronic level. System I is referred to as the principal system in the text. It includes both $(I)^3\Delta_3 \leftarrow X^3\Delta_3$ and $(I)^3\Delta_2 \leftarrow X^3\Delta_2$ components. Systems II and III correspond to $(II)^3\Delta_3 \leftarrow X^3\Delta_3$ and $(III)^3\Delta_2 \leftarrow X^3\Delta_2$ transitions, respectively. Two other $\Omega' = 3 \leftarrow X^3\Delta_3$ type bands were identified from the deperturbation procedure (see text). Their vibrational assignments are unknown.

observations imply an $\Omega' = 3 \leftarrow \Omega'' = 3$ transition which we believe to be a $(I)^3\Delta_3 \leftarrow X^3\Delta_3$ transition. Based on the strong intensities associated with the principal system, the lower $^3\Delta$ state was assigned to the ground state of the molecule, and is an inverted state so that the $\Sigma = 1$ spin component, *i.e.*, $^3\Delta_3$, is the lowest. Compelling evidence to support this interpretation comes from the fact that weaker bands are found accompanying each principal band of the system. The weaker bands lie approximately $150cm^{-1}$ to lower energies and, while qualitatively similar in appearance to the $\Omega' = 3 \leftarrow \Omega'' = 3$ bands, have as first lines R(2), Q(2), and P(3), characteristic of a $\Omega' = 2 \leftarrow \Omega'' = 2$ transition. These weaker bands (Figure 4.3), with their R-branch bandheads at 496.7nm, 480.4nm, 465.38nm, and 451.5nm for $Fe^{12}C$, and 496.7nm, 480.8nm, 466.0nm, and 452.8nm for $Fe^{13}C$, are believed to be the corresponding $(I)^3\Delta_2 \leftarrow X^3\Delta_2$ transitions of the principal system. A typical spectrum of the $^3\Delta_2 \leftarrow X^3\Delta_2$ system is shown in Figure 4-3. We searched for, but could not locate with confidence, the third, expected $(I)^3\Delta_1 \leftarrow X^3\Delta_1$ transitions. Evidently, the low temperature molecular beam conditions prevented the $X^3\Delta_1$ substate from being effectively populated. Notably, the $X^3\Delta_1$ substate was also not observed in the two other laboratories that subsequently researched this molecule. Allen *et al.* synthesized FeC in a mixture of iron vapor (produced using a high temperature Broida-type oven near 1400 °C, carried by helium gas) and methane gas [102]. They recorded a pure rotational spectrum of FeC from both $X^3\Delta_3$ and $X^3\Delta_2$ spin-orbit components, but were unable to observe any signal originating from $X^3\Delta_1$, even though they were able to measure, in a different experiment, lines originating in the $X^6\Delta_{-1/2}$ component of FeF,

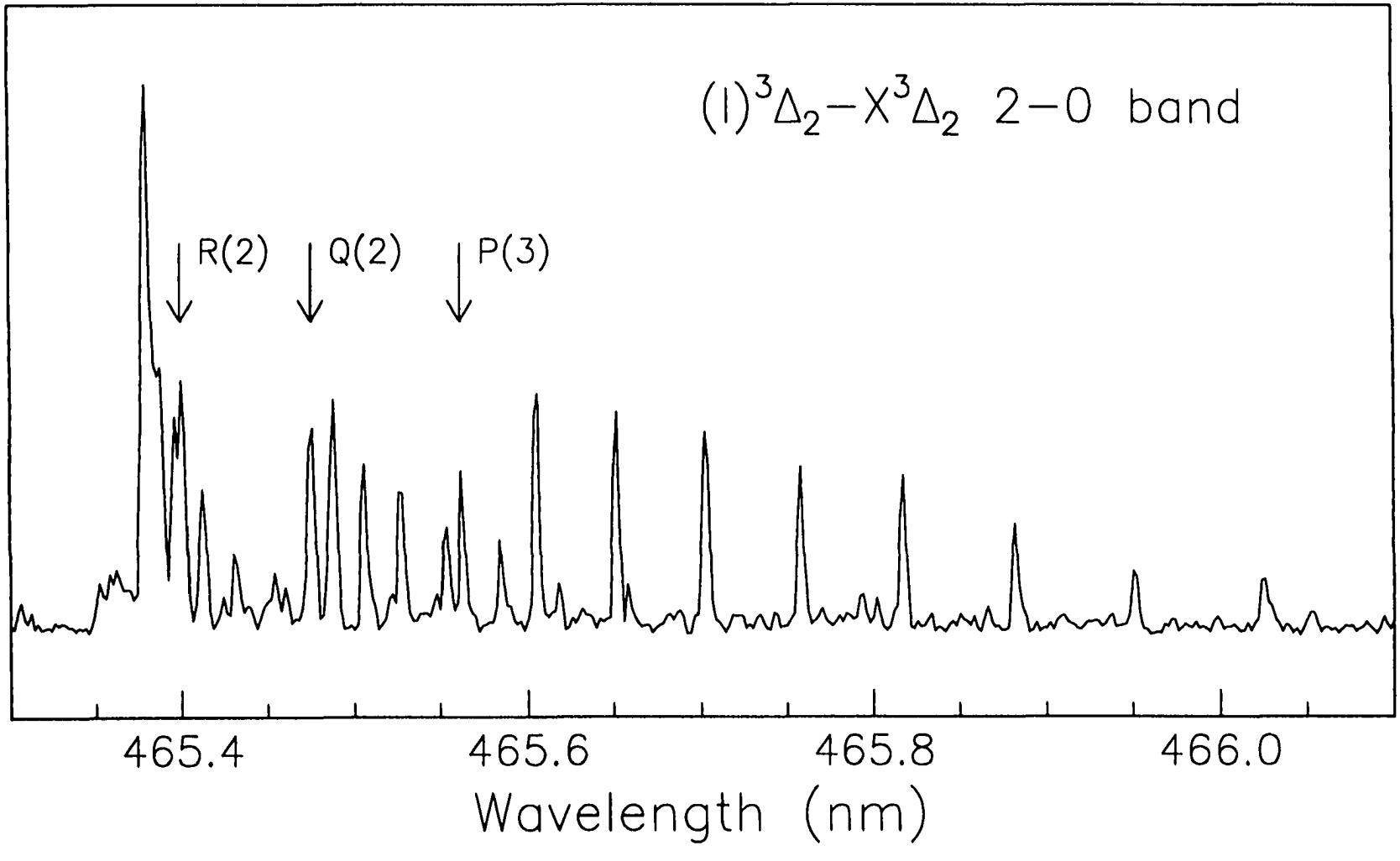

Figure 4.3 The $Fe^{12}C$ LIF spectrum of the $(I)^3\Delta_2 \leftarrow X^3\Delta_2$ 2-0 band at 465.4nm. The first lines in the P, Q, and R branches are marked with arrows.

which lies about 780cm^{-1} above the lowest $X^6\Delta_{7/2}$ state. In a jet-cooled resonance two-photon ionization (R2PI) spectrum of FeC reported by Brugh and Morse [103], all observed bands originate from the lowest $X^3\Delta_3$ spin-orbit state. This is probably due to the extremely low temperature condition associated with their experiment.

Several other bands of FeC do not fit into the scheme described above. First, additional $\Omega' = 3 \leftarrow X^3\Delta_3$ bands of moderate intensity occur to slightly longer wavelengths of the system I 2-0 and 3-0 bands. We attribute these bands, whose R-branch bandheads are at 464.0nm and 464.7nm for $Fe^{12}C$, and 464.7nm and 450.89nm for $Fe^{13}C$, to transitions to a different excited electronic state with $\Omega' = 3$ (system II). The isotope shifts indicate that these two bands are the 2-0 and 3-0 band of the system, respectively. Second, weak bands, which we refer to as system III, having $\Omega' = 2 \leftarrow \Omega'' = 2$ character, are found at 458.7nm and 444.1nm for $Fe^{12}C$. Only one band of the system III, with its bandhead at 459.1nm, was identified for $Fe^{13}C$. A 1-0 assignment for the band is in accordance with its isotopic shift. Our previous analysis [18] concluded that a lower state, different from the $X^3\Delta_2$ state is involved for this system, based on the values of the rotational constants B″. Because of the limited resolution of the experiments, it can not be ruled out that the system originates from the $X^3\Delta_2$ state. In fact, the recently recorded DF spectra of these bands favor an assignment in which the $X^3\Delta_2$ state is their lower state.

4.3 Rotational Analyses

Twenty-two bands, 12 for $Fe^{12}C$ and 10 for $Fe^{13}C$, have been rotationally analyzed. Line measurements and rotational assignments for the strongest $(I)^3\Delta_3 - X^3\Delta_3$ $0-0$ bands at 493nm are listed in Table 4.1. A number of factors have conspired to limit the precision with which we have been able to determine the molecular constants: (i) the line width of our dye laser is of the order of $0.2cm^{-1}$; (ii) the molecules under study are rotationally cold ($T_{rot}\approx 30K$), effectively restricting the range of observable data to $J<20$; (iii) a substantial change in bond length accompanies the electronic excitation. The bandheads form at low J with the result that the R-branch lines suffer from congestion and overlapping; and (iv) several bands are significantly perturbed

Lower state rotational constants B_0'' were obtained, for each individual band, from the second combination differences:

$$\Delta_2 F''(J) = R(J-1) - P(J+1) = B_0''(4J+2) \qquad (4.1)$$

where J is the total rotational quantum number, R(J) and P(J) are the corresponding spectral line positions in wavenumbers, and B_0'' is the rotational constant of the lower state. No account was taken of centrifugal distortion of the lower state because it was assumed to be small for these low J levels. Allen *et al.* measured the centrifugal distortion constants for $\Omega=3$ and $\Omega=2$ components of the ground $X^3\Delta$ state of $Fe^{12}C$ and obtained $D(\Omega=3)=1.6142\times10^{-6}cm^{-1}$ and $D(\Omega=2)=1.6687\times10^{-6}cm^{-1}$ [102]. The influence of centrifugal distortion would not lead to a noticeable effect even at the highest J (<16) observed in our experiment. All the B'' values determined in this way are consistent with each other for bands with the same Ω'' values. The deviations are within the experimental

resolution limit. This indicates that all observed LIF bands originate from either the lowest $\Omega''=3$ vibronic state ($v''=0$ of $X^3\Delta_3$) or the lowest $\Omega''=2$ vibronic state ($v''=0$ of $X^3\Delta_2$), as expected from a jet-cooled molecular beam experiment. The weighted average of B_0'' for $Fe^{12}C$ is 0.6698(10)cm^{-1} (Table 4.2) for the $X^3\Delta_3$ state and 0.6739(10)cm^{-1} for the $X^3\Delta_2$ state, consistent with the more accurate values of 0.66964318(7)cm^{-1} and 0.67286424(7)cm^{-1}, respectively, determined later in the high resolution millimeter wave study [102].

Analysis of the $Fe^{13}C$ bands yield $B_0''=0.6272(10)cm^{-1}$ and $B_0''=0.6302(10)cm^{-1}$, respectively, for the $X^3\Delta_3$ state and the $X^3\Delta_2$ state. The experimentally determined $B_0''(Fe^{12}C)/B_0''(Fe^{13}C)$ ratios of rotational constants have been compared with the mass-spectrometric ρ^2 value of 0.9365. The measured ratios are 0.9364(30) and 0.9352(30), respectively, for the $X^3\Delta_3$ state and the $X^3\Delta_2$ state. The good agreement between the calculated and the experimental ρ^2 values further confirms the carrier to be FeC, effectively eliminating other, improbable, even electron species such as $FeCH^-$ or $FeCH^-$.

Upper state rotational constants, B_v', and band origins, ν_0, were then determined, band by band, by a least squares fitting procedure of all observed lines to the standard formula:

$$\nu = \nu_0 + B_v'J'(J'+1) - B_0''J''(J''+1) \qquad (4.2)$$

with the B_0'' values fixed and ignoring all centrifugal distortion and Λ-type doubling effects. The results are summarized in Table 4.2.

Table 4.2(a) Bandheads, band origins, rotational constants, and vibronic assignments of the observed $^{56}Fe^{12}C$ bands.

Bandhead (nm)	Band Origin (cm^{-1})	B'_v (cm^{-1})	B''_0 (cm^{-1})	Vibrational Assignment	Designation
493.01	20273.6	0.5813	0.6698	0-0	$(I)^3\Delta_3 - X^3\Delta_3$
476.20	20989.7	0.5732	0.6698	1-0	$(I)^3\Delta_3 - X^3\Delta_3$
461.07	21679.3	0.5616	0.6698	2-0	$(I)^3\Delta_3 - X^3\Delta_3$
448.00	22309.9 [i]	0.5512 [i]	0.6698	3-0	$(I)^3\Delta_3 - X^3\Delta_3$
496.66	20124.1	0.5954	0.6739	0-0	$(I)^3\Delta_2 - X^3\Delta_2$
480.38	20806.7	0.5846	0.6739	1-0	$(I)^3\Delta_2 - X^3\Delta_2$
465.38	21478.2	0.5728	0.6739	2-0	$(I)^3\Delta_2 - X^3\Delta_2$
451.51	22138.4	0.5563	0.6739	3-0	$(I)^3\Delta_2 - X^3\Delta_2$
464.01	21542.6	0.5321	0.6698	2-0 [ii]	$(II)^3\Delta_3 - X^3\Delta_3$
449.99	22214.4	0.5106	0.6698	3-0 [ii]	$(II)^3\Delta_3 - X^3\Delta_3$
458.71	21790.4	0.5665	0.6739	1-0 [ii]	$(III)^3\Delta_2 - X^3\Delta_2$
444.08	22508.9	0.5521	0.6739	2-0 [ii]	$(III)^3\Delta_2 - X^3\Delta_2$

Note:

i) This rotational constant was deduced from the deperturbation analysis.

ii) Tentative vibrational assignments based on the isotope shifts between $^{56}Fe^{12}C$ bands and $^{56}Fe^{13}C$ bands.

iii) B''_0 values were obtained by averaging combination differences of all bands sharing the same lower state. Uncertainties for B''_0 are $\pm 0.001 cm^{-1}$. Band origins and B'_v were determined by least square fitting all observed spectral lines to formula (4.2) with B''_0 fixed at the values given in this table. Uncertainties for the band origins and B'_v are $\pm 1 cm^{-1}$ and ± 0.001 cm^{-1}, respectively. The quoted uncertainties should be considered as the upper limits, mainly contributed from our excitation laser wavelength calibrations and linewidth.

Table 4.2(b) Bandheads, band origins, rotational constants, and vibronic assignments of the observed $^{56}Fe^{13}C$ bands.

Bandhead (nm)	Band Origin (cm^{-1})	B'_v (cm^{-1})	B''_0 (cm^{-1})	Vibrational Assignment	Designation
492.98	20275.2	0.5439	0.6272	0-0	$(I)^3\Delta_3 - X^3\Delta_3$
476.55	20974.6	0.5362	0.6272	1-0	$(I)^3\Delta_3 - X^3\Delta_3$
461.77	~21645	P	0.6272	2-0	$(I)^3\Delta_3 - X^3\Delta_3$
449.00	22263.1	0.494 [iii]	0.6272	3-0	$(I)^3\Delta_3 - X^3\Delta_3$
437.66	22839.7	0.5150	0.6272	4-0	$(I)^3\Delta_3 - X^3\Delta_3$
496.74	~20123	P	0.6302	0-0	$(I)^3\Delta_2 - X^3\Delta_2$
480.81	20788.7	0.5397	0.6302	1-0	$(I)^3\Delta_2 - X^3\Delta_2$
466.03	21448.0	0.5398	0.6302	2-0	$(I)^3\Delta_2 - X^3\Delta_2$
452.76	22077.4	0.5260	0.6302	3-0	$(I)^3\Delta_2 - X^3\Delta_2$
464.69	21511.0	0.5077	0.6272	2-0 [ii]	$(II)^3\Delta_3 - X^3\Delta_3$
450.90	22169.3	0.487 [iii]	0.6272	3-0 [ii]	$(II)^3\Delta_3 - X^3\Delta_3$
459.14	21769.8	0.5506	0.6302	1-0 [ii]	$(III)^3\Delta_2 - X^3\Delta_2$

Note:

i) See the notes of Table 4.2(a) for uncertainties.

ii) Tentative vibrational assignments based on the isotope shifts between $^{56}Fe^{12}C$ bands and $^{56}Fe^{13}C$ bands.

iii) The fit for these bands was not good because of the perturbations.

P) Severely perturbed bands.

4.4 The Vibrational Analyses and Isotope Shifts

For system I the vibrational assignment is straightforward due to the fact that the v′=0←v″=0 band at 493.0nm is readily identified from its small negative isotope shift (Figure 4.1). The band origins of the system were then fitted to the formula:

$$\nu_0 = T_e + \omega_e'(v' + \tfrac{1}{2}) - \omega_e'x_e'(v' + \tfrac{1}{2})^2 \qquad (4.3)$$

to extract values for T_e, ω_e', and $\omega_e'x_e'$. The fit of the $(I)^3\Delta_3 \leftarrow X^3\Delta_3$ transition bands to (4-3) with the band origin values and the vibrational numbering given in Table 4.2 yields $T_e = 19896 \pm 11 cm^{-1}$, $\omega_e' = 763 \pm 14 cm^{-1}$, and $\omega_e'x_e' = 21 \pm 4 cm^{-1}$ for $Fe^{12}C$, and $T_e = 19905 \pm 6 cm^{-1}$, $\omega_e' = 748 \pm 6 cm^{-1}$, and $\omega_e'x_e' = 21 \pm 1 cm^{-1}$ for $Fe^{13}C$. The two sets of parameters are consistent with each other within the quoted uncertainties. The fit of the $(I)^3\Delta_2 \leftarrow X^3\Delta_2$ transition bands yields similar results, giving $T_e = 19773 \pm 6 cm^{-1}$, $\omega_e' = 703 \pm 5 cm^{-1}$, and $\omega_e'x_e' = 8 \pm 1 cm^{-1}$ for $Fe^{12}C$, and $T_e = 19780 \pm 6 cm^{-1}$, $\omega_e' = 689 \pm 6 cm^{-1}$, and $\omega_e'x_e' = 9 \pm 1 cm^{-1}$ for $Fe^{13}C$. However, the uncertainties associated with these fitting parameters are much larger than the experimental error and suggest the existence of extensive perturbations.

The shift of a v′-0 band origin upon an isotope substitution can be calculated as:

$$\begin{aligned}
\Delta\nu_0(v'-0) &= \nu_0 - \nu_0' \\
&= (1-\rho)\omega_e'(v'+\tfrac{1}{2}) - (1-\rho^2)\omega_e'x_e'(v'+\tfrac{1}{2})^2 \\
&\quad -(1-\rho)\tfrac{1}{2}\omega_e'' + (1-\rho^2)\tfrac{1}{4}\omega_e''x_e'' \\
&= \tfrac{1}{2}(1-\rho)(\omega_e' - \omega_e'') - \tfrac{1}{4}(1-\rho^2)(\omega_e'x_e' - \omega_e''x_e'') \\
&\quad +(1-\rho)v'[\omega_e' - (1+\rho)\omega_e'x_e'(v'+1)] \\
&= \Delta\nu_0(v'=0) + (1-\rho)v'\Delta G_{v'+\frac{1}{2}}
\end{aligned} \qquad (4.4)$$

where

$$\rho = \sqrt{\frac{\mu}{\mu'}} = \sqrt{\frac{\mu_{^{56}Fe^{12}C}}{\mu_{^{56}Fe^{13}C}}} = 0.9677 \qquad (4.5)$$

is the mass spectrometric parameter and very close to 1.

$$\Delta v_0(v'=0) = \tfrac{1}{2}(1-\rho)(\omega_e' - \omega_e'') - \tfrac{1}{4}(1-\rho^2)(\omega_e' x_e' - \omega_e'' x_e') \qquad (4.6)$$

is the 0-0 band shift, normally negligible compared with other $\Delta v \neq 0$ bands.

$$\Delta G_{v'+\frac{1}{2}} = \omega_e' - 2\omega_e' x_e'(v'+1) \qquad (4.7)$$

is the separation between the successive vibrational levels G(v') and G(v'+1).

In Figure 4.4 the measured isotope shifts and the calculated ones using (4.4) and data from Table 4.2, are compared for all band systems. It is evident that there is a systematic discrepancy between them. The measured isotope shifts are significantly smaller than the calculated ones. This, again, indicates the existence of perturbations among the excited vibronic states.

Similar irregular isotope shifts were also observed in CrN [36]. Some low-lying electronic states of CrN are shown schematically in Figure 4.5 [57]. The $B^4\Sigma^-$ state is known to be strongly perturbed by the nearby $d^2\Pi$ state, while the $A^4\Pi$ is only weakly perturbed. The band origins of A-X and B-X transitions for both isotopic species $Cr^{14}N$ and $Cr^{15}N$ were measured [36]. Isotope shifts were compared with calculated values based on (4.4). While there is a good agreement between the calculated and the observed shifts for the A-X bands, large disagreements, similar to that found in FeC, were identified for the B-X bands in CrN. These disagreements may be attributed to the strong interactions between the B and the d states.

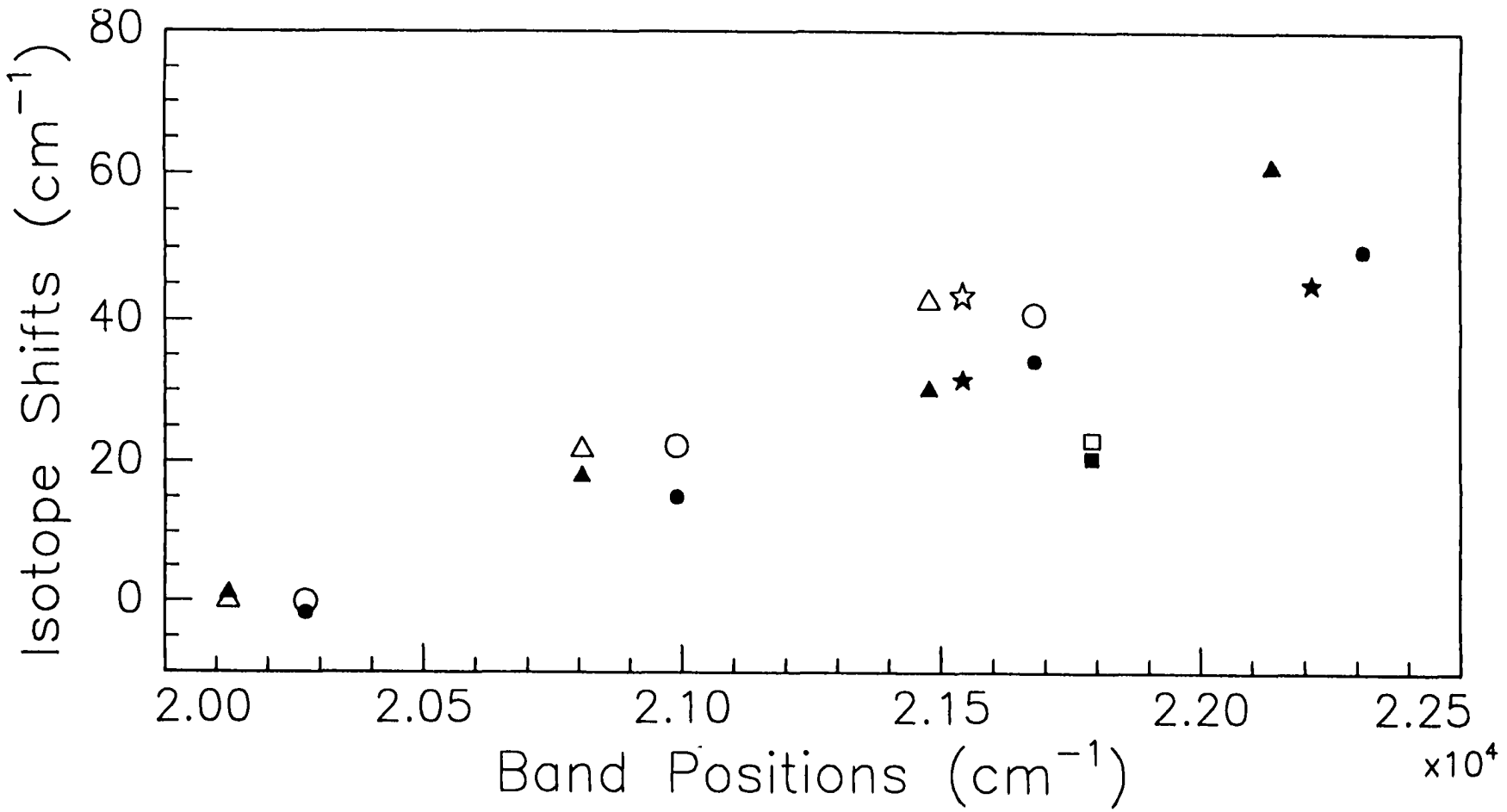

Figure 4.4 Isotope shifts of all observed bands. Filled symbols represent experimentally measured isotope shifts, whereas the open symbols displays calculated isotope shifts. Triangle: the Ω=2 bands of system I; Circle: the Ω=3 bands of system I; Star: system II; Square: system III. Experimental errors are ±2 cm^{-1}.

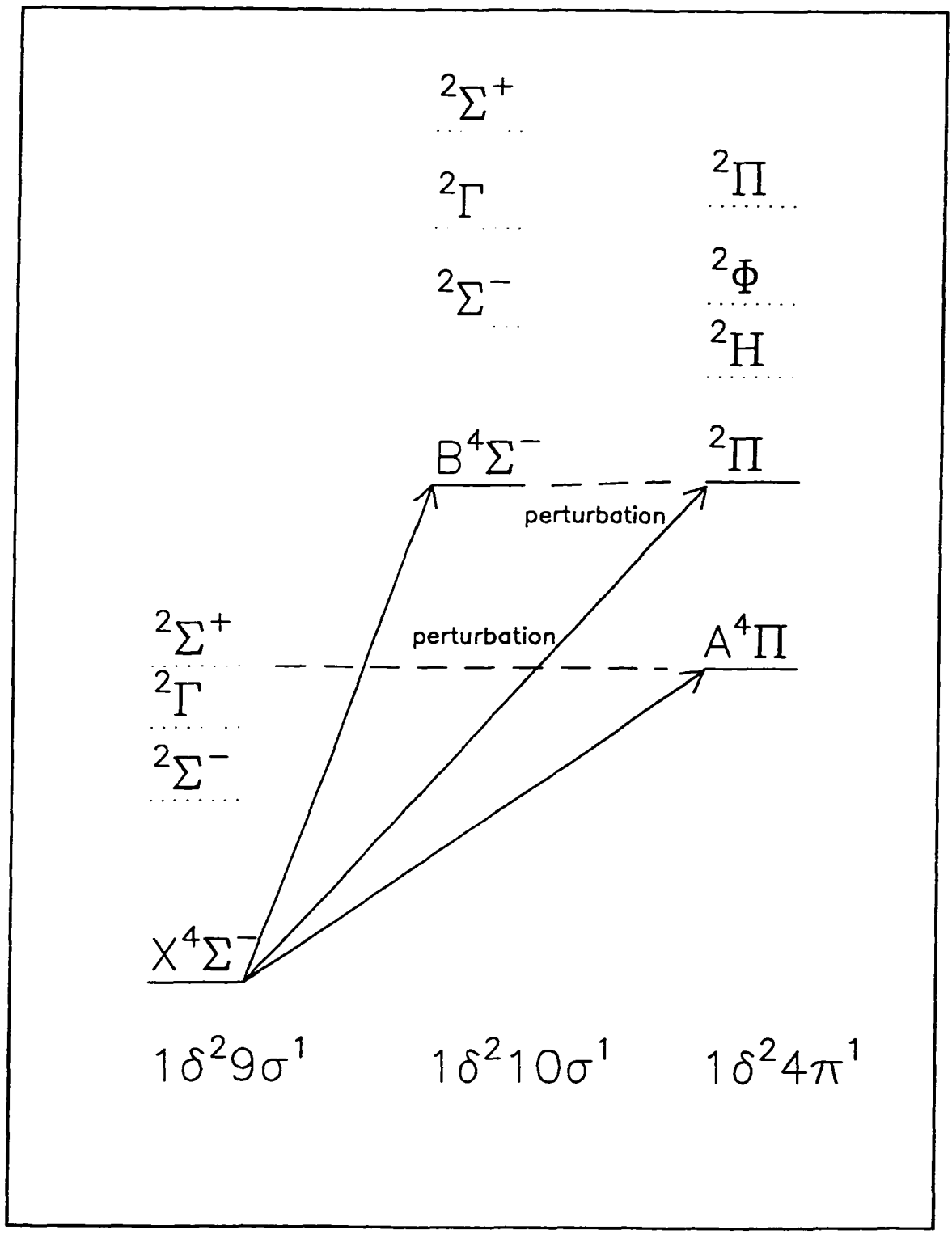

Figure 4.5 Electron configurations and related states of CrN. (adapted from reference [57])

Blue-shifted bandheads due to the naturally occurring minor species $^{54}Fe^{12}C$ and $^{54}Fe^{13}C$ appear in the spectra, but their structure is generally too weak (the natural abundance of ^{54}Fe, ^{56}Fe, ^{57}Fe, and ^{58}Fe are 5.84%, 91.68%, 2.17%, and 0.31% [105], respectively), and overlapped with the strong ^{56}FeC bands to permit detailed rotational analysis. However, the observed band head shifts (Table 4.3) qualitatively confirm the vibrational assignments.

Table 4.3 Observed isotope band head shifts due to the naturally occurring minor species $^{54}Fe^{12}C$ and $^{54}Fe^{13}C$

Bandhead (nm)	$\Delta\nu(^{54}FeC-^{56}FeC)$ ($\pm 0.1 cm^{-1}$)	Vibrational Assignment	Designation
		$Fe^{12}C$	
476.20	0.62	1-0	$(I)^3\Delta_3 \leftarrow X^3\Delta_3$
461.07	3.48	2-0	$(I)^3\Delta_3 \leftarrow X^3\Delta_3$
464.01	3.71	2-0	$(II)^3\Delta_3 \leftarrow X^3\Delta_3$
449.99	4.64	3-0	$(II)^3\Delta_3 \leftarrow X^3\Delta_3$
480.33	1.90	1-0	$(I)^3\Delta_2 \leftarrow X^3\Delta_2$
		$Fe^{13}C$	
476.55	1.67	1-0	$(I)^3\Delta_3 \leftarrow X^3\Delta_3$
461.77	3.37	2-0	$(I)^3\Delta_3 \leftarrow X^3\Delta_3$
449.00	5.75	3-0	$(I)^3\Delta_3 \leftarrow X^3\Delta_3$
437.66	8.25	4-0	$(I)^3\Delta_3 \leftarrow X^3\Delta_3$

4.5 Excited State Lifetimes

The excited state lifetimes were measured at the R-band heads for a majority of the observed vibronic transitions. Such measurements provide complementary information about the excited states and are important for vibronic assignments, especially when the spectrum is strongly perturbed.

Figure 4.6 is the LIF signal intensity curve for the strongest 493nm band. It represents the initial promotion (at time zero) and the decay of the excited state population. Theoretically if the molecules are excited instantaneously at t=0, the signal can be described as an exponential function of time:

$$I(t) = A\exp\left(-\frac{t}{\tau}\right) \qquad t \geq 0 \tag{4.8}$$

where A is a constant scaling factor; τ is the lifetime of the excited state.

In practice (4.8) has to be modified due to the finite pulse width of the excitation laser and the response time of the detecting system. A convolution with a Gaussian function was used:

$$\begin{aligned} I(t) &= A\int_0^{\infty} \exp\left(-\frac{t'}{\tau}\right)\exp\left[-\left(\frac{t-t'}{\tau_g}\right)^2\right]dt' \\ &= A\exp\left(-\frac{t}{\tau}\right)\operatorname{erfc}\left(\frac{\tau_g}{2\tau}-\frac{t}{\tau_g}\right) \end{aligned} \tag{4.9}$$

where τ_g is the "time constant" of the Gaussian function and erfc(x) is the complementary error function defined as:

$$\operatorname{erfc}(x) = \frac{2}{\sqrt{\pi}}\int_x^{\infty} \exp(-x^2)dx \tag{4.10}$$

All decay curves were analyzed with (4.9). The results are listed in Table 4.4. It

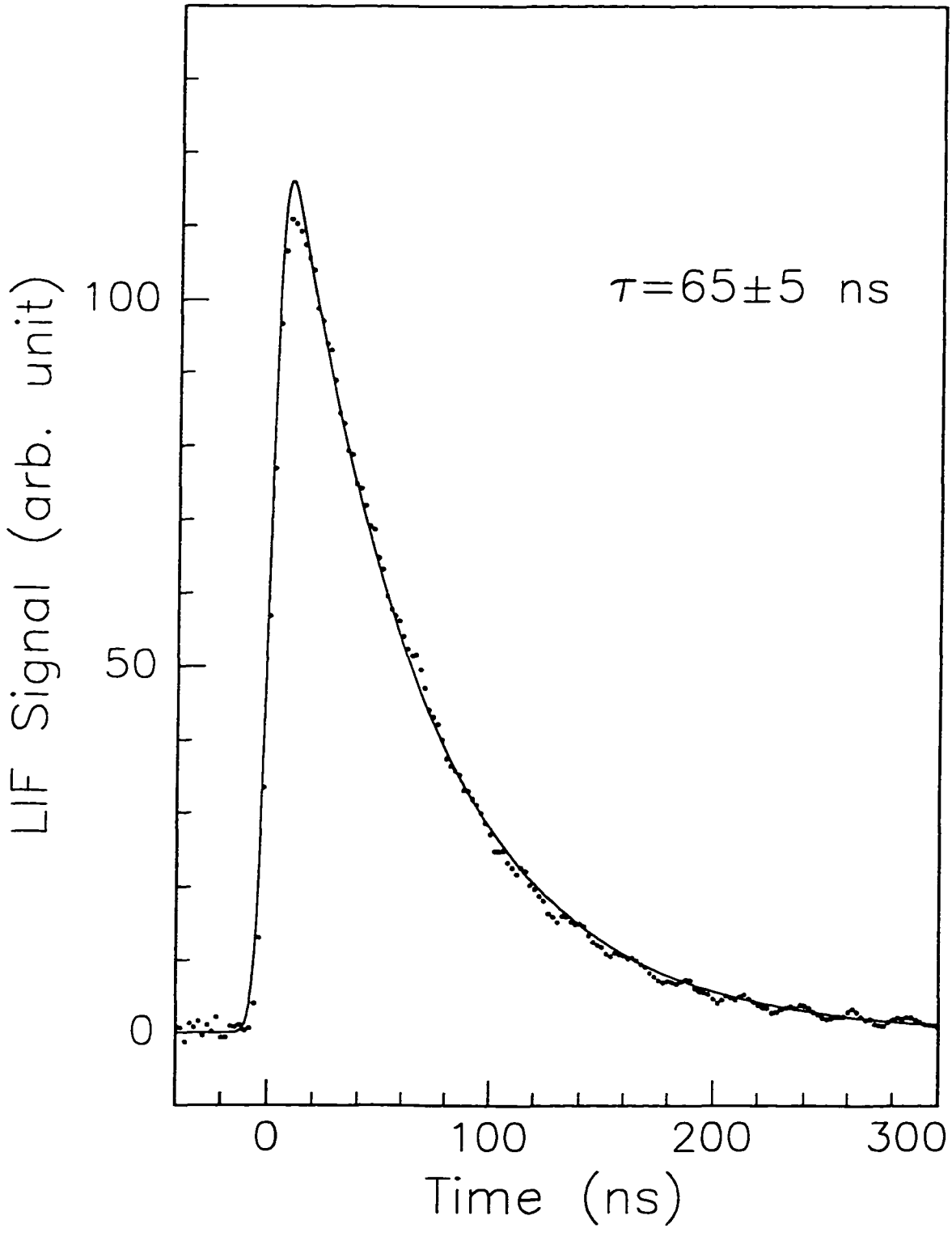

Figure 4.6 The LIF decay curve observed at 493.0nm. The dots are experimental data and the solid line is a simulation curve.

Table 4.4 Excited state lifetimes of FeC.

Excited State	Band	$Fe^{12}C$ (ns)	$Fe^{12}C$ (ns)
$(I)^3\Delta_3$	0-0	65	70
	1-0	75	77
	2-0	95	127
	3-0	~108	108
	4-0	...	84
$(I)^3\Delta_2$	2-0	77	73
	3-0	83	70
$(II)^3\Delta_3$	2-0	~234	196
	3-0	320	236
$(III)^3\Delta_2$	1-0	99	92
	2-0	116	...

Note: The symbol ~ indicates that the observed lifetimes are sensitive to the excitation laser wavelength whereas ... means that there are no experimental data. The experimental uncertainties are ±5 ns.

may be noted that the $(I)^3\Delta_3$ and $(I)^3\Delta_2$ states have lifetimes of 60-90 ns, whereas the $(II)^3\Delta_3$ state has a lifetime of ~250 ns. The $(III)^3\Delta_2$ state, on the other hand, has a lifetime of ~100 ns.

4.6. Dispersed Fluorescence Spectra

The dispersed fluorescence (DF) spectrum for each of the $Fe^{12}C$ bands was recorded. The spectra are shown in Figure 4.7-4.10. All low-lying vibronic states deduced from these DF spectra are listed in Table 4.5. Figure 4.7 displays the dispersed fluorescence spectra following excitations to the v'=0, 1, 2, and 3 vibrational levels of the $(I)^3\Delta_3$ electronic state. Only one vibrational progression, corresponding to transitions back to the ground $X^3\Delta_3$ state, can be identified. Figure 4.8 shows the DF spectra following the excitations to the v'=0, 1, 2, 3 and 4 vibrational levels of the $(I)^3\Delta_2$ electronic state. The similarities between Figure 4.7 and Figure 4.8 support the assignment that they are the $\Omega' = 3 - \Omega'' = 3$ and $\Omega' = 2 - \Omega'' = 2$ components of a $^3\Delta_3 - X^3\Delta_3$ transition.

In Figure 4.8, in addition to the peaks corresponding to transitions back to the ground electronic state, a small peak can be identified at 3427cm^{-1} following excitations to the v=1 and v=2 rotational levels. This peak is believed to correspond to transitions from the excited vibronic states to the $^1\Delta_2$ state which has the same electron configuration as the ground state. It indicates that the $(I)^3\Delta_2$ state is, to a certain extent, mixed with a $^1\Delta_2$ state via spin-orbit interactions. To confirm the $^1\Delta_2$ assignment, the DF spectra excited from the weak system III transitions were also recorded (Figure 4.10). These spectra are compared with two others from the $(I)^3\Delta_2$ state. They are displayed in Figure 4.11. The spectral peaks associated with the $^1\Delta_2$ state can be unambiguously assigned.

This assignment locates the $^1\Delta_2$ state at 3480±50 cm^{-1} above the $X^3\Delta_2$ state. Since no cross transition between $\Omega = 3$ states and $\Omega = 2$ states was observed, the location of

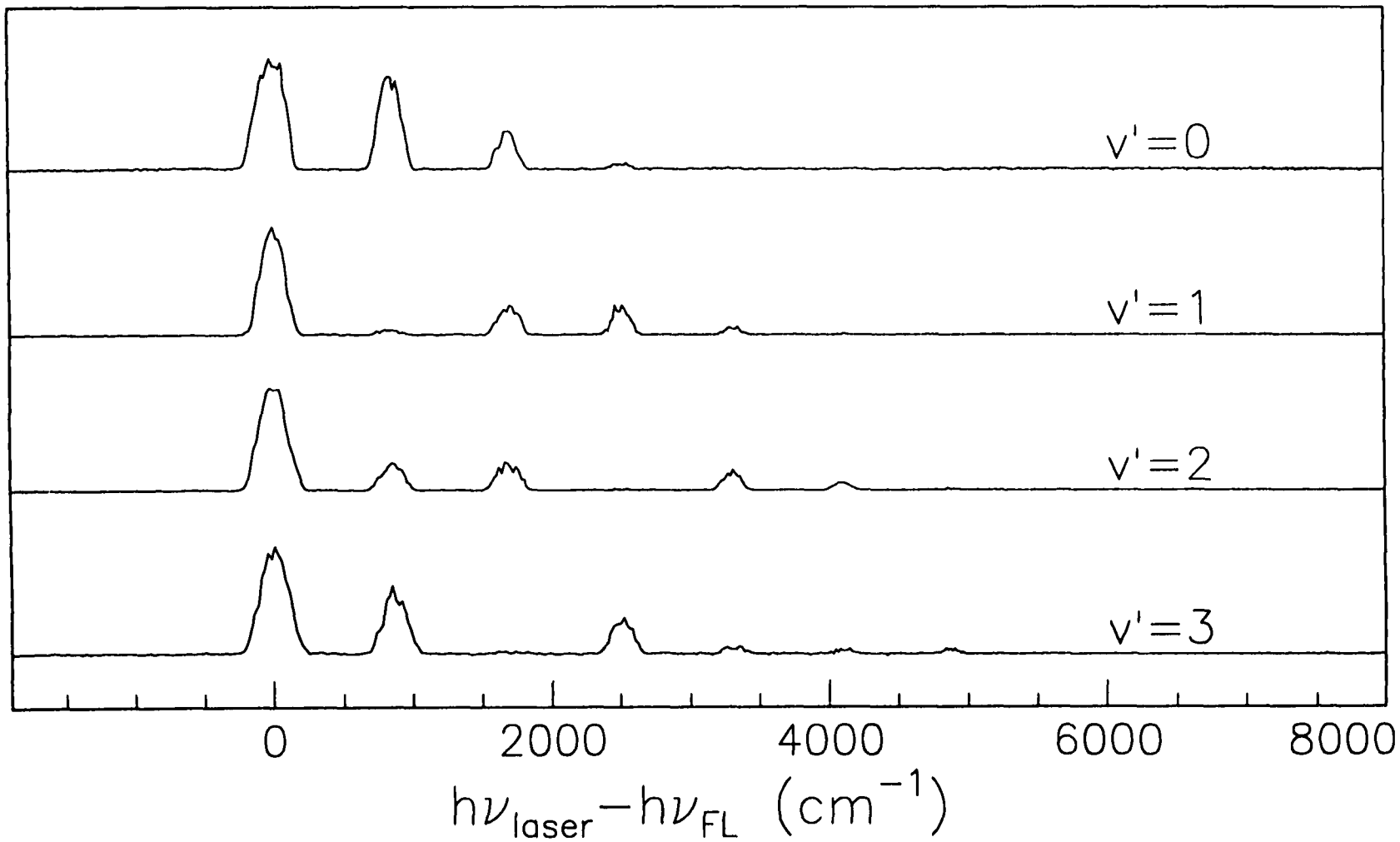

Figure 4.7 Dispersed fluorescence spectra of $Fe^{12}C$ following the excitation to the $(1)^3\Delta_3$ state.

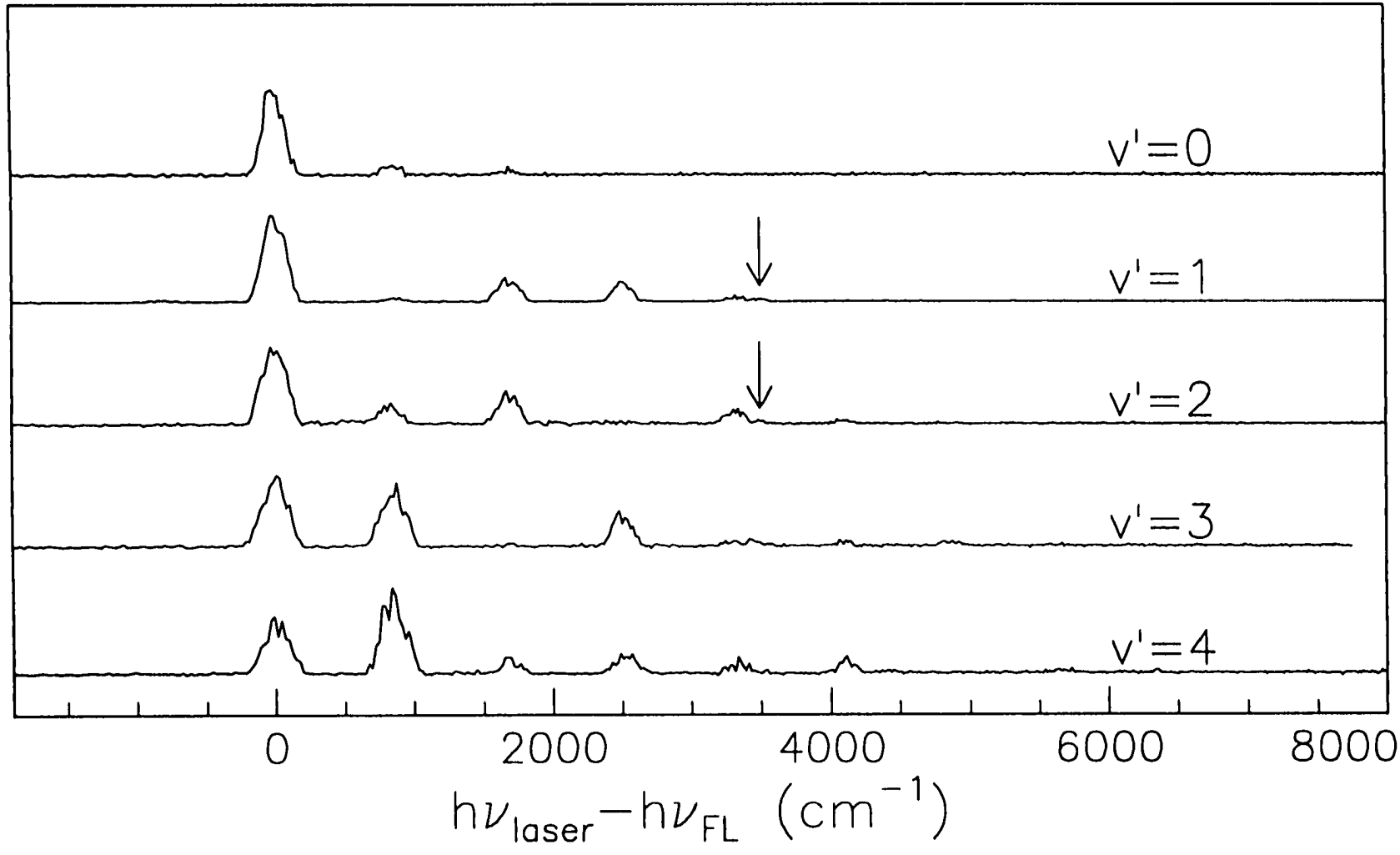

Figure 4.8 Dispersed fluorescence spectra of $Fe^{12}C$ following the excitation to the $(I)^3\Delta_2$ state. The weak peaks marked by arrows correspond to transitions to the $^1\Delta_2$ state.

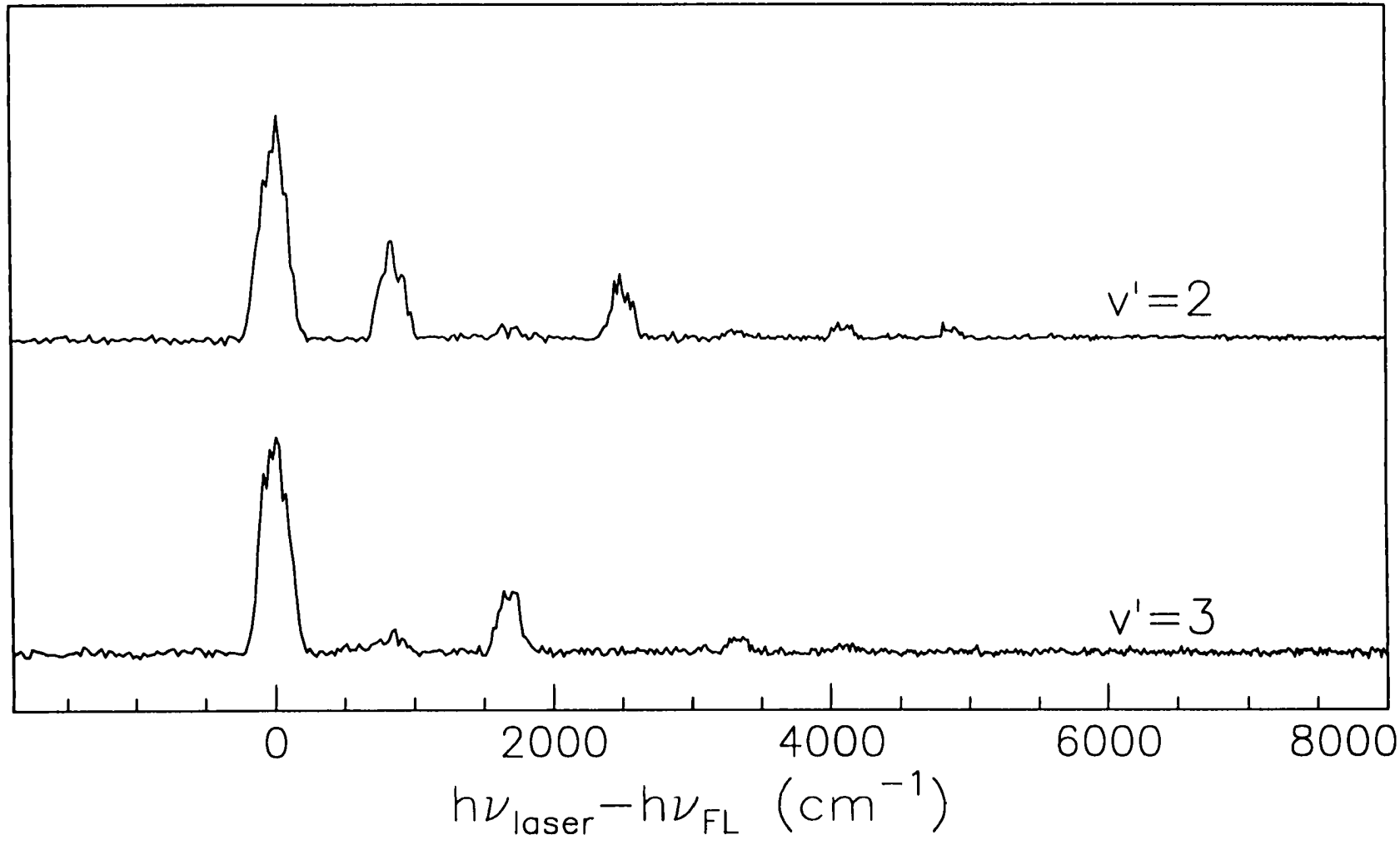

Figure 4.9 Dispersed fluorescence spectra of $Fe^{12}C$ following the excitation to the $(II)^3\Delta_3$ state.

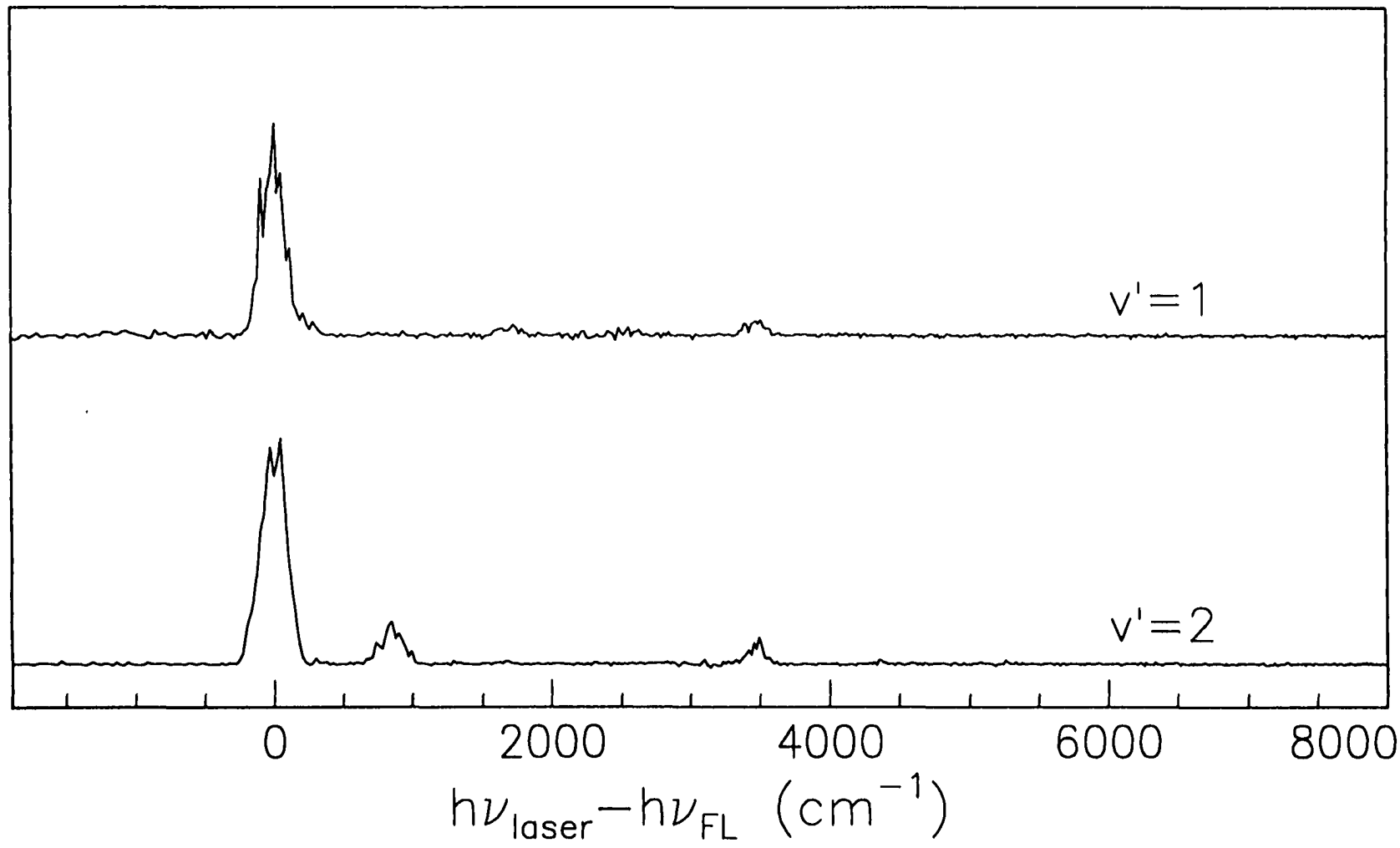

Figure 4.10 Dispersed fluorescence spectra of $Fe^{12}C$ following the excitation to the $(III)^3\Delta_2$ state.

Table 4.5 Observed low lying vibronic state energies of FeC from dispersed fluorescence spectra.

Vibrational Quantum Number v	$X^3\Delta_3$	$X^3\Delta_2$	$^1\Delta_2$
0	0	a [ii]	a+3480
1	856	a+843	
2	1691	a+1684	
3	2511	a+2512	
4	3309	a+3327	
5	4097	a+4105	
6	4872		

Note:

i) Uncertainties are $\pm 50 cm^{-1}$.

ii) a is the energy gap between the $X^3\Delta_3$ and $X^3\Delta_2$ states. As discussed in section 4.8, it was estimated to be $372 \pm 0.5 cm^{-1}$.

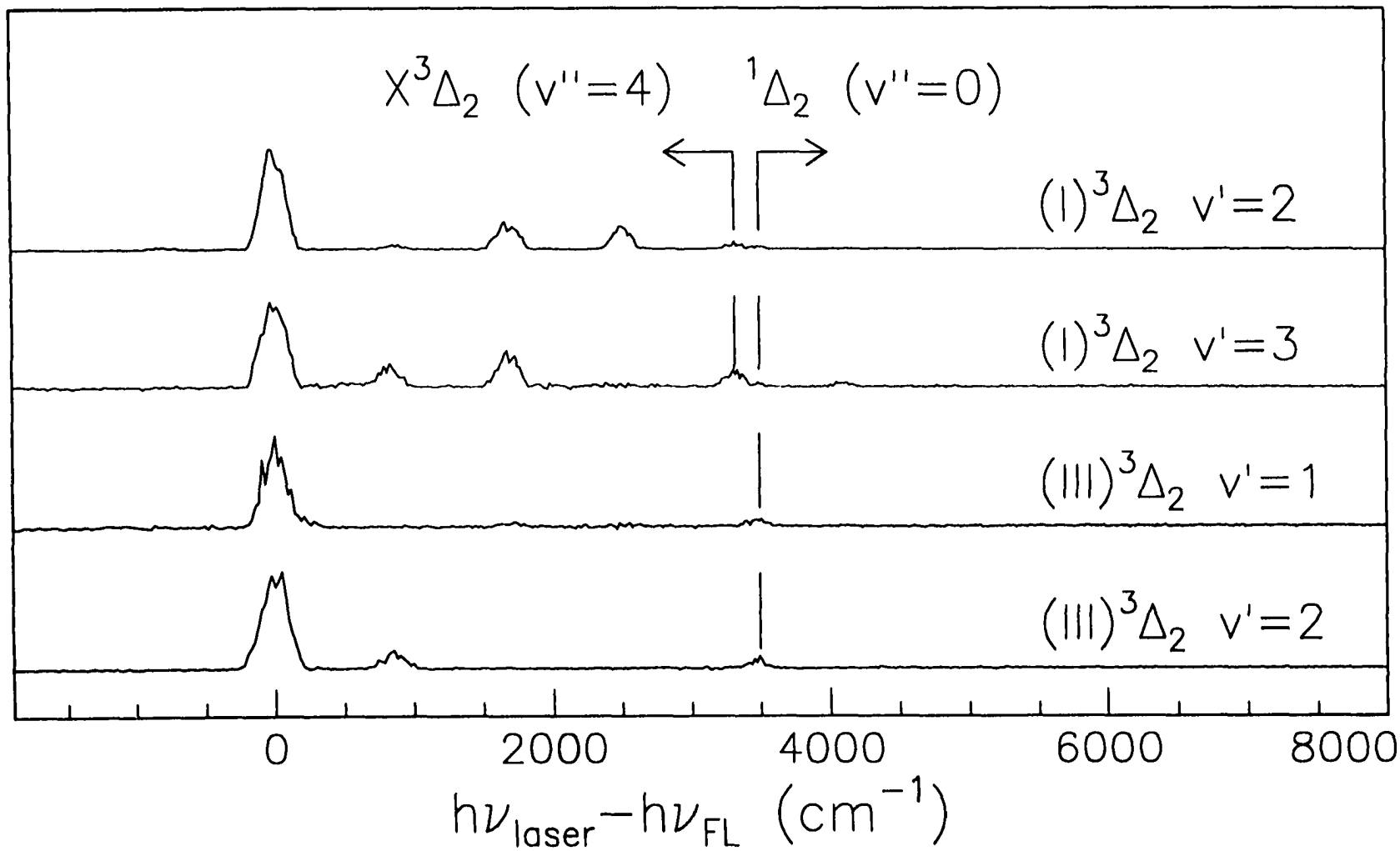

Figure 4.11 Dispersed fluorescence spectra of $Fe^{12}C$ following the excitation to the $(I)^3\Delta_2$ and the $(III)^3\Delta_2$ states. Peaks corresponding to the $X^3\Delta_2$ and the $^1\Delta_2$ states are clearly resolved.

the $X^3\Delta_2$ state relative to the ground $X^3\Delta_3$ state cannot be determined experimentally from the LIF spectrum directly. The location of the $X^3\Delta_2$ state, however, can be inferred from the analysis of the spin-orbit coupling and the experimentally determined rotational constants. A detailed discussion of this point is presented in section 4.8.

4.7 Molecular Orbitals and Electron Configurations

Although there are no previous *ab initio* calculations on FeC, results of *ab initio* calculations on other metal diatomic systems can be used to obtain a qualitative picture of the molecular orbitals (MOs) and the electronic configurations of iron carbide. In Figure 4.12, a schematic MO diagram, constructed based on the diagrams of metal oxides [2], is presented.

Several considerations are important in determining the energetic and bonding characteristics of these orbitals. In general the MOs for carbides are significantly different from those for monoxides [2]. First, the carbon 2s and 2p atomic orbitals (AOs) are much closer in energy than the corresponding AOs in oxygen. Thus the carbon 2s orbital participates more actively in the forming of MOs. As a result the 7σ orbitals (mainly a 2s atomic orbital) becomes slightly bonding, and, more importantly, the 9σ orbital (mainly a 4s atomic orbital) becomes slightly anti-bonding. Secondly, strong $3d\pi$-$2p\pi$ bonding is expected in monocarbides because of the better energy matching. As a consequence the carbide 4π orbital is much higher in energy than the corresponding oxide 4π orbital.

Based on the MO diagram (Figure 4.12), possible ground electronic state symmetries for FeC are $^1\Sigma^+(1\delta^4)$ and $^{1,3}\Delta_i(1\delta^3 9\sigma^1)$. The possibility of $^1\Sigma$ for the ground state can be ruled out, because a $^1\Sigma$ state has Ω=0 whereas from the experiments the ground state has Ω=3. The $^1\Delta$ state should lie higher than the $^3\Delta$ state based on Hund's rule [68]. Hence the electronic ground state symmetry is assigned to be $^3\Delta_i$.

Indeed the experimentally observed principal vibronic band system consist of pairs (with separation of ~150cm^{-1}) of bands with $\Omega'' = 3$ and $\Omega'' = 2$ and similar B values.

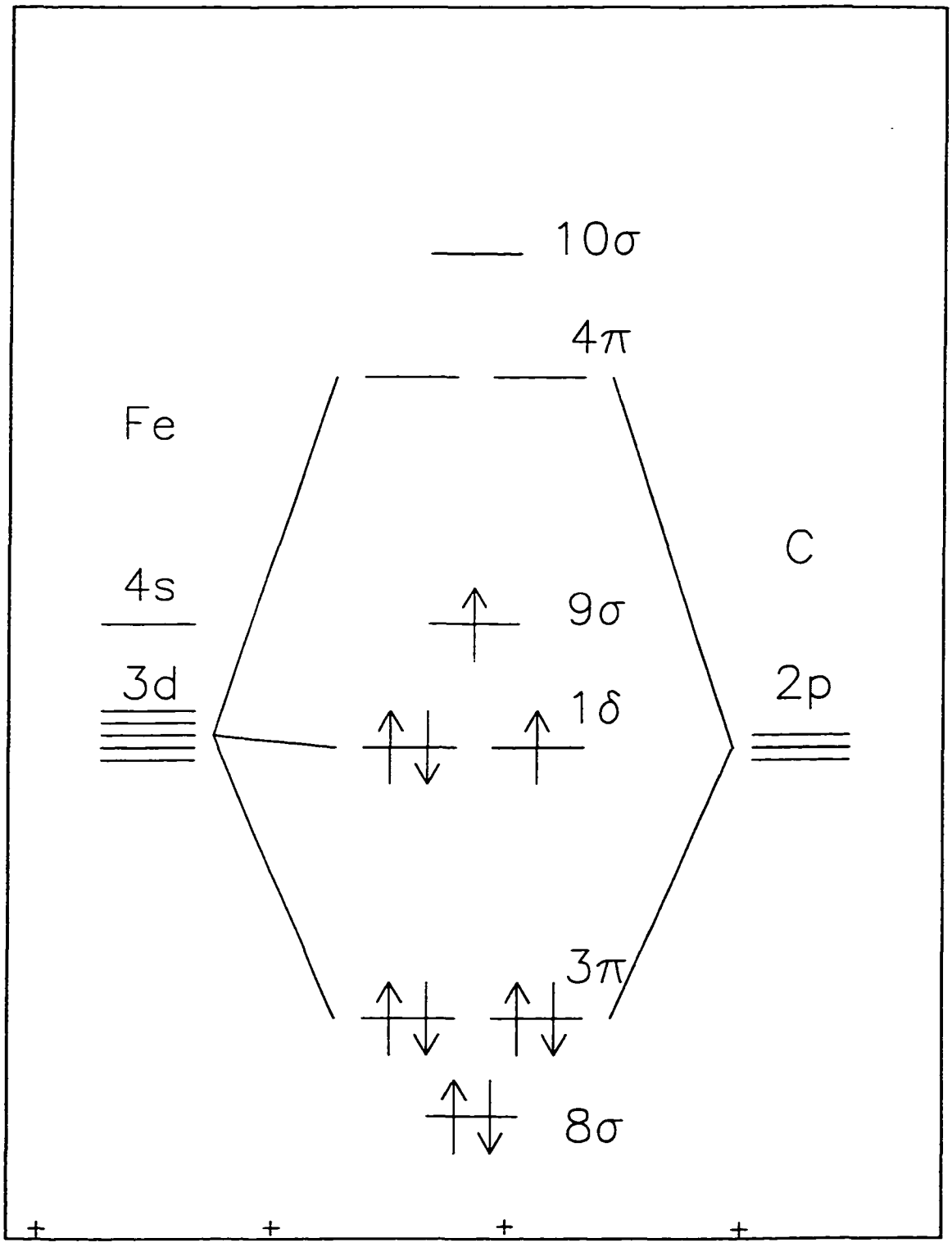

Figure 4.12 The qualitative FeC molecular orbital diagram and the electron configuration of the $^3\Delta_i$ ground state.

The corresponding upper states have identical Ω values to the lower states. With the observation that a weak Q branch is present in each of the vibronic bands, it is most likely that Hund's case (a) to case (a) transitions with selection rules of $\Delta\Lambda=0$ and $\Delta S=0$ are involved. In each pair of bands, the intensity for the $\Omega' = 3 \leftarrow \Omega'' = 3$ band is greater than that for the corresponding $\Omega' = 2 \leftarrow \Omega'' = 2$. All these observations clearly indicate that the ground state is inverted with $\Lambda \neq 0$ and only the two lowest spin components are significantly populated under the jet-cooled condition, which is fully consistent with an $X^3\Delta_i(1\delta^3 9\sigma^1)$ assignment.

Ab initio calculations on isovalent RuC [99-101] revealed that there are three very low lying electronic states, *viz.* $^1\Sigma$, $^1\Delta$ and $^3\Delta$, which is consistent with the MO diagram. The triplet Δ state was predicted to be the ground state. However, the most recent molecular beam experiment [33] has contradicted both the *ab initio* calculations [99-101] and the early high temperature furnace experiments [20-21]. The low temperature molecular beam experiment unambiguously demonstrates that the ground state of RuC is a $^1\Sigma$ state.

The difference in symmetry in the ground states of RuC and FeC can be understood in terms of atomic energy levels. According to the *ab initio* calculations the Δ states can be regarded as being derived from the $3d^74s^1$ metal atomic configuration, while the Σ states originate from the $3d^8$ configuration. These states have different asymptotic limits. Under the influence of the ligand field of carbon the d^8 configuration will be lowered relative to the d^7s^1 configuration because of the instability of the s orbital. Thus the relative molecular electronic state energy depends on the delicate balance of the

bonding between different atomic electronic configurations and the relative energy changes of the relevant atomic electron configurations due to the presence of the ligand. From table I of reference [99] the energy ordering of different configurations for a neutral Ru atom is d^7s^1 (0 au) < d^6s^2 (0.0458 au) < d^8 (0.0831 au). The d^8 configuration is clearly over estimated in the calculation compared with the experimentally determined value of 0.0401 au. This might account for the difference between the results of the calculation and experiment because the $^1\Sigma$ state is mainly from the d^8 configuration. On the other hand, the energy ordering of different configurations for a neutral Fe atom is d^6s^2 < d^7s^1 < d^8. The ligand field of carbon will stabilize the d^7s^1 configuration more than the d^6s^2 one, but not strongly enough to further push the d^8 configuration to the lowest position.

4.8 Spin-Orbit Constants

The spin-orbit coupling constant of the ground state can be estimated from the observed effective rotational constants of the Ω=2 and Ω=3 components of the $^3\Delta_i$ state. As a first approximation, [68]

$$A\Lambda = \frac{2B^2(\Omega=2)}{B(\Omega=3)-B(\Omega=2)} \tag{4.11}$$

was used and yielded AΛ=-220±50 cm^{-1}.

Based on the MO diagram (Figure 4.12) and the spin eigenfunction (Table 2.1), the wavefunctions of the $^3\Delta_i$ state can be expressed, following the procedure outlined in section 2.3, as

$$\Phi(^3\Delta_3) = \left|\delta^+(1)\alpha(1)\ \delta^+(2)\beta(2)\ \delta^-(3)\alpha(3)\ \sigma(4)\alpha(4)\right| \tag{4.12}$$

$$\Phi(^3\Delta_2) = \frac{1}{\sqrt{2}}\left(\left|\delta^+(1)\alpha(1)\ \delta^+(2)\beta(2)\ \delta^-(3)\alpha(3)\ \sigma(4)\beta(4)\right| + \left|\delta^+(1)\alpha(1)\ \delta^+(2)\beta(2)\ \delta^-(3)\beta(3)\ \sigma(4)\alpha(4)\right|\right) \tag{4.13}$$

$$\Phi(^3\Delta_1) = \left|\delta^+(1)\alpha(1)\ \delta^+(2)\beta(2)\ \delta^-(3)\beta(3)\ \sigma(4)\beta(4)\right| \tag{4.14}$$

which gives a spin-orbit constant [18, 60]:

$$A\Lambda = -a_\delta = -\zeta_{3d}(Fe) = -417\,cm^{-1} \tag{4.15}$$

where $\zeta_{3d}(Fe)$ is the atomic spin-orbit constant of Fe [60]. The discrepancy of ~ 200 cm^{-1} between (4.11) and (4.15) suggests that there is a mixing of the $^3\Delta_2$ component with the $^1\Delta_2$ state at higher energy which lowers the observed B values of the Ω=2 component. The wavefunction of the $^1\Delta_2$ state can be written as

$$\Phi(^1\Delta_2) = \frac{1}{\sqrt{2}}\left(\left|\delta^+(1)\alpha(1)\,\delta^+(2)\beta(2)\,\delta^-(3)\alpha(3)\,\sigma(4)\beta(4)\right| - \left|\delta^+(1)\alpha(1)\,\delta^+(2)\beta(2)\,\delta^-(3)\beta(3)\,\sigma(4)\alpha(4)\right|\right) \quad (4.16)$$

If there is no interaction from other electronic states, the zeroth order potential surfaces for the four spin-orbit states can be assumed to be the same in shape but different in energies. Under this assumption they have exactly the same set of vibrational wavefunctions, therefore only vibronic states with same vibrational quantum number can interact with each other. The interactions are independent of vibrational quantum number. Among these four states they can be coupled homogeneously and heterogeneously. The three spin-orbit components of the triplet state interact through the S-uncoupling operator whereas the Ω=2 component interacts with the singlet state by spin-orbit interaction. Nonzero matrix elements connecting these four states are ([60], page 39, table 2.2)

$$<^3\Delta_1|H|^3\Delta_2> = -\sqrt{2}B\sqrt{x-2} \quad (4.17)$$

$$<^3\Delta_2|H|^3\Delta_3> = -\sqrt{2}B\sqrt{x-6} \quad (4.18)$$

and

$$<^1\Delta_2|H|^3\Delta_2> = <^3\Delta_1|H|^3\Delta_1> = -<^3\Delta_3|H|^3\Delta_3> = T \quad (4\text{-}19)$$

where B is the true (unperturbed) rotational constant (supposed to be the same for all of these four states); x=J(J+1); T is a constant which has a value equal to -AΛ.

The secular equation is:

$$\begin{vmatrix} T-E & -\sqrt{2}B\sqrt{x-2} & 0 & 0 \\ -\sqrt{2}B\sqrt{x-2} & -E & -\sqrt{2}B\sqrt{x-6} & T \\ 0 & -\sqrt{2}B\sqrt{x-6} & -T-E & 0 \\ 0 & T & 0 & E_{13}-E \end{vmatrix} = 0 \quad (4.20)$$

or

$$(E - T)(E - E_{13}E - T) = 4B\ (E - E_{13})[(x-4)E + 2T] \qquad (4.21)$$

where E_{13} is defined as the energy spacing between the $^1\Delta_2$ state and the $^3\Delta_2$ state if $A\Lambda=0$; T is a positive number in accord with the fact that the $^3\Delta_i$ state is inverted; E is the eigenenergy not including the rotational and rotational energy terms.

If we treat the B^2 term in (4.21) as a small perturbation, then the zeroth solutions of (4.21) are, by setting $B^2=0$

$$E_0(^1\Delta_2) = \frac{1}{2}\left(E_{13} + \sqrt{E_{13}^2 + 4T^2}\right) \qquad (4.22)$$

$$E_0(^3\Delta_1) = T \qquad (4.23)$$

$$E_0(^3\Delta_2) = \frac{1}{2}\left(E_{13} - \sqrt{E_{13}^2 + 4T^2}\right) \qquad (4.24)$$

$$E_0(^3\Delta_3) = -T \qquad (4.25)$$

Now letting $E=E_0 + yB^2$ in (4.21), and keeping only the B^2 terms

$$y = \frac{4(E_0 - E_{13})[(x-4)E_0 + 2T]}{(E_0^2 - T^2)(2E_0 - E_{13}) + 2E_0(E_0^2 - E_{13}E_0 - T^2)} \qquad (4.26)$$

which yields the first order solution of (4.21):

$$\begin{aligned} E_1(^1\Delta_2) &= \frac{2B^2}{E_{13}} \frac{1}{1 + \frac{E_{13}E_0}{2T^2}} \left(x - 4 + \frac{2T}{E_0}\right) \\ &= \frac{2B^2}{E_{13}} \frac{1}{1 + \frac{E_{13}}{4T}\left[\frac{E_{13}}{T} + \sqrt{\left(\frac{E_{13}}{T}\right)^2 + 4}\right]} \left(x - 4 + \frac{4}{\frac{E_{13}}{T} + \sqrt{\left(\frac{E_{13}}{T}\right)^2 + 4}}\right) \end{aligned} \qquad (4.27)$$

$$E_1(^3\Delta_1) = \frac{2B^2(E_{13}-E_0)}{E_{13}E_0}(x-4+\frac{2T}{E_0}) = \frac{2B^2}{E_{13}}(\frac{E_{13}}{T}-1)(x-2) \tag{4.28}$$

$$E_1(^3\Delta_2) = \frac{2B^2}{E_{13}}\frac{1}{1+\frac{E_{13}E_0}{2T^2}}(x-4+\frac{2T}{E_0}) = \frac{2B^2}{E_{13}}\frac{1}{1+\frac{E_{13}}{4T}\left[\frac{E_{13}}{T}-\sqrt{(\frac{E_{13}}{T})^2+4}\right]}\left(x-4+\frac{4}{\frac{E_{13}}{T}-\sqrt{(\frac{E_{13}}{T})^2+4}}\right) \tag{4.29}$$

$$E_1(^3\Delta_3) = \frac{2B^2(E_{13}-E_0)}{E_{13}E_0}(x-4+\frac{2T}{E_0}) = -\frac{2B^2}{E_{13}}(\frac{E_{13}}{T}+1)(x-6) \tag{4.30}$$

Because of the J dependence of the first order solutions, effective rotational constants for these four electronic states have to be modified to:

$$B_{eff}(^1\Delta_2) = B+\frac{2B^2}{E_{13}}\frac{1}{1+\frac{E_{13}}{2T}\left[\frac{E_{13}}{2T}+\sqrt{(\frac{E_{13}}{2T})^2+4}\right]} \tag{4.31}$$

$$B_{eff}(^3\Delta_1) = B+\frac{2B^2}{E_{13}}(\frac{E_{13}}{T}-1) \tag{4.32}$$

$$B_{eff}(^3\Delta_2) = B+\frac{2B^2}{E_{13}}\frac{1}{1+\frac{E_{13}}{2T}\left[\frac{E_{13}}{2T}-\sqrt{(\frac{E_{13}}{2T})^2+4}\right]} \tag{4.33}$$

$$B_{eff}(^3\Delta_3) = B-\frac{2B^2}{E_{13}}(\frac{E_{13}}{T}+1) \tag{4.34}$$

When the energy separation between the singlet and the triplet states is very large compared with the spin-orbit interaction spacing among the spin components of the triplet state, *i.e.*, if $E_{13} >> T$, the effective rotational constants given by (4.31)-(4.34) are

simplified to

$$B_{eff}(^1\Delta_2) = B \tag{4.35}$$

$$B_{eff}(^3\Delta_1) = B + \frac{2B^2}{T} \tag{4.36}$$

$$B_{eff}(^3\Delta_2) = B \tag{4.37}$$

$$B_{eff}(^3\Delta_3) = B - \frac{2B^2}{T} \tag{4.38}$$

which are consistent with the formulas given in reference [68], and validate the formula (4.11). When E_{13} is comparable with T the more accurate expressions (4.31)-(4.34) must be used.

Since

$$1 + \frac{E_{13}}{2T}\left[\frac{E_{13}}{2T} - \sqrt{\left(\frac{E_{13}}{2T}\right)^2 + 4}\right] \tag{4.39}$$

is a very flat function of $\frac{E_{13}}{2T}$ (Figure 4.13), it can be approximated almost as a constant of $\frac{1}{2}$ when $\frac{E_{13}}{2T} > 2$. Therefore the following approximation is valid for $B_{eff}(^3\Delta_2)$.

$$B_{eff}(^3\Delta_2) = B + \frac{4B^2}{E_{13}} \tag{4.40}$$

Now we have

$$B_{eff}(^3\Delta_2) - B_{eff}(^3\Delta_3) = \frac{2B^2}{T}\left(1 + 3\frac{T}{E_{13}}\right) \tag{4.41}$$

Substituting $T = 417\text{cm}^{-1}$ into (4.41), and using more accurate parameters from [102]: $B_{eff}(^3\Delta_2) = 0.67286424\text{cm}^{-1}$ and $B_{eff}(^3\Delta_3) = 0.66964318\text{cm}^{-1}$, (4.41) yields

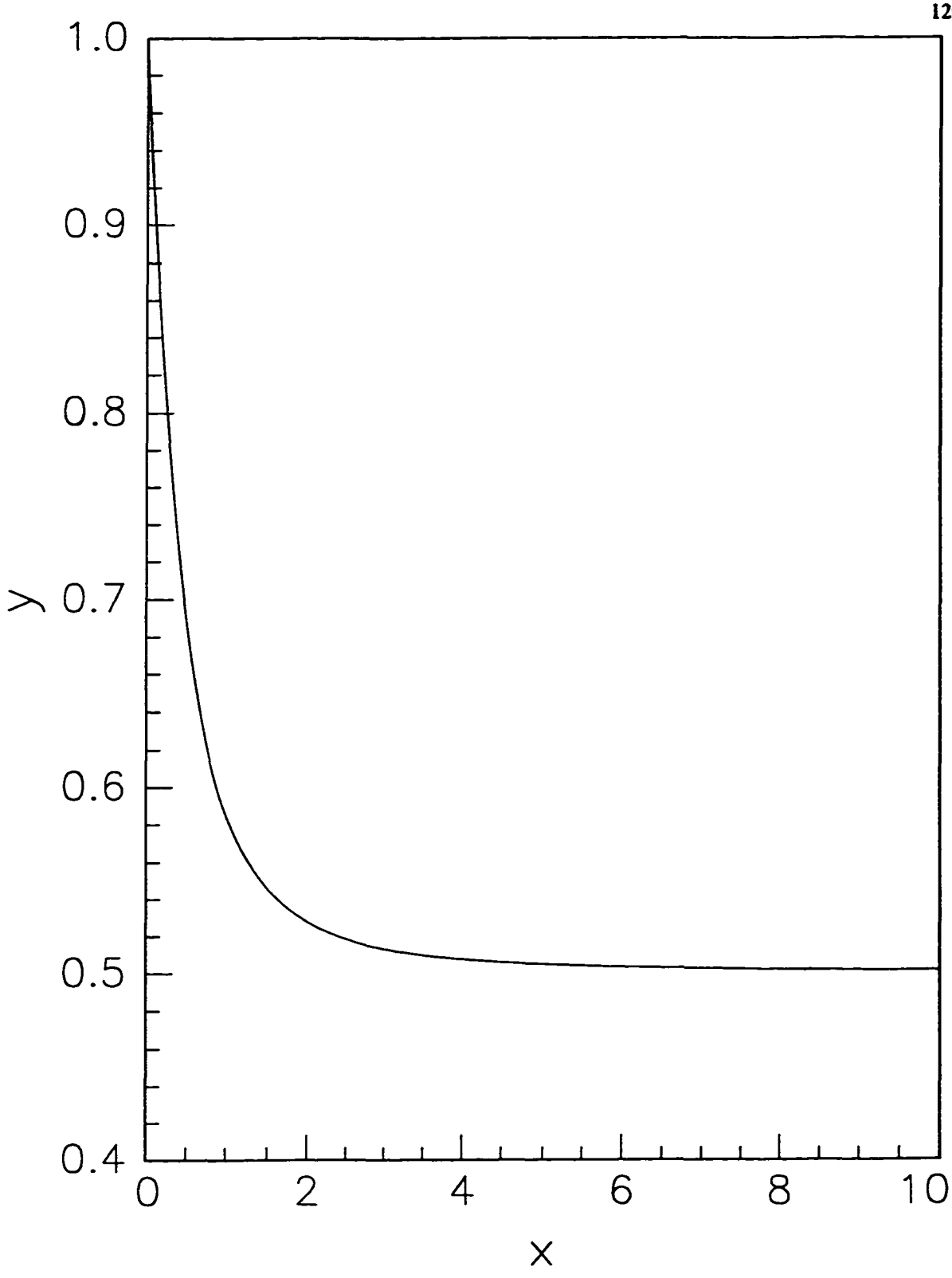

Figure 4.13 Function $y = 1 + x(x - \sqrt{x^2 + 1})$. It is almost constant at 0.5 when x>2.

$E_{13} = 6.2T = 2585cm^{-1}$.

The locations of the $^3\Delta_2$ and $^1\Delta_2$ states relative to $X^3\Delta_3$ state can also be estimated from formulas (4.22)-(4.25) as:

$$E(^3\Delta_2) = T + \frac{1}{2}\left(E_{13} - \sqrt{E_{13}^2 + 4T^2}\right) = 351\,cm^{-1} \qquad (4.42)$$

$$E(^1\Delta_2) = T + \frac{1}{2}\left(E_{13} + \sqrt{E_{13}^2 + 4T^2}\right) = 3068\,cm^{-1} \qquad (4.43)$$

It is noted that the energy gap between $^3\Delta_2$ and $^1\Delta_2$ states was measured to be $3480\pm50cm^{-1}$(Table 4.5), which is much larger than the value we obtain from (4.42) and (4.43). This might be caused by overestimating the constant T which is equal to the molecular spin-orbit constant a_δ. Figure 4.14 shows a relationship between the spin-orbit constant T and the energy spacing between $^3\Delta_2$ and $^1\Delta_2$ states obtained by solving B and T from (4.32) and (4.33) while keep the spacing E_{13} as a constant. One of the points marked in the figure gives $E_{13}=2659cm^{-1}$, $T=417cm^{-1}$, which corresponds to $T=\zeta_{3d}(Fe)$. Another point in the figure gives $E_{13}=3480cm^{-1}$, $T=372cm^{-1}$, which yields the correct energy spacing between the triplet and the singlet states but requires a smaller molecular spin-orbit constant. The reduced molecular spin-orbit constant $a_\delta=372\pm0.5cm^{-1}$ for the ground $X^3\Delta_1$ state of FeC is similar to that of the observed molecular spin-orbit constant ($a_\delta=379.78cm^{-1}$) of the ground $X^5\Delta_1$ state of FeO [2].

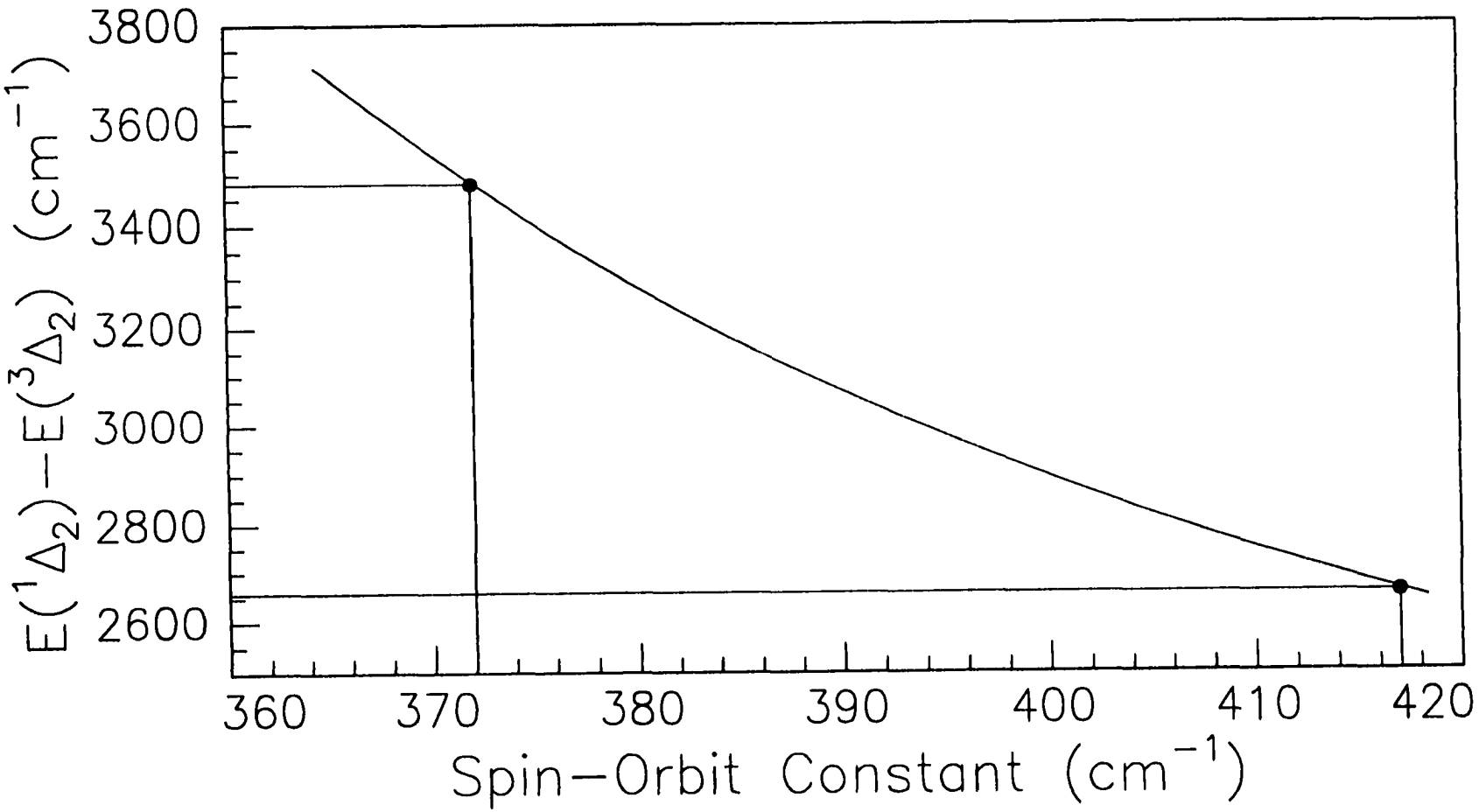

Figure 4.14 Determination of the molecular spin-orbit constant from the energy spacing between the triplet and the singlet states. The point at the left upper corner has an energy spacing of $3480cm^{-1}$, which yields a spin-orbit constant $372cm^{-1}$. The point at right lower corner corresponds to a spin-orbit constant $417cm^{-1}$, the value taken from atomic Fe, which predicts the spacing to be $2659cm^{-1}$.

4.9 The Electron Configurations of the Excited States

In our LIF studies of $Fe^{12}C$, 12 bands in the region 20,000cm^{-1} to 23,300cm^{-1} were identified, and grouped into four electronic transitions. Two transitions have $\Omega' = 3 \leftarrow \Omega'' = 3$ character whereas the other two have $\Omega' = 2 \leftarrow \Omega'' = 2$ character. The ground state was assigned to have $^3\Delta_i$ symmetry, an assignment confirmed by Allen *et al.* in their millimeter-wave studies [102]. Brugh and Morse discovered six additional electronic states in their resonance two-photon ionization (R2PI) spectroscopic studies [103]: three of them possess $\Omega' = 3$, one has $\Omega' = 4$, and two other states have $\Omega' = 2$. A summary of the currently known information about the electronic states of FeC is listed in Table 4.6.

It is noted that the excited electronic states can be grouped according to their bond lengths into two categories. States in one category have B values very similar to that of the ground electronic state, others have B values significantly smaller than that of the ground electronic state. Given the fact that the bonding orbitals in FeC (Figure 4-12) are mainly carbon-centered orbitals while those non-bonding and anti-bonding orbitals are mainly metal-centered orbitals, the two categories can be associated with two different promotions of electrons from the ground electronic state configuration, as in the case of metal oxides [2]. The ground states of FeC have some ionic bonding character because all carbon-centered bonding orbitals in Figure 4-12 are fully occupied. The situation can be thought of as the metal atom possessing a formal positive charge while the carbon atom possesses the same amount of negative charge. The electrostatic attraction between two partially charged atoms helps, to a certain extent, to hold the atoms together. Upon an electronic transition, if an electron is moved from a metal-centered non-bonding orbital to

Table 4.6 Summary of all currently known electronic states of FeC.

T_0 (cm^{-1})	Ω	B (cm^{-1})	Designation
~21072 [i] +a [ii]	2	B_1=0.5635(10)	$^3\Delta_2$ ($7\sigma^2 8\sigma^2 3\pi^3 1\delta^3 9\sigma^1 4\pi^1$) [iii]
20124.1(1) +a [ii]	2	B_0=0.5954(10)	$^3\Delta_2$ ($7\sigma^2 8\sigma^2 3\pi^3 1\delta^3 9\sigma^1 4\pi^1$) [iii]
20273.6(1)	3	B_0=0.5813(10)	$^3\Delta_3$ ($7\sigma^2 8\sigma^2 3\pi^3 1\delta^3 9\sigma^1 4\pi^1$) [iii]
~20199 [iv]	3	B_2=0.5321(10)	$^3\Delta_3$ ($7\sigma^2 8\sigma^2 3\pi^3 1\delta^3 9\sigma^1 4\pi^1$) [iii]
15890.9893(38) [v]	2	B_0=0.654156(37) [v]	$^3\Pi_2$ [vii]
15454.2026(22) [v]	3	B_0=0.654156(37) [v]	$^3\Delta_3$ ($7\sigma^2 8\sigma^2 3\pi^4 1\delta^3 9\sigma^0 11\sigma^1$) [iii]
13175.1019(31) [v]	3	B_0=0.675270(70) [v]	$^3\Delta_3$ ($7\sigma^2 8\sigma^2 3\pi^4 1\delta^3 9\sigma^0 10\sigma^1$) [iii]
13168(4) [v]	3	B_e=0.55545(16) [v]	$^3\Delta_3$ ($7\sigma^2 8\sigma^1 3\pi^4 1\delta^3 9\sigma^2$) [vii]
13063.5551(45) [v]	4	B_0=0.648961(94) [v]	$^3\Phi_4$ [vii]
12045.8686(57) [v]	2	B_0=0.651788(62) [v]	$^3\Pi_2$ [vii]
a [ii]	2	B_0=0.67286424(7)[vi]	$X^3\Delta_2$ ($7\sigma^2 8\sigma^2 3\pi^4 1\delta^3 9\sigma^1$) [iii]
0	3	B_0=0.66964318(7)[vi]	$X^3\Delta_3$ ($7\sigma^2 8\sigma^2 3\pi^4 1\delta^3 9\sigma^1$) [iii]

i) term value deduced from v=1 and v=2 vibrational states.

ii) a was estimated to be 372±0.5cm^{-1} in section 4.8

iii) details of the assignments are given in section 4.9

iv) term value deduced from v=2 and v=3 vibrational states

v) data from [103]

vi) data from [102]

vii) assignments from [103]

a metal-centered anti-bonding or non-bonding orbital, this will not change the charge distribution between the two atoms significantly and will therefore not change the bond length significantly. On the other hand, if an electron in a carbon-centered bonding orbital is promoted to a metal-centered non-bonding orbital or an anti-bonding orbital, it effectively transfers back some negative charge from the carbon atom to the metal atom. In this case, the effective negative charge on the carbon atom is reduced. The electrostatic attraction in the molecule will decrease, thereby increasing the bond length in the excited state.

In light of the relationship between charge transfer and bond length, if electrostatic attraction is a dominant factor in determining bond length, all observed electronic states can be assigned according to their B values, Ω values, and their energies. In this assignment, it is also assumed that the selection rules of $\Delta\Lambda = 0,\pm 1$ and $\Delta\Sigma = 0$ are enforced in this molecule. Brugh and Morse [103] assigned the first excited Ω=3 state, *i.e.*, the [13.17]Ω=3[1] state, of FeC as a $^3\Delta_3$ state deriving from the $8\sigma^1 3\pi^4 9\sigma^2 1\delta^3$ molecular electron configuration. This corresponds to a $9\sigma \leftarrow 8\sigma$ electronic excitation from the ground state. The assignment was made based on the similarities of bond length changes and vertical energies between the [13.17]Ω=3 state of FeC and the $[14.0]^2\Sigma^+$ state of CoC which has been well characterized as having a molecular configuration $8\sigma^1 3\pi^4 9\sigma^2 1\delta^2$ [34-35]. The next higher Ω=3 state is the [13.17]Ω=3 state which is very close to the first excited Ω=3 state but has a significantly different bond length to the first

[1] Hund's case (c) notation [135], the number in the square bracket is the v=0 vibrational energy of the electronic state, in units of 10^3 cm^{-1}, relative to the ground vibronic state.

one. This state can only rise from exciting an electron from a metal centered orbital to another metal-centered orbital. The lowest such state is a $^3\Delta_3$ state with electronic configuration $8\sigma^2 3\pi^4 1\delta^3 10\sigma^1$, corresponding to a $10\sigma \leftarrow 9\sigma$ excitation from the ground state. It was noticed that the bond length of this state is even shorter than that of the ground state. This can be explained by the increased charge transfer when the electron in the 4s-dominated 9σ orbital is moved to the 10σ orbital which is a metal centered 3d-2p anti-bonding orbital. The third excited Ω=3 state has a similar, but slightly longer, bond length than the ground state, and is about 2000cm^{-1} higher than the second excited $^3\Delta_3$ state. This state may be assigned to the $^3\Delta_3$ state with configuration $8\sigma^2 3\pi^4 1\delta^3 11\sigma^1$, from the $11\sigma \leftarrow 9\sigma$ excitation. The 11σ orbital is dominated by the metal 4p atomic orbital and is mainly nonbonding because of the large energy difference between the metal 4p orbitals and the carbon 2p orbitals. The remaining, much higher in energy, two Ω=3 states are common in their significantly longer bond length compared with the ground state. They may be assigned to the $^3\Delta_3(8\sigma^2 3\pi^3 1\delta^3 9\sigma^1 4\pi^1)$ state from a $4\pi \leftarrow 3\pi$ excitation. Regarding this assignment, it is noted that there are two excited $^3\Delta$ states (with T_e of 2.19 and 2.94eV, respectively) in the *ab initio* calculations for RuC [99] with very large bond length changes (~24%) upon excitation from the ground state. They are derived from a mixture of two dominant configurations, *i.e.*, $11\sigma^2 5\pi^3 2\delta^3 12\sigma^1 6\pi^1$ and $11\sigma^1 5\pi^3 2\delta^3 12\sigma^2 6\pi^1$, which are the analogs of the $8\sigma^2 3\pi^3 1\delta^3 9\sigma^1 4\pi^1$ and $8\sigma^1 3\pi^3 1\delta^3 9\sigma^2 4\pi^1$ configurations for FeC, respectively. The energies for those RuC $^3\Delta$ states are close to the highest observed $^3\Delta$ electronic states in FeC (2.51eV). A close

examination of the $8\sigma^2 3\pi^3 1\delta^3 9\sigma^1 4\pi^1$ configuration reveals that there could be as many as six $^3\Delta$ electronic states arising from this configuration. The configuration can distribute electrons in two distinct ways, *i.e.*, $8\sigma^2 3\pi^{+2} 3\pi^{-1} 1\delta^{+2} \delta^{-1} 9\sigma^1 4\pi^{-1}$ and $8\sigma^2 3\pi^{+1} 3\pi^{-2} 1\delta^{+2} \delta^{-1} 9\sigma^1 4\pi^{+1}$, depending on whether a $3\pi^+$ electron or a $3\pi^-$ electron gets promoted. Furthermore, the four unpaired electrons can be spin coupled in three different ways corresponding to the three spin wavefunctions (Table 2-1). For the Ω=2 states, the lowest one is definitely the Ω=2 spin component of the ground electronic state $X^3\Delta_1$ and its energy is estimated to be 372 cm^{-1} above the Ω=3 spin component of the ground state based on the rotational constants. The two highest observed Ω=2 states are, respectively, the accompanying $^3\Delta_2$ spin components of the two $^3\Delta_1$ states derived from the $8\sigma^2 3\pi^3 1\delta^3 9\sigma^1 4\pi^1$ configuration. The electronic configuration assignment for the other observed Ω=2 states, as well as the Ω=4 state, is troublesome. Brugh and Morse pointed out [103] that the configurations $8\sigma^2 3\pi^4 1\delta^3 9\sigma^0 4\pi^1$, $8\sigma^2 3\pi^4 1\delta^2 9\sigma^1 4\pi^1$ and $8\sigma^2 3\pi^3 1\delta^3 9\sigma^2$ undoubtedly played a role in some of the transitions observed in their experiment.

4.10 Perturbation in the Observed Spectra

From the observed lifetimes (Table 4.4), it is apparent that for $(I)^3\Delta_3$ states, the vibrational levels with v' =2 and 3 are significantly perturbed by states with longer lifetimes. The most likely perturbers in this case are the nearby vibrational levels of the $(II)^3\Delta_3$ state. Given the fact that the $(II)^3\Delta_3$ levels have longer measured lifetimes, the effect of perturbations will be to increase the lifetimes of the $(I)^3\Delta_3$ levels. The most strongly perturbed band is the $(I)^3\Delta_3 \leftarrow X^3\Delta_3$ (3-0) band (Figure 4.15).

In section 4.4. we have noted the discrepancy between the experimentally observed isotopic shifts and the calculated ones (Figure 4.4), indicating severe electronic perturbations involving multi-vibrational states. In order to investigate the origin of these perturbations a program has been written to calculate the vibrational wavefunctions using Morse potential surfaces. Franck-Condon factors for the $(I)^3\Delta_3 \leftarrow X^3\Delta_3$ transitions were calculated and compared with dispersed fluorescence spectra. Even the experimental patterns can not be reproduced with the bond lengths and the vibrational constants of the two electronic states. Many parameters have been used, including bond lengths and vibrational constants. Isotope shifts were calculated by diagonalizing a Hamiltonian matrix coupling more than ten vibrational states from each electronic state. Irregular isotopic shift patterns were obtained in the calculations, but no conclusion can be made at the present time. A rigorous treatment will be necessary, possibly involving high resolution experimental studies.

The $(I)^3\Delta_3 \leftarrow X^3\Delta_3$ (3-0) band (Figure 4.15) is the most complicated $Fe^{12}C$ band in appearance. Three sets of P, Q, and R branches can be recognized in the

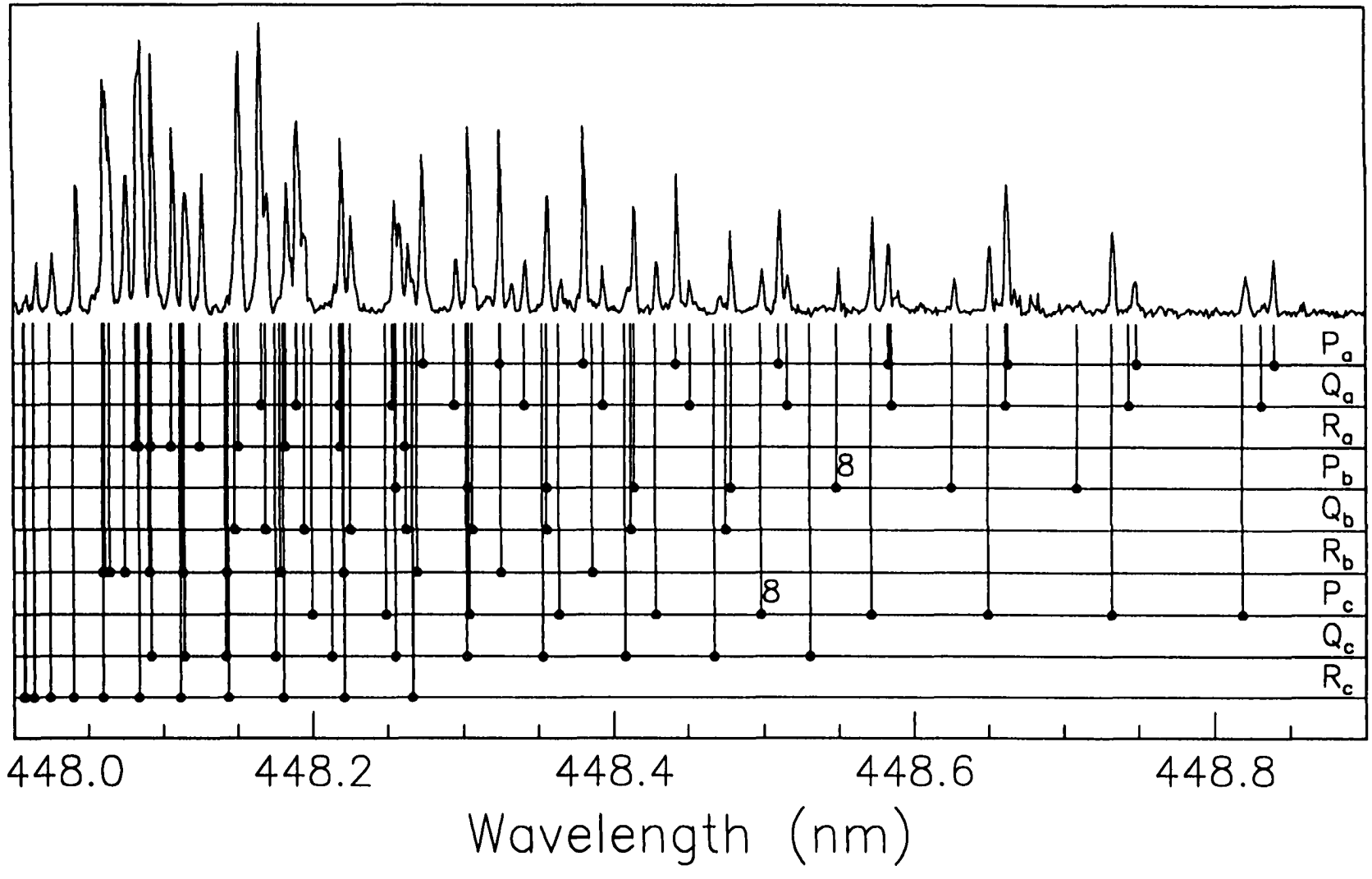

Figure 4.15 The strongly perturbed 448nm band of $Fe^{12}C$. The $P_b(8)$ and $P_c(8)$ lines, which have similar intensities, are labeled.

spectrum. They are named set (a), set (b), and set (c), respectively, in order of increasing energy. This band is qualitatively similar to the 566.5nm band of the extensively studied FeO "orange" system, where three interacting vibronic states are involved [106]. Set (a) has the lowest energies. It has relatively normal intensity patterns with rotational quantum number J, and has a well resolved P(4) line, indicating a $\Omega' = 3 \leftarrow \Omega'' = 3$ type transition associated with it. Set (c) has the highest energies. It shows an intensity pattern rising with J values. Because of the weak intensities associated with the low J spectral lines and the unfortunate overlap of these lines with others, it is not possible to determine the Ω values for the electronic states associated with this set of branches. However the intensity pattern hints that the low J levels of this electronic state are not connected to the ground state levels directly, but rather borrow intensities from another electronic state. Set (b) shows an opposite intensity pattern to that of set (c); the intensity drops rapidly with increasing J values. The relatively strong low J spectral lines support Q(3) and P(4) assignments and indicate an electronic state with Ω=3 as the upper state.

The rotational energy levels deduced from these three sets of P, Q, and R branches are given in Table 4.7. and shown in Figures 4.17-4.18 The energy *versus* J(J+1) curve for set (a) rotational energy levels is reasonably linear, given the fact that the line position accuracy is only $\pm 0.1 cm^{-1}$. The other two curves are clearly bent in opposite directions, showing a relatively strong interaction between them. The average energies of set (b) and set (c) shows a linear relationship with J(J+1). The interactions of these two sets with set (a) must be very small, if any, compared with the interaction between the sets themselves. Nevertheless, a 3×3 matrix model was developed to fit the observed rotational levels. The

Table 4.7 Rotational energies (in cm-1) of the three interacting excited vibronic states associated with the 448nm band

J	Set (a)	Set (b)	Set (c)
3	22314.93	22315.7	
4	22319.04	22320.13	
5	22324.30	22325.53	22328.13
6	22330.61	22332.04	22334.48
7	22337.95	22339.54	22342.03
8	22346.36	22348.06	22350.61
9	22355.86	22357.65	22360.34
10	22366.36	22368.30	22371.20
11	22377.89	22379.87	22383.25
12	22390.37		22396.30
13	22404.12		

matrix has the form:

$$\begin{bmatrix} e_1 & H_{12} & H_{13} \\ H_{12} & e_2 & H_{23} \\ H_{13} & H_{23} & e_3 \end{bmatrix} \tag{4.44}$$

where

$$e_i = \nu_i + B_i J(J+1) \tag{4.55}$$

with $i = 1,2,$ and 3, are the rotational energy level expressions for the three deperturbed vibronic states (the basis states); H_{ij} are the off-diagonal elements connecting those states. Since the Ω value for one of the involved electronic states cannot be assigned directly from the spectrum, three coupling schemes were tested in the fitting process:

test I: $\Omega_1 = \Omega_2 = \Omega_3 = 3$; all off-diagonal elements are constant

test II: $\Omega_1 = \Omega_2 = 3$; $\Omega_3 = 2$; H_{13} and H_{23} were multiplied by $\sqrt{J(J+1)-6}$

test III: $\Omega_1 = \Omega_2 = 3$; $\Omega_3 = 4$; H_{13} and H_{23} were multiplied by $\sqrt{J(J+1)-12}$.

The matrix was diagonized and fitted to the observed rotational energy levels, with all nine parameters optimized during the fitting procedure. All three tests gave satisfactory results (Table 4.8 and Figures 4.16-4.17) as far as the line positions are concerned. Within the fitting uncertainties all three tests show that the interactions between basis state 1 and other two basis states are negligible.

The curves of the deperturbed rotational levels as function of J(J+1) for basis states 2 and state 3 cross each other for all three tests. The crossing point is around J=7 for test I and J=10 for tests II and III. From the intensity patterns of the set (b) and set (c) spectral lines it can be concluded that the intensity is carried by the basis state 2. For low J

Table 4.8 Spectroscopic parameters (in cm^{-1}) of the deperturbed three excited vibronic states associated with the 448nm band

	T_1	T_2	T_3	H_{12}
Test I	22311.56	22309.89	22308.57	1.240
Test II	22312.26	22309.19	22308.57	0.1437
Test III	22312.30	22309.14	22308.57	0.1482

Note:

a) All tests yielded same results for the rotational constants. They are B_1= 0.5218 cm^{-1}, B_2=0.5512 cm^{-1}, and B_3=0.5249 cm^{-1}.

b) H_{13} and H_{23} were determined to be 0 in all three tests.

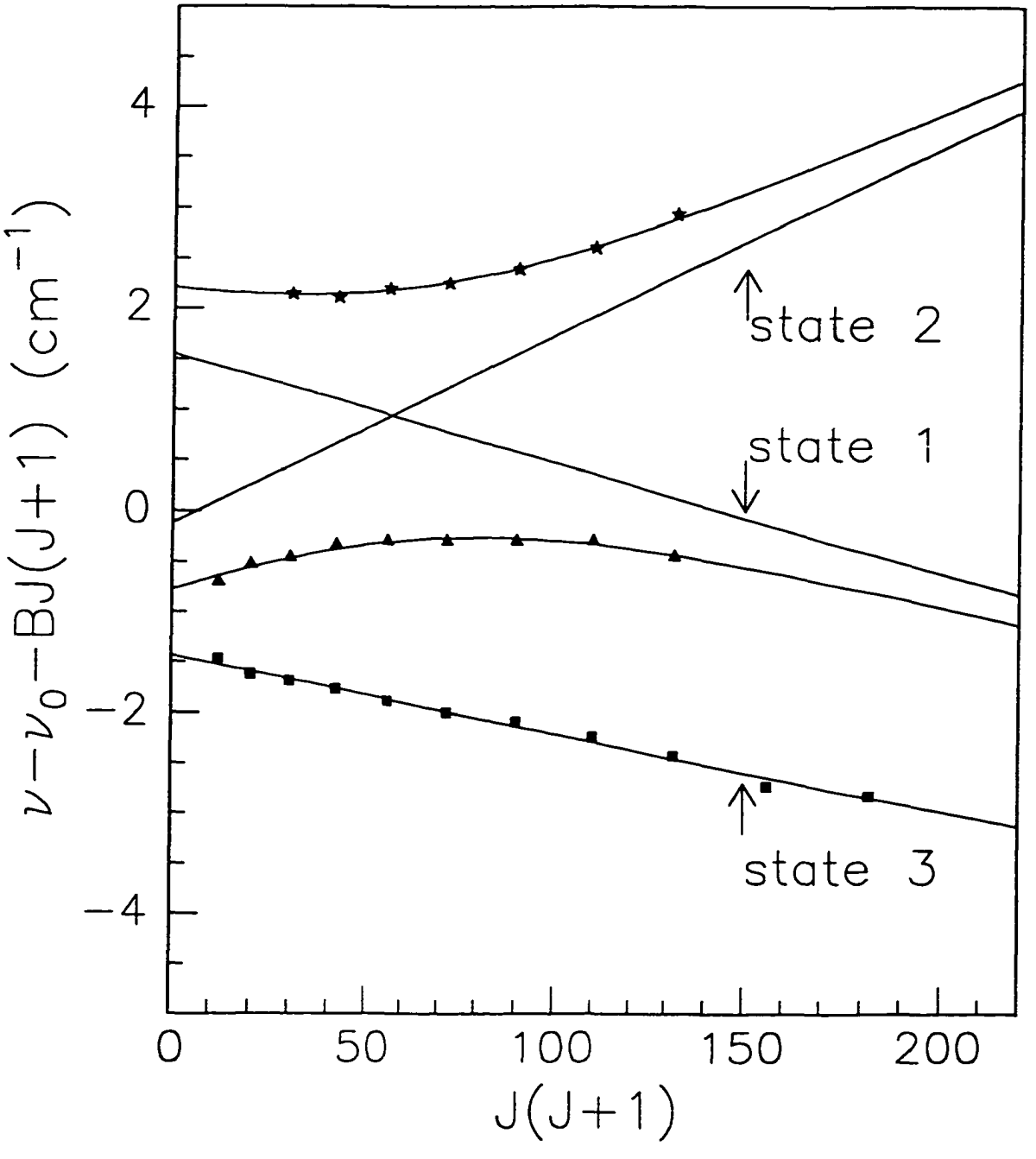

Figure 4.16 The deperturbation analysis of the 448nm band assuming homogeneous interactions. The three diabatic basis levels are represented by solid lines and indicated by arrows. The adiabatic energy levels resulted from the interactions are also represented by solid lines which go through the experimental data points. The experimentally observed energy levels are represented by squares, triangles, and stars for set (a), set (b), and set (c), respectively. ν_0=22310cm^{-1}, B=0.5326cm^{-1}.

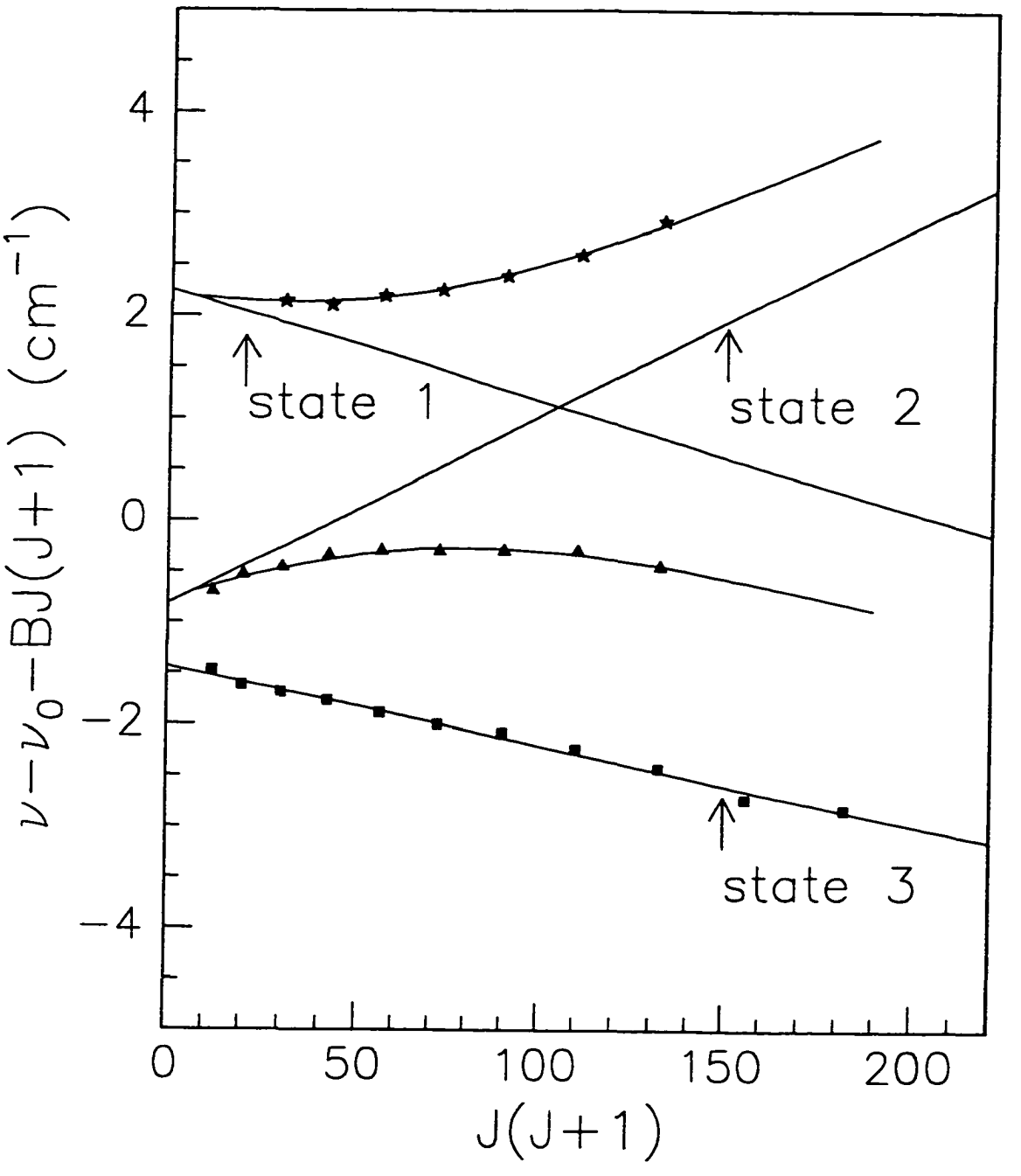

Figure 4.17 The deperturbation analysis of the 448nm band assuming heterogeneous interactions. The three diabatic basis levels are represented by solid lines and indicated by arrows. The adiabatic energy levels resulted from the interactions are also represented by solid lines which go through the experimental data points. The experimentally observed energy levels are represented by squares, triangles, and stars for set (a), set (b), and set (c), respectively. ν_0=22310cm^{-1}, B=0.5326cm^{-1}.

levels, before the crossing point, basis state 2 is mainly responsible for the spectral lines in set (b), and therefore the set (b) intensity is stronger than that of set (c) at low J. At high J levels, after the crossing point, basis state 2 contributes more to the spectral lines in set (c), which reverses the intensity pattern between set (b) and set (c). It is expected that the line intensities should be the same for set (b) and set (c) when the upper rotational quantum number J is around the value near the crossing point. Inspection of the spectrum (Figure 4.15) reveals that the intensities of Q(7) and P(8) in set (b) are, respectively, comparable with those in set (c), strongly supporting the coupling scheme represented by test I, *i.e.*, all three electronic states involved in the band have Ω values of 3.

Of all three Ω=3 vibronic states at 22310cm^{-1}, state 2 is most possibly the state corresponding to the 3-0 band of the principal system (Table 4.2.). This could be justified by the fact that i). it is the bright state carrying intensity and ii). its rotational constant B is consistent with other bands in the system (Figure 4.18).

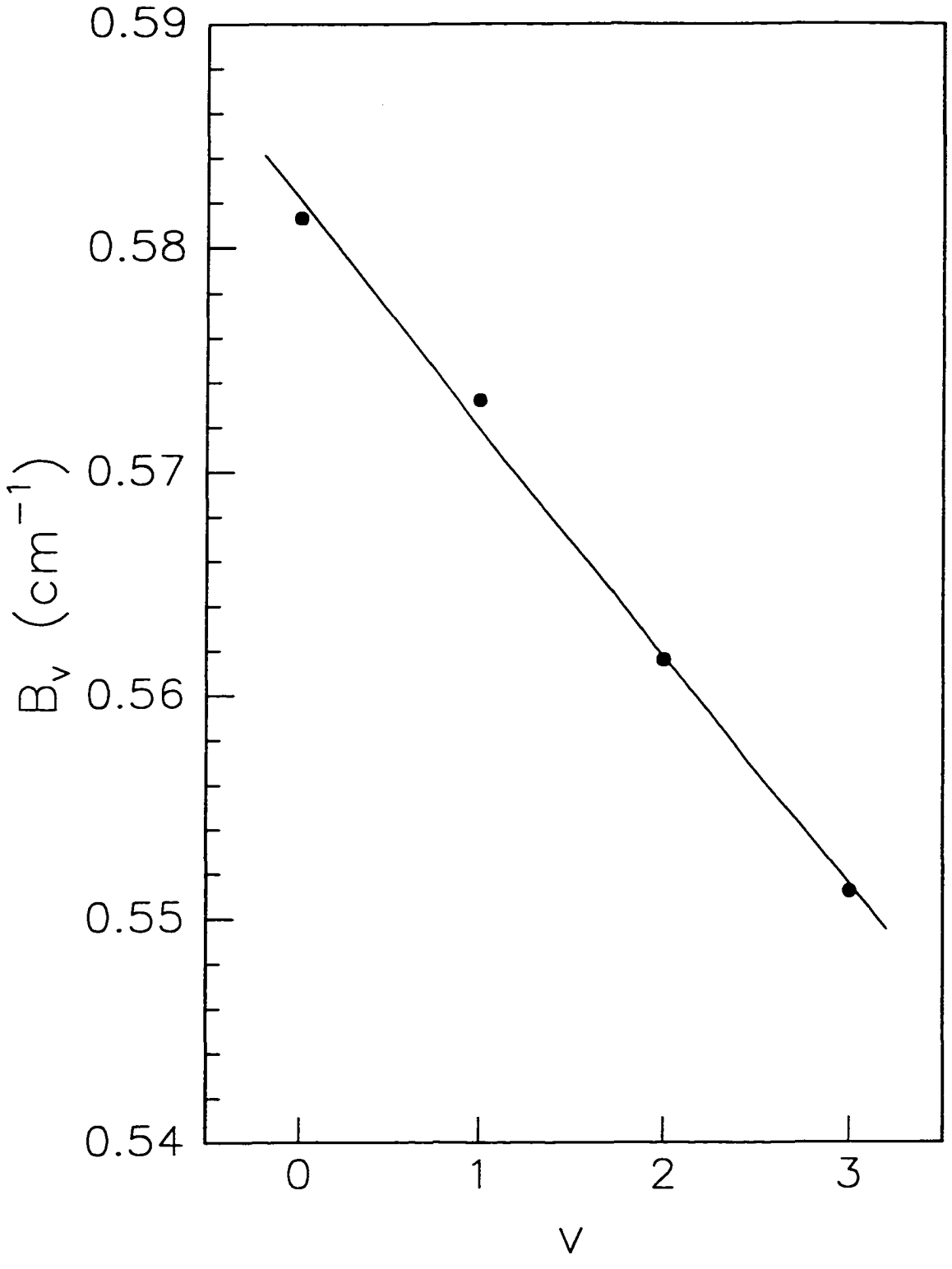

Figure 4.18 Rotational constant B_v of the $(I)^3\Delta_3$ state. B_3 was obtained from the deperturbation analysis.

4.11 Concluding Remarks

The ground state of FeC has been established to be an inverted $^3\Delta$ ($1\delta^3 9\sigma^1$) state. The electron configuration of the ground state revealed that molecular orbitals of 3d metal carbides are different from those of 3d metal oxides. The anti-bonding 4π orbitals in 3d metal carbides are significantly higher in energy, compared with the non-bonding 1δ and 9σ orbitals, than the corresponding orbitals in 3d metal oxides. This could be verified through high level *ab initio* calculations.

A four-state interaction model has been developed to investigate the influence of the $^1\Delta$ state, which has the same electron configuration as the ground state, on the ground $^3\Delta$ state. It was concluded that the singlet state affected the effective rotational constants, as well as the relative energies, of the spin components of the triplet state significantly. The spin-orbit constant can be inferred from effective rotational constants of the two lowest spin components of the triplet state and the location of the singlet state. This model is expected to be applicable to other similar molecular systems where spin-orbit interactions are significant. The molecular spin-orbit constant of FeC, calculated from this model, is similar to that of FeO. A direct measurement of the relative energies of the three spin components in the triplet ground state will be the best test of this model.

The observed excited vibronic states between 20000cm^{-1} and 23000cm^{-1} with Ω=3 and Ω=2 were assigned to be, respectively, the $^3\Delta_3$ and $^3\Delta_2$ states arising from promotion of an electron from a bonding 3π orbital to an anti-bonding 4π orbital. Since as many as six $^3\Delta$ states can be formed upon this promotion, it is not surprising that perturbations have been indicated by the measurements of lifetimes and isotope shifts. Deperturbation

analyses were performed on a strongly perturbed band at 488nm. Three vibronic states with Ω=3 were involved in the band. Further studies on many weak features in the LIF spectrum will reveal more information on the excited states of FeC.

Chapter 5

Spectroscopic Studies of Rhenium Nitride (ReN)

5.1 Introduction

Rhenium, the last discovered naturally occurring element, was isolated in 1925 [107]. It plays an important role in catalytic chemistry [108 and references therein]. Studies of rhenium chemistry have offered first examples of many multiple bonds - double, triple, and quadruple - between transition metal atoms [107]. However, little is known of its interaction with such non-metal atoms as hydrogen, fluorine, oxygen, nitrogen, and carbon. An investigation of the molecular spectra of the diatomic molecules formed by the combination of rhenium with these atoms provides simple models from which information on the bonding action of rhenium may be derived.

Ab initio calculations on ReH were performed by Dai and Balasubramanian [109] in 1993. The ground electronic state was predicted to have an Ω value of 0^- and be characterized by a $^7\Sigma_0^+$ symmetry. No experimental data are available for this molecule.

Launila *et al* presented an extensive survey and a rotational analysis of band systems attributed to the ReF molecule in 1994 [110]. The observed bands were interpreted as transitions involving two different lower Ω=0 states and a number of different excited electronic states. Neither energy difference between the two lower Ω=0 states, nor which of them is the ground state, is known. However, a comparison of vibrational frequencies of these two states reveals that they correlate to two different configurations of Re^+ (*i.e.*, $5d^5 6s^1$ and $5d^4 6s^2$).

For more than a decade, the molecule ReO was the only rhenium-containing diatomic molecule which had been characterized spectroscopically [111-113] until ReF

[110] and ReN [114] were discovered in 1994. Balfour and co-workers surveyed the emission spectrum of ReO from the near ultraviolet through the photographic infrared, using conventional spectrographic methods, and identified fourteen electronic states [113]. For the ground state it was concluded that $\Lambda'' \geq 2$, but the electronic symmetry and multiplicity of the state remained a mystery. On the basis of SCF calculations on the related MnO, Pinchemel and Schamps predicted a $^6\Sigma$ ground state [115], whereas Weltner suggested a $^4\Pi$ state from ligand field considerations [116]. One obvious way to solve this problem was to determine the Ω values of the states involved through experiment and then compare the Ω'' value with electronic states derived from configurations with possible low energy. In a recent jet-cooled molecular beam absorption experiment Balfour *et al.* [117] established Ω=2.5 for the ground state and assigned it to a $^2\Delta_1(3\delta^3 16\sigma^2)$ electronic state.

ReN was first discovered in 1994 [114]. Since then significant progress has been made in the identification of new electronic states and perturbations [117-118]. This chapter presents our current understanding of ReN.

5.2 The Ground Electronic State

A strong electronic transition system was observed in two independent investigations of low temperature laser-induced-fluorescence (LIF) spectroscopy and high temperature Fourier transform spectroscopy. In the LIF experiment performed in our laboratory the rhenium mononitride was produced via laser ablation of a rhenium rod in a vacuum chamber, followed by chemical reaction of the resultant plasma with ammonia (NH_3) gas seeded 5% in a helium beam. The laser excitation spectrum (Figure 5.1) showed clearly a Q-branch and R(0) as the first spectral line in the R branch. It was therefore determined that the transition was of $\Omega'=1\leftarrow\Omega''=0$ type. In the Fourier transform experiment conducted by Ram and Bernath, on the other hand, the ReN molecule was observed in a rhenium hollow cathode lamp with a slow continuous flow of 5mTorr N_2 seeded in 3Torr neon. The Fourier transform spectrum provided accurate spectroscopic constants for the ground state as well as the excited state (Table 5.1 and Table 5.2).

Since there is no *ab initio* calculation available for this molecule, an electronic structure for the ground electronic state can only be deduced based on the experimental results and comparison with other relevant radicals. The most relevant species are other group 7 metal nitrides, *i.e.*, MnN and TcN. Unfortunately neither of these molecules have been studied experimentally or theoretically.

A molecular orbital (MO) diagram is presented in Figure 5.2 to aid the understanding of the electronic structure of ReN. This diagram is similar to the one used for FeC (Figure 4.12). Several differences between ReN and FeC have to be considered. First, relativistic effects stabilize the metal 6s atomic orbital relative to the 5d atomic orbital [119], resulting in a smaller 6s-5d orbital energy gap in the third transition row

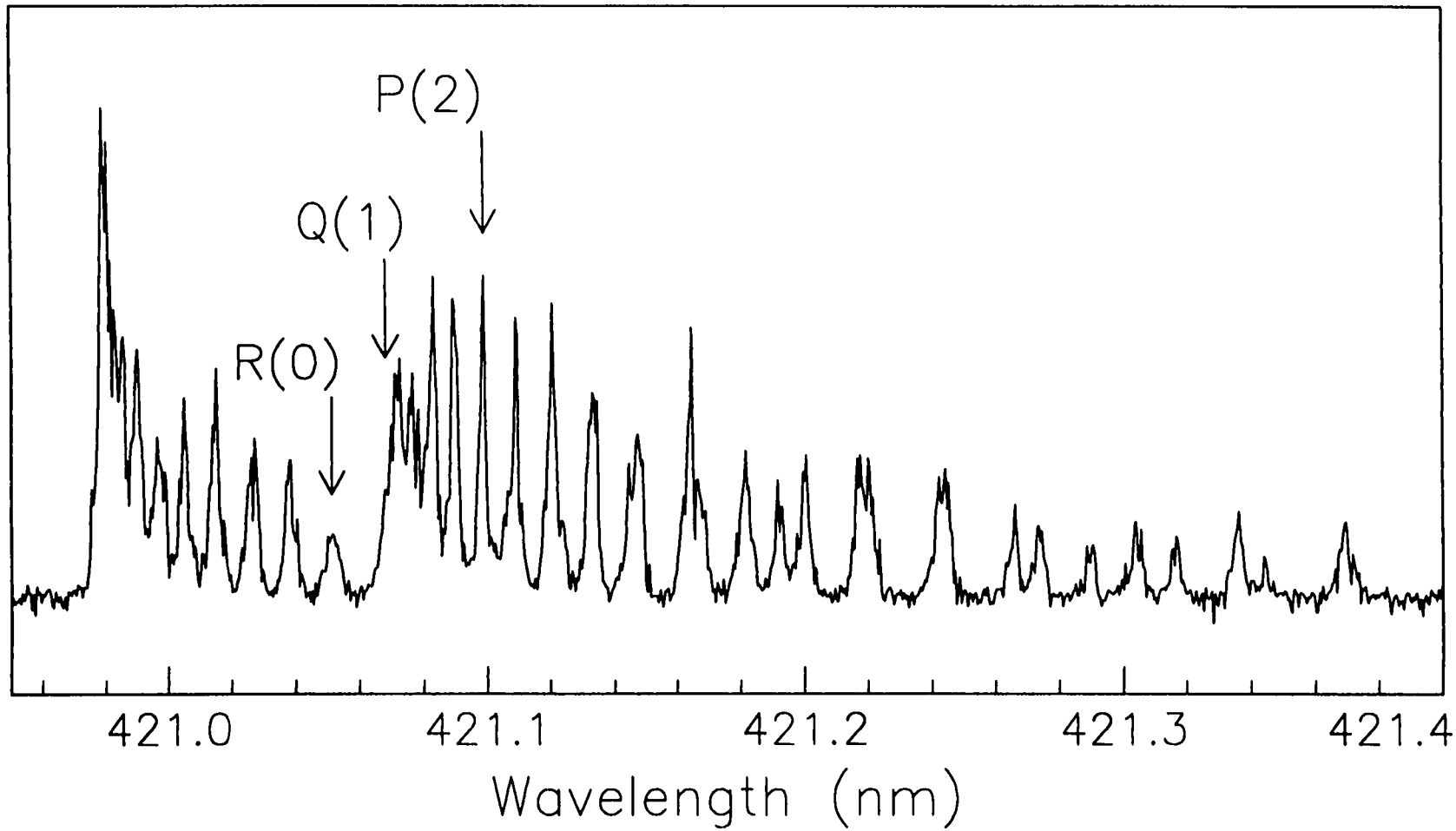

Figure 5.1 The laser excitation spectrum of the 0-0 band of the [23.8]1-X0$^+$ system of the $^{187}Re^{14}N$ molecule at 420.9nm. It shows clearly the R(0) line and the Q branch, unambiguously supporting the $\Omega'=1\leftarrow\Omega''=0$ assignment.

Table 5.1 Rotational constants (in cm^{-1}) obtained for the $X0^+$ state of $^{185}Re^{14}N$ and $^{187}Re^{14}N$.

Constants	$^{185}Re^{14}N$		$^{187}Re^{14}N$	
	v=0	v=1	v=0	v=1
T_v	0.0	1121.9216(19)	0.0	1121.5192(15)
B_v	0.481207(19)	0.478651(19)	0.4811223(88)	0.4785388(93)
$10^7 \times D_v$	2.877(75)	2.910(77)	4.019(14)	4.005(20)
$10^{12} \times H_v$	-7.59(88)	-8.28(92)	4.907(67)	4.62(19)

Note: The numbers in parentheses are one standard deviation in the last digit. (adapted from [114])

Table 5.2 Rotational constants (in cm^{-1}) obtained for the [23.8]1 state of $^{185}Re^{14}N$ and $^{187}Re^{14}N$.

Constants	$^{185}Re^{14}N$		$^{187}Re^{14}N$	
	v=0	v=1	v=0	v=1
T_v	23746.4159(11)	24617.4042(14)	23746.4185(9)	24617.0742(10)
B_v	0.439895(18)	0.437273(19)	0.4397988(90)	0.4372113(88)
$10^7 \times D_v$	3.782(73)	4.593(73)	4.783(16)	5.695(13)
$10^{11} \times H_v$	-0.728(85)	-1.201(84)	0.4016(90)	~
$10^4 \times q_v$	-4.797(11)	-4.744(34)	-4.7244(75)	-4.442(20)
$10^8 \times q_{Dv}$	0.635(28)	5.51(25)	0.490(17)	1.962(94)
$10^{12} \times q_{Hv}$	~	-9.39(56)	~	2.13(10)
$10^{15} \times q_{Lv}$	~	1.085(41)	~	~

Note: The numbers in parentheses are one standard deviation in the last digit. (adapted from [114])

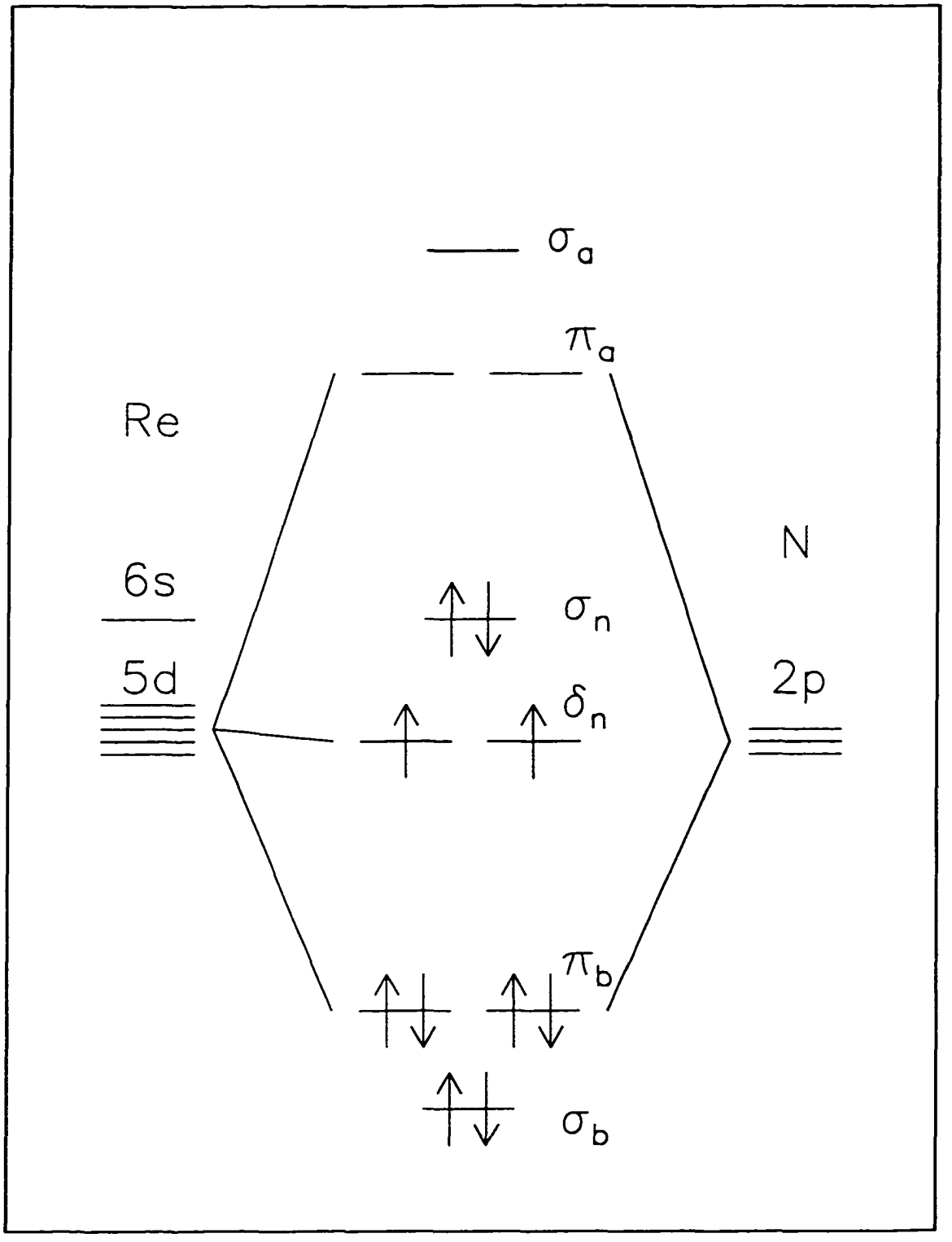

Figure 5.2 The qualitative ReN molecular orbital diagram and the electronic configuration of the $^3\Sigma^-$ ground state.

compared with the 4s-3d gap in the first row. This difference places the non-bonding σ_n molecular orbital (mainly the 6s atomic orbital) closer to the non-bonding δ_n molecular orbital (mainly the 5d atomic orbital) in the case of ReN. Second, the nitrogen 2s atomic orbital is not significantly involved in the covalent molecular orbitals because of the larger 2p-2s orbital energy gap. This prevents the σ_n orbital from being pushed up by the 2s orbital as in the case of metal carbides.

FeC and RuC are isovalent molecules of ReN. In Chapter 4 we have determined that the ground electronic state of FeC is $^3\Delta_i$ $(\delta_n^3\sigma_n^1)$. The ground electronic state of RuC has been determined experimentally by Morse and his co-workers to be the $^1\Sigma^+(\delta_n^4\sigma_n^0)$ state [33]. Since a $^3\Delta_i$ electronic state has no Ω=0 component, it can be ruled out immediately. On the other hand, the only component of a $^1\Sigma^+$ state is Ω=0$^+$, so the $^1\Sigma_0^+$ state is a candidate for the ground electronic state of ReN.

WO is another isovalent molecule of ReN. Several $\Delta\Omega$=0 and $\Delta\Omega$=1 electronic transitions have been observed by Samoilova *et al.* [120]. The authors concluded that the WO ground state is most probably the 0$^-$ component of a case (c) $^3\Sigma^-$ $(\delta_n^2\sigma_n^2)$ state. The Ω=0$^+$ and Ω=1 components of an isolated $^3\Sigma^-$ state are almost degenerate, but the strong spin-orbit interaction between the Ω=0$^-$ component and the $^1\Sigma^+$ state from the same configuration will push the Ω=0$^-$ component much lower than the Ω=1 component. This may well explain the experimentally observed Ω=0 ground state of ReN.

CrO and MoO, whose ground electronic states are both $^5\Pi_r$ $(\delta_n^2\sigma_n^1\pi_a^1)$ [2, 121], are also isovalent molecules of ReN. Even though a $^5\Pi_r$ state has an Ω=0 component, the energy ordering of its components is (from the highest to the lowest):

$^5\Pi_3, ^5\Pi_2, ^5\Pi_1, ^5\Pi_0, ^5\Pi_{-1}$. Clearly an isolated $^5\Pi_r$ state can not be the ground state of ReN because its Ω=0 component is not the lowest one. However, it is possible that the Ω=0 component of the $^5\Pi_r$ state may be pushed down by the Ω=0 component of a $^3\Pi_r$ state with the same configuration. Further considerations are necessary in order to assign the ReN ground state symmetry.

As discussed in Chapter 4, the ground states of 3d metal nitrides involve three covalent bonding orbitals. The anti-bonding π_a orbitals are high in energy and therefore do not normally participate in the ground state configuration unless all bonding and non-bonding orbitals are full. This also applies to 4d and 5d metal nitrides. The ground state of RhN definitely has Ω=0 as has been established both experimentally [122] and theoretically [123]. This suggests a $^1\Sigma(\delta_n^4\sigma_n^2)$ state with two empty π_a orbitals. The same symmetry for the ground state was established for IrN in a high resolution molecular beam study [124]. Another piece of evidence comes from comparison of the isovalent molecules PtN and IrO. The ground state of IrO is $^4\Delta_i(\delta_n^3\sigma_n^2\pi_a^2)$ [125], whereas the ground state of PtN is $^2\Pi(\delta_n^4\sigma_n^2\pi_a^1)$ [120] in which one electron is moved from the π_a orbital to the δ_n orbital. So the $^5\Pi_r$ state is unlikely to be the ground state of ReN because the corresponding configuration requires one electron in the anti-bonding π_a orbital while other non-bonding orbitals are not fully filled.

In Chapter 4 we have also discussed the competition between the non-bonding σ_n and δ_n orbitals in a diatomic 3d metal-ligand system. For early metal oxides [2] the σ_n orbital is (effectively) lower than the δ_n orbitals so that the filling process for ScO, TiO, and VO is $\sigma_n^1 \rightarrow \sigma_n^1\delta_n^1 \rightarrow \sigma_n^1\delta_n^2$. But the σ_n orbital "catches up" with increasing atomic

number and eventually becomes higher than the δ_n orbitals, so that the filling process for MnO, FeO, CoO, and NiO is $\sigma_n^1\delta_n^2\pi_n^2 \rightarrow \sigma_n^1\delta_n^3\pi_n^2 \rightarrow \sigma_n^2\delta_n^3\pi_n^2 \rightarrow \sigma_n^2\delta_n^4\pi_n^2$. The effective relative σ_n orbital energy also changes with ligand, and the trend is that the σ_n orbital energy increases from oxides to carbides. For example, the filling process from TiC to NiC is $\sigma_n^0\delta_n^0 \rightarrow \sigma_n^0\delta_n^1 \rightarrow \sigma_n^0\delta_n^2 \rightarrow (\sigma_n^1\delta_n^2 ?) \rightarrow \sigma_n^1\delta_n^3 \rightarrow \sigma^1\delta^4 \rightarrow \sigma_n^2\delta_n^4$. This also applies to 4d and 5d metal systems. For example, the isovalent molecules ZrO [127], NbN [128], and MoC [33] have ground states of $^1\Sigma(\delta_n^0\sigma_n^2)$, $^3\Delta(\delta_n^1\sigma_n^1)$, and $^3\Sigma(\delta_n^2\sigma_n^0)$, respectively This clearly indicates the effective increase in energy of the σ_n orbital compared to the δ_n orbitals as the ligand changes from oxygen to carbon. The trend in 5d metal diatomic systems can be gauged by the isovalent molecules TaO and WN, which have ground states of $^2\Delta(\delta_n^1\sigma_n^2)$ [129] and $^4\Sigma(\delta_n^2\sigma_n^1)$ [130], respectively.

As we move from 3d to 4d metals, the σ_n orbital becomes higher in energy compared with the δ_n orbitals, especially for late metals. This effect may be attributed to the more diffuse 4d orbitals [39]. For instance, the ratio of the radial extent of the 4s to 3d orbital varies from about 2.0 in Sc to 3.4 in Cu whereas that of the 5s to 4d varies from 1.6 in Y to 2.7 in Ag [39]. The diffusion of the 4d orbitals decreases the electron-electron repulsion within the 4d orbitals and therefore lowers the effective energy of the 4d orbitals. Because of the correlation between molecular orbitals and atomic orbitals, it is not surprising to see that the effective energy of σ_n orbitals in 4d metal-ligand system is effectively higher than the corresponding σ_n orbitals in 3d metal systems, especially for late metals in the series. This effect explains the differences between FeC $^3\Delta_i(\delta_n^3\sigma_n^1)$ [18] and RuC $^1\Sigma^+(\delta_n^4\sigma_n^0)$ [33], CoO $^4\Delta_i(\delta_n^3\sigma_n^2\pi_a^2)$ [2] and RhO $^4\Sigma^-(\delta_n^4\sigma_n^1\pi_a^2)$ [131-132].

5d orbitals are even more diffuse than the 4d orbitals. But the relativistic correction stabilizes the 6s orbital relative to the 5d orbitals, making the non-bonding σ_n orbital lower than the δ_n orbitals again. This effect is reflected in the differences between TiO $^3\Delta_r(\delta_n^1\sigma_n^1)$ [2] and HfO $^1\Sigma^+(\delta_n^0\sigma_n^2)$ [133], VO $^4\Sigma^-(\delta_n^2\sigma_n^1)$ [2] and TaO $^2\Delta_r(\delta_n^1\sigma_n^2)$ [129], CoC $^2\Sigma(\delta_n^4\sigma_n^1)$ [34-35] and IrC $^2\Delta(\delta_n^3\sigma_n^2)$ [134].

Based on the above discussions we favor a $^3\Sigma^-(\delta_n^2\sigma_n^2)$ ground state assignment for ReN. To support this assignment, it is noted that all 5d metal oxides have their non-bonding σ_n orbital filled first, showing a strongly stabilized σ_n orbital compared with corresponding orbital for 3d metal oxides. This trend is expected to remain for nitrides and carbides.

5.3 Deperturbation Analysis of the [18.5]1 State

A total of eighteen bands attributable to ReN were observed, all in the 375-542nm region (Table 5.3), though we surveyed up to 720nm. These bands were classified into five systems (Figure 5.3), according to their positions, their Ω' values, and the isotopic shifts from naturally occurring ^{185}Re (37.4%) and ^{187}Re (62.6%) [105]. All these systems originate from the same ground vibronic state and have either $\Delta\Omega=0$ or $\Delta\Omega=1$. Of the five excited electronic states, the lowest three have $\Omega=1$ while the upper two have $\Omega=0$. Because of the expected strong spin-orbit interactions for a heavy species like ReN we assume Hund's case (c) coupling for these excited states and label them with their v=0 vibronic energies, in units of 10^3 cm^{-1} relative to the ground vibronic state in square bracket, followed by their Ω assignments [135].

No local rotational perturbations have been observed in the spectrum, but vibrational irregularities are common. Both vibrational energy spacing and vibronic state lifetimes vary significantly within a given system. This indicates the existence of strong and complicated perturbations.

In all but one of the bands observed, a rotational analysis was achieved without difficulty [108]. However, even though no local rotational perturbations were observed, the attempted rotational analysis of the (0-0) band (Figure 5.4) of the [18.5]1-X0$^+$ system did not produce satisfactory results [108, 117]. Inspection of the spectrum shows a Q branch which is highly blended and doubly headed, an R branch which forms a band head at a fairly high J (≈20), and a P branch whose line spacing is *narrower* than the corresponding spacing in the R branch. These facts suggest that the rotational parameter of the upper state, B′, is approximately equal to that of the lower state, B″, which is

Table 5.3 Bandheads, band origins, rotational constants, and vibronic assignment of the observed $^{187}Re^{14}N$ bands. The uncertainty for the band origins is $\pm 0.1 cm^{-1}$; it is $\pm 0.0005 cm^{-1}$ for rotational constants.

Bandhead (nm)	Band Origin (cm^{-1})	B'_v (cm^{-1})	B''_0 (cm^{-1})	Vibrational Assignment	Designation
540.09	18509.6[i]	0.4695[i]	0.4372[ii]	0-0	[18.5]1-X0$^+$
512.43	19495.1[i]	0.4649[i]	0.4372[ii]	1-0	[18.5]1-X0$^+$
488.27	20467.5	0.4597	0.4372[ii]	2-0	[18.5]1-X0$^+$
466.34	21431.9	0.4543	0.4372[ii]	3-0	[18.5]1-X0$^+$
451.34	22148.3	0.4381	0.4372[ii]	0-0	[22.2]1-X0$^+$
433.42	23064.5	0.4341	0.4372[ii]	1-0	[22.2]1-X0$^+$
417.19	23961.3	0.4300	0.4372[ii]	2-0	[22.2]1-X0$^+$
402.65	24826.8	0.4252	0.4372[ii]	3-0	[22.2]1-X0$^+$
389.59	25658.6	0.4216	0.4372[ii]	4-0	[22.2]1-X0$^+$
377.45	26485.9	0.4232	0.4372[ii]	5-0	[22.2]1-X0$^+$
420.92	23746.4	0.4399	0.4372[ii]	0-0	[23.8]1-X0$^+$
406.03	24617.1	0.4373	0.4372[ii]	1-0	[23.8]1-X0$^+$
391.93	25505.6	0.4336	0.4372[ii]	2-0	[23.8]1-X0$^+$
379.24	26359.2	0.4280	0.4372[ii]	3-0	[23.8]1-X0$^+$
404.52	24705.9	0.4619	0.4372[ii]	0-0	[24.7]0-X0$^+$
390.24	25610.0	0.4611	0.4372[ii]	1-0	[24.7]0-X0$^+$
375.51	26617.4	0.4567	0.4372[ii]	2-0	[24.7]0-X0$^+$
384.20	26023.9	0.4732	0.4372[ii]	0-0	[26.0]0-X0$^+$

i) The constants for v=0 and v=1 vibrational levels of the [18.5]1 state are those after deperturbation. B′(v=1) was taken to be $0.4666 cm^{-1}$ before deperturbation.

ii) B″ was fixed at this value (taken from [114]) in the least-square-fitting.

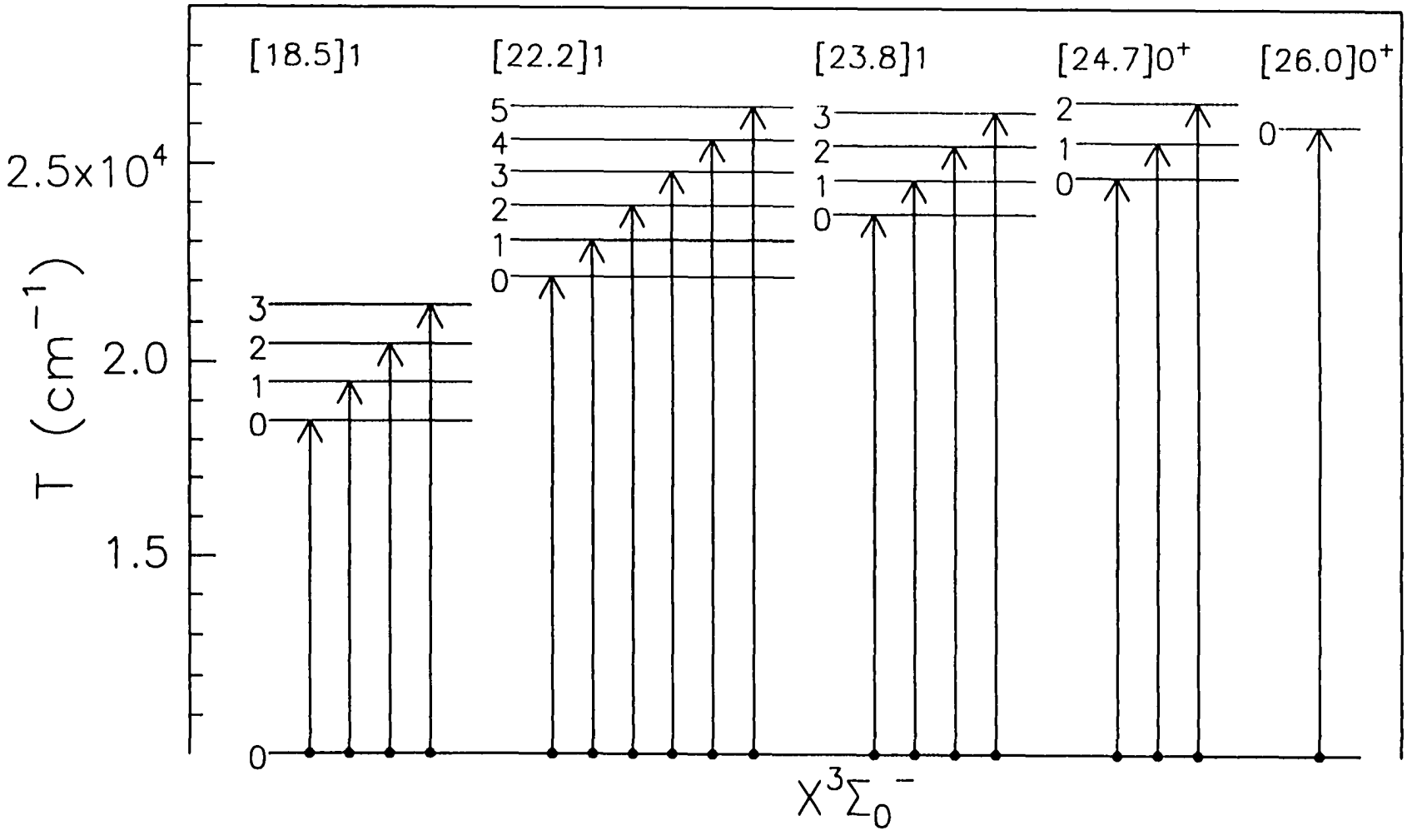

Figure 5.3 Observed vibronic transitions in the LIF spectrum of $^{187}Re^{14}N$. They have been classified into five transition systems according to their positions and their Ω' values. The assignments were confirmed by the isotope shifts from naturally occurring ^{185}Re and ^{187}Re. In the figure the vibrational quantum numbers are indicated on the left side of each level

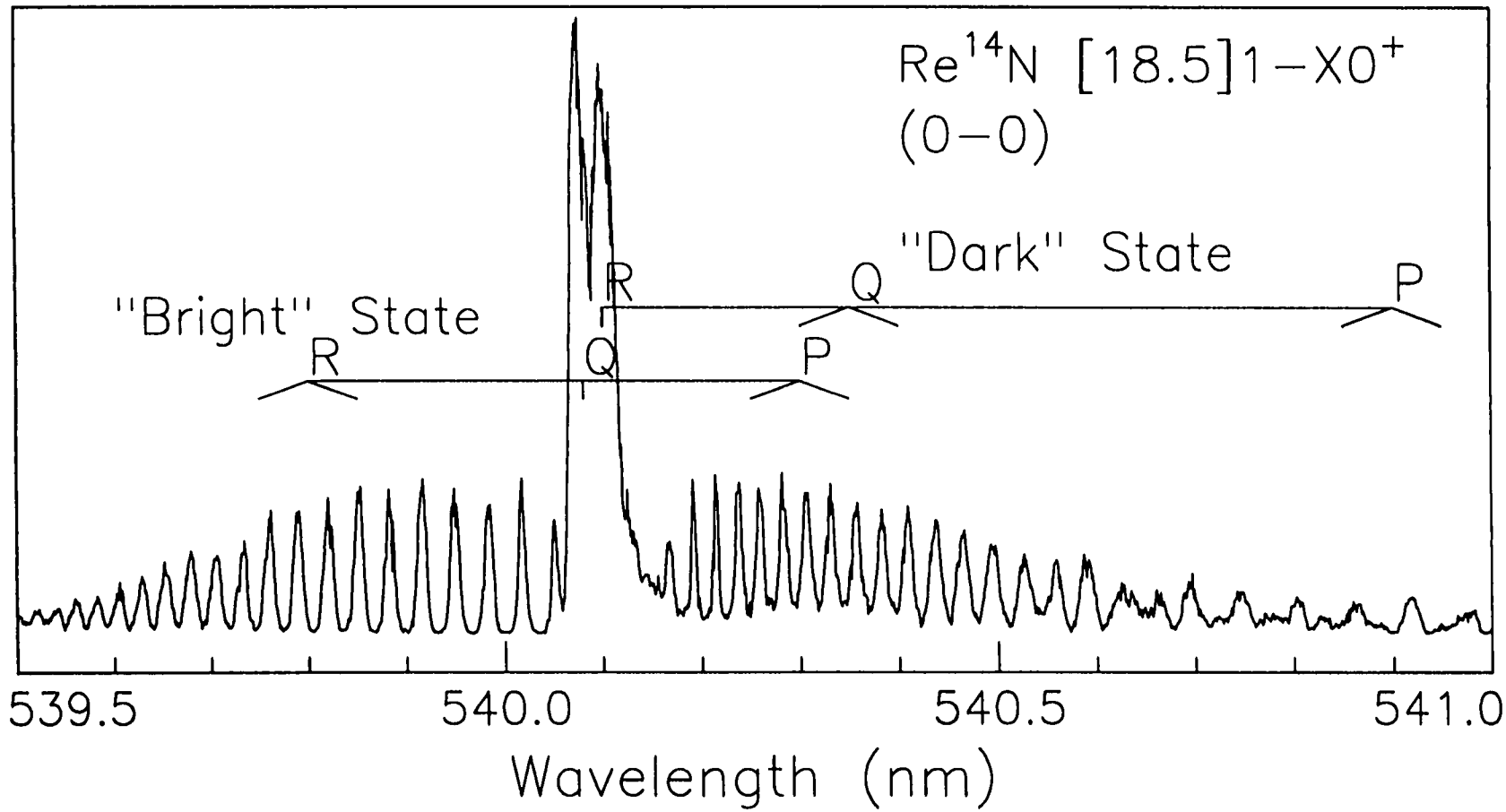

Figure 5.4 The perturbed 0-0 band of the [18.5]1-X0$^+$ system at 540nm. The transition has two overlapping transitions involving interacting states. One transition is associated with the Ω'=1 "bright" state whereas the other is associated with a Ω'=2 "dark" excited state.

known to be much larger than the rotational parameters of other upper vibronic states of the [18.5]1-X0$^+$ system. Actually the Δ_2F combination differences of the band yielded very unreasonable spectroscopic constants for the upper state (Figure 5.5). The conclusion was reached that the [18.5]1 (v=0) vibronic state experiences a global perturbation, the only one of eighteen excited vibronic states identified in the $Re^{14}N$ spectrum, all of which were fairly close to (all within 8000 cm^{-1} of) one another, to do so [108].

In order to probe the nature of the perturbation we recorded the corresponding $Re^{15}N$ spectrum in the same region. This $Re^{15}N$ spectrum is displayed in Figure 5.6a. It contains a small contribution from $Re^{14}N$, present as an impurity, which can readily be identified by direct comparison with the spectrum of pure $Re^{14}N$ (Figure 5.6b).

The experiment was repeated on the $Re^{14}N$ band and it was found that at the high J end of the P branch region the excited state lifetimes were much longer than that at the low J end. Moreover, dispersed fluorescence experiments showed that while the low J′ rotational levels emit almost exclusively to the ground electronic state the high J′ rotational levels have significant transition probabilities to another electronic state. These same characteristics were observed in the Q band head on the longer wavelength side.

A careful examination of the band revealed that the long series of P branch lines is actually composed of two different branches, the "real" P branch and an additional branch at longer wavelengths. It is immediately clear that the additional branch is a new P branch of a weak band, and that the additional "Q" head at the longer wavelength side of the "real" Q head is actually the R head of the new weak band. By comparing the R(J-1)-P(J+1) differences with the known lower level spacings we were able to establish an absolute J assignment for the new P branch (Table 5.4).

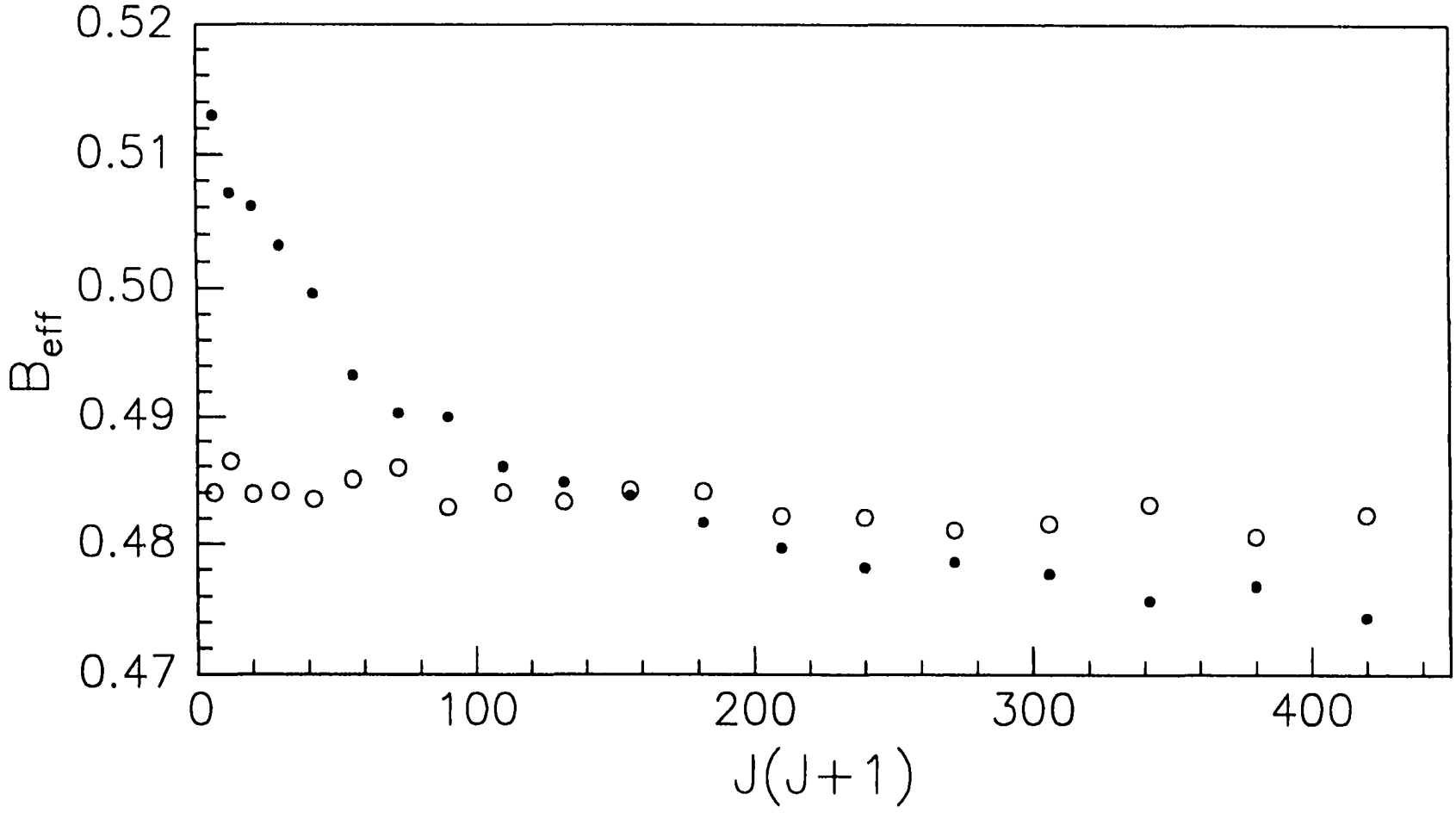

Figure 5.5 The effective rotational constant B defined from the combination differences: $B'_{eff}(J) = (R(J) - P(J)) / (4J + 2)$ and $B''_{eff}(J) = (R(J-1) - P(J+1)) / (4J + 2)$. The dots are for the upper state's rotational constant $B'_{eff}(J)$ whereas the circles are for the lower state's rotational constant $B''_{eff}(J)$. $B'_{eff}(J)$ depends on J(J+1) strongly but not linearly.

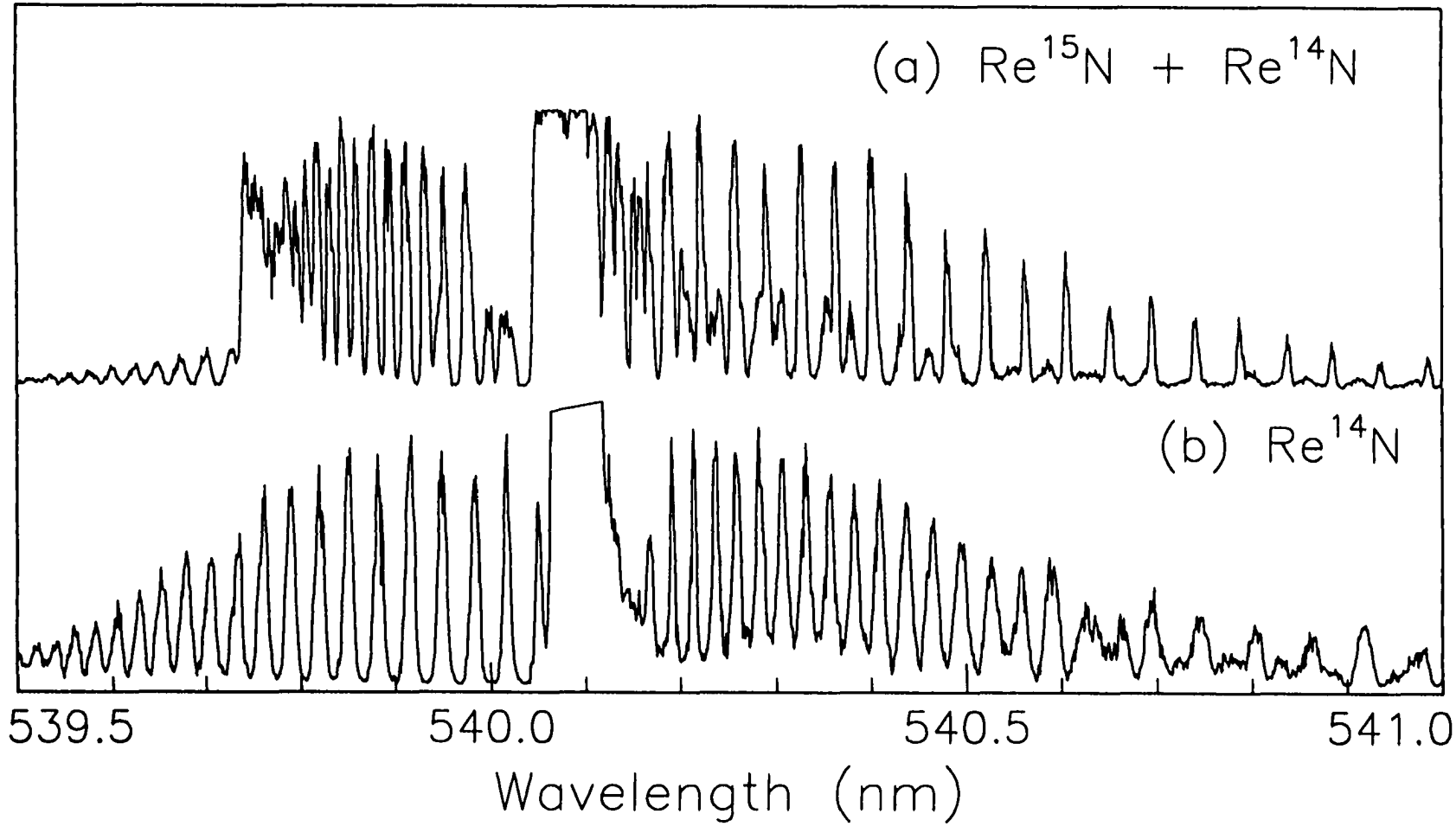

Figure 5.6 $Re^{14}N$ and $Re^{15}N$ [18.5]1-$X0^+$ bands near 540nm. The $Re^{15}N$ spectrum (a) contains a small contribution from $Re^{14}N$, present as an impurity, which can readily be identified by direct comparison with the spectrum of pure $Re^{14}N$ (b).

Table 5.4 Rotational assignments of the 540nm band. Only R and P branches corresponding to the "bright" state and the P branch corresponding to the "dark" state can be assigned. Line positions are in cm^{-1}.

J	$R_{bright}(J)$	$P_{bright}(J)$	$P_{dark}(J)$
1	18511.73		
2	18512.85	18507.72	
3	18513.99	18506.89	
4	18515.15	18506.04	
5	18516.35	18505.28	
6	18517.49	18504.50	
7	18518.58	18503.78	
8	18519.61	18502.94	
9	18520.68	18502.06	
10	18521.67	18501.26	18491.90
11	18522.65	18500.35	18489.71
12	18523.63	18499.44	18487.87
13	18524.45	18498.44	18485.99
14	18525.31	18497.49	18483.92
15	18526.13	18496.48	18482.02
16	18527.01	18495.42	18480.08
17	18527.82	18494.38	18477.96
18	18528.50	18493.30	18475.77
19	18529.26	18492.07	18473.69
20	18529.91	18491.01	18471.49
21	18530.60	18489.71	18469.11
22	18531.18		18466.93
23	18531.71	18487.28	18464.51
24	18532.18	18485.99	18462.08
25			18459.65
26			18457.11
27			18454.59
28			18452.04
29			18449.39
30			18446.78
31			18443.97
32			18441.25
33			18438.40
34			18435.60
35			18432.51
36			18429.52
37			18426.49
38			18423.61
39			18420.35

Obviously the newly observed weak band corresponds to a weak transition. Given the fact that the upper state of this band is very close to the [18.5]1 v=0 vibronic state and that this vibronic state is severely perturbed, it is possible that the newly identified state is a so called "dark" state, which has no direct connection with the ground state by an electric dipole allowed transition, but borrows transition intensities from a bright state such as the [18.5]1 state by mutual interactions (perturbations).

As discussed in Chapter 3 there are two classes of perturbations among electronic states: homogeneous perturbations between states with the same Ω value, and heterogeneous perturbations between states with Ω values which differ by one. The coupling matrix elements for the former are independent of the rotational quantum number J whereas, for the latter, they increase roughly linearly with J.

We take the diagonal matrix elements to be

$$H_{11} = T_1 + B_1 J'(J'+1) - D_1[J'(J'+1)]^2 \qquad (5.1)$$

and

$$H_{22} = T_2 + B_2 J'(J'+1) - D_2[J'(J'+1)]^2 \qquad (5.2)$$

for the bright state and the dark state, respectively. The deperturbation analyses were attempted using both homogeneous and heterogeneous coupling matrix elements as follows:

Homogeneous Coupling: $H_{12} = H_e$ (5.3)

Heterogeneous Coupling: $H_{12} = H_e\sqrt{J'(J'+1) - \Omega_1\Omega_2}$ (5.4)

where H_e is taken as a constant independent of the quantum number J.

A satisfactory least squares fit, using the strong and well resolved R and P lines associated with the bright state together with the weak but well resolved P lines associated

with the dark state, proved possible only with the heterogeneous perturbation scheme. The spectroscopic constants obtained from the deperturbation analysis are listed in Table 5.5. These constants were then used to reconstruct (simulate) the spectrum. The simulated spectrum is compared with the experimental one in Figure 5.7. In the simulation the *f* levels (associated with the Q branch) of both states were assumed to be degenerate with the *e* levels (associated with the P and R branches) and to be perturbed in the same fashion as the *e* levels in order to reproduce the appearance of the spectrum in the Q head region.

When heterogeneous perturbations are involved, the perturbing dark state must have an Ω value different by one from that of the perturbed bright state. Given that the bright state has an Ω=1, the possible values of Ω for the dark state are then 0 and 2. The observation that both *e* and *f* levels are perturbed in an identical way eliminates the possibility of Ω=0, since a state with Ω=0 has only one set of rotational levels (*e* levels for a 0^+ state or *f* levels for a 0^- state) and therefore only *e* levels or *f* levels of the bright state would be perturbed.

The Ω=2 assignment of the dark state is confirmed by the existence of a dark Q branch. By comparing the respective baselines for the R branch and the P branch regions associated with the bright state in the experimental spectrum, it is clear that the P branch region contains an underlying background. Our simulation suggests that this background comes from the Q branch structure of the transition to the dark state.

In Figure 5.8 the B value of the deperturbed v=0 bright state is compared with B values from higher vibrational levels of the same electronic state, obtained from our early studies [117]. It is evident from the graph that the deperturbed B value for v=0 is now in line with the B values of other vibronic states, (with the exception of v=1). The

Table 5.5 Spectroscopic parameters (in cm^{-1}) of the deperturbed $Re^{14}N$ [18.5]1 (v′=0,1) and [18.5]2 (v′=0,1) vibronic states.

State	T_e(±0.1)	B_e (±0.0010)	D_e (±2)
[18.5]1 v′=0	18 509.6	0.4695	9×10^{-7}
[18.5]1 v′=1	19 495.1	0.4649	5×10^{-7}
[18.5]2 v′=0	18 505.8	0.4541	7×10^{-7}
[18.5]2 v′=1	19 474.1	0.4501	0

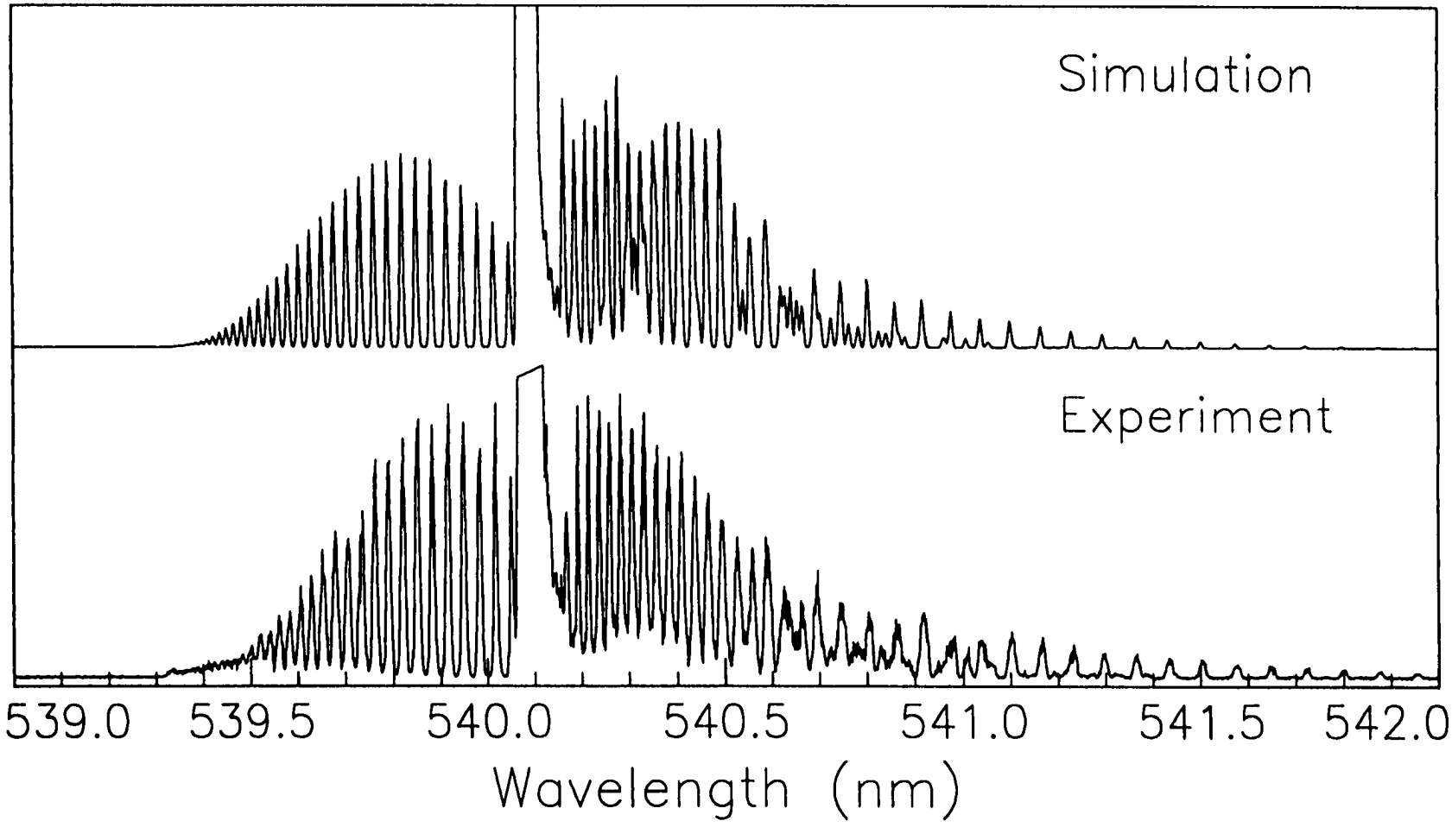

Figure 5.7 The experimental $Re^{14}N$ 540nm band and a simulation based on our deperturbation analysis. In the simulation both *e* and *f* levels are assumed to be perturbed in an identical fashion. Any $^{185}Re^{14}N$-$^{187}Re^{14}N$ isotopic splitting is assumed negligible.

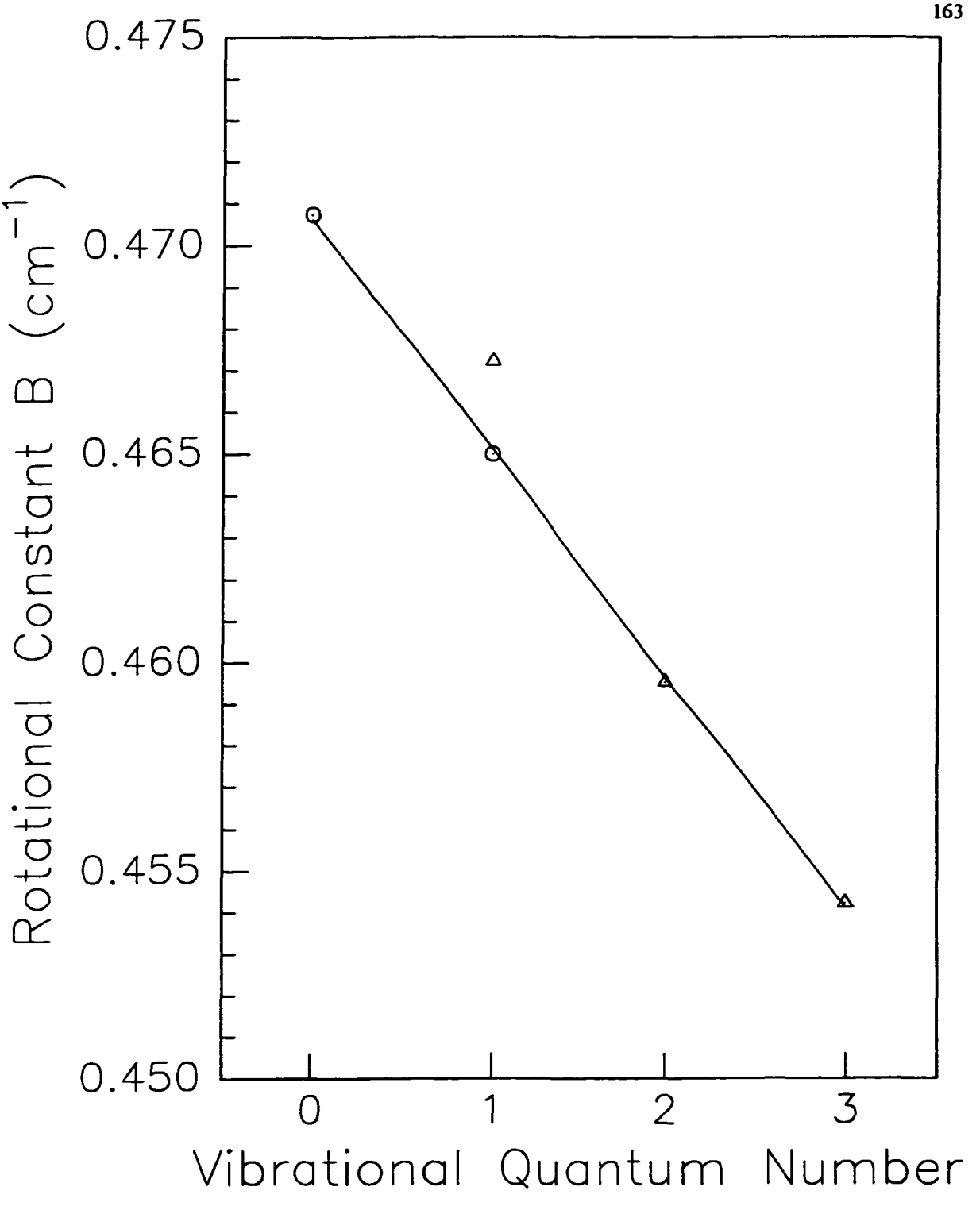

Figure 5.8 Rotational constants of the vibrational levels of the [18.5]1 state. Open circles represent values obtained from our deperturbation analysis whereas the open triangles are those from our previous rotational analysis.

experimental value of B(v=1) clearly deviates from the linear relationship established by B(v=0), B(v=2), and B(v=3), even though the deviation is not very large. The obvious conclusion is that the [18.5]1 v=1 vibronic state also suffers perturbations.

The spectrum of the [18.5]1-X0+ (1-0) band was then re-examined to locate the possible perturbing dark state. The emission from the dark state was separated from that of the bright state by using narrow entrance and exit slits in the monochromator which serves as a band-pass-filter before the PMT to selectively detect LIF to different lower states, and using very strong excitation (probe) laser radiation to enhance the weak signal. The results are shown in Figure 5.9. The spectrum in Figure 5.9(a) was recorded with slits removed from the monochromator. The P branch at high J region shows the possible existence of a perturbing state. The spectrum in Figure 5.9(b) was recorded with a pair of 0.5 mm slits in the monochromator which was parked at the wavelength corresponding to the strong transition from the bright state to the ground state. It is essentially free of any contribution from the dark state. The spectrum in Figure 5.9(c) was recorded with the 0.5mm slits but with the monochromator parked at a wavelength corresponding to the strongest transition from the dark state to a low lying electronic state. The excitation laser was intensified by an amplifier to obtain a stronger signal.

Several features are worth mentioning in the spectrum in Figure 5.9(c). First, all P, Q, and R branches can be identified in the spectrum, confirming the Ω=2 assignment of the dark state. Secondly, spectral lines from the high J rotational levels of the bright state are present in the spectrum, indicating stronger couplings between the two states at higher rotational levels. This is consistent with the proposed heterogeneous coupling scheme. Thirdly, isotopic shifts due to naturally occurring ^{185}ReN and ^{187}ReN molecules are clear

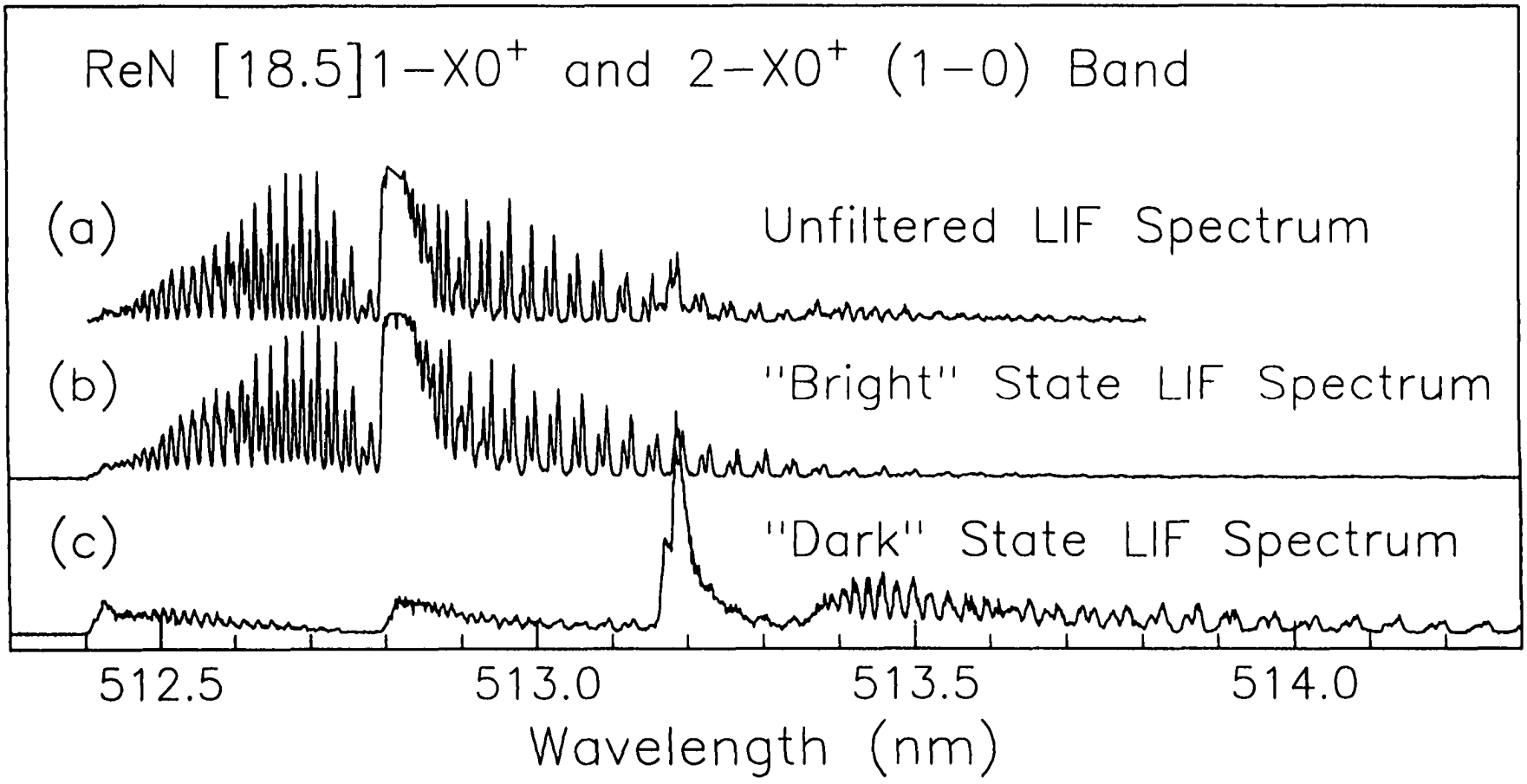

Figure 5.9 LIF spectra associated with the [18.5]1-X0' and [18.5]2-X0' systems. In (a) the LIF spectrum was recorded with emissions to all lower states whereas in (b) and (c) the emission to different lower states was monitored to separate the LIF spectra associated with the "bright" and the "dark" states.

both in the P branch lines and the R band head of the dark transition. The magnitude of the shifts is comparable with that seen for the bright transition as shown in Figure 5.9(b). This observation indicates that a vibrational quantum number v=1 can be assigned to this dark vibronic state and suggests that the previous dark vibronic state associated with the [18.5]1-X0$^+$ (0-0) band should have a vibrational quantum number v=0. Indeed there is no detectable isotopic shift in Figure 5.7, the logical result of the vibrational assignment of the dark state.

A deperturbation of the two (1-0) bands was carried out in the same way as for the two (0-0) bands. The resulting spectroscopic constants are also included in Table 5.5. It is satisfying to note that the deperturbed rotational parameter B(v=1) is consistent with the relationship established by the other three B's (Figure 5.8).

The (2-0) band of the [18.5]1-X0$^+$ system appears unperturbed. However the v=2 dark vibronic state can still be located about 32 cm^{-1} lower than the bright vibronic state (Figure 5.10). No deperturbation analysis was performed on these two vibronic states for two reasons: 1) the dark state was too weak to allow for a rotational assignment; 2) because of the large energy difference between the two states, the low J rotational energy levels of the bright state were not significantly perturbed (H_{12} is a monotonically increasing function of J). The B value for the bright vibronic state determined from the low J spectra lines was not severely affected by the perturbation.

In order to confirm further the proposed J-dependent heterogeneous coupling we made measurements of the excited state lifetimes in the v=0, v=1, v=2, and v=3 vibrational levels of the bright Ω=1 state. The lifetimes, as a function of rotational quantum number J, are graphed in Figure 5.11. For the v=0 vibronic state the lifetimes depend significantly on

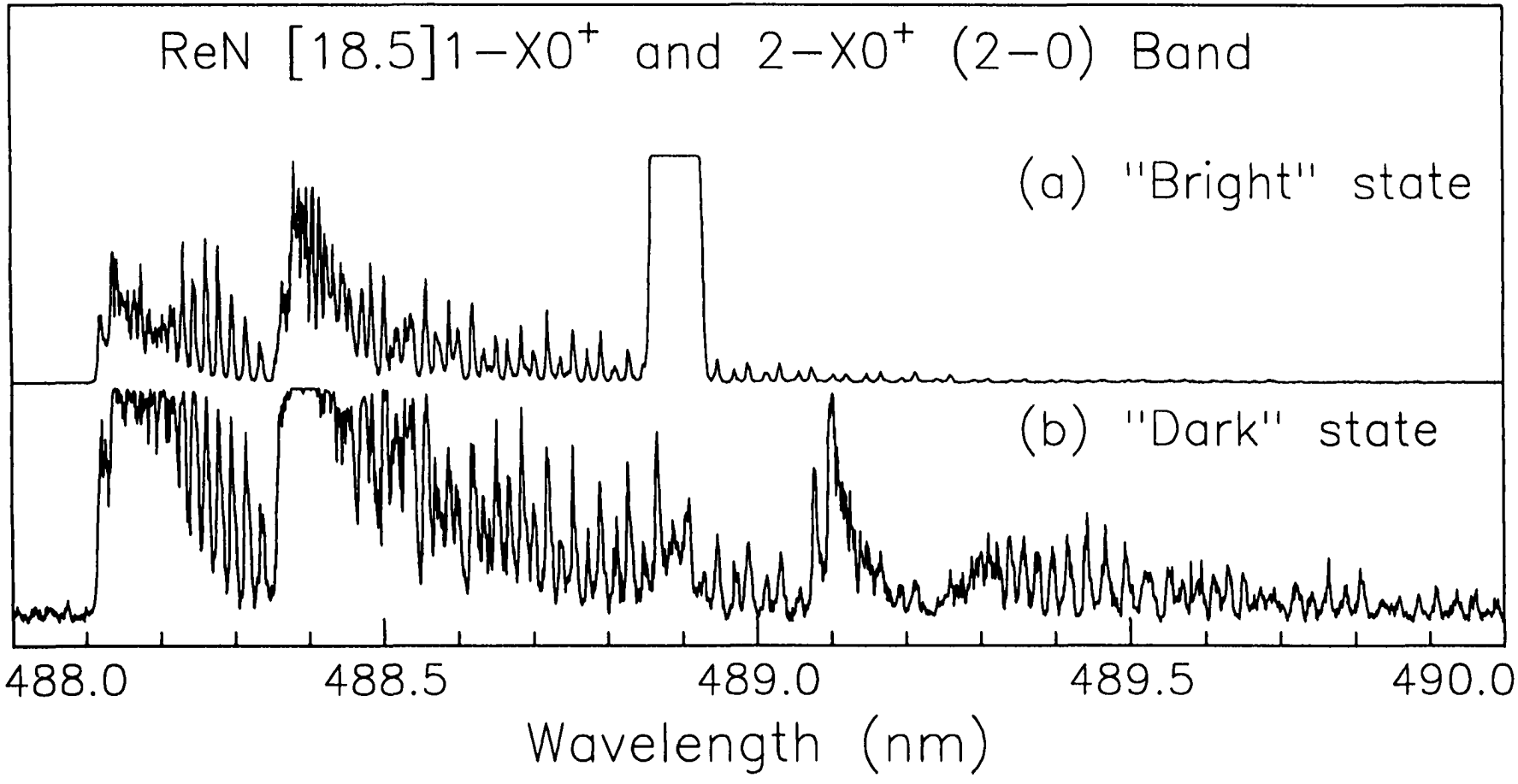

Figure 5.10 LIF spectra associated with the [18.5]1-X0' and [18.5]2-X0' systems. In (a) the LIF spectrum was recorded with emissions to all lower states. The strong peak at 488.9nm is a Re atomic line. No trace of the dark state can be identified in this spectrum. The spectrum in (b) was recorded by monitoring emissions from the dark state.

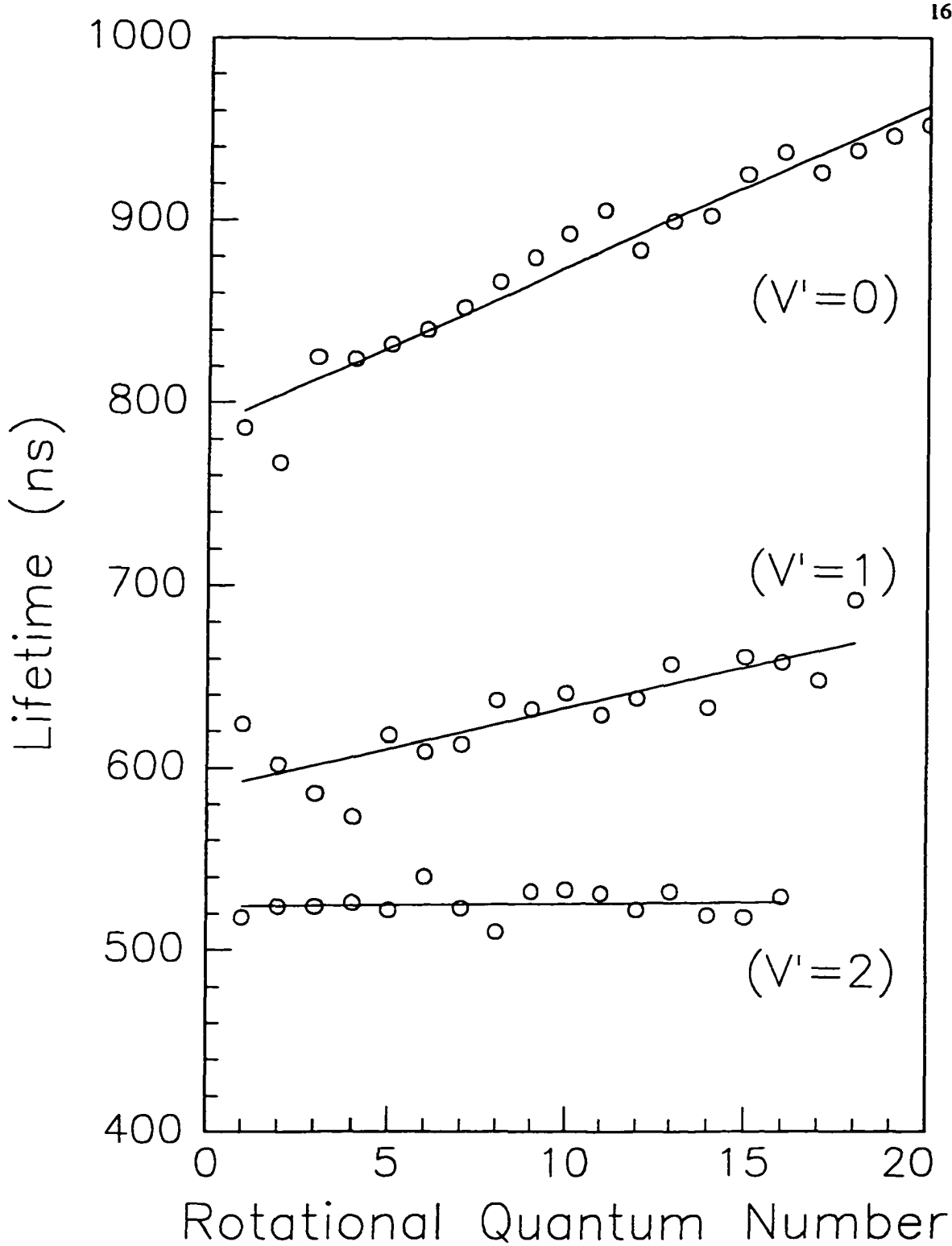

Figure 5.11 Lifetimes of the [18.5]1 state as a function of vibrational and rotational quantum numbers.

the rotational quantum number J, indicating an increasing mixture of the bright and the dark vibronic states, as expected from a heterogeneous coupling. For the v=1 vibronic state the J dependence of the lifetimes is less significant than for the v=0 state. This is the result of the larger energy spacing between the two v=1 vibronic states and the weaker coupling matrix elements between them. For the v=2 state the dependence can hardly be seen.

An important feature of Figure 5.11 is that the lifetimes at low rotational energy levels where the influence of the heterogeneous coupling is very small are also dependent on the vibrational quantum number v. This can only be explained by strong and complicated homogeneous interactions with other states.

The dispersed fluorescence (DF) spectra originating from different excited vibronic states are shown in Figures 5.12-5.17. Table 5.6 lists all the energies of the observed low lying vibronic states. Since all excited electronic states and the ground state have very similar vibrational constants and internuclear distances, emissions with $\Delta v=v'-v''=0$ are expected to be significantly stronger than others. The emission spectrum from the $v'=0$ vibronic state of the [18.5]1-X0$^+$ system in Figure 5.12 meets this expectation that emission to the $v''=0$ vibrational state of the ground electronic state is the strongest. The spectrum from the $v'=1$ state shows an intensity maximum for emission to the $v''=0$ state The spectrum from the $v'=2$ state shows a familiar oscillating intensity pattern, but the $v'=2$ - $v''=2$ transition belongs to the weak category. For emission from the $v'=3$ state it may be noted that the $v'=3$ - $v''=3$ emission, expected to be the strongest, is entirely absent.

The last piece of evidence for the existence of complicated homogeneous

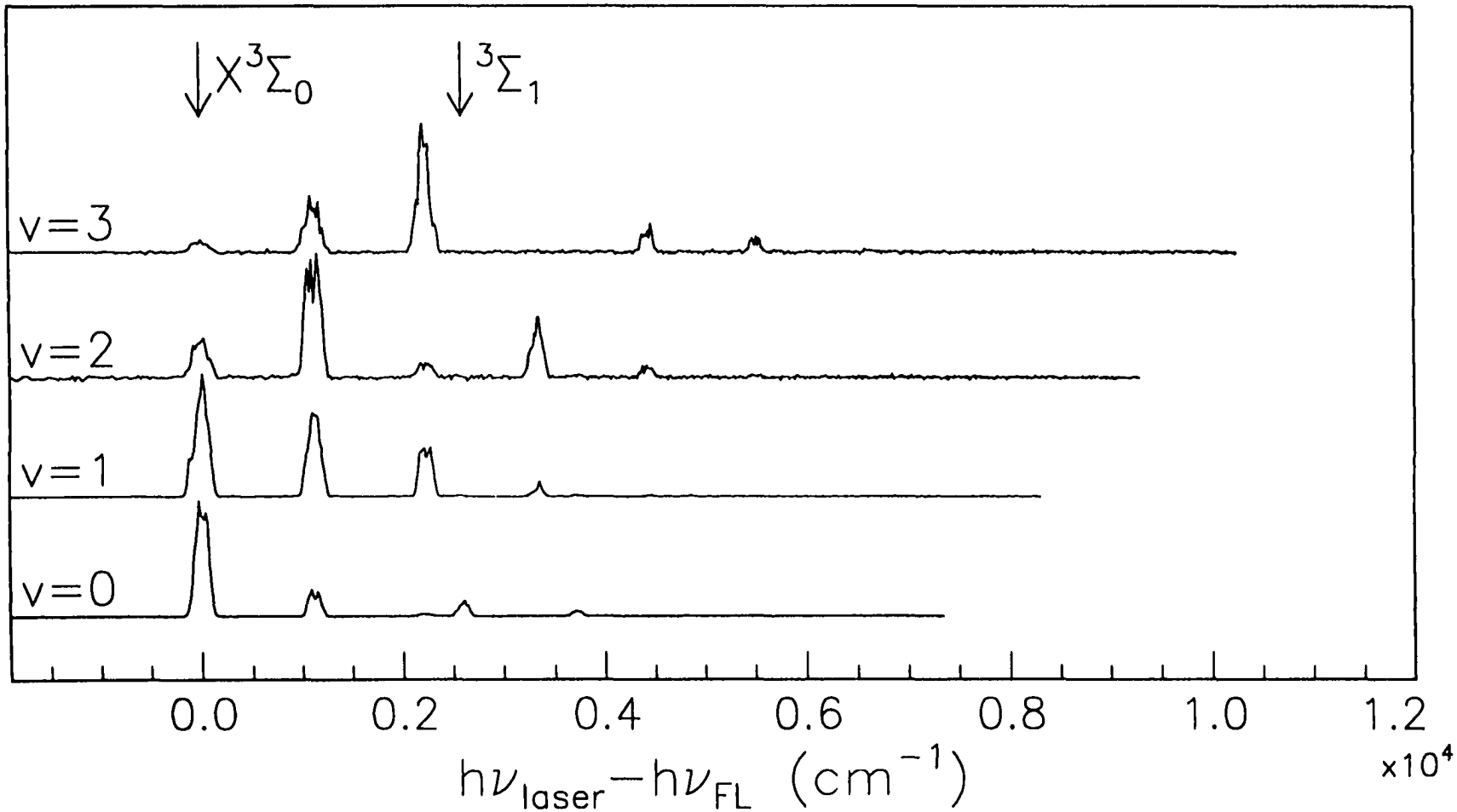

Figure 5.12 Dispersed fluorescence spectra of ReN, following the excitation to the [18.5]1 state. Line positions corresponding to transitions to v″=0 lower vibronic states are marked with arrows and the corresponding designation gives assignments of the states.

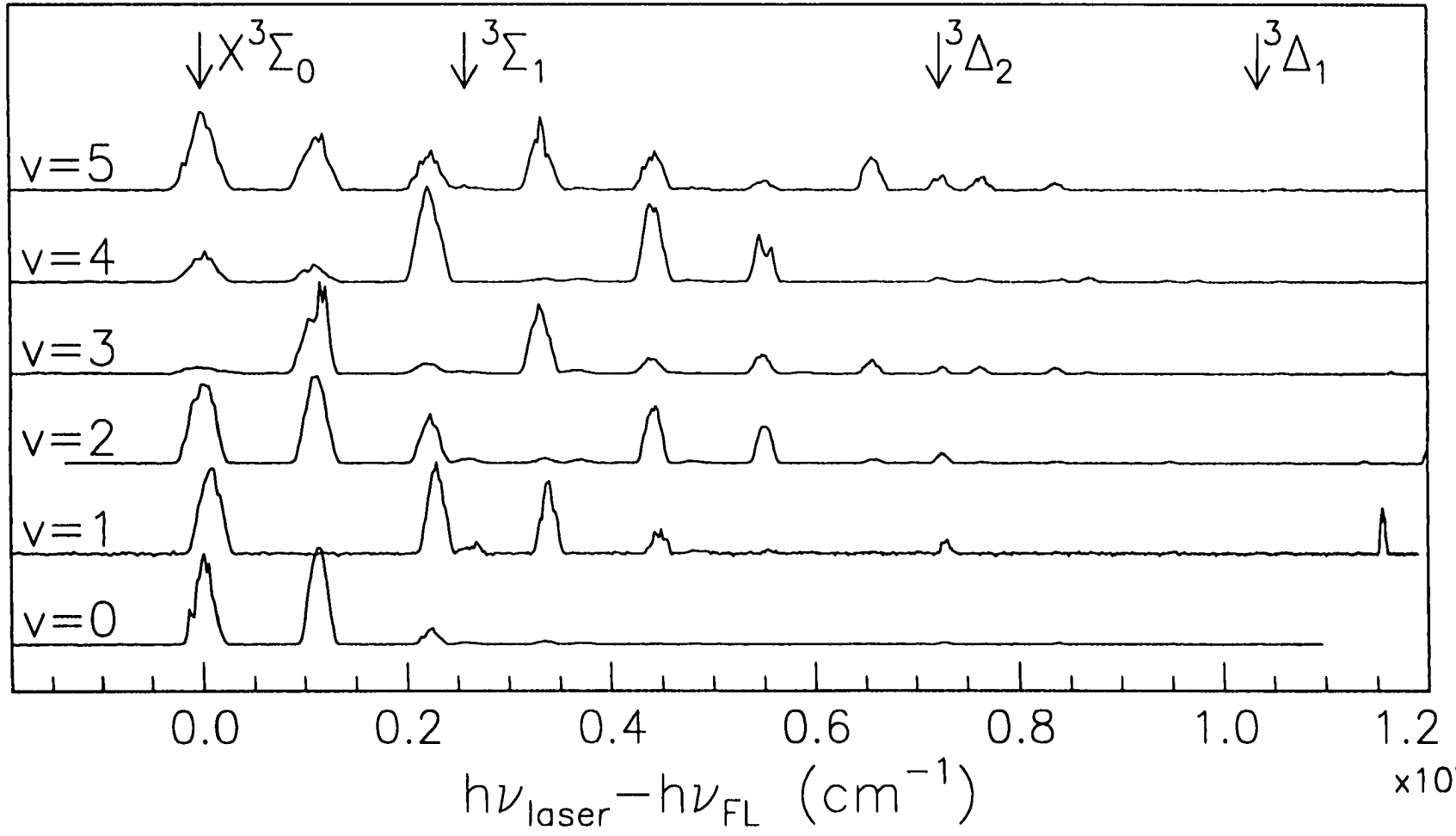

Figure 5.13 Dispersed fluorescence spectra of ReN, following the excitation to the [22.2]1 state. Line positions corresponding to transitions to v″=0 lower vibronic states are marked with arrows and the corresponding designation gives assignments of the states.

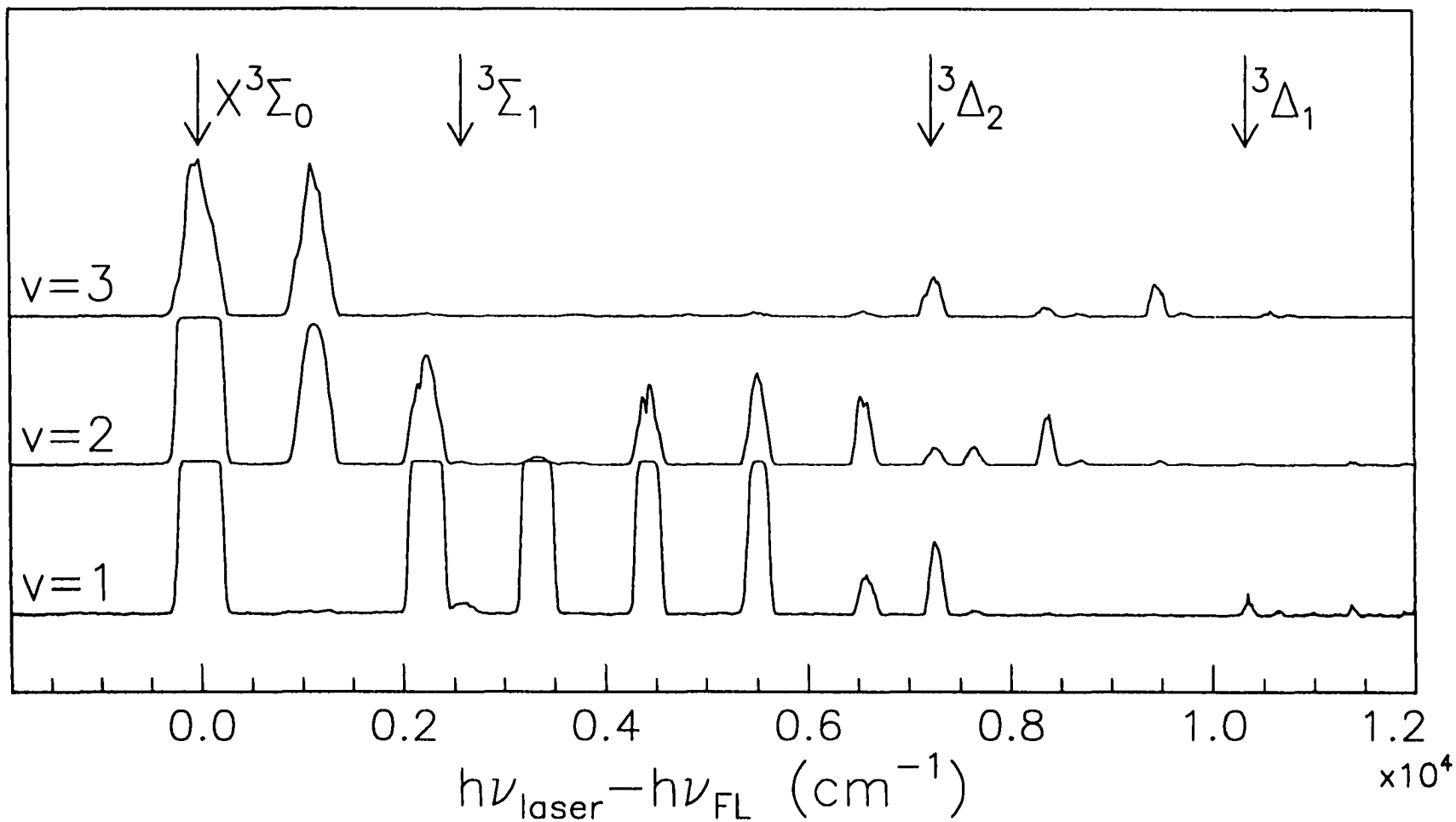

Figure 5.14 Dispersed fluorescence spectra of ReN, following the excitation to the [23.8]1 state. Line positions corresponding to transitions to v″=0 lower vibronic states are marked with arrows and the corresponding designation gives assignments of the states.

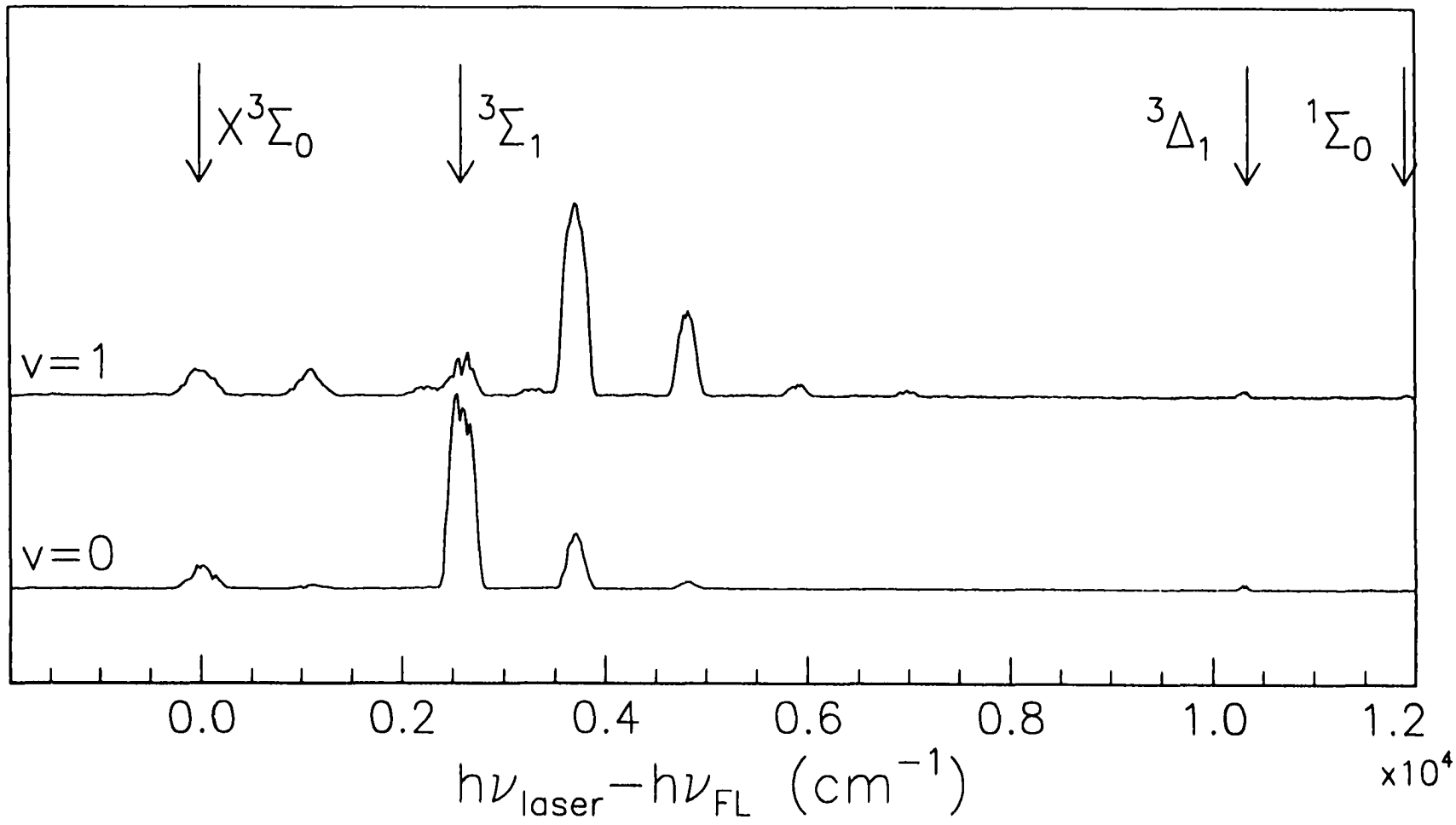

Figure 5.15 Dispersed fluorescence spectra of ReN, following the excitation to the [24.7]0' state. Line positions corresponding to transitions to v''=0 lower vibronic states are marked with arrows and the corresponding designation gives assignments of the states.

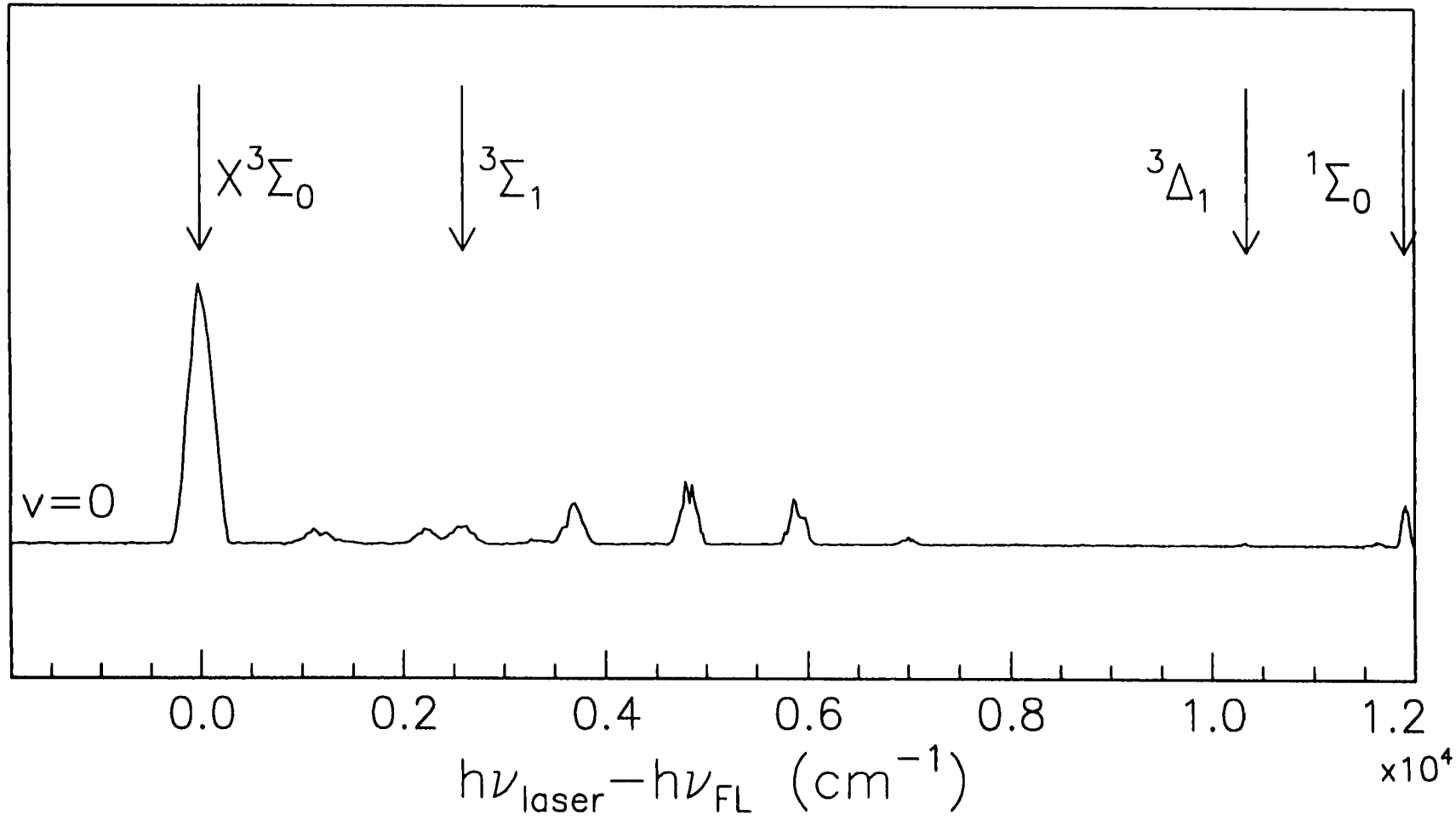

Figure 5.16 Dispersed fluorescence spectra of ReN, following the excitation to the [26.0]0' state. Line positions corresponding to transitions to v″=0 lower vibronic states are marked with arrows and the corresponding designation gives assignments of the states.

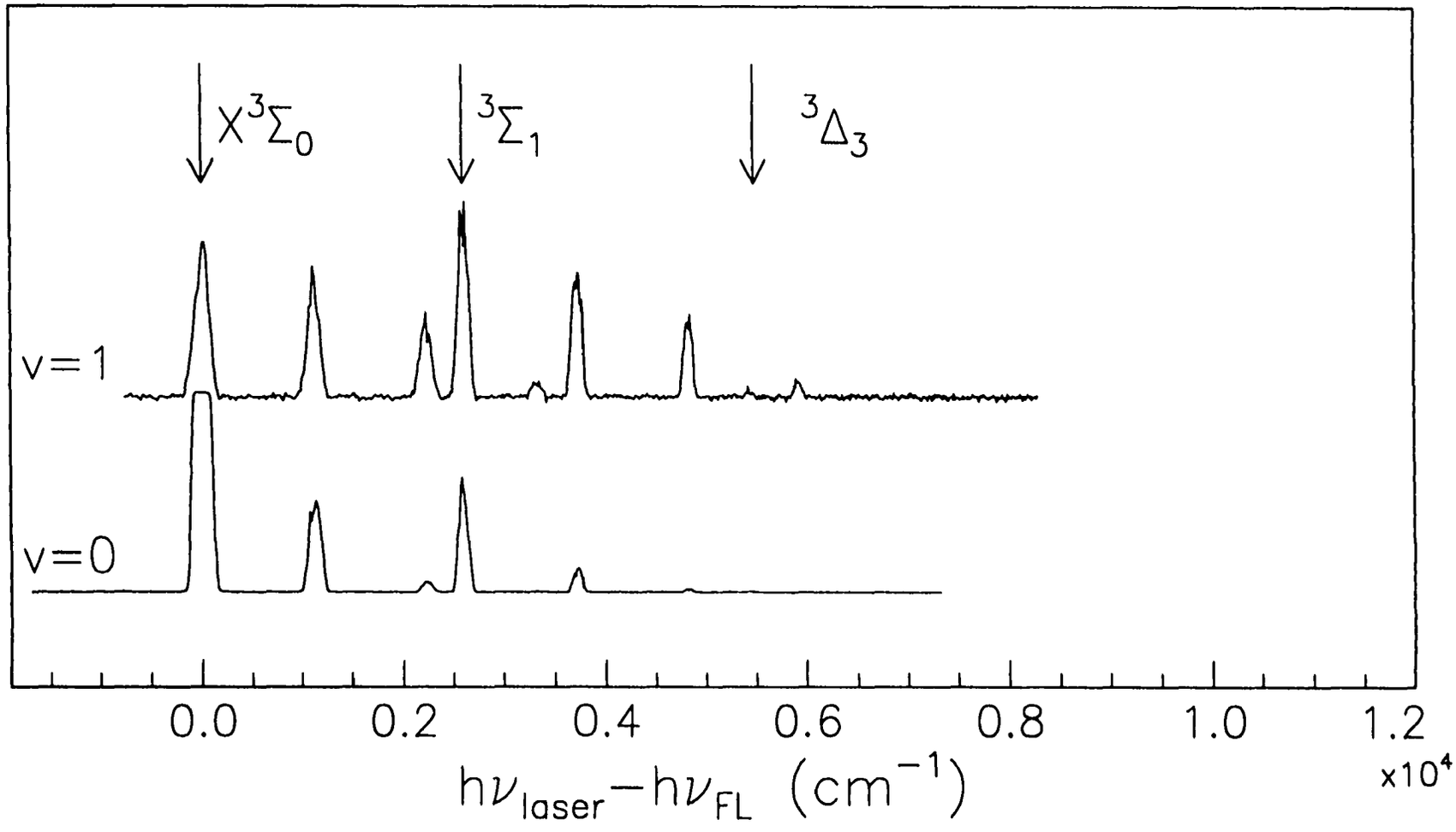

Figure 5.17 Dispersed fluorescence spectra of ReN, following the excitation to the [18.5]2 state. Line positions corresponding to transitions to v″=0 lower vibronic states are marked with arrows and the corresponding designation gives assignments of the states.

Table 5.6 Summary of all observed low-lying vibronic states of $^{187}Re^{14}N$ from dispersed fluorescence spectra. Uncertainties for T are $\pm 50 cm^{-1}$.

Electronic State	Vibrational Quantum Number v	T (cm^{-1})
$X^3\Sigma^-_{0^+}$	0	0
	1	1112[i]
	2	2230
	3	3356
	4	4424
	5	5506
	6	6591
	7	7654
	8	8687
$^3\Sigma^-_{0^+}$	0	2609
	1	3711
	2	4820
	3	5904
	4	6977
$^3\Delta_3$	0	5440
$^3\Delta_2$	0	7265
	1	8378
	2	9480
	3	10632
	4	11658
$^3\Delta_1$	0	10363
	1	11384
$^1\Sigma^+_{0^+}$	0	11907

i. This term was determined to be T=1121.5192(15) cm^{-1} in the Fourier transform experiment (See Table 5.1)

perturbations, in addition to the heterogeneous perturbations, comes from a comparison of the $Re^{14}N$ and $Re^{15}N$ spectra of the [18.5]1-X0$^+$ (0-0) band at 540nm. Clearly the two isotopic spectra differ much more than is to be anticipated from simply a difference in reduced masses. In the $Re^{14}N$ spectrum because of the nearby Ω=2 dark state (about 4cm^{-1} lower) the upper Ω=1 bright state is strongly perturbed. The corresponding $Re^{15}N$ spectrum, however, is not significantly perturbed and is very similar to the spectrum of the $Re^{14}N$ (2-0) band at 488nm (Figure 5.10). This is due to the relatively large bright-dark state energy difference (about 38cm^{-1} for 488nm band). On the other hand, the shift of the two v=0 vibronic states, upon isotopic replacement, can be estimated in the harmonic approximation using numbers from Table 5.5:

$$\begin{aligned}\Delta\nu &= \tfrac{1}{2}(1-\rho)\left(\Delta G_{1/2}(\text{bright}) - \Delta G_{1/2}(\text{dark})\right) \\ &\approx 0.27\ \text{cm}^{-1}\end{aligned} \qquad (5.5)$$

where $\Delta G_{1/2}$ is the energy gap between the v=0 and v=1 vibrational levels of the corresponding electronic state. The value calculated from (5.5) is too small to have any effective impact on the perturbation pattern. Since the energy of the bright vibronic state changes more or less as expected, as evidenced by the little-changed band positions in Figure 5.6, it is the dark vibronic state that has moved at least several tens of wavenumbers more than it should. The implication is that the dark state also suffers perturbations from another electronic state, and that probably vibrational quantum numbers larger than zero are involved.

5.4 The Low Lying Electronic States

Figure 5.18 displays the connectivity between the upper and the lower electronic states deduced from the DF spectra (Figure 5.12-5.17). It also provides a summary of all observed electronic states for the molecule ReN. The states lying higher than 15000cm^{-1} were probed by LIF excitation spectra (Table 5.3 and Figure 5.3), while others were recognized from the DF spectra (Table 5.6 and Figures 5.12-5.17). Since no rotational assignments for the DF spectra can be made, the Ω values of the low lying electronic states had to be deduced from other considerations, for example, by examining the connections between the low lying electronic states and other states with well-determined Ω values.

The ground state has been established to have Ω=0. The first excited state at T=2600 cm^{-1} is connected to upper states with Ω=0, 1, and 2. Following the general selection rule for electric dipole allowed transitions ΔΩ=0 and ±1, we deduce this state must have Ω=1. The second excited state at T=5450cm^{-1} is connected very weakly only to the dark Ω=2 state. We infer its Ω value must be 3

According to the MO diagram in Figure 5.2, the ground and the first excited states may be assigned as the $\Omega = 0^+$ and the Ω=1 components, respectively, of a $^3\Sigma^-$ electronic state. The separation of these two components arises mainly because of the second order spin-orbit interaction between the $^3\Sigma_0^-$ and $^1\Sigma_0^+$ electronic states. Both of these Σ states are from the same electron configuration $\delta_n^2\sigma_n^2$. Using the wavefunctions listed in Table 2.1 and the procedure outlined in section 2.3, we obtained the wavefunctions of, and the coupling matrix element between, these two components as:

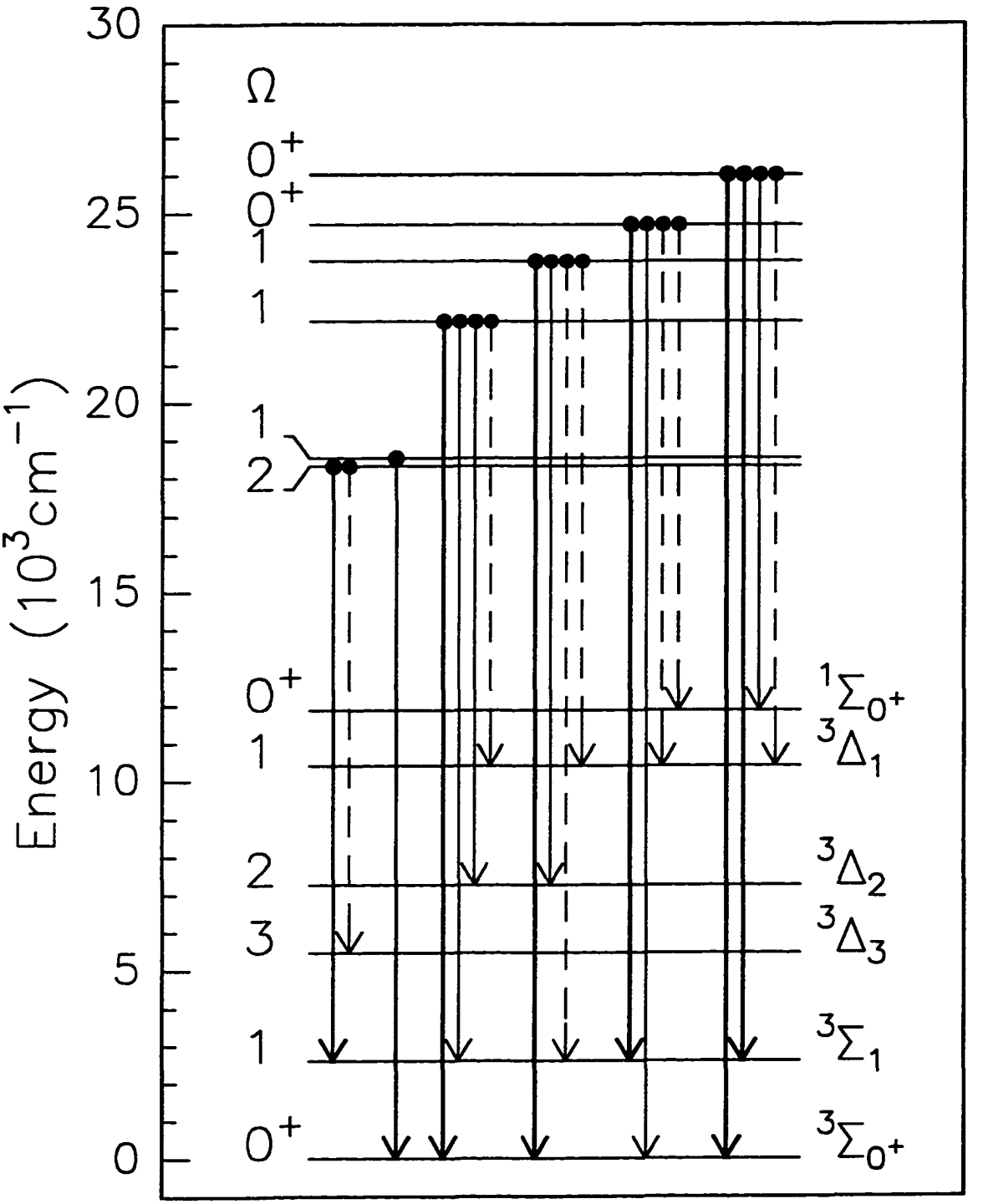

Figure 5.18 Observed emissions and electronic states of ReN. Refer to the text for the assignment of these states. Thick lines indicate strong emissions, thin lines represent weak emissions, and dashed lines stand for very weak emissions.

$$<^3\Sigma_0^-|\hat{H}^{so}|^1\Sigma_0^+> = 2a_\delta$$
$$= 2\xi_{5d}(\mathrm{Re}) \qquad (5.6)$$
$$= 5090\ \mathrm{cm}^{-1}$$

where $\xi_{5d}(\mathrm{Re}) = 2545\ \mathrm{cm}^{-1}$ is the atomic spin-orbit parameter [60]. The position of the $^1\Sigma_0^+$ including the interaction with the $^3\Sigma^-$ can be obtained, using (2.157)-(2.158), at

$$T(^1\Sigma_0^+) = \frac{|<^3\Sigma_0^-|\hat{H}^{so}|^1\Sigma_0^+>|^2 + T^2(^3\Sigma_1^-)}{T(^3\Sigma_1^-)} \qquad (5.7)$$
$$= 12480 \pm 275\ \mathrm{cm}^{-1}$$

The observed state at $11870\mathrm{cm}^{-1}$ is very close to this calculated position, and therefore is assigned to be the $^1\Sigma_0^+$ state.

The difference between the calculated position of the $^1\Sigma_0^+$ state and the experimentally observed $^1\Sigma_0^+$ state may come from spin-orbit interactions between the $\delta_n^2\sigma_n^2$ configuration, which has $^1\Sigma^+$ and $^3\Sigma^-$ states, and the $\delta_n^2\sigma_n^1\pi_a^1$ configuration, which has $^1\Pi, ^3\Pi$, and $^5\Pi$ states. The individual coupling matrix element between states from these two configurations is proportional to a constant parameter

$$a_{\pi\sigma} = <\pi_a|\hat{a}\hat{l}^+|\sigma_n> \qquad (5.8)$$

where $\hat{l}^+$ is the raising operator, defined in (2.45), for single electron orbital angular momentum l. The operator â is defined in (2.164). For instance, the following matrix elements are deduced

$$<^5\Pi_1|\hat{H}^{so}|^3\Sigma_1^-> = \sqrt{\frac{1}{24}}a_{\pi\sigma} \qquad (5.9)$$

and

$$<^3\Pi_0(1)|\hat{H}^{so}|^1\Sigma_0^+> = a_{\pi\sigma} \tag{5.10}$$

where $^3\Pi_0(1)$ corresponds to the first triplet spin eigenfunction for four electrons in Table 2.1. If half of both the σ and π orbitals originate from the atomic d orbitals, the constant parameter, $a_{\pi\sigma}$, can be related to the atomic spin-orbital parameter $\xi_{5d}(Re)$:

$$\begin{aligned} <\pi_a|\hat{al}^+|\sigma_n> &= \tfrac{1}{2}<d_1|\hat{al}^+|d_0> \\ &= \tfrac{1}{2}\sqrt{2\cdot(2+1)-1\cdot 0}<d|\hat{al}^+|d> \\ &= \sqrt{\tfrac{3}{2}}\xi_{5d}(Re) \\ &= 3117\,cm^{-1} \end{aligned} \tag{5.11}$$

Then a $^3\Pi_0(1)$ state 10000cm^{-1} higher than the $^1\Sigma_0^+$ state can push the latter down about 900cm^{-1}.

A more reasonable assumption about the σ_n orbital, based on the *ab initio* calculations on other metal-ligand diatomic systems, is that the σ_n orbital is mainly from the atomic 6s orbital. Meanwhile the 6p atomic orbital may contribute significantly to the π_a orbital to dilute the 5d contamination in the molecular orbital. In this case the magnitude of the constant parameter, $a_{\pi\sigma}$, is negligible. If we let $a_{\pi\sigma}$=0, the off-diagonal spin-orbit matrix element between $^1\Sigma_0^+$ and $^3\Sigma_0^-$ can be calculated as

$$\begin{aligned} <^3\Sigma_0^-|\hat{H}^{so}|^1\Sigma_0^+> &= \sqrt{T(^3\Sigma_0^-)\cdot T(^1\Sigma_0^+) - T^2(^1\Sigma_0^+)} \\ &= 4930\pm 150\,cm^{-1} \end{aligned} \tag{5.12}$$

which is not far from the value in (5.6).

We now turn to the second excited state at T=5450cm^{-1} which has been assigned a Ω value of 3. The only reasonable explanation for this state is the lowest component of the expected $\delta^3\sigma^1$ $^3\Delta_i(\delta_n^3\sigma_n^1)$ electronic state. From the discussion in Chapter 4 on FeC, the energy spacing between the Ω=1 and Ω=3 components of the $^3\Delta_i$ state should be

$2a_\delta = 2\xi_{5d}(Re) = 5090\ cm^{-1}$. The state at T=10350cm^{-1} is very close to this predicted position and has connections to both Ω=1 and Ω=0 highly excited states, therefore it is assigned to be the Ω=1 component of the $^3\Delta_1$ electronic state. The state at T=7250cm^{-1} lying between the Ω=1 and the Ω=3 components of the $^3\Delta_1$ state, is taken to be the Ω=2 component of the $^3\Delta_1$ state. This assignment is confirmed by the fact that no emission was detected between this state and other higher Ω=0 states (Figure 5.18). The value of a_δ determined from the $^3\Delta_3$ and $^3\Delta_1$ states

$$a_\delta = \frac{T(^3\Delta_1) - T(^3\Delta_3)}{2} = 2445 \pm 100\ cm^{-1} \qquad (5.13)$$

is very close to the value determined from the $^3\Sigma_0^-$ and $^1\Sigma_0^+$ states:

$$a_\delta = \frac{1}{2}\langle ^3\Sigma_0^- | H^{so} | ^1\Sigma_0^+ \rangle = 2465 \pm 75\ cm^{-1} \qquad (5.14)$$

Without interactions with other configurations the states at 5450cm^{-1} and 10340cm^{-1} are, respectively, the pure Ω=3 and Ω=1 components of the $^3\Delta_1$ state:

$$|[5.4]3\rangle = |^3\Delta_3\rangle \qquad (5.15)$$

$$|[10.3]1\rangle = |^3\Delta_1\rangle \qquad (5.16)$$

The position of the state at T=7260cm^{-1}, which is assumed to be the $^3\Delta_2$, deviates from the middle point of the $^3\Delta_1$ and $^3\Delta_3$ states by ΔE=635cm^{-1} as a result of the spin-orbit interaction between $^3\Delta_2$ and $^1\Delta_2$. Since the coupling matrix element is the same as a_δ from (4.15), the position of the $^1\Delta_2$ state can be estimated to be:

$$T(^1\Delta_2) = T(^3\Delta_2) + \frac{a_\delta^2 + \Delta E^2}{\Delta E} \qquad (5.17)$$
$$= 17390\ cm^{-1}$$

This is very close to the location of the observed dark state perturbing the bright [18.5]1 state. The perturbing dark state may therefore be assigned to $^1\Delta_2$.

5.5 Conclusions

Detailed LIF studies have been carried out on ReN. Rotational analysis of the ReN LIF excitation spectrum revealed a strongly perturbed excited vibronic state at ~18510 cm^{-1} ([18.5]1 v=0). Deperturbation analyses of the [18.5]1-X0$^+$ (0-0) band at 540nm revealed that heterogeneous interactions (J_a-uncoupling) are responsible for the perturbations. The perturbing state is a "dark" state with Ω=2 (the [18.5]2 state). The energies of the v=0, v=1, and v=2 vibrational levels of the dark state have been determined. The "bright" excited state lifetimes exhibit a large variation with rotational and vibrational quanta. This is consistent with the heterogeneous interaction mechanism. It also indicates the existence of additional homogeneous perturbations.

Many low-lying vibronic states were observed in the dispersed fluorescence spectra of ReN. Analyses of these vibronic states determined that the electronic symmetries of these states are, in Hund's case (a) notation, $^3\Sigma_1^-$, $^3\Delta_3$, $^3\Delta_2$, $^3\Delta_1$, and $^1\Sigma_0^+$, respectively, based on their energies and their connections with other high-lying electronic states. The spin-orbit constant of the non-bonding molecular orbital δ_n has been calculated to be 2455±50cm^{-1}. From our analysis, it is suggested that the dark perturbing [18.5]2 state is the $^1\Delta_2$ state with an electron configuration of $\delta_n^3\sigma_n^1$.

Chapter 6

Other Published Work

The work described in Chapters 1 through 5 of this thesis represents only a part of the research carried out by the author during his graduate studies at the University of Victoria. Additional work has already been completed and published. There is no necessity to repeat here the description of this additional research in detail. However, a summary, in the form of the publication abstracts, is given below.

The work can be classified into two categories: i) nonadiabatic photodissociation dynamics, including papers on the photodissociation of BrCl, of Cl_2, of BrNO, and of ClNO; ii) molecular spectroscopic studies, including papers on the laser spectroscopy of C_3, of ReN, and of FeC. This thesis is based on laser spectroscopy, focusing on unpublished recent results.

1. Vibrational Modification of the Spatial Anisotropy Parameter in Photodissociation. A Classical Trajectory Study

Hans-Peter Loock, Jianying Cao, and Charles X. W. Qian

Chem. Phys. Lett. **206** (1993) 422-428

Classical trajectory calculations have been performed to explore the vibrational influence on the spatial anisotropy parameter β in triatomic molecular photodissociation. Our calculations indicate that in a fast dissociation, accompanied by a large angular momentum excitation of the diatomic fragment, the recoil direction can change as much as 20° thereby resulting in a measurable modification of β.

2. Non-adiabatic Photodissociation Dynamics of BrCl

Jianying Cao, Hans-Peter Loock, and Charles X. W. Qian

Can. J. Chem. **72** (1994) 758-761

Nozzle-cooled BrCl was excited with tunable laser radiation at selected wavelengths between 389 and 500nm. The chlorine atomic fragments in their $Cl^*(^2P_{1/2})$ and $Cl(^2P_{3/2})$ state were state-selectively probed by resonance-enhanced multiphoton ionization. The branching ratio ($Cl^*/(Cl+Cl^*)$) was measured as a function of the excitation wavelength. The relative Cl^* yield reaches a maximum at around λ_{phot}=460nm. Decomposition of these branching ratios into Cl and Cl^* photofragment-yield-spectra provides insight into the BrCl B-state $^3\Pi(0^+)$ non-adiabatic dissociation dynamics. Our results suggest that the dissociation mechanism involves non-adiabatic transitions among 0^+ potential energy curves.

3. The Nonadiabatic Photodissociation of BrNO at 355nm

Jianying Cao, Hans-Peter Loock, and Charles X. W. Qian

J. Chem. Phys. **101** (1994) 3395-3398

Nozzle cooled BrNO molecules were dissociated with a polarized laser at 355nm. The NO fragments were then state-selectively probed using a second tunable laser. Resonance-enhanced multiphoton ionization and fragment time-of-flight techniques were combined to obtain scalar and vector properties of the NO fragment. For each of the NO states probed, the Br^*/Br ratio was determined. From these data, a comprehensive picture of the dissociation process was obtained. The excitation at 355nm has a transition dipole moment parallel to the Br-N bond ($\beta \approx 2.0$). The NO fragment was observed with high rotational excitation ($J \approx 50$) and nonstatistical spin-orbit and Λ-doublet state distributions.

4. Laser-induced Fluorescence Spectroscopy of the $\tilde{A}^1\Pi_u - \tilde{X}^1\Sigma_g^+$ Transition in Jet-Cooled C_3

Walter J. Balfour, Jianying Cao, C. V. V. Prasad, and Charles X. W. Qian

J. Chem. Phys. **102** (1994) 10343-10349

C_3 radicals have been produced in a plasma of rhenium with methane doped in helium and cooled in a supersonic free jet expansion. More than 50 vibronic bands in the laser induced fluorescence spectrum of the $\tilde{A}^1\Pi_u - \tilde{X}^1\Sigma_g^+$ electronic transition have been recorded in the region 370-415nm at 0.4cm^{-1} resolution. The observations include bands identified by Gausset *et al.* (1965) and many bands not previously characterized. Rotational analyses have been made for a majority of the bands and the number of located Renner-Teller levels of the $\tilde{A}$ state has been considerably extended. The (002) level is tentatively identified. A comparison of the experimentally determined energy level pattern in the $\tilde{A}$ state with theoretical predictions has suggested a number of revisions to previous assignments and evidence is presented to contradict suggestions from earlier work that the (020) level of the $\tilde{A}$ state is perturbed.

5. Laser and Fourier Transform Spectroscopy of the [23.8]1-X0$^+$ System of ReN

R. S. Ram, P. F. Bernath, W. J. Balfour, J. Cao, C. X. W. Qian, and S. J. Rixon

J. Mol. Spectrosc. **168** (1994) 350-362

The emission spectrum of ReN has been observed in the 400-476nm spectral region using a Fourier transform spectrometer. The bands were excited in a rhenium cathode lamp in the presence of a trace of N_2. The observed bands, with the 0-0 band at 23746.42 cm^{-1}, have been assigned as the [23.8]1-X0$^+$ electronic transition. A rotational analysis of the 0-1, 0-0, and 1-0 bands for both ^{187}ReN and ^{185}ReN isotopomers has been performed. The principal ground state equilibrium molecular constants for ^{187}ReN obtained from this analysis are $B_e''=0.482414(11)cm^{-1}$, $r_e''=1.63780(2)\,\mathring{A}$, while the corresponding excited state values are $B_e'=0.441093(13)cm^{-1}$, $r_e'=1.71280(3)\,\mathring{A}$. The 0-0 band was also observed by pulsed dye laser excitation spectroscopy using a free jet expansion source. In this experiment, the ReN was made by laser vaporization of a rhenium rod followed by reaction with NH_3. The excited [23.8]1 state has a fluorescence lifetime of 201±1 nsec. There are no previously reported observations of the ReN molecule.

6. Atomic Photofragment v-j Correlation: Dissociation of Cl_2 at 355nm

Yifei Wang, Hans-Peter Loock, Jianying Cao, and Charles X. W. Qian

J. Chem. Phys. **102** (1995) 808-814

The photodissociation of Cl_2 at 355nm was studied by measuring the angular distribution of the chlorine fragments in their electronic ground state ($^2P_{3/2}$). Resonance-enhanced multiphoton ionization and time-of-flight (TOF) techniques were combined to obtain state-selective photofragment TOF profiles. It was observed that the shape of these photofragment TOF profiles depends sensitively on the polarizations of both the photolysis and the probe lasers. The dependence on the photolysis laser polarization reveals the angular distribution of the photofragments whereas the dependence on the probe laser polarization can be understood in terms of the atomic photofragment v-j correlation. Since the ground state Cl fragment has an electronic angular momentum greater than $\frac{1}{2}\hbar$, it can be aligned along the direction of fragment recoil. A theoretical treatment based on the adiabatic approximation is presented here to explain the observed polarization dependence of the photofragment TOF profiles.

7. Electronic Spectroscopy of Jet-cooled Iron Monocarbide. The $^3\Delta_i \leftarrow {}^3\Delta_i$ Transition near 493nm

Walter J. Balfour, Jianying Cao, C. V. V. Prasad, and Charles X. W. Qian

J. Chem. Phys. **103** (1995) 4046-4051

We report the first gas phase spectroscopic study of iron monocarbide. FeC molecules were generated in a laser vaporization molecular beam source and detected by laser induced fluorescence. Twenty-six vibronic bands have been recorded in the 430-500 nm region. Rotational analyses have been carried out for 22 of the bands. There are three lower states involved, two with $\Omega''=2$ and one with $\Omega''=3$. Based on our experimental observations and the *ab initio* calculations on RuC [Shim *et al.* J. Phys. Chem. **91** 3171 (1987)] the observed bands are interpreted as $^3\Delta_i \leftarrow {}^3\Delta_i$ and $^1\Delta \leftarrow {}^1\Delta$ transitions. The ground state electronic configuration is assigned to $1\delta^3 9\sigma^1$. Evidence for three excited electronic states (one $^3\Delta_i$ state, one $^1\Delta$ state, and another state with $\Omega'=3$) and for perturbations in several of their vibrational levels is presented.

8. Product Fine Structure State Populations and Nonadiabatic Dissociation Dynamics: $Cl^*(^2P_{1/2})/Cl\ (^2P_{3/2})$ Branching Ratio in the Visible and near Ultraviolet Photodissociation of Nitrosyl Chloride

Jianying Cao, Yifei Wang, and Charles X. W. Qian

J. Chem. Phys. **103** (1995) 9653-9660

Chlorine atoms in their ^2P_j states were observed using resonance-enhanced multiphoton ionization and time-of-flight techniques, following the photodissociation of nitrosyl chloride at preselected wavelengths (*i.e.*, 600, 562, 478, and 355 nm). The fine structure branching ratio and the spatial anisotropy parameter were determined. Combining these observations with results from previous studies, a complete picture about product fine structure state population is obtained. The observed fine structure populations are explained with the aid of a new correlation diagram in the C_s point group. The adiabatic, nonadiabatic, and diabatic dissociation dynamics involving several avoided crossings at large interfragment separations are discussed.

9. The Visible Spectrum of Rhenium Mononitride

Walter J. Balfour, Jianying Cao, Charles X. W. Qian, and Scott J. Rixon

J. Mol. Spectrosc. **183** (1997) 113-118

The rhenium mononitride radical has been produced in a molecular beam laser vaporization source and its laser-induced-fluorescence spectrum has been observed in the 375-542nm region. Sixteen new bands have been observed and rotational analyses have been carried out for 15 of these. The bands have been classified into several electronic systems based on $^{185}Re/^{187}Re$ isotopic shifts, $\Delta G(v+\frac{1}{2})$ vibrational quanta, rotational constants, and excited state lifetimes. Three further bands were previously identified as belonging to the [23.8]1-X0$^+$ system. In addition to the ReN study, an examination of the rotationally resolved spectrum of ReO has shown that its ground state has $\Omega''=\frac{5}{2}$. Electron configurations $\delta^2\sigma^2$ and $\delta^3\sigma^2$ have been proposed for the ground states of ReN and ReO, respectively. Possible electron configurations for the excited states of ReN have been identified.

References

1. M. Gerloch and E. C. Constable, *Transition Metal Chemistry - The Valence Shell in d-Block Chemistry*, (VCH Publishers, New York, 1994)

2. A. J. Merer, Annu. Rev. Phys. Chem., **40**, (1989), 407

3. N. M. White and R. F. Wing, Astrophys. J., **222,** (1978), 209

4. P. W. Merrill, A. J. Deutsch, and P. C. Keenan, Astrophys. J., **136,** (1962), 21

5. W. W. Morgan and P. C. Keenan, Annu. Rev. Astron. Astrophys., **11**, (1973), 29

6. H. L. Johnson and W. W. Morgan, Astrophys. J., **117,** (1953), 313

7. J. G. Phillips and S. P. Davis, Publ. Astron. Soc. Pacific, **99**, (1987), 839

8. R. F. Wing, J. Cohen, and J. W. Brault, Astrophys. J., **216,** (1977), 659

9. R. E. S. Clegg and D. L. Lambert, Astrophys. J., **226,** (1978), 931

10. A. J. Merer, C. M. Walmsley, and E. Churchwell, Astrophys. J., **256,** (1982), 151

11. Y. Kasai, K. Obi, Y. Ohshima, Y. Endo, and K. Kawaguchi, J. Chem. Phys.,**103**, (1995), 90

12. K. Kawaguchi, E. Kagi, T. Hirano, S. Tahano, and S. Saito, Astrophys. J., **406,** (1993), L39

13. L. M. Ziurys, A. J. Apponi, M. Guelin, and J. Cernicharo, Astrophys. J., **445,** (1995), L47

14. J. Cernicharo and M. Guelin, Astron. Astrophys., **183**, (1987), L10

15. B. E. Turner, T. C. Steimle, and W. L. Meerts, Astrophys. J., **426,** (1994), L97

16. R. S. Ram, P. F. Bernath, and S. P. Davis, J. Mol. Spectrosc., **179**, (1996), 282

17. J. Cernicharo, C. A. Gottlieb, M. Guelin, P. Thaddeus, and J. M. Vrtilek, Astrophys. J., **341,** (1989), L25

18. W. J. Balfour, J. Cao, C. V. V. Prasad, and C. X. W. Qian, J. Chem. Phys., **103**, (1995), 4046

19. B. Simard, P. A. Hackett, and W. J. Balfour, Chem. Phys. Lett. **230**, (1994), 103

20. R. Scullman and B. Thelin, Phys. Scr., **5**, (1972), 201

21. R. Scullman and B. Thelin, Phys. Scr., **3**, (1971), 19

22. J. M. Brom, W. R. M. Braham, and W. Weltner, J. Chem. Phys., **57**, (1973), 4116

23. A. Lagerqvist and R. Scullman, Ark. Fys., **32**, (1965), 479

24. B. Kaving and R. Scullman, J. Mol. Spectrosc., **32**, (1969), 475

25. A. J. Marr, M. E. Flores, and T. C. Steimle, J. Chem. Phys., **104**, (1996), 8113

26. K. Jansson and R. Scullman, J. Mol. Spectrosc., **36**, (1970), 248

27. K. Jansson, R. Scullman, and B. Yttermo, Chem. Phys. Lett., **4**, (1969), 188

28. T. C. Steimle, K. Y. Jung, and B. Z. Li, J. Chem. Phys., **103**, (1995), 1767

29. T. C. Steimle, K. Y. Jung, and B. Z. Li, J. Chem. Phys., **102**, (1995), 5937

30. O. Appelblad and R. Scullman, Phys. Scr., **7**, (1973), 65

31. O. Appelblad, R. F. Barrow, and R. Scullman, Proc. Phys. Soc., **91**, (1967), 260

32. R. Scullman and R. F. Barrow, Ark. Fys., **33**, (1966), 231

33. M. D. Morse, private communication

34. A. G. Adam and J. R. D. Peers, J. Mol. Spectrosc., **181**, (1997), 24

35. M. Barnes, A. J. Merer, and G. F. Metha, J. Chem. Phys., **103**, (1995), 8360

36. C. Zhou, private communication

37. C. M. T. Chan, H. Li, N. S. K. Sze, and A. S. C. Cheung, J. Mol. Spectrosc., **180**, (1996), 145

38. R. S. Ram, P. F. Bernath, and S. P. Davis, J. Mol. Spectrosc., **179**, (1996), 282

39. S. R. Langhoff and C. W. Bauschlicher, Ann. Rev. Phys. Chem., **39**, (1988), 181

40. C. E. Moore, *Atomic Energy Levels, Natl. Bur. Stand., USA, Circ. No. 467* (U.S. GPO, Washington, D.C., 1949)

41. S. P. Beaton, K. M. Evenson, T. Nelis, and J. M. Brown, J. Chem. Phys., **89**, (1988), 4446

42. A. E. Stevens, C. S. Feigerle, and W. C. Lineberger, J. Chem. Phys., **78**, (1983), 5420

43. S. R. Langhoff and C. W. Bauschlicher, J. Mol. Spectrosc., **141**, (1990), 243

44. B. Pouilly, J. Schamps, D. J. W. Lumley, and R. F. Barrow, J. Phys. B **11**, (1978), 2281

45. B. Pouilly, J. Schamps, D. J. W.Lumley, and R. F. Barrow, J. Phys. B **11**, (1978), 2286

46. C. W. Bauschlicher, Chem. Phys., **211**, (1996), 163

47. M. Bencheikh, J. Mol. Spectrosc., **183**, (1997), 419

48. S. P. Walch and C. W. Bauschlicher, J. Chem. Phys., **78**, (1983), 4587

49. P. D. Chong, S. R. Langhoff, C. W. Bauschlicher, S. P. Walch, and H. Partridge, J. Chem. Phys., **85**, (1996), 2850

50. R. S. Ram and P. F. Bernath, J. Chem. Phys., **96**, (1992), 6344

51. B. Simard, H. Niki, and P. A. Hackett, J. Chem. Phys., **92**, (1990), 7012

52. D. A. Fletcher, K. J. Jung, and T. C. Steimle, J. Chem. Phys., **99**, (1993), 4288

53. B. Simard, C. Masoni, and P. A. Hackett, J. Mol. Spectrosc., **136**, (1989), 44

54. S. L. Peter and T. M. Dunn, J. Chem. Phys., **90**, (1989), 5333

55. W. J. Balfour, A. J. Merer, H. Niki, B. Simard, and P. A. Hackett, J. Chem. Phys., **99**, (1993), 3288

56. W. J. Balfour, C. X. W. Qian, and C. Zhou, J. Chem. Phys., **106**, (1997), 4383

57. C. Zhou, W. J. Balfour, and C. X. W. Qian, J. Chem. Phys., **107**, (1997), 4473

58. A. S. C. Cheung, R. M. Gordon, and A. J. Merer, J. Mol. Spectrosc., **87**, (1981), 289

59. E. Domek, Sitzungsber. Akad. Wiss. Wien, 2a, **119**, (1910), 437

60. H. Lefebvre-Brion and R. W. Field, *Perturbations in the Spectra of Diatomic Molecules*, (Academic Press, Inc., Orlando, Florida, 1986)

61. A. S. C. Cheung, A. M. Lyyra, A. J. Merer, and A. W. Taylor, J. Mol. Spectrosc., **102**, (1983), 224

62. J. H. Walker, T. E. H. Walker, and H. P. Kelly, J. Chem. Phys., **57**, (1972), 2094

63. P. R. Scott and W. G. Richards, J. Chem. Phys., **63**, (1975), 1690

64. C. W. Bauschlicher and S. R. Langhoff, Chem. Phys. Lett., **145**, (1988), 205

65. M. Sodupe, J. M.Luch, A. Oliva, F. Illas, and J. Rubio, J. Chem. Phys., **92**, (1990), 2478

66. A. W. Taylor, Ph.D. Dissertation, University of British Columbia, 1986

67. M. Krauss and W. J. Stevens, J. Chem. Phys., **82**, (1985), 5584

68. G. Herzberg, *Molecular Spectra and Molecular Structure, I. Spectra of Diatomic Molecules*, (Krieger Publishing Company, Malabar, Florida, 1989)

69. P. F. Bernath, *Spectra of Atoms and Molecules*, (Oxford University Press, Inc., 1995)

70. M. Born and R. Oppenheimer, Ann. Physik, **84**, (1927), 457

71. L. D. Landau and E. M. Lifshitz, *Relativistic Quantum Theory*, (Pergamon Press Ltd., New York, 1977)

72. L. D. Landau and E. M. Lifshitz, *Quantum Mechanics*, (Pergamon Press Ltd., New York, 1977)

73. I. Kopp and J. T. Hougen, Can. J. Phys., **45**, (1967), 2581

74. J. M. Brown, J. T. Hougen, K. P. Huber, J. W. C. Johns, I. Kopp, H. Lefebvre-Brion, A. J. Merer, D. A. Ramsay, J. Rostas, and R. N. Zare, J. Mol. Spectrosc., **55**, (1975), 500

75. R. N. Zare, *Angular Momentum - Understanding Spatial Aspects in Chemistry and Physics*, (John Wiley & Sons, Inc., New York, 1988)

76. P. R. Bunker, J. Mol. Spectrosc., **28**, (1968), 422

77. J. L. Femenias, Can. J. Phys., **55**, (1977), 1733

78. R. D. L. Kronig, *Band Spectra and Molecular Structure*, (Cambridge, London, 1930)

79. J. M. Brown, E. A. Colbourn, J. K. G. Watson, and F. D. Wayne, J. Mol. Spectrosc., **74**, (1979), 294

80. E. Hirota, J. M. Brown, J. T. Hougen, T. Shida, and N. Hirota, J. Mol. Spectrosc., **168**, (1994), 628

81. J. T. Hougen, *The Calculation of Rotational Energy Levels and Rotational Line Intensities in Diatomic Molecules*, Nat. Bur. Stand. (U.S.), monograph 115, 1970

82. T. G. Dietz, M. A. Duncan, D. E. Powers, and R. E. Smalley, J. Chem. Phys., **74**, (1981), 6511

83. D. E. Powers, S. G. Hansen, M. E. Geusic, D. L. Michalopoulos, and R. E. Smalley, J. Chem. Phys., **78**, (1983), 2866

84. S. C. Richtsmeier, E. K. Parks, K. Liu, L. G. Pobo, and S. J. Riley, J. Chem. Phys., **82**, (1985), 3659

85. L. A. Heimbrook, M. Rasanen, and V. E. Bondybey, J. Phys. Chem., **91**, (1987), 2468

86. B. Simard, S. A. Mitchell, L. M. Hendel, and P. A. Hackett, Faraday Discuss. Chem. Soc., **86**, (1988), 163

87. D. Proch and T. Trickl, Rev. Sci. Instrum., **60**, (1989), 713

88. W. Demtroder *Laser spectroscopy - Basic Concepts and Instrumentation*, (Springer-Verlag Berlin Heidelberg, Berlin, 1981)

89. C. W. Bauschlicher, J. Chem. Phys., **86**, (1987), 5591

90. A. E. Stevens, C. S. Feigerle, and W. C. Lineberger, J. Chem. Phys., **78**, (1983), 5420

91. W. J. Balfour, B. Lindgren, and S. O'Connor, Phys. Scr., **28**, (1983), 551

92. R. S. Ram, P. F. Bernath, and S. P. Davis, J. Mol. Spectrosc., **179**, (1996), 282

93. J. M. Delaval, C. Dufour, and J. Schamps, J. Phys. B, **13**, (1980), 4757

94. S. M. Harris and R. F. Barrow, J. Mol. Spectrosc., **84**, (1980), 334

95. G. V. Chertihin, L. Andrews, and M. Neurock, J. Phys. Chem., **100**, (1996), 4609

96. A. Fiedler and S. Iwata, Chem. Phys. Lett., **271**, (1997), 143

97. P. E. M. Siegbahn and M. R. A. Blomberg, Chem. Phys., **87**, (1984), 189

98. M. R. A. Blomberg and P. E. M. Siegbahn, Theor. Chim. Acta, **81**, (1992), 365

99. I. Shim, H. C. Finkbeiner, and K. A. Gingerich, J. Phys. Chem., **91**, (1987), 3171

100. I. Shim and K. A. Gingerich, Surf. Sci., **156**, (1985), 623

101. I. Shim and K. A. Gingerich, J. Chem. Phys., **81**, (1984), 5937

102. M. D. Allen, T. C. Pesch, and L. M. Ziurys, Astrophys. J., **472**, (1996), L57

103. D. J. Brugh and M. D. Morse, J. Chem. Phys. (to be published)

104. C. V. V. Prasad and P. F. Bernath, Astrophys. J., **426**, (1994), 812

105. C. H. Townes and A. L. Schawlow, *Microwave Spectroscopy*, (McGraw-Hill Book Company, 1955)

106. M. Barnes, M. M. Fraser, P. G. Hajigeorgiou, A. J. Merer, and S. D. Rosner, J. Mol. Spectrosc., **170**, (1995), 449

107. F. A. Cotton and R. A. Walton, *Multiple Bonds Between Metal Atoms*, (John Wiley & Sons, 1982)

108. S. J. Rixon, M. Sc. thesis, University of Victoria, 1996

109. D. Dai and K. Balasubramanian, J. Mol. Spectrosc., **158**, (1993), 455

110. O. Launila, A. M. James, and B. Simard, J. Mol. Spectrosc., **164**, (1994), 559

111. W. J. Balfour and R. S. Ram, J. Mol. Spectrosc., **100**, (1983), 164

112. W. J. Balfour and F. B. Orth, J. Mol. Spectrosc., **84**, (1980), 424

113. W. J. Balfour and R. S. Ram, Can. J. Phys., **62**, (1984), 1524

114. R. S. Ram, P. F. Bernath, W. J. Balfour, J. Cao, C. X. W. Qian, and S. J. Rixon, J. Mol. Spectrosc., **168**, (1994), 350

115. B. Pinchemel and J. Schamps, Chem. Phys., **18**, (1976), 481

116. W. Weltner, Ber. Bunsenges. Phys. Chem., **82**, (1978), 80

117. W. J. Balfour, J. Cao, C. X. W. Qian, and S. J. Rixon, J. Mol. Spectrosc., **183**, (1997), 113

118. J. Cao, W. J. Balfour, and C. X. W. Qian, (to be published)

119. R. L. Martin, and P. J. Hay, J. Chem. Phys., **75**, (1981), 4539

120. A. N. Samoilova, Y. M. Efremov, and L. V. Gurvich, J. Mol. Spectrosc., **86**, (1981), 1

121. E. Broclawik and D. R. Salahub, Int. J. Quant. Chem., **52**, (1994), 1017

122. Uvic, unpublished results on RhN

123. I. Shim, K. Mandix, and K. A. Gingerich, J. Mol. Structure, **393**, (1997), 127

124. T. C. Steimle, A. J. Marr, S. A. Beaton, and J. M. Brown, J. Chem. Phys., **106**, (1997), 2073

125. K. Jansson and R. Scullman, J. Mol. Spectrosc., **43**, (1972) 208

126. T. C. Steimle, K. Y. Jung, and B. Z. Li, J. Chem. Phys., **103**, (1995), 1767

127. W. Weltner and D. McLeod, J. Phys. Chem., **69**, (1965), 3488

128. T. M. Dunn and K. M. Rao, Nature (London), **222**, (1969),266

129. A. Al-Khalili, G. Edvinsson, U. Hallsten, A. Taklif, S. Wallin, and O. Launila, C1, 24th International Symposium on Free Radicals, August 17-22, 1997, Tallberg, Sweden

130. R. S. Ram and P. F. Bernath, J. Opt. Soc. Am. B, **11**, (1994), 225

131. G. J. Mains and J. M. White, J. Phys. Chem., **95**, (1991), 112

132. unpublished results on RhO, Uvic

133. L. A. Kaledin, J. E. McCord, and M. C. Heaven, J. Mol. Spectrosc., **173**, (1995), 37

134. A. J. Marr, M. E. Flores, and T. C. Steimle, J. Chem. Phys., **104**, (1996), 8183

135. C. Linton, M. Dulick, R. W. Field, P. Carette, P. C. Leyland, and R. F. Barrow, J. Mol. Spectrosc., **102**, (1983), 441